Title

Brain Connectivity, Methodology and Applications to the Normal Brain and Dementia

Permalink

https://escholarship.org/uc/item/2v41174x

Author

Daianu, Madelaine

Publication Date

2014

Peer reviewed|Thesis/dissertation

UNIVERISTY OF CALIFORNIA

Los Angeles

Brain Connectivity,

Methodology and Applications to the Normal Brain and Dementia

A dissertation submitted in partial satisfaction

of the requirements for degree Doctor of Philosophy

in Bioengineering

By

Madelaine Daianu

2014

ABSTRACT OF THE DISSERTATION

Brain Connectivity,

Methodology and Applications to the Normal Brain and Dementia

by

Madelaine Daianu

Doctor of Philosophy in Bioengineering

University of California, Los Angeles, 2014

Professor Daniel Ennis, Chair

The human brain, one of the most complex structures known, is composed of more than 100 billion neurons that process, disseminate, transform and attract information through more than a 100 trillion synapses. Interactions among brain cells give us the freedom to think, feel, move and maintain homeostasis all at the same time. To understand the systematic communication among brain cells, we require not only knowledge at elementary levels, but also at macroscopic level – aimed at the discovery of the emerging patterns and properties of neuronal interactions. Here, we used diffusion imaging to reveal the organization of neural pathways by capturing subtle changes in white matter make-up through measures sensitive to fiber integrity and microstructure – otherwise not detectable with standard MRI techniques. In addition, tractography was performed to infer neural pathways and connectivity patterns, yielding additional, more complex mathematical metrics describing the "connectomics" of brain networks. To assess the brain's network, graph theory was used – a branch of mathematics employed to model the topological

organization of the white matter structure. Similarly, algebraic connectivity was also applied, not previously seen in the context of brain networks, which uses linear algebra and matrix theory to study the properties of graphs. These methods have all contributed to the discovery of potential biomarkers that can aid the understanding of white matter deterioration in the brain; special focus was directed towards neurodegenerative diseases such as Alzheimer's disease and all of its clinical stages, as well as frontotemporal dementia.

The dissertation of Madelaine Daianu is approved.

Paul M. Thompson

Luminita A. Vese

Ricky Taira

Danny J.J. Wang

Daniel Ennis, Committee Chair

University of California, Los Angeles

2014

TABLE OF CONTENTS

LIST OF FIGURES

ACKNOWLEDGEMENTS

To all of my mentors, family, friends and colleagues – thank you for your valuable support. Special thanks to Dr. Neda Jahanshad for her dedication as a mentor.

Co-author Acknowledgements

Chapters 1 through 6 are based on the following articles. I would like to thank all the co-authors for their great contribution:

- **Daianu M**, Jahanshad N, Villalon-Reina JE, Leonardo CD, Mendez MF, Bartzokis G, Thompson PM. Cost inefficient structural brain networks in frontotemporal dementia and Alzheimer's disease. **Brain**. *To be submitted,* March 2014.

- **Daianu M,** Jahanshad N, Nir TM, Leonardo CD, Jack CR Jr, Weiner MW, Bernstein M, Thompson PM. Algebraic connectivity of brain networks shows patterns of segregation leading to reduced network robustness in Alzheimer's disease. **MICCAI 2014,** Boston, MA, USA, *submitted*, February 28 2014.

- **Daianu M**, Jahanshad N, Nir TM, Dennis EL, Leonardo CD, Jack CR Jr, Weiner MW, Bernstein M, Thompson PM. Structural brain network and rich club disruptions in mild

cognitive impairment and Alzheimer's disease. **Neurobiology of Aging**, *submitted*, January 7 2014.

- Roussotte FF*, **Daianu M***, Jahanshad N, Leonardo CD, Thompson PM. Neuroimaging and Genetic Risk for Alzheimer's Disease and Addiction-Related Degenerative Brain Disorders. **Brain Imaging and Behavior**, 2013 Oct 20. [Epub ahead of print] **indicates equal contribution.*

- **Daianu M**, Jahanshad N, Nir TM, Toga AW, Jack CR Jr, Weiner MW, Thompson PM and the Alzheimer's Disease Neuroimaging Initiative. Breakdown of Brain Connectivity between Normal Aging and Alzheimer's Disease: A Structural *k*-core Network Analysis. **Brain Connectivity**, 2013;3(4):407-22. [**Press Release**]

- **Daianu M**, Dennis EL, Jahanshad N, Nir TM, Toga AW, Jack CR Jr, Weiner MW, Thompson PM and the Alzheimer's Disease Neuroimaging Initiative. Disrupted Brain Connectivity in Alzheimer's Disease: Effects of Network Thresholding. In **MMBC'13 MICCAI** Workshop on Mathematical Methods for Brain Connectivity, Nagoya, Japan, *accepted,* June 2013.

- **Daianu M**, Jahanshad N, Nir TM, Dennis EL, Toga AW, Jack CR Jr, Weiner MW, Thompson PM and the Alzheimer's Disease Neuroimaging Initiative (2012). Analyzing the Structural *k*-Core of Brain Connectivity Networks in Normal Aging and Alzheimer's Disease. In **NIBAD'12 MICCAI** Workshop on Novel Imaging Biomarkers for Alzheimer's Disease and Related Disorders, Nice, France, 2012, pp. 52–62.

- **Daianu M**, Jahanshad N, Dennis EL, Toga AW, McMahon KL, de Zubicaray GI, Martin NG, Wright MJ, Hickie IB, Thompson PM. Lateralization in the Developmental Human

Connectome: 4-Tesla High Angular Resolution Diffusion Imaging (HARDI) Tractography in 576 Twins. **IEEE ISBI 2012**, pp. 526–529.

VITA

2008-2011	Grader, Mathematics Department, University of Illinois a Chicago
2008-2011	Undergraduate researcher, Neural Engineering and Vision Laboratory, University of Illinois at Chicago
2009	Laboratory technician, Neural Engineering and Vision Laboratory, University of Illinois at Chicago
2009-2010	Tutor in mathematics and bioengineering related courses, University of Illinois at Chicago
2010	Undergraduate Researcher, NSF Supported Internship, Lavik Lab, Case Western Reserve University
2010-2011	Undergraduate Researcher, Laboratory for Product and Process Design, University of Illinois at Chicago
2011	Awarded 1st place in the Medical Application Category, Engineering EXPO, University of Illinois at Chicago
2011	BS in Bioengineering – Concentration in Neuroscience and Minor in Mathematics, *Cum Laude*, University of Illinois at Chicago
2012-2013	Grantee of National Institute of Health Ruth L. Kirschstein National Research Service Award (T32-GM008185) training grant for Systems and Integrative Biology (SIB), UCLA
2012	Travel grant to the IEEE International Symposium on Biomedical Imaging, Barcelona, Spain

2013	Invited speaker for the Medical Image Computing and Computer Assisted Intervention: Mathematical Methods for Brain Connectivity Workshops, Nagoya, Japan
2013	Invited peer-reviewer for Human Brain Mapping
2011-present	Co-author on 11 peer-reviewed publications, 6 peer-reviewed conference papers and 5 conference abstracts

SELECT PUBLICATIONS

1. **Daianu M**, et al. Cost inefficient structural brain networks in frontotemporal dementia and Alzheimer's disease. **Brain**. *To be submitted,* March 2014.

2. **Daianu M**, et al. Structural brain network and rich club disruptions in mild cognitive impairment and Alzheimer's disease. **Neurobiology of Aging**, *submitted*, January 7 2014.

3. **Daianu M,** et al. Algebraic connectivity of brain networks shows patterns of segregation leading to reduced network robustness in Alzheimer's disease. **MICCAI 2014,** Boston, MA, USA, *submitted*, February 28 2014.

4. Roussotte FF*, **Daianu M***, et al. **Brain Imaging and Behavior**, 2013 Oct 20. [Epub ahead of print] **indicates equal contribution.*

5. **Daianu M**, et al. Breakdown of Brain Connectivity between Normal Aging and Alzheimer's Disease: A Structural *k*-core Network Analysis. **Brain Connectivity**, 2013;3(4):407-22. [Press Release]

6. **Daianu M**, et al. Disrupted Brain Connectivity in Alzheimer's Disease: Effects of Network Thresholding. In **MMBC'13 MICCAI** Workshop on Mathematical Methods for Brain Connectivity, Nagoya, Japan*, accepted,* June 2013.

7. **Daianu M**, et al. Alzheimer's Disease Disrupts Rich Club Organization in Brain Connectivity Networks**. IEEE ISBI** 2013, pp. 266 – 269.

8. **Daianu M**, et al. Analyzing the Structural k-Core of Brain Connectivity Networks in Normal Aging and Alzheimer's Disease. In **NIBAD'12 MICCAI** Workshop on Novel Imaging Biomarkers for Alzheimer's Disease and Related Disorders, Nice, France, 2012, pp. 52–62.

9. **Daianu M**, et al. Lateralization in the Developmental Human Connectome: 4-Tesla High Angular Resolution Diffusion Imaging (HARDI) Tractography in 576 Twins. **IEEE ISBI** 2012, pp. 526–529.

10. Eschenburg E, et al. Analysis of Structural Brain Connectivity in 6 Cases of Hemispherectomy. **ISBI** 2014, *accepted,* November 2013.

11. Joshi A, et al. Neural Pathways correlates of resting state skin conductance levels in dementia patients. **Social Neuroscience**. *To be submitted,* March 2014.

CHAPTER 1

Introduction

Graph theory studies the properties of mathematical structures, or graphs, designed to model connections between pairs of points. Graph theory was first applied by Leonhard Euler in 1736, who prefigured the idea of topology through the negative resolution for his famous Seven Bridges of Konigsberg problem. His assessment that there was no feasible way to walk through the city of Konigsberg by crossing each of the seven bridges only once, has helped him develop rigorous technique of analysis for the now emerging field of graph theory (Euler, 1741).

Since Euler, graph theory has been applied to many distinct sciences, including social sciences – used to understand the web of social relations, computer science, and currently, natural sciences with particular interest in the study of complex biological systems (Sporns, 2011). Modern network approaches using theoretical network models have vastly contributed to the emerging field of *brain connectomics* – a field of analysis that combines some of the most advanced areas of study in medicine, neuroscience and engineering to characterize and quantify the brain in terms of its structural and functional connections. Brain connectomics, also refereed to as *brain connectivity*, is the leading focus of this PhD work with studies embracing the analysis of neuroimaging from its raw form to advanced mathematical applications, aimed at the discovery of disease biomarkers.

1.1 Neuroimaging and brain connectomics

The brain is a network of multiple scales and can be described at elementary level, in terms of its synaptic connections, at a higher level, in terms of its connections between cortico-cortico and

cortico-deep gray neurons, or at a more macroscopic level, looking at connections between cortical areas in the form of bundles of white matter tracts (Petrella, 2011). The complex macroscopic structural organization of the brain can be visualized through *in vivo* brain mapping methods that unveil the integrity of the brain's white matter. The rapidly emerging field of connectomics employs data from structural imaging – diffusion weighted imaging (DWI) as well as methods of analysis such as the one described above – graph theory, a branch of mathematics that has been employed lately to model the topological organization of brain's networks. These forms of analysis have been of great interest in the disease-oriented neuroimaging research and are aimed at testing a long-suspected idea that each focal neurodegenerative syndrome targets a specific large-scale network (Seeley, 2010).

1.2 Diffusion tensor imaging

The highly myelinated white matter make-up of the brain comprises of interconnecting axons that allow information transfer between functioning gray matter structures and cortical regions. Disruptions in axonal integrity can alter the communication among brain regions, leading to neuronal degeneration and other psychiatric illnesses. The composition of the white matter allows the calculation of the apparent diffusivity of water molecules along the fiber tracts, which depends of the angle between the fiber-tract axis and the magnetic field gradient (Basser et al., 1994). Myelinated cell membranes, and other oriented molecular structures, favor water diffusion along the membrane and obstruct it perpendicular to the membrane; this is known as anisotropic diffusion at macroscopic (voxel size) scale. From a sequence of DWIs, three orthopedic directions and principal diffusivities can be determined to describe the effective

diffusion coefficient at each voxel in anisotropic medium and is known as *diffusion tensor*

imaging (DTI; Basser et al., 1994; Basser and Pierpaoli, 1996).
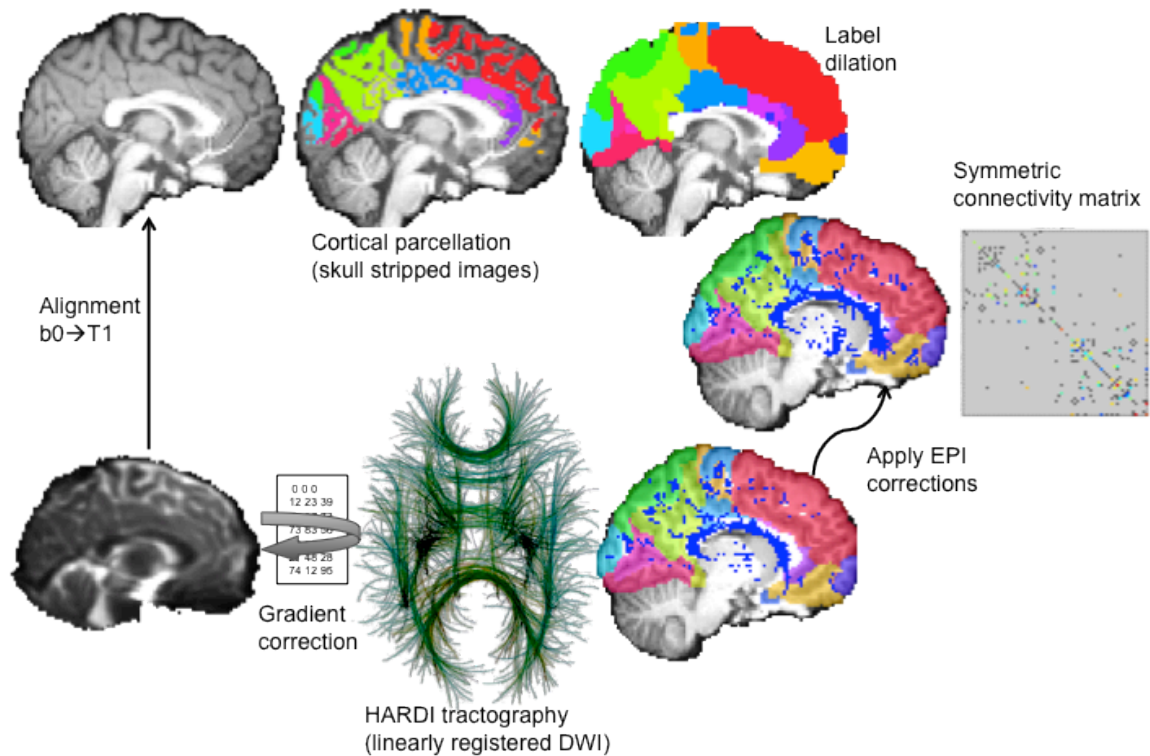
Figure 1. Workflow illustrating the assessment of (*N*) cortical parcellations into regions of interest using high-resolution anatomical T1-weighted images in parallel with full brain tractography performed using DTI. Images are registered into the same space and the proportion of fibers interconnecting a pair of cortical regions is described in an element-wise *NxN* connectivity matrix (Jahanshad et al., 2013).

DTI has been used to derive measures of diffusion anisotropy and isotropy of water molecules, fiber tract organization and macrostructural organization of white matter (Basser and Pierpaoli, 1996) – otherwise not detectable with standard MRI techniques. More recently, advancements in image acquisition and reconstruction have been employed to aid the limitations of DTI, which oftentimes lead to artificial reductions in anisotropic measures and inflation of the diffusion values in voxels where fiber crossing occurs. The single tensor model used by DTI may be

incapable or resolving adjacency and intermixing of fibers pathways, therefore, *high angular resolution imaging* (HARDI; Tuch et al., 2002) and diffusion spectroscopic imaging (DSI, Wedeen et al., 2012) have been developed. In this work, a constant solid angle orientation distribution function (CSA-ODF) was used, which determines the marginal probability of diffusion in a given direction (Aganj, 2010).

The reconstruction of white matter microstructure at voxelwise level is known as *tractography* and allows the tracing of fiber bundles throughout the brain. After computing the CSA-ODF, the white matter bundles were recovered using the Hough transform method – a form of probabilistic tractography. Throughout this work, tractography is used in combination with anatomical T1-weighted MRI images to infer neural pathways and connectivity patterns, yielding more complex mathematical metrics describing fiber networks in the form of connectivity matrices (**Fig. 1**). The computational methods will be further described in the upcoming chapters.

1.3 *NxN* **Connectivity matrix creation**

Considering the white matter tractography and the cortical parcellations from anatomical T1-weighted images, the fiber bundles connecting each pair of ROI can be detected. From this, a baseline *NxN* connectivity matrix can be created for each subject. Each element in the matrix can describe various measures. For instance, it can describe the density of fibers connecting two ROIs (*i.e.*, the total number of fibers), or the estimated proportion of the total number of fibers (*i.e.*, normalized fiber density).

1.4 Algebraic Connectivity

The connectivity patterns can be described as mathematical representation of a network, or a graph, comprising of nodes and sets of edges that interconnect these nodes. The network nodes are typically defined as regions of interest (ROIs) - in our case on the cortex, segmented from anatomical MRI. These nodes are considered to be linked by 'edges' whose weights denote some measure of connectivity between the two regions, such as the density or integrity of fiber tracts. Topological changes in the brain's networks may be analyzed using graph theory, as introduced above, or more exotic connectivity measures, such as algebraic connectivity.

Algebraic graph theory is a branch of mathematics that uses linear algebra and matrix theory to study the properties of graphs (Norman, 1993). In algebraic graph theory, the Laplacian matrix is used to study the *spectrum* of a graph, which is the topic of study in another branch of mathematics known as *spectral graph theory* (Mohar, 1991). Recently, spectral theory has been applied to better reconstruct brain activity by considering the edges of a graph describing anatomical connectivity (Hammond et al., 2013). Other applications of algebraic graph theory are in the fields of circuit design, parallel and distributive computing, data representation (Chung et al., 1994) and the online web (Bounova et al., 2012). In this work, we are the first to introduce the application of algebraic graph theory to extract graph properties from human brain connectivity networks to better understand the structural changes in Alzheimer's disease.

1.5 Organization of the dissertation

The following chapters describe how brain connectivity, with the use of various forms of graph theory, can quantify topological changes and alterations in the developing brain and most importantly, in dementia. Topological changes in the brain's network may be applied to study

either structural and functional brain networks (Sporns, 2011; Lee et al., 2012). All chapters presented here employ the analysis of structural connectivity.
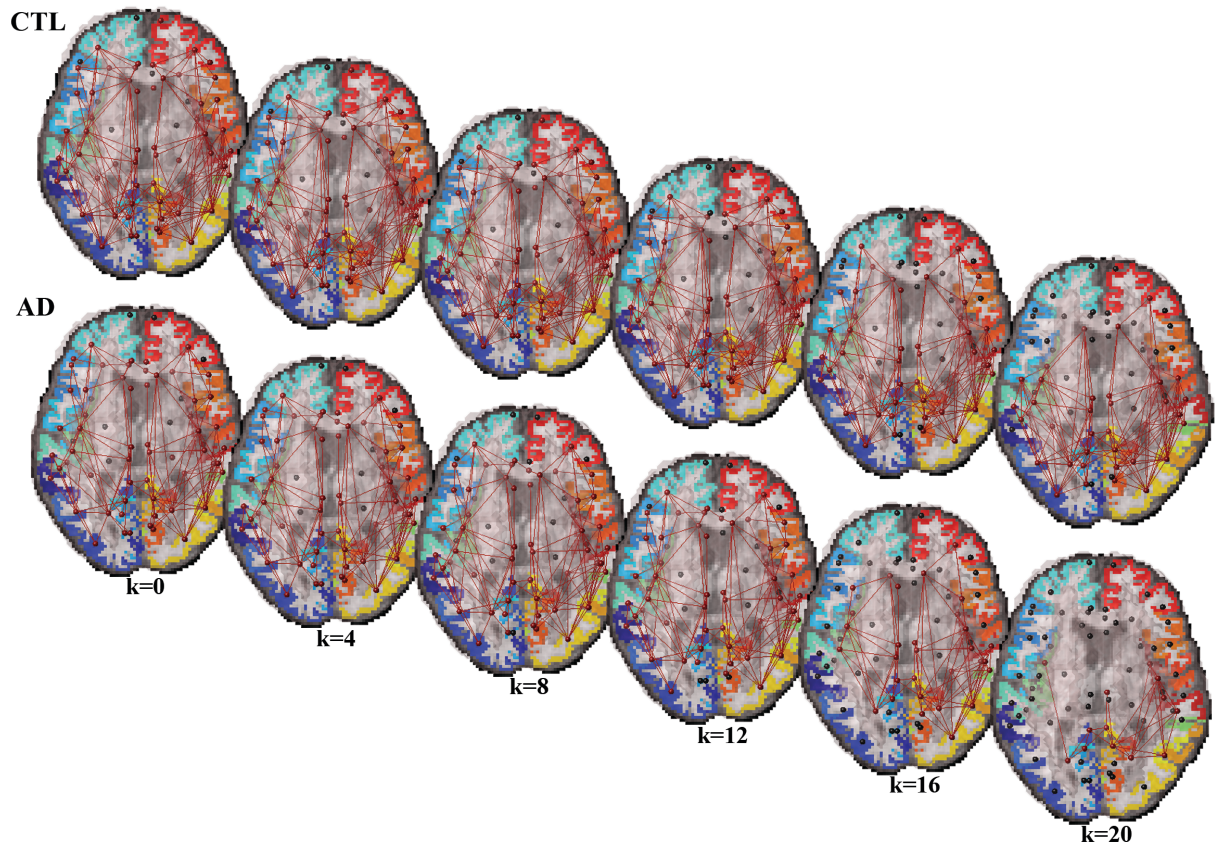
Figure 2. Set of network nodes and edges illustrating thresholding effects averaged in 50 controls (CTL) and 37 Alzheimer's disease (AD) subjects.

All upcoming work is intended to aid the understanding of the developing, aging and diseased brain – with special attention given to the destructive alterations caused by Alzheimer's disease (AD). In *Chapter 2*, efforts are directed towards understanding the disruptions in the structural brain networks of AD subjects. This was assessed using densely interconnected networks (*k*-cores) where drastic alterations were found among the white matter integrity, specifically in the left hemisphere of AD patients. Here, we show that graph metrics can serve as a distillation of

the overall brain's network leading to highlighted disease effects, such as a more pronounced loss in nodal assignments in the left hemisphere of AD subjects.

Chapter 3 focuses on understanding the challenges in the post-processing of brain images and applications of various levels of brain network thresholding (**Fig. 2**). Network thresholding can be used to remove unreliable connections, and therefore, enhancing the SNR as well as important disease effects manifested on the connectivity networks in the diseased brain. As an extended application to this, a variety of graph theory metrics were applied to quantify networks, at a wide range of thresholding levels, including the "rich club" coefficient – *i.e.*, a core of nodes with a high degree (k) – that are more densely interconnected among themselves than expected by chance. With disease progression, the rich club effect increased, which was not expected or shown a priori. In working out how this may arise, a range of connectivity metrics, both functions and non-functions of the rich club coefficient, were assessed (*i.e.*, nodal degree, efficiency, path length, clustering coefficient etc.). Finally, all measures were ranked in the order of their effect size for distinguishing patients from controls, as possible biomarkers for AD.

In *Chapter 4*, a network communication cost measure is introduced to study aspects of cost related to the network's spatial embedding. Cost networks are functions of the fiber density and path length that interconnect pairs of ROIs – the higher the number of fibers linking two brain regions and the longer their fiber length, the higher the communication cost of the network. Our findings indicate that high-cost networks structures uptake more than 50% of the brain's capacity in both healthy and disease; these highly central, high-cost networks are disrupted in neurodegenerative diseases, such as frontotemporal dementia (FTD) and early AD, indicating that disease strikes the core composition of the brain's connectome.

The second part of *Chapter 4* introduces the notion of algebraic connectivity in assessing brain networks – never before applied to assess connectivity in the context of dementia. Linear algebra derived measures, such as the Fiedler value (*i.e.*, second smallest eigenvector of a Laplacian matrix) along with additional supporting measures, detected a decrease in the AD brain network's robustness with increasingly segregated network components, indicating a less efficient distribution of the network overall, when compared to normal participants.

Chapter 5 we assessed HARDI data on how brain connectivity measures relate to brain asymmetry (left vs. right hemispheric differences) in a large healthy developmental dataset. This is important as asymmetries can heighten interest in possible differences in the vulnerability of the two hemispheres to various types of neuropathology and age-related decline (Thompson et al., 2003).

Chapter 6 is a full review of multi-modal neuroimaging technologies that can be used to study the brain during different stages of AD. Furthermore, this work reviews recent neuroimaging studies of genetic polymorphism associated with increased risk for late-onset AD.

Finally, *Chapter 7* introduces *Future Goals* intended for postdoctoral work on innovative and novel image processing protocols on DWIs in a human Tau mouse model. Preliminary work on a DWI processing protocol in mouse is introduced, which is the first protocol to be developed in the *Imaging Genetics Center* to assess structural changes in mouse. This is further aimed at large scale connectivity analyses and the validation of mathematical models to link imaging signals to cellular and biochemical correlates.

CHAPTER <u>2</u>

Disruptions in the Alzheimer's disease connectome

2.1 The structural *k*-Core in Alzheimer's disease

This section is adapted from:

Daianu M, et al. Breakdown of Brain Connectivity between Normal Aging and Alzheimer's Disease: A Structural *k*-core Network Analysis. Brain Connectivity, 2013;3(4):407-22. [Press Release]

Breakdown of Brain Connectivity Between Normal Aging and Alzheimer's Disease: A Structural *k*-Core Network Analysis

Madelaine Daianu,[1] Neda Jahanshad,[1] Talia M. Nir,[1] Arthur W. Toga,[1] Clifford R. Jack, Jr.,[2]
Michael W. Weiner,[3,4] and Paul M. Thompson,[1] for the Alzheimer's Disease Neuroimaging Initiative[*]

Abstract

Brain connectivity analyses show considerable promise for understanding how our neural pathways gradually break down in aging and Alzheimer's disease (AD). Even so, we know very little about how the brain's networks change in AD, and which metrics are best to evaluate these changes. To better understand how AD affects brain connectivity, we analyzed anatomical connectivity based on 3-T diffusion-weighted images from 111 subjects (15 with AD, 68 with mild cognitive impairment, and 28 healthy elderly; mean age, 73.7 ± 7.6 SD years). We performed whole brain tractography based on the orientation distribution functions, and compiled connectivity matrices showing the proportions of detected fibers interconnecting 68 cortical regions. We computed a variety of measures sensitive to anatomical network topology, including the structural backbone—the so-called "*k*-core"—of the anatomical network, and the nodal degree. We found widespread network disruptions, as connections were lost in AD. Among other connectivity measures showing disease effects, network nodal degree, normalized characteristic path length, and efficiency decreased with disease, while normalized small-worldness increased, in the whole brain and left and right hemispheres individually. The normalized clustering coefficient also increased in the whole brain; we discuss factors that may cause this effect. The proportions of fibers intersecting left and right cortical regions were asymmetrical in all diagnostic groups. This asymmetry may intensify as disease progressed. Connectivity metrics based on the *k*-core may help understand brain network breakdown as cognitive impairment increases, revealing how degenerative diseases affect the human connectome.

Key words: Alzheimer's disease; asymmetry; brain connectivity; diffusion tensor imaging; efficiency; *k*-core; mild cognitive impairment; nodal degree; small-world; tractography

Introduction

ALZHEIMER'S DISEASE (AD) is a progressive, degenerative brain disease affecting around one in eight people (13%) aged 65 or older (Alzheimer's Association Colorado, 2011). As AD progresses, many cognitive domains gradually decline, including memory (Filippi et al., 2012); beta-amyloid and tau proteins accumulate in the brain, leading to inflammation, neuronal atrophy, and cell death (Wang et al., 2012). The brain's gray matter shows widespread neuronal loss, and many studies have revealed widespread cortical and hippocampal atrophy in AD. As neurons are lost, white matter volume is also reduced, due to both myelin degeneration and axon loss in neural fiber tracts (Bartzokis, 2009; Braak and Braak, 1996; Braskie et al., 2012a, b; Hua et al., 2008). Fluid-attenuated inversion-recovery or T2-weighted scans are often used to evaluate white matter hyperintensities—a sign of cerebrovascular disease—and there is growing evidence that breakdown of the brain's fiber networks may explain some of the symptoms as the disease progresses.

As new methods emerge to assess brain connectivity, some research groups have begun to use diffusion-weighted imaging (DWI) and resting state functional magnetic resonance imaging (rs-fMRI) to study the global breakdown of

---

[1]Department of Neurology, Imaging Genetics Center, Laboratory of Neuro Imaging, UCLA School of Medicine, Los Angeles, California.
[2]Department of Radiology, Mayo Clinic, Rochester, Minnesota.
[3]Department of Radiology, Medicine, and Psychiatry, University of California San Francisco, San Francisco, California.
[4]San Francisco VA Medical Center, U.S. Department of Veteran Affairs, San Francisco, California.

network integration in degenerative disease (Buckner, 2005; Delbeuck et al., 2003; Gili et al., 2012; Wegrzyn et al., 2011). Neuropsychological deficits are often attributed to a *disconnection* between brain regions (Wernicke, 1874/1977; Lichtheim, 1885); the notion of a "disconnection syndrome" was introduced by Geschwind (1965).

Evidence supporting a disconnection process in AD has emerged from various techniques, including MRI, electroencephalography, and positron emission tomography (PET). On MRI, AD patients show a lower density of associative white matter fibers in the cingulum, the splenium of the corpus callosum and the superior longitudinal fasciculus (Rose et al., 2000). At the same time, interhemispheric functional synchronization also breaks down (Azari et al., 1992). Coherence studies by Wada and colleagues (1998) found disturbed interhemispheric functional connectivity in AD. Interhemispheric disturbances in AD have been linked to the disconnection syndrome observed clinically (Delbeuck et al., 2003). PET studies also show reduced metabolism in a network of regions, with greater amyloid deposition in the posterior cingulate, retrosplenial, and lateral parietal cortex (Buckner, 2005). fMRI also shows deactivated regions that overlap with medial parietal/posterior cingulate regions that show reduced resting metabolic activity in AD subjects, compared to normal elderly and young adults (Lustig et al., 2003).

Diffusion imaging has recently been added to several large-scale neuroimaging studies, including the Alzheimer's Disease Neuroimaging Initiative (ADNI), to monitor white matter deterioration using metrics not available with standard anatomical MRI. Diffusion MRI yields measures related to fiber integrity in AD, such as the mean diffusivity and fractional anisotropy of local water diffusion (Clerx et al., 2012); in addition, tractography methods can infer neural pathways and connectivity patterns, yielding additional, more complex mathematical metrics describing fiber networks.

Network analysis has only recently been applied to study AD. Many mathematically novel metrics have been proposed, such as a network's "structural backbone"—or *k*-core (Hagmann et al., 2008)—but have not yet been studied in AD. Here, we analyzed several network measures in normal elderly subjects, and people with early and late mild cognitive impairment (MCI), and AD. We mapped the whole brain, left, and right hemisphere "structural cores" of the brain in Alzheimer's patients and compared them to the cores in healthy controls. A network's structural core is based on using *k*-core decomposition (Hagmann et al., 2008) to find important sets of nodes that are highly and mutually interconnected.* We hypothesized that the core graph of connections would highlight alterations and disconnections in regions that change structurally in AD versus controls, such as the temporal, parietal, and frontal association areas (Azari et al., 1992; Horwitz et al., 1987). We also expected network breakdown in the posterior cingulate, posterior medial cortex and lateral parietal cortex (Buckner, 2005; Lustig et al., 2003; Xie and He, 2012).

In addition to using *k*-core analysis for the first time to assess AD-associated anatomical network changes, we studied several global topological properties on the brain's binarized *k*-core. To avoid testing too many primary hypotheses, and thereby inflating the false positive rate or reducing power by applying a heavy correction for multiple comparisons, we chose for our primary analysis to strictly focus on the nodal degree, normalized characteristic path length, efficiency, normalized clustering coefficient, and normalized small-world effect, comparing AD patients and controls. All network properties were derived from the *k*-cores for each of the subjects. Also, we were interested in brain laterality in disease as some (but not all) prior studies report that the left hemisphere is more atrophied in AD with a greater reduction in gray matter (20–30% local loss), relative to the right hemisphere (Thompson et al., 2001). This lateralized brain dysfunction was also studied by Loewenstein and colleagues (1989) who reported left hemisphere hypometabolism in the frontal, temporal, parietal lobes, and basal ganglia-thalamus of AD patients. In their study, these apparent asymmetries were not correlated with the severity or duration of AD. Little is known about left-right hemisphere differences, and as interconnectivity may play a significant role in AD, we compared left and right hemisphere networks to see if first, network asymmetries were detectable in general, and second, if they were altered with the clinical progression of AD.

Methods

Subjects and diffusion imaging of the brain

Data collection for ADNI2 is still ongoing, at the time of writing (December 2012). The ADNI began in 2005 as a large multisite longitudinal study, which uses a variety of imaging methods (including MRI and PET) to study how AD progresses, and to define biomarkers to monitor and predict disease progression. The second phase of ADNI—known as ADNI2—added new imaging modalities—diffusion tensor imaging (DTI), rs-fMRI, and arterial spin labeling (Jack et al., 2010) to supplement the methods available to track disease progression.

Here we analyzed DWI from the 111 subjects with available data; Table 1 shows their demographics and diagnostic information. All 111 subjects underwent whole brain MRI scanning on 3 T GE Medical Systems scanners, at a variety of sites across North America. Table 2 shows a breakdown of the

TABLE 1. DEMOGRAPHIC INFORMATION FOR ALZHEIMER'S DISEASE NEUROIMAGING INITIATIVE SUBJECTS SCANNED WITH DIFFUSION MAGNETIC RESONANCE IMAGING

	Controls	eMCI	lMCI	AD	Total
N	28	57	11	15	111
Age	73.0	73.7	76.3	75.6	73.7
Sex	14M/14F	34M/23F	7M/4F	9M/6F	64M/47F

One hundred eleven subjects had been scanned at the time of writing (December 2012). Their minimum age was 55.3 and maximum age was 90.4. Based on a *t*-test, the control group did not differ in age from any of the cognitively impaired groups. *p*-Values from *t*-tests comparing the mean age of the controls to the ages of the eMCI, lMCI and AD groups were 0.67, 0.094, and 0.30.

AD, Alzheimer's disease; eMCI, early mild cognitive impairment; lMCI, late mild cognitive impairment.

*Although a *k*-core is often a group of nodes that are highly and mutually interconnected, this does not always have to be the case. For low values of *k*, the *k*-cores are not highly connected (they have a low degree). Although the core itself must be interconnected, it may well not have a (relatively) higher level of interconnectivity than other subnetworks of the network.

TABLE 2. ACQUISITION SITES

Site	1	2	3	4	5	6	7	8	9	10	11	12	13	14
# scans	12	3	9	7	10	4	8	0	13	12	10	7	9	7

Number of scans acquired at each of the 13 sites, note there are no images from Site 8.

sites where the scans were acquired. Standard anatomical T1-weighted spoiled gradient echo sequences were collected (256×256 matrix; voxel size $= 1.2 \times 1.0 \times 1.0 \, \text{mm}^3$; inversion time [TI] $= 400 \, \text{msec}$, repetition time [TR] $= 6.984 \, \text{msec}$; echo time [TE] $= 2.848 \, \text{msec}$; flip angle $= 11°$) in the same session as the DWI (256×256 matrix; voxel size: $2.7 \times 2.7 \times 2.7 \, \text{mm}^3$; scan time $= 9 \, \text{min}$). Forty-six separate images were acquired for each DTI scan: 5 T2-weighted images with no diffusion sensitization (b_0 images) and 41 DWI ($b = 1000 \, \text{sec/mm}^2$). This protocol was chosen after a comparison of several different protocols, to optimize the signal-to-noise ratio in a fixed scan time (Jahanshad et al., 2010; Zhan et al., 2012; Zhan et al., 2013b).

Image analysis. Diffusion imaging may be used in conjunction with an automatically labeled set of regions from anatomical MRI to perform connectivity mapping and network analysis of the brain's fiber connections. Many analyses of brain connectivity have been conducted in this way (Dennis et al., 2012a, b; Dennis and Thompson, 2012; Jahanshad et al., 2011, 2012; Zalesky, 2009; Zhan et al., 2012). Connectivity matrices were compiled using a processing pipeline described previously (Braskie et al., 2012a, b; Dennis et al., 2012b; Jahanshad et al., 2011, 2012; Nir et al., 2012a, b).

Preprocessing and coregistration. Nonbrain regions were automatically removed from each T1-weighted MRI scan, and from a T2-weighted image from the DWI set using the FSL tool "BET" (http://fsl.fmrib.ox.ac.uk/fsl/). Anatomical scans subsequently underwent intensity inhomogeneity normalization using the MNI "nu_correct" tool (www.bic.mni.mcgill.ca/software/). All T1-weighted images were linearly aligned using FSL (with six degrees of freedom) to a common space with 1 mm isotropic voxels and a $220 \times 220 \times 220$ voxel matrix. The DWIs were corrected for eddy current distortions using the FSL tools (http://fsl.fmrib.ox.ac.uk/fsl/). For each subject, the five images with no diffusion sensitization were averaged, linearly aligned, and resampled to a downsampled version of their T1-weighted image ($110 \times 110 \times 110$, $2 \times 2 \times 2 \, \text{mm}$). b_0 maps were elastically registered to the T1-weighted scan to compensate for susceptibility artifacts. Images were visually inspected and there were no misalignments or cases where the field of view did not cover the full brain (i.e., cropping).

Tractography and cortical extraction. The transformation matrix from linearly aligning the mean b_0 image to the T1-weighted volume was applied to each of the 41 gradient directions to properly reorient the orientation distribution functions (ODF). We also performed whole brain tractography as described in (Aganj et al., 2011) on the sets of DWI volumes. Only linear registration was performed before tractography, as nonlinear registration before tractography could introduce possible processing artifacts. Gradient directions for each

DWI volume were corrected for according to the transformation matrix obtained from the linear registration. The tractography method uses a fiber detection approach based on the Hough transform; the Hough transform algorithm is a probabilistic fiber tracking method that is based on a voting process. The algorithm tests candidate three-dimensional (3D) polynomial curves in a diffusion imaging volume by assigning a score to each curve that passes through a seed point in a d-dimensional space. The goal of the algorithm is to find all potential curves that pass through chosen seed points while computing their scores and finally, selecting the curve with the highest score. Curves with the highest scores are stored in a d-dimensional array, called the Hough transform, and can represent potential fiber tracts in the brain. The results are obtained through a voting process where real-valued local votes for curves that are derived from diffusion data help define the candidate tract score. If the curve passes through a voxel, the vote (which is the integrand of the score integral) outputs a value other than zero, and if it does not pass though a voxel, then the output is zero (Aganj et al., 2011); to better detect crossing fibers, the method uses a constant solid angle orientation density function (Aganj et al., 2010) rather than a diffusion tensor, to model the local diffusion propagator. The angular resolution of the ADNI data is limited to avoid long scan times that may tend to increase patient attrition. Even so, this ODF model makes best use of this limited angular resolution (even if the protocol is not ideal for resolving fiber crossing).

Elastic deformations obtained from the echo-planar imaging distortion correction, mapping the average b_0 image to the T1-weighted image, were then applied to each recovered fiber's 3D coordinates to more accurately align the anatomy (we assume that the anatomical scan serves as a relatively undistorted anatomical reference). Each subject's dataset contained ~10,000 useable fibers (3D curves) in total.

Thirty-four cortical labels per hemisphere, listed in the Desikan-Killiany atlas (Desikan et al., 2006), were automatically extracted from all aligned T1-weighted structural MRI scans using FreeSurfer version 5.0 (http://surfer.nmr.mgh.harvard.edu/) (Fischl et al., 2004). The resulting T1-weighted images and cortical models were aligned to the original T1-weighted input image space and down-sampled using nearest neighbor interpolation (to avoid intermixing of labels) to the space of the DWIs. To ensure tracts would intersect labeled cortical regions, labels were dilated with an isotropic box kernel of width 5 voxels (Jahanshad et al., 2011).

$N \times N$ matrices representing structural connectivity. For each subject, a baseline 68×68 connectivity matrix was created (34 left and 34 right hemisphere regions of interest as listed in Table 3). Each matrix element represents the proportion of the total number of fibers, in that subject, connecting one cortical region to another. For the purposes of this paper, we use the word fiber to denote a single curve extracted via tractography; if all subjects had no detected fibers at all for a specific matrix element, then that connection was considered invalid, or insufficiently consistent in the population, and was not included in the analysis.

Brain network measures

Topological changes in the brain's networks may be analyzed using graph theory, a branch of mathematics

1	Banks of the superior temporal sulcus
2	Caudal anterior cingulate
3	Caudal middle frontal
4	—N/A—
5	Cuneus
6	Entorhinal
7	Fusiform
8	Inferior parietal
9	Inferior temporal
10	Isthmus of the cingulate
11	Lateral occipital
12	Lateral orbitofrontal
13	Lingual
14	Medial orbitofrontal
15	Middle temporal
16	Parahippocampal
17	Paracentral
18	*Pars opercularis*
19	*Pars orbitalis*
20	*Pars triangularis*
21	Peri-calcarine
22	Postcentral
23	Posterior cingulate
24	Precentral
25	Precuneus
26	Rostral anterior cingulate
27	Rostral middle frontal
28	Superior frontal
29	Superior parietal
30	Superior temporal
31	Supra-marginal
32	Frontal pole
33	Temporal pole
34	Transverse temporal
35	Insula

Index of the cortical labels extracted from the anatomical MRI scans using FreeSurfer (Fischl et al., 2004). In the latest version of FreeSurfer (version 5.0), cortical area #4 was not parcellated and is therefore, excluded; to ease comparison with prior papers using this numbering scheme, no region is assigned the number 4.

increasingly applied to study structural and functional brain networks (Lee et al., 2012; Sporns, 2011).

These types of analyses on brain networks require that the brain's components be represented as a graph. The network's nodes are typically defined as regions of interest segmented automatically from coregistered anatomical MRI. In DTI studies, these network nodes are considered to be linked by "edges" with weights that denote some measure of the connectivity between the two regions, such as the density or integrity of fibers recovered using tractography (Bullmore and Sporns, 2009; Hagmann et al., 2008). Different measures of connectivity are used in different studies—connectivity matrices typically represent some descriptive parameter about the connection between all pairs of anatomical regions studied. The most common topological network measures used to describe the integrity of the healthy or diseased human brain network include the nodal degree, characteristic path length, efficiency, clustering coefficient and "small-worldness" (Sporns, 2011). The characteristic path length, a measure of integration, is the average shortest path length in a network:

$$L = \frac{1}{n}\sum_{i \in N} L_i = \frac{\sum_{j \in N, j \neq i} d_{ij}}{n-1} \tag{1}$$

where L_i is the average distance between node i and all other nodes in the networks, d_{ij} is the shortest path length, (i,j) is a link between nodes i and j, and n is the number of nodes (Sporns, 2011).

Efficiency is a global and generally robust measure, and is approximately the inverse of the characteristic path length:

$$E = \frac{1}{n}\sum_{i \in N} \frac{\sum_{j \in N, j \neq i} d_{ij}^{-1}}{n-1} \tag{2}$$

The clustering coefficient, a measure of segregation, is the fraction of a node's neighbors that are neighbors of each other:

$$C = \frac{1}{n}\sum_{i \in N} C_i = \frac{1}{n}\sum_{i \in N} \frac{\frac{1}{2}\sum_{j,h \in N} a_{ij}a_{ih}a_{jh}}{k_i(k_i-1)} \tag{3}$$

where C_i is the clustering coefficient of node i ($C_i = 0$, $k_i < 2$), k_i is the degree of a node i, $k_i = \sum_{j \in N} a_{ij}$ where a_{ij} is the connection status between nodes i and j when a link between (i,j) exists (Sporns, 2011).

Furthermore, the small-world effect is the ratio of the mean clustering coefficient to the characteristic path length after both are normalized based on data from corresponding random networks:

$$S = \frac{\frac{C}{C_{rand}}}{\frac{L}{L_{rand}}} = \gamma / \lambda \tag{4}$$

where C and C_{rand} are the unrandomized and randomized mean clustering coefficients, while L is L_{rand} are the unrandomized and randomized characteristic path lengths (Sporns, 2011). The clustering coefficient was normalized by computing the ratio of the clustering coefficient in the brain network to the clustering coefficient computed in 100 simulated random networks and was denoted by gamma, γ. Similarly, the normalized path length was the ratio of the path length in the brain network to the path length computed in 100 simulated random networks, and was denoted by lambda, λ. These summary measures have been widely employed in studies using various imaging modalities and analytic methods (Dennis and Thompson, 2012), and their reproducibility has also been evaluated (Dennis et al., 2012c).

In graph theory, a connection matrix may be compiled that describes the topology of a network. A square matrix can represent any network of connections, but the network is normally displayed as a graph, that is, a discrete set of nodes and edges (Sporns, 2011). In our analysis, the matrix entries store the total number of fibers connecting each pair of regions (the nodes); these could also be considered as the "weights" of the edges that *connect* a pair of nodes. Some matrix entries are null (zero), as not all pairs of regions are connected. Based on these matrices for all 111 subjects, we went on to map the so-called "structural core" of each subject's anatomical network.

We analyzed the whole brain, left, and right hemispheres separately; in the single-hemisphere analyses, to focus our attention on the connections specific to the hemisphere we chose not to evaluate fibers that crossed between the hemispheres. In other words, we considered the subnetwork that only had nodes that were entirely within a specific hemisphere. Then, we compared the left and right hemispheres in

healthy and AD subjects to analyze the topology and integrity of the fiber bundles.

To model the basic architecture of the neural networks, we used a *k*-core decomposition algorithm that disentangles hierarchical structure by focusing on what is called the "central cores" of the networks (Alvarez-Hamelin et al., 2006). The *k*-core decomposition outputs a network core that consists of highly and mutually interconnected nodes (Hagmann et al., 2008). This is done by identifying subsets of graphs (*k*-cores) by recursively removing nodes with degrees lower than *k*, such that *k* serves as a degree threshold for nodes (Alvarez-Hamelin et al., 2006). Then, each node is assigned a *core number* (Daianu et al., 2012b; Hagmann et al., 2008): larger values of *k* correspond to nodes that have larger degrees and are "more central" within a network (Alvarez-Hamelin et al., 2006).

For a graph $G = (N,E)$ with $|N| = n$ nodes and $|E| = e$ edges, a *k*-core is computed by assigning a subgraph, $H = (B,E|B)$ where set $B \subseteq N$ is a *k*-core of order *k* if $\forall \nu \in B$: degree$_H \geq k$, and H is the maximum subgraph satisfying this property (Alvarez-Hamelin et al., 2006). In other words, to compute the "18-core" (for example) of the connectivity matrix, all nodes that have a degree 18 or higher would be kept. These would be output in a 34×34 matrix (the same size as the connectivity matrix); nodes that do not satisfy this condition are replaced with zeroes. For this study, we selected a value of $k = 18$; this value was selected empirically, as it represents the minimal value where the majority ($>50\%$) of nodes within each hemisphere would still remain connected. In other words, most nodes would be connected to at least one remaining node. On the other hand, it is *not* required that the remaining nodes in a *k*-core must form one single *totally connected* graph, in which information could travel from any node to any other via a path of edges.

We also computed topological network measures including: (1) global nodal degree (average of all nodal degrees); (2) normalized characteristic path length (λ); (3) efficiency; (4) normalized clustering coefficient (γ); and (5) a parameter describing the normalized small-world effect for the whole brain, left, and right hemisphere binarized *k*-core matrices, in all subjects. These measures are detailed in (Sporns, 2011). We applied these measures to the whole brain 68×68 *k*-core matrices, left hemisphere 34×34 *k*-core matrices and the right hemisphere 34×34 *k*-core matrices. We compared the two brain hemispheres *within* each group (controls, early mild cognitive impairment [eMCI], late mild cognitive impairment [lMCI] and AD), to test for left/right asymmetries in connectivity. To assess diagnostic group differences, we analyzed the difference between the network measures in the whole brain in controls and whole brain in AD subjects, differences between the network measures in the left hemisphere in controls and the left hemisphere in AD subjects, and then we did the same for the right hemisphere.

We separately fitted a random effects regression model to the *k*-core matrices of controls and AD subjects to test for diagnostic group differences, in the left hemisphere, and then separately in the right hemisphere (with controls coded as 0 and AD subjects coded as 1). We covaried for age and sex and used acquisition site as a random regression variable. The fiber density strengths in the *k*-core structures were compared across every node that was in the *k*-core of at least one subject. The global network measures were compared across the whole brain, left, and right hemispheres, separately. To test how the clinical test scores were correlated with the fiber densities in the *k*-core matrices in the whole brain, left, and right hemispheres, we performed a random effects regression across all subjects and used the scanning site as a random regression variable while covarying for age and sex.

Furthermore, we also separately fitted a random effects regression to the connectivity matrix data from 28 controls, 57 eMCI, 11 lMCI, and 15 AD subjects to test for differences between the connectivity matrices of the left and right hemispheres (same setup as above). In this primary analysis, we did not covary for disease, to increase power. However, we tested if the asymmetry in the brain intensifies with disease progression using a random effects regression among subjects, while using site as a random regression variable and covarying for age and sex. To simplify the presentation, we show the regression results as a matrix, to indicate differences between the left, $C_L(x,y)$, and right, $C_R(x,y)$, hemisphere connectivity matrices across all 111 subjects (Fig. 3). Similarly, we applied a random effects regression to test for any differences in derived network topology measures for the left versus the right hemisphere subnetworks.

Results

First, we compared the connectivity matrices of the left and right hemispheres across all subjects (controls, eMCI, lMCI and AD) and found significant differences in a total of 115 connections, while covarying for age and sex and accounting for scanning site. A total of 208 "valid" connections were examined (i.e., connections that occurred in all subjects), so 115 is 55%, when analyzing connections that were present in $>80\%$ of the subjects (false discovery rate [FDR] $p = 0.037$). By only examining edges that were present in nearly all subjects, we may still have somewhat underestimated the degree to which connectivity is asymmetric, but this is a reasonable estimate of the large degree of hemispheric difference in connections that are reliably extracted across an entire population. In other words, over half of the valid connections showed an asymmetry. We further "filtered" these connectivity matrices and thresholded the nodes by degree, to retain the majority ($>50\%$) of the nodes that were connected within each hemisphere ($k = 18$) in our 34×34 *k*-core matrices. After we defined the *k*-cores for the whole brain, left, and right hemispheres in healthy and diseased subjects, we tested for disease effects, and relationships to clinical scores.

Disease-related differences in networks

When the networks were pared down to the *k*-cores for all subjects ($k = 18$)—the network "backbone"—we were able to detect disease effects on connectivity. In comparing AD and control groups, we found prominent group differences between the weighted *k*-core elements of different cortical regions across the entire brain. For this regression to be well-defined, we included only those nodes that are in the *k*-cores for at least one of the subjects. Considering the left hemisphere first, certain regions differed between AD and controls, and, as expected, showed lower fiber density in AD between the middle temporal and fusiform area, lower fiber density in AD between inferior temporal and fusiform area, lower fiber density in the *pars triangularis* and caudal middle frontal, lower fiber density between the precentral
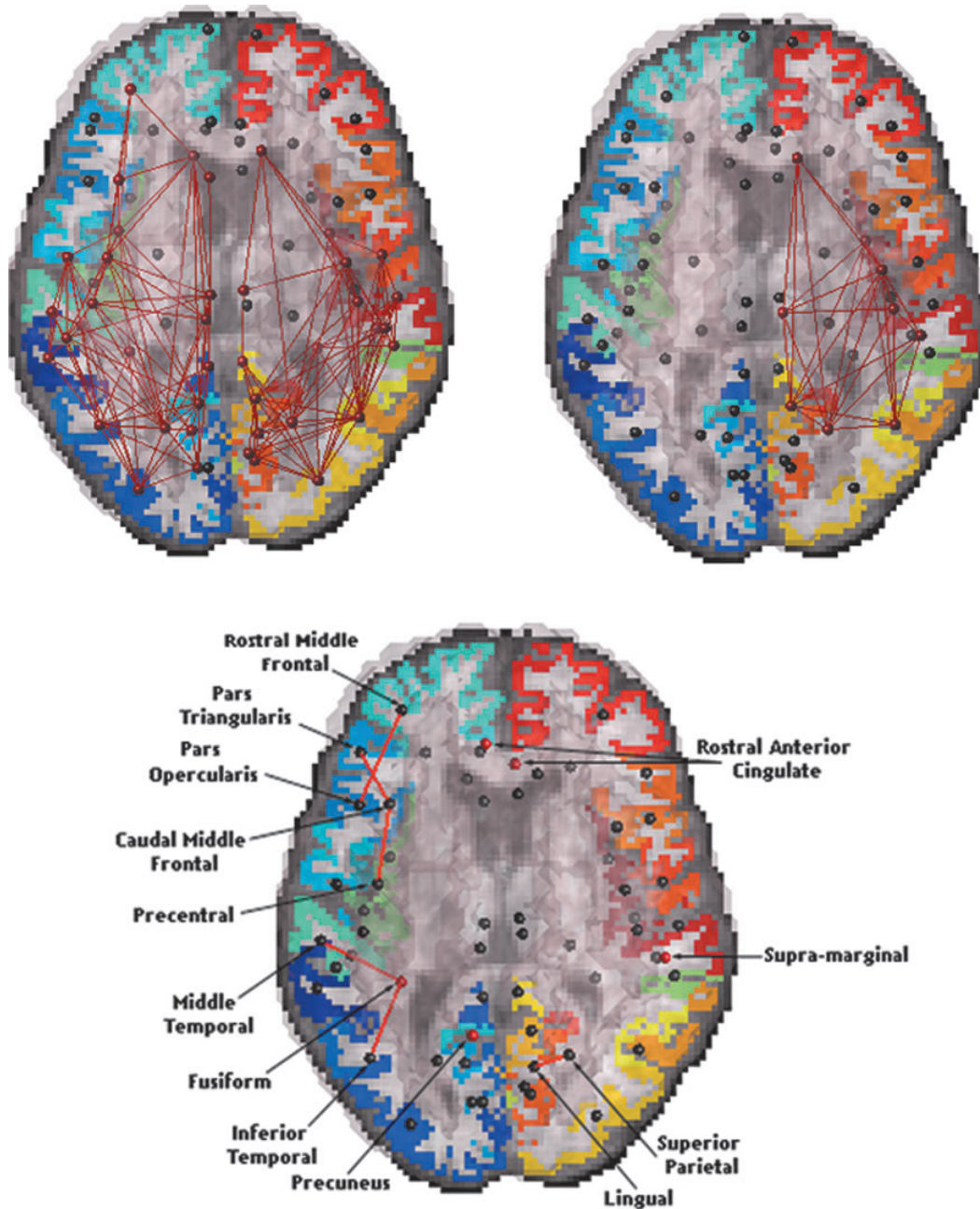
FIG. 1. *k*-core networks of controls and Alzheimer's disease (AD) subjects. Set of nodes present in the weighted *k*-cores of *all* 28 controls, *k* = 18, (top left panel) and *all* 15 AD subjects (top right panel). The *k*-value was preselected to include at least half (i.e., the majority) of the detectable connected nodes per hemisphere (34 × 34). Results are presented over the whole brain. With disease progression, the left hemisphere of AD subjects loses consistency in its *k*-core assignments (false discovery rate [FDR] critical *p*-value = 0.0015). Bottom panel shows *p*-values from the whole brain from a random effects regression between the *k*-cores (*k* = 18) of controls and AD subjects (where controls were coded as 0 and AD subjects coded as 1) using age and sex as covariates and site as a random grouping variable; the significant connections that survived FDR were between the following cortical regions: the middle temporal and fusiform, inferior temporal and fusiform, *pars triangularis* and caudal middle frontal, precentral and caudal middle frontal, rostral middle frontal and *pars opercularis*, and superior parietal and lingual; also, a significant difference in the proportion of total fibers was detected in the following regions: fusiform, precuneus, rostral cingulate, and supra-marginal. Small black spheres show cortical areas where group differences were not detected.

16

Table 4. Mean Network Measures in Controls (CTL) and Alzheimer's Disease Subjects

	CTL					AD				
	NOD	λ	EFF	γ	SW	NOD	λ	EFF	γ	SW
WB	19.78	0.29	0.27	2.03	7.08	15.22	0.23	0.20	2.30	10.38
LH	16.00	0.49	0.43	NS	2.80	12.59	0.39	0.33	NS	3.60
RH	15.54	0.47	0.42	NS	2.90	12.66	0.39	0.34	NS	3.57

The mean nodal degree, normalized characteristic path length and efficiency decreased significantly between controls and AD subjects in all analyses. The normalized clustering coefficient increased in the whole brain of AD, while the normalized small-world effect increased in AD in all analyses, relative to controls. Mean values were rounded off to the nearest hundredth.

NOD, global nodal degree; λ, normalized characteristic path length; EFF, efficiency; γ, normalized clustering coefficient; SW, normalized small-world effect; WB, whole brain; LH, left hemisphere; RH, right hemisphere; NS, not significant.

and caudal middle frontal, lower fiber density between the rostral middle frontal and *pars opercularis*, and a lower proportion of fibers in the fusiform, precuneus and rostral anterior cingulate (Fig. 1). The medial temporal lobe is among the first brain regions to show atrophy in MCI and AD (Thompson et al., 2003). Deterioration in its connectivity to other brain regions is in line with current thinking about disconnection in AD. Considering the right hemisphere, the AD group showed lower fiber density between the superior parietal and lingual areas relative to controls, a lower proportion of fibers in the rostral anterior cingulate and higher proportion of fibers in the supra-marginal region, relative to controls.

Relative to controls, the AD group lost *all* k-core connections in the left hemisphere (FDR critical *p*-value = 0.0015). Note that this does *not* mean that all those fibers are gone from the brain; when defining the *k*-core, the thresholding operation on the nodal degree makes sure that only fibers with a very high number of connections are retained, and these no longer exist, at least in the left hemisphere. Figure 1 shows regions with the most drastic changes. Some, but not all, studies report a slightly greater effect of AD on the left hemisphere (i.e., group differences in some brain measures may show larger effect sizes on the left). Even so, any laterality may just reflect a recruitment bias where patients with language dysfunction, arising from left hemisphere atrophy, tend to enroll in greater proportions than those who do not have language problems (Thompson et al., 2003).

Brain network measures: global nodal degree, efficiency, normalized characteristic path length, normalized clustering coefficient and normalized small-world effect

We computed the network nodal degree, efficiency, normalized characteristic path length, normalized clustering coefficient, and normalized small-world measures (these are global measures of the overall network properties) from the binarized *k*-cores of controls and AD subjects in the whole brain, left, and right hemispheres, separately. Based on a random effects regression between the brain network measures in healthy subjects and AD subjects, we determined that with increasing disease burden, the nodal degree, normalized characteristic path length and efficiency significantly *declined* in AD subjects, relative to controls in the whole brain, left, and right hemispheres (means are in Table 4 and *p*-values are in Table 5). Efficiency was expected to decline (according to prior studies, e.g., Lo et al. [2010]), while the small-world effect was expected to be altered, but not in a direction pre-

dictable *a priori*; here, the normalized small-world effect *increased* in AD in all analyses, relative to controls. The normalized clustering coefficient significantly *increased* in the whole brain of AD compared to controls and did not show detectable differences when the left and right hemispheres were considered independently.

The nodal degree, efficiency and normalized characteristic path length of the proportions of fibers (that passed FDR) were lower in AD in the whole brain, left, and right hemispheres, relative to controls. This decrease was consistent among the MCI groups: the eMCI and lMCI groups took intermediate values between those for controls and AD groups (Fig. 2). The normalized clustering coefficient of the proportion of fibers was higher in AD in the whole brain (no significant changes were detected in the left and right hemispheres between controls and AD). The slight increase in the clustering coefficient and decrease in the normalized characteristic path length led to an increase in the proportion of fibers in the small-world effect in AD in all analyses, relative to controls (Tables 4 and 5).

Relation to clinical scores

To assess whether the network breakdown related to differences in clinical test scores, we also ran a random effects regression to test for any associations with the most widely used clinical scores, namely the Mini Mental State Examination (MMSE), Clinical Dementia Rating Global Score (CDR-Glob), Clinical Dementia Rating Sum of Boxes (CDR-SOB),

Table 5. Differences in Fiber Networks for the Whole Brain, Left, and Right Hemispheres Between Controls (CTL) and Alzheimer's Disease Subjects

CTL vs. AD (p-values)	Network measures				
	NOD	λ	EFF	γ	SW
WB	3.86E-05	3.86E-05	4.02E-05	0.0038	9.06E-06
LH	2.91E-04	2.89E-04	3.08E-04	NS	2.99E-03
RH	1.51E-04	1.47E-04	1.85E-04	NS	9.03E-04

p-Values are shown, based on fitting a random effects model to the network measures (degree, normalized characteristic path length, efficiency, normalized clustering coefficient and normalized small-world) applied on the *k*-core (*k* = 18) to test for diagnostic group differences between controls and AD subjects in the whole brain, left hemisphere, and then separately in the right hemisphere (with controls coded as 0 and AD subjects coded as 1). We covaried for age and sex and used acquisition site as a random regression variable.
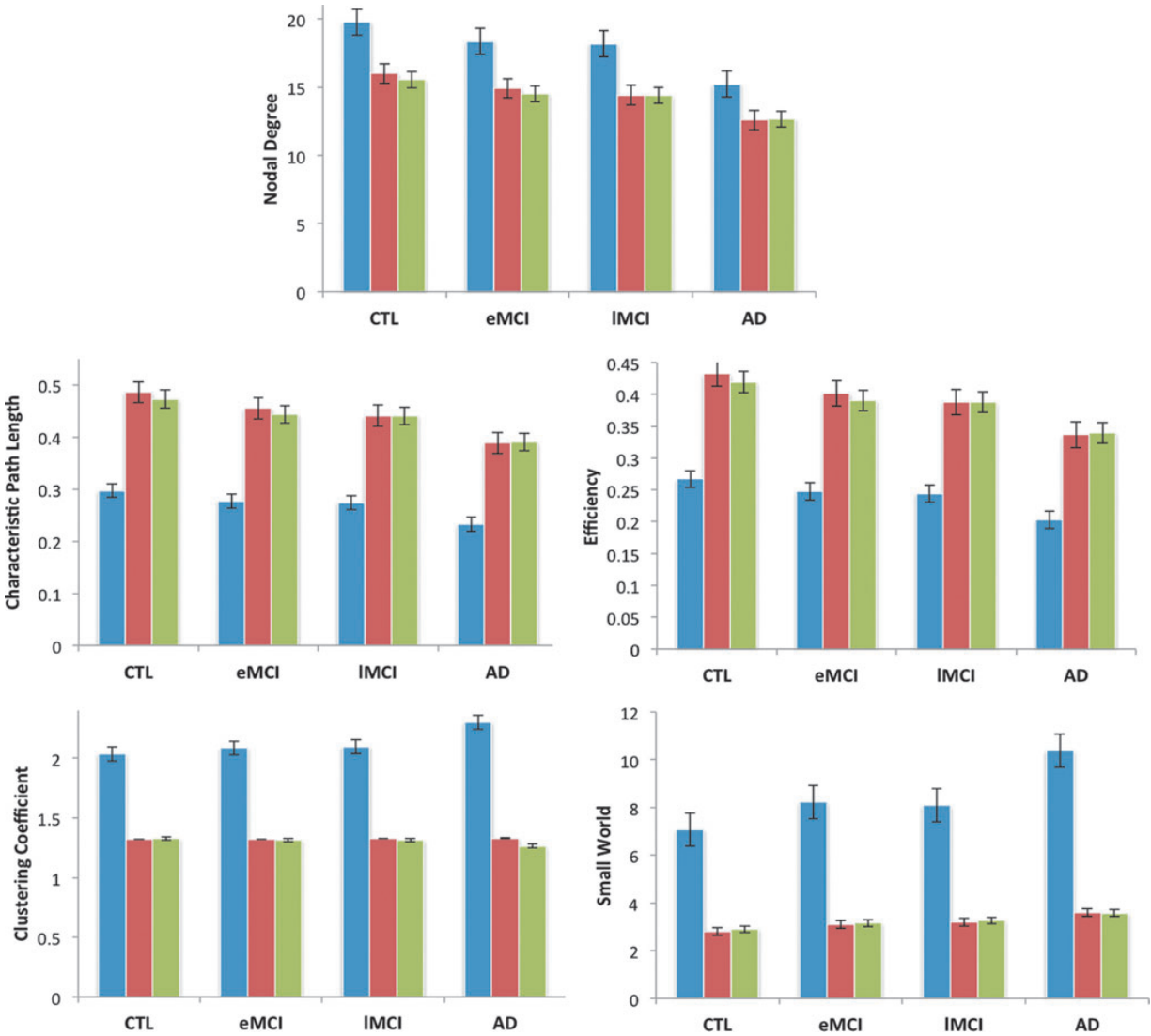
17

FIG. 2. Mean values for network measures in the brain for all diagnostic groups. The bar graph shows mean values (and standard errors) for the fiber network nodal degree, normalized characteristic path length, efficiency, normalized clustering coefficient, and normalized small-world effect for controls (CTL), early mild cognitive impairment (eMCI), late mild cognitive impairment (lMCI) and AD groups in the whole brain (blue), left hemisphere (red) and right hemisphere (green). The nodal degree, normalized characteristic path length and efficiency *declined* in AD subjects, relative to controls in the whole brain, left, and right hemispheres (*p*-values in Table 4) based on a regression setting controls to 0 and AD subjects to 1; this can be seen by comparing each block of three bars to each succeeding block of three bars, which corresponds to increasing disease burden. The normalized small-world effect *increased* in AD, relative to controls, and the normalized clustering coefficient *increased* in the whole brain but did not show detectable differences in the left and right hemispheres individually between controls and AD subjects.

11 item Alzheimer's Disease Assessment Scale-Cognitive Subscale (ADAS-11) and 13-item Alzheimer's Disease Assessment Scale-Cognitive Subscale (ADAS-13) scales. These regressions used clinical scores to predict any differences on the *k*-core across all subjects in the study.

Analyses were run on the whole brain, left, and right hemispheres separately (Table 6). Clinical test scores were *all* related to differences in some cortical regions. Consistent relationships with all clinical scores were found for the connections between the superior frontal cortex and caudal anterior cingulate (see in bold, Table 6). As MMSE scores decreased, the fiber density of the *k*-cores also decreased (as might be expected) between the superior frontal cortex and caudal anterior cingulate in the whole brain analysis. Also as expected, with increases in the disease burden scores ADAS-11, ADAS-13, CDR-Glob, and CDR-SOB, fiber density in the *k*-cores decreased between the superior frontal and caudal anterior cingulate, in the whole brain analyses.

TABLE 6. CLINICAL CORRELATES OF NETWORK BREAKDOWN

Scores	Whole brain	Left hemisphere	Right hemisphere
MMSE	1 connection: **63 and 37** (critical FDR $p = 8.50E-05$)	15 connections: 3 and 3, **7 and 7**, 8 and 7, 9 and 7, 9 and 9, 15 and 7, 15 and 9, 24 and 3, 27 and 3, 27 and 27, 29 and 7, 29 and 8, **30 and 7**, 31 and 8, 35 and 7 (critical FDR $p = 0.004$)	10 connections: 11 and 1, 24 and 22, 31 and 22, 31 and 24, 31 and 25, **31 and 31**, 35 and 17, **35 and 31**, 35 and 35 (critical FDR $p = 0.002$)
ADAS-11	11 connections: 15 and 13, 25 and 15, 28 and 20, 45 and 42, 46 and 40, 51 and 48, 51 and 51, 60 and 23, **63 and 37**, 64 and 25, 65 and 54 (critical FDR $p = 0.002$)	13 connections: **7 and 7**, 9 and 7, 9 and 9, 15 and 7, 23 and 8, 25 and 11, 25 and 23, 27 and 27, 29 and 18, **30 and 7**, 30 and 9, 31 and 8, 35 and 7 (critical FDR $p = 0.004$)	16 connections: 8 and 8, 9 and 1, 11 and 1, 22 and 18, 24 and 22, 31 and 17, 31 and 18, 31 and 22, 31 and 24, 31 and 25, **31 and 31**, 35 and 3, 35 and 17, 35 and 24, **35 and 31**, 35 and 35 (critical FDR $p = 0.004$)
ADAS-13	10 connections: 15 and 13, 25 and 15, 28 and 20, 45 and 42, 46 and 40, 51 and 48, 51 and 51, **63 and 37**, 64 and 25, 65 and 54 (critical FDR $p = 0.002$)	13 connections: **7 and 7**, 9 and 7, 9 and 9, 15 and 7, 23 and 8, 25 and 11, 25 and 23, 27 and 27, 28 and 18, 29 and 8, **30 and 7**, 30 and 9, 31 and 8 (critical FDR $p = 0.004$)	7 connections: 8 and 8, 11 and 1, 31 and 18, 31 and 22, 35 and 17, 35 and 24, 35 and 35 (critical FDR $p = 0.002$)
CDR-Glob	28 connections: 14 and 12, 18 and 17, 20 and 12, 20 and 18, 20 and 20, 24 and 10, 25 and 15, 26 and 2, 27 and 14, 27 and 20, 27 and 24, 28 and 20, 30 and 11, 35 and 20, 43 and 10, 48 and 10, 48 and 25, 58 and 25, 60 and 13, 61 and 12, 61 and 26, 61 and 27, 61 and 28, 61 and 47, 61 and 61, 62 and 61, **63 and 37**, 64 and 25 (critical FDR $p = 0.007$)	23 connections: **7 and 7**, 8 and 7, 8 and 8, 21 and 7, 23 and 8, 24 and 3, 24 and 10, 25 and 7, 25 and 8, 25 and 11, 25 and 13, 25 and 15, 25 and 17, 25 and 23, 25 and 24, 25 and 25, 28 and 3, 28 and 25, 28 and 28, 29 and 8, 29 and 25, 29 and 28, **30 and 7** (critical FDR $p = 0.007$)	8 connections: 8 and 8, 29 and 8, 29 and 23, 29 and 29, **31 and 31**, 35 and 24, **35 and 31**, 35 and 35 (critical FDR $p = 0.002$)
CDR-SOB	10 connections: 23 and 8, 24 and 10, 28 and 20, 30 and 11, 31 and 3, 37 and 37, 48 and 10, 48 and 25, **63 and 37**, 64 and 25 (critical FDR $p = 0.002$)	6 connections: 3 and 3, **7 and 7**, 8 and 7, 15 and 7, 25 and 25, **28 and 3** (critical FDR $p = 0.001$)	7 connections: 31 and 17, 31 and 25, **31 and 31**, 35 and 17, 35 and 24, **35 and 31**, 35 and 35 (critical FDR $p = 0.002$)

Here we show various differences in brain networks that are associated with standard measures of clinical decline. Random effects regression tests were performed for clinical scores on the MMSE, CDR-Glob, CDR-sob, ADAS-11 and ADAS-13 in the whole brain, left, and right hemispheres separately for the *k*-cores of all subjects (controls, eMCI, MCI and AD) in connections present in 80% of subjects. We used site as a random regression variable, and controlled for age and sex. All the nodes that showed significant differences are listed. Significant connections that are common across all clinical scores are shown in bold and the critical FDR *p*-value for correcting over all valid connections is shown.

MMSE, Mini Mental State Examination; ADAS-11, 11 item Alzheimer's Disease Assessment Scale-Cognitive Subscale; ADAS-13, 13-item Alzheimer's Disease Assessment Scale-Cognitive Subscale; CDR-Glob, Clinical Dementia Rating Sum of Boxes; CDR-Glob, Clinical Dementia Rating Global Score; FDR, false discovery rate.

Effects on the fiber densities of the left and right hemispheres were found in cortical regions that mostly overlapped with the differences in the *k*-cores of AD subjects versus controls. Clinical test scores were *all* related to differences in some cortical regions—such as in the proportion of total fibers in the fusiform region for the left hemisphere, and in the proportion of total fibers in the supramarginal region for the right hemisphere in all subjects (except for the ADAS-13 score). All test scores increased as the fiber density of the *k*-cores decreased in the fusiform area of the left hemisphere, except for the MMSE score, which decreased as the fiber density also decreased. This result is expected, as higher MMSE scores denote better cognitive performance and higher scores on other tests represent greater cognitive impairment. For the right hemisphere, MMSE increased as the fiber density of the *k*-cores decreased in the supra-marginal region. In the meantime, ADAS-11, CDR-Glob, and CDR-SOB decreased as the fiber density also decreased in the supra-

marginal region of the right hemisphere. Overall, there were no particular connections with significant correlations to all clinical scores; in fact, it was more that the *aggregate* number of connections linked with clinical scores was higher than would be expected by chance.

Left/right asymmetries in network

To further understand how these network alterations may differ by hemisphere with disease progression, we analyzed differences between left and right hemispheres in each group as well as the nodal degree measures applied to the structural *k*-core of each group. For these, we performed random effects regressions that returned significant differences between the left and right hemisphere connectivity matrices in each group: 28 controls, 57 eMCI, 11 lMCI, and 15 AD subjects (Fig. 3). We might expect the number of connections with significant asymmetries to increase, if the disease does not
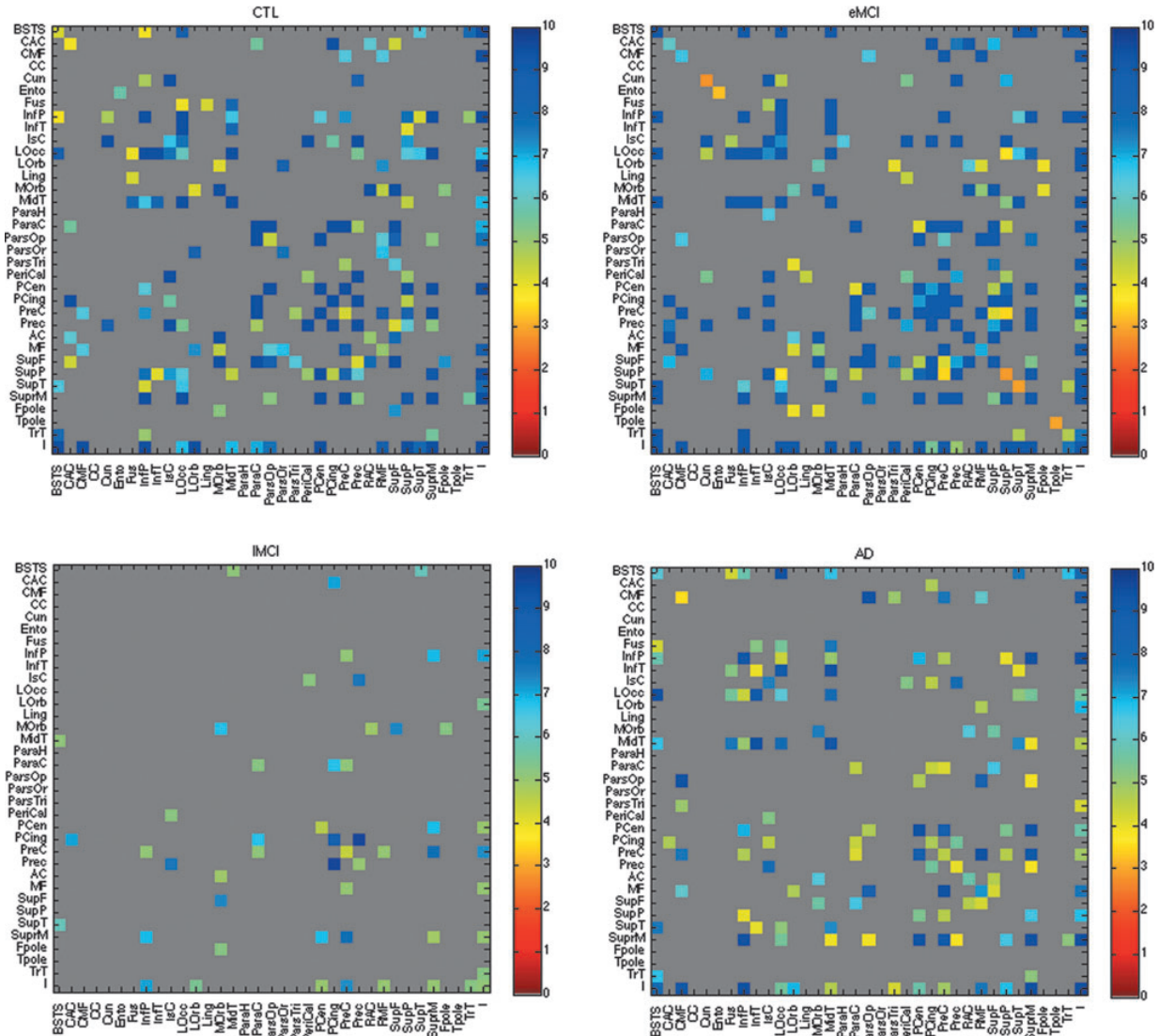
FIG. 3. Asymmetries in anatomical connectivity in controls, early and late MCI, and AD. These maps show asymmetries in the density of connections between all pairs of cortical regions. We show, in color, the $-\log_{10}$ of the p-values from the regression model comparing the left, $C_L(x,y)$, and right, $C_R(x,y)$, hemisphere connectivity matrices in 28 controls (top left, FDR critical p-value = 0.020; higher critical values denote stronger effects) and 57 eMCI subjects (top right, FDR critical p-value = 0.030), 11 lMCI subjects (bottom left, FDR critical p-value = 0.007) and 15 AD subjects (bottom right, FDR critical p-value = 0.021). We covaried for age and sex and used the scanning site as a random grouping variable in the regression. The same cortical regions were considered in all four groups. Dark gray regions indicate cortical areas where no significant hemispheric differences were detected. Based on a random effects regression, the asymmetry in the connection matrix intensified with disease progression. This could be due to the overall decrease in the number of fiber connections with increasing disease severity.

progress symmetrically, and if the variance does not also increase. For this, we computed the number of asymmetric connections for each subjects by taking the difference of the weighted connections (fiber densities) in the connectivity matrices between the left and right hemispheres and regressed it over the clinical scores while covarying for age and sex in all subjects and using site as a random regression variable. We found significant results for most scores with FDR critical p-values of 3.0E-03 for MMSE, 2.0E-04 for CDR-Glob, 4.0E-

03 for ADAS-11, and 1.7E-03 for ADAS-13; no significant results were found for CDR-SOB. These results indicate that the asymmetry becomes more pronounced with disease progression. Similarly, as a *post hoc* exploratory test, we took the difference between the left and right hemisphere nodal degree measures in all subjects and regressed it against the clinical scores, while covarying for age and sex and using site as a random regression variable, but we did not detect significant effects.

TABLE 7. LEFT-RIGHT ASYMMETRIES IN MEASURES OF ANATOMICAL BRAIN CONNECTIVITY

	Left-right asymmetries			
Network measures	Controls (28 subjects)	eMCI (57 subjects)	lMCI (11 subjects)	AD (15 subjects)
k-core elements	151 connections (p = 0.020)	145 connections (p = 0.027)	9 connections (p = 0.0012)	63 connections (p = 0.014)
NOD	NS	NS	NS	NS
EFF	NS	NS	NS	NS
λ	NS	NS	NS	NS
γ	NS	NS	NS	NS
SW	NS	NS	NS	NS

Connections that differed between left and right hemispheres, for the different diagnostic groups. Results are computed from a random effects regression model (using zeroes for the left hemisphere and ones for the right hemisphere) comparing the weighted *k*-core measures between the left and right hemispheres in 28 controls, 57 eMCI, 11 lMCI and 15 AD subjects (not all connections are named in this paper due to space limits), as well network measures applied on the binarized *k*-core matrices. The *p*-values reported here are the FDR critical *p*-values.

Also, we performed random effects regression to test for differences between the left and right hemispheres in the weighted *k*-core and nodal degree. We found left-right hemisphere differences in the *k*-core matrices for all groups (Table 7). There were no significant differences in the network measures, nodal degree, efficiency, normalized characteristic path length, normalized clustering coefficient and normalized small-world between the left hemispheres in either diagnostic group. The number of *k*-core connections showed decreasing asymmetries between healthy and diseased for controls (151 connections), eMCI (145 connections), and AD (63 connections), except the lMCI group (nine connections) that might have been affected by the unevenly small number of subjects. We should also bear in mind that there are at least another two factors affecting the number of connections where asymmetries are picked up. First, the *k*-core loses nodes drastically as disease progresses, so the number of nodes present where asymmetry can be detected is falling rapidly. As such, there is a downward trend in the number of nodes showing an asymmetry. Second, one has to bear in mind that the sample size of the 4 diagnostic groups is uneven—28 for controls, 57 for eMCI, but only 11 for lMCI and 15 for AD. The power to detect asymmetry is higher when the sample size is higher, as a smaller effect size can be declared significant in a larger sample. Together, these processes seem to account for the changes in the number of connections declared asymmetric as the disease progresses.

Analyzing the stability of the structural core: perturbation of k *levels*

To understand how the different thresholds (different levels of *k*-core) affect graph theory measures, we computed the structural backbone using $k = 16, 17, 19$ and 20, in addition to $k = 18$ in all 111 subjects. We compared how the nodal degree, and the network efficiency—perhaps the most commonly computed measure in brain connectivity studies—changed as a function of *k*. We compared every *k*-level across all subjects in the whole brain, left, and right hemispheres separately with every other *k*-level in that group (i.e., nodal degree for all subjects at $k1 = 16, 17, 18$, and 19 was compared to nodal degree in all subjects at $k2 = (k1 + 1) = 17, 18, 19$ and 20 using a two-tailed paired *t*-test and performed FDR correction on all $(5 \times 5 - 5)/2$ comparisons. Nodal degree FDR critical *p*-values in the left and right hemispheres are 3.0E-03 and 2.7E-03

and efficiency FDR critical *p*-values in the left and right hemispheres are 4.5E-03 and 5.4E-04 (Fig. 4).

Discussion

Here we report how AD affects structural brain connectivity in a sample of 111 subjects (comprising patients, controls, and those at risk of AD). We studied fundamental anatomical brain subnetworks called the "*k*-cores". AD affected a variety of network metrics describing the topological organization of the brain's white matter. From the *k*-cores, we determined the most highly interconnected networks in the left and right hemispheres and analyzed whether these regions remained intact or altered with disease progression. The *k*-core was found to be a useful distillation of the overall brain network, rather than using the full connectivity matrix, as it eliminated the least reliable connections; these less reliable connections can arise due to tract tracing errors. To the extent that they do contain errors, this may worsen the signal-to-noise ratio and make it more difficult to detect disease effects. As an empirical observation, the *k*-core did indeed enhance the disease effects, as the entire *k*-core was "lost" in the left hemisphere of AD subjects. These findings are important to locate brain regions that change with disease progression. Ultimately they may help in assessing effects of treatments, or other interventions, on the brain.

We found significant differences between the left and right hemisphere connectivity matrices in all subjects (FDR critical $p = 0.037$), which led to further analyses of the core networks that survived with disease progression. In our *k*-core analyses comparing AD subjects to healthy controls, *all* the *k*-core elements in the left hemisphere were lost in AD subjects, suggesting that brain network topology changes drastically with disease progression (Fig. 1). We must emphasize that this does not mean that those fibers are completely absent in AD, but the thresholding implicit in creating the *k*-core homes in on the highly connected elements. So, according to this definition, none of these highly connected elements remained in the left hemisphere in AD. The main connections and regions that significantly differed in their *k*-core topology between controls and AD were found between the middle temporal and fusiform, inferior temporal and fusiform, *pars triangularis* and caudal middle frontal, precentral and caudal middle frontal, rostral middle frontal and *pars opercularis*, and superior parietal and lingual; also, a significant difference in
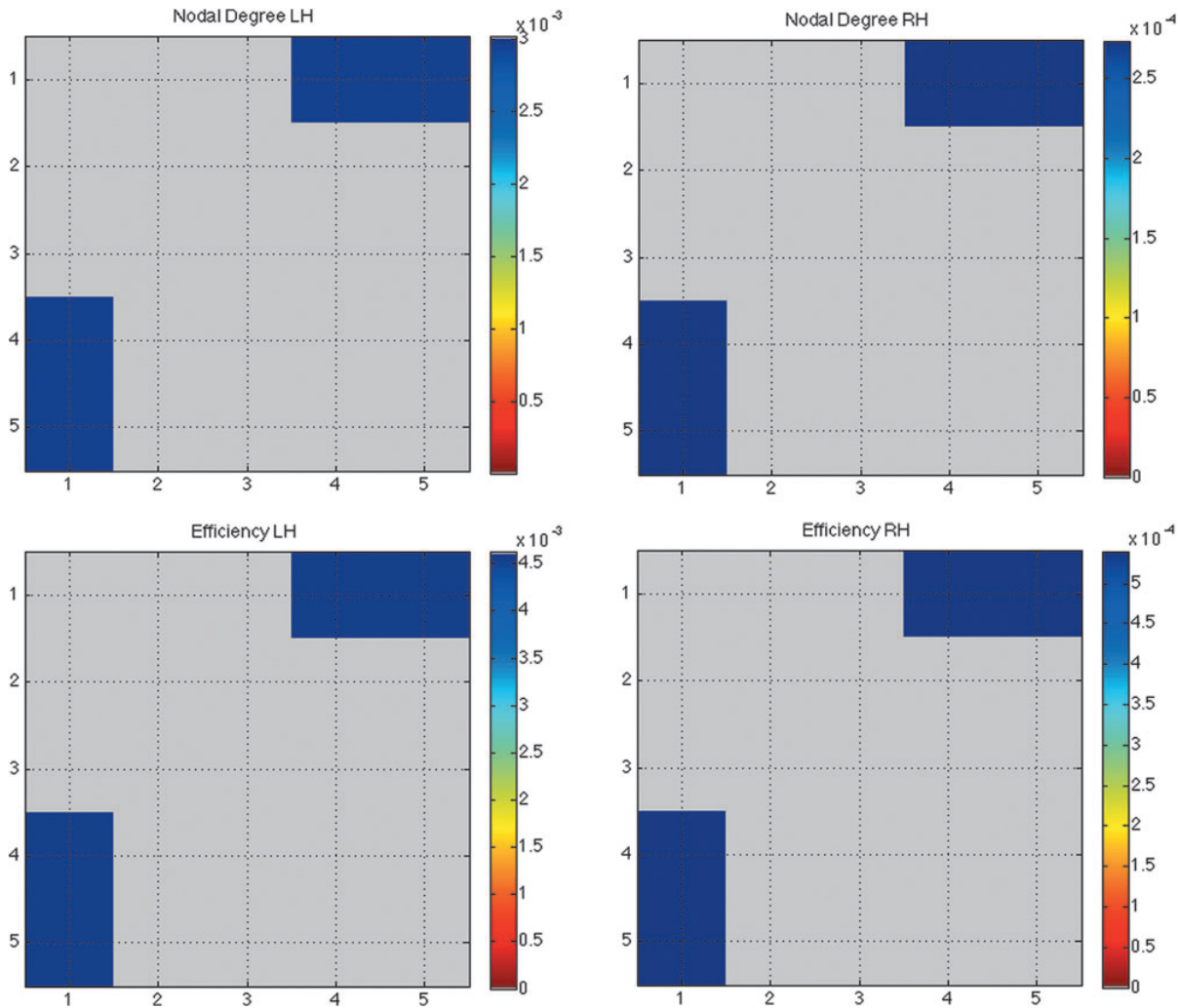
FIG. 4. Effects of perturbations in the k-core threshold on nodal degree and efficiency. Matrix (5×5) representing the p-values from a two-tailed t-test comparing nodal degree and efficiency measures across five k-levels ($k = 16,17,18,19$ and 20) in all 111 subjects (nodal degree FDR critical p-values in the left and right hemispheres are 3.0E-03 and 2.7E-03 and efficiency FDR critical p-values in the left and right hemispheres are 4.5E-03 and 5.4E-04). In other words, we compared k-levels $k1 = \{16,17,18,19\}$ to $k2 = (k1 + 1) = \{17,18,19,20\}$ across all subjects. There were no significant differences across k-levels in the whole brain in all 111 subjects. The greatest differences in the network measures were found between lowest and highest k-values (blue p-values).

the proportion of total fibers was detected in the following regions: fusiform, precuneus, and rostral anterior cingulate. Some of these nodes are part of the temporal and parietal lobes, which are known to be among the earliest regions consistently affected by AD pathology (Thompson et al., 2003). Yao and colleagues (2010) analyzed the "structural brain network" in patients with AD, and found that the regions that showed the most significant changes in the interregional correlations between 98 controls and 91 AD include the temporal lobe, fusiform, superior parietal region and orbital frontal gyrus (Xie and He, 2012; Yao et al., 2010). Most of these regions showed differences here, in groups with progressively advancing disease. We note, however, that the Yao and colleagues analyses assessed correlations among regional volumes using standard anatomical MRI. This is not the same definition of brain connectivity as that

involved here with DTI, which assesses pathways between brain regions.

We computed five important network measures—global nodal degree, normalized characteristic path length, efficiency, normalized clustering coefficient and normalized small-worldness—that may be useful in the future as possible new biomarkers of AD. Nodal degree decreased with disease progression by 23% in the whole brain, 21% in the left hemisphere and 19% in the right hemisphere of AD subjects compared to controls. The normalized characteristic path length decreased by 22% in the whole brain, 20% in the left hemisphere, and 17% in the right hemisphere. Efficiency decreased by 24% in the whole brain, 22% in the left hemisphere of AD subjects compared to controls, and by 19% in their right hemisphere. This indicates that the disease effects can be quantified using network efficiency measures in the early stages

of the disease such as in eMCI and lMCI patients. Here both efficiency and normalized path length measures were found to decrease. It is important to note that efficiency is expected to increase as characteristic path length decreases only when the path length is unnormalized. Path length should be normalized using appropriately constructed random networks, as the absolute (unnormalized) value of the path length provides limited information on the integration in the brain network (Sporns, 2011); the path length varies greatly with the size and density of individual graphs, whereas efficiency is a more robust measure—the average of the inverse of the distance matrix (Sporns, 2011), and was not normalized here. Also, the decrease in global efficiency is in general agreement with previous structural connectivity studies (Lo et al., 2010), bearing in mind the differences between the studies in acquisition and analysis. A lower efficiency may suggest a less optimal organization of the brain network structures in AD subjects (Xie and He, 2012) and perhaps even reduced signal propagation among brain regions (Lo et al., 2010).

Meanwhile, the normalized small-world effect increased by 47% in the whole brain, 28% in the left hemisphere and 23% in the right hemisphere of AD subjects, compared to controls. The increase in the normalized small-world effect was consistent among the eMCI and lMCI subject groups (Fig. 2). Small-worldness depends on several factors that are all changing in AD, and the results of all the changes may be nonintuitive or not predictable at the outset. Small-worldness may be a biologically or functionally advantageous property, as it is found in many biological networks and may be functionally advantageous relative to random networks. As such, one might not predict that the property would increase in AD, as there is clearly no functional advantage to having AD. Compared to random networks, which tend to have short average path lengths and relatively low clustering, the small world effect tends to be higher when a network has a high level of clustering, or when the average path lengths become shorter. This is because the small-worldness is based on the ratio of the clustering coefficient to the path length, after normalizing each of those to values in a random network. The loss of fibers in AD can remove some connections from a network that is thresholded based on the nodal degree. This led to a decrease in average normalized path length in the whole brain, left, and right hemispheres, while the normalized clustering coefficient increased in the whole brain by 13% (and did not change significantly in the left and right hemispheres), so the normalized small-world effect also increased in the whole brain, left, and right hemispheres. The increase in clustering coefficient does not always indicate a densely interconnected and coherent brain system; in fact, it can be disproportionately influenced by nodes with low nodal degree, which is a phenomenon observed in AD–the nodal degree decreases relative to controls (Fig. 2).

Furthermore, we found network asymmetries—between left and right hemispheres—in all diagnostic groups. This is not entirely surprising: as shown Figure 3, there is a clear asymmetry between the left and right hemisphere networks, regardless of the diagnostic group. This may even intensify as the disease progresses as the clinical scores between the left and right hemisphere connectivity matrices were significantly different. Regions with connectional asymmetry were scattered all over the brain. A related pattern of diffuse asymmetries was also observed in a recent de-

velopmental study of adolescents and young adults (Daianu et al., 2012a). These increasing asymmetries may be due to age or disease, or both, and it is not clear whether they are harmful or benign.

We further analyzed the differences in the *k*-core, nodal degree, normalized characteristic path length, efficiency, normalized clustering coefficient, and normalized small-world effect of the *k*-core in the left and right hemisphere in all groups (Table 7). We found differences in all diagnostic groups for the *k*-core measure; however, no differences were found for the rest of the network topology measures between the left and right hemispheres. We previously reviewed evidence for asymmetries in disease progression in AD (Thompson et al., 2003); evidence is mixed, and not all studies support an asymmetry, but the differences in connectivity measures and their variance by hemisphere make it plausible that some connections may show stronger differences in one hemisphere than the other. To corroborate this, longitudinal data will be helpful, when available, from a period long enough to show substantial decline.

Another important aspect to consider is that highly connected *k*-cores contain hubs that are thought to facilitate integrative processes due to their densely connected nodes. Hubs have high nodal degrees and tend to form a *rich club*—a set of high-degree nodes that are more densely interconnected among themselves than nodes of a lower degree (see, e.g., van den Heuvel and Sporns, 2011, which describes the rich-club organization of the human connectome). The "rich club of the hubs" is a related but separate concept from that of the *k*-core—used in the current study—as the rich club coefficient evaluates a range of *k*-core matrices (i.e., with $k=1$, 2, 3…, etc.); here, we analyzed the *k*-core at $k=18$ because this was the minimal value for which the majority ($>50\%$) of nodes within each hemisphere would still remain connected. At $k=18$, we have a highly and mutually interconnected network of the brain. However, a smaller *k* value (<18) will apply a lower threshold to the network, including nodes with lower degrees, and leading to less interconnected networks. Recently (in Daianu et al., 2013), we found that the rich club coefficient increased in AD with increasing *k* and decreasing nodal degree in the residual *k*-core (i.e., when a smaller percentage of nodes are retained), relative to controls. The rich club is a slightly more elaborate concept than the *k*-core. The *k*-core is simply a network—part of the original network—found by thresholding the network to retain only those nodes with high nodal degree (i.e., with degree *k* or higher). The rich club coefficient, $\Phi(k)$, is a ratio of the number of connections among nodes of degree *k* or higher versus the total possible number of connections if those nodes were fully connected. The rich club is a more complex notion than the *k*-core: it is a function defined on all the *k*-cores, which can be tested statistically for signs of rich club organization.

To test the reliability of our measures, we analyzed the stability of the structural core at $k=18$ by comparing the *k*-core in all subjects over a variety of *k*-levels. Based on a two-tailed paired *t*-test, the perturbation in the *k*-levels was significant between the minimum and maximum *k*-level comparisons for the networks measures (nodal degree and efficiency) in the left and right hemispheres separately, while these perturbation did not affect the network measures significantly in the whole brain in all 111 subjects (Fig. 4). All significant changes were found between *k*-levels 16 and 19 and 16 and 20 for

23

nodal degree and efficiency. There were no significant changes with small perturbations of k-levels (i.e., between k and $k+1$); as described above, all changes were detected between levels k and $k+3$ as well as $k+4$ (i.e., $k=16$ and $k=19$).

This study has several limitations. Our study was conducted at 3 T, so connectivity studies at higher fields, or with different protocols, may reveal group differences in additional regions (in Zhan et al., 2013a, we compare connectivity computed at 7 and 3 T in the same subjects). Even so, the use of higher fields may not necessarily become standard for academic or clinical studies in the near future. Another limitation of our work, is the small and uneven number of subjects in each diagnostic group (28 controls, 57 eMCI, 11 lMCI and 15 AD subjects). ADNI2 subjects are continuing to be scanned, so our future work will assess larger cohorts to verify how connectivity measures change over time as AD progresses. In future work, we will also aim to study the specific effects of amyloid pathology on brain network dysfunction using amyloid imaging. These changes may have a tighter relationship to amyloid than to clinical diagnosis, although that remains to be evaluated.

Another factor to consider is the tractography method used. In this paper, we generated around 10,000 fibers per subject, using the Hough transform method (Aganj et al., 2011), but some other tractography algorithms such as FACT (Mori et al., 1999) and TEND (Lazar et al., 2003) generate up to hundreds of thousands. As such, it is of interest whether this density of sampling is sufficient to compute network metrics that are stable, and have converged, and have sufficient power to pick up group differences. Our group previously studied the effect fiber density has on network measures and on the power to distinguish disease effects (Prasad et al., 2013). High-density fiber matrices were most helpful for picking up the more subtle clinical differences. However, based on the current study, the networks in AD are significantly different from controls so that the inference about differences between controls and diseased might not be influenced by fiber counts. One final limitation is our use of thresholding to define the k-core, even though the threshold was chosen in a principled way. Other mathematical work (Lee et al., 2012) has defined novel distance metrics on *filtrations* of networks, in an attempt to retain the full information on the set of all networks defined by thresholding the nodal degree at different thresholds. However, we tested the reliability of our structural core at $k=18$ by comparing it to k-cores computed at $k=16$, 17, 19 and 20 and found that immediate k-levels do not perturb the structural network significantly. Clearly, these and other more advanced metrics on graphs and graph filtrations may also show promise in defining how networks decay and change as disease progresses.

Conclusion

In this study, we tested for alterations in the core graph of connections in the brain caused by disconnections in AD and how the clinical progression of AD affects network measures and possibly, network asymmetries in the brain. We found that AD wipes out the core connections in the left hemisphere, relative to controls, and affects the topology of the brain network—therefore, altering the network measures. Lastly, we found that network asymmetries were present in all diagnostic groups and may intensify with disease progression.

Author Disclosure Statement

No competing financial interests exist.

References

Aganj I, Lenglet C, Jahanshad N, Yacoub E, Thompson PM, Sapiro G. 2011. A Hough transform global probabilistic approach to multiple-subject diffusion MRI tractography. Med Image Anal 15:414–425.

Aganj I, Lenglet C, Sapiro G, Yacoub E, Ugurbil K, Harel N. 2010. Reconstruction of the orientation distribution function in single and multiple shell Q-ball imaging within constant solid angle. Magn Reson Med 64:554–566.

Alvarez-Hamelin JI, Dall'Asta L, Barrat A, Vespignani A. 2006. Large scale networks fingerprinting and visualization using k-core decomposition. In: Weiss Y, Scholkopf B, Platt J (eds.). Advances in Neural Information Processing Systems (NIPS) Cambridge, MA: MIT Press, 18:41–50.

Alzheimer's Association Colorado. 2011. Fact Sheet Alzheimer's Disease. www.alz.org/co/in_my_community_11039.asp Last accessed Sept. 7, 2012.

Azari NP, Rapoport SI, Grady CL, Schapiro MB, Salerno JA, Gonzales-Aviles A. 1992. Patterns of interregional correlations of cerebral glucose metabolic rates in patients with dementia of the Alzheimer's type. Neurodegeneration 1: 101–111.

Bartzokis G. 2009. Alzheimer's disease as homeostatic responses to age-related myelin breakdown. Neurobiol Aging 32:1341–1371.

Braak H, Braak E. 1991. Neuropathological stageing of Alzheimer-related changes. Acta Neuropathol 82:239–259.

Braak H, Braak E. 1996. Development of Alzheimer-related neurofibrillary changes in the neocortex inversely recapitulates cortical myelogenesis. Acta Neuropathol 67:677–685.

Braskie MN, Jahanshad N, Stein JL, Barysheva M, Johnson K, McMahon KL, de Zubicaray GI, Martin NG, Wright MJ, Ringman JM, Toga AW, Thompson PM. 2012a. Relationship of a variant in the NTRK1 gene to white matter microstructure in young adults. J Neurosci 32:5964–5972.

Braskie MN, Jahanshad N, Stein JL, Barysheva M, McMahon KL, de Zubicaray GI, Martin NG, Wright KL, Ringman JM, Toga AW, Thompson PM. 2012b. Common Alzheimer's disease risk variant within the CLU gene affect white matter microstructure in young adults. J Neurosci 31:6764–6770.

Buckner R. 2005. Molecular, structural, and functional characterization of Alzheimer's disease: evidence for a relationship between default activity, amyloid, and memory. J Neurosci 25:7709–7717.

Bullmore E, Sporns O. 2009. Complex brain networks: graph theoretical analysis of structural and functional systems. Nature 10:186–198.

Clerx L, Visser PJ, Verhey F, Aaten P. 2012. New MRI markers for Alzheimer's disease: a meta-analysis of diffusion tensor imaging and a comparison with medial temporal lobe measurements. J Alzheimers Dis 29:405–429.

Daianu M, Dennis E, Jahanshad N, Nir TM, Toga AW, Jack, Jr. CR, Weiner MW, Thompson PM and the Alzheimer s Disease Neuroimaging Initiative. Alzheimer s Disease Disrupts Rich Club Organization in Brain Connectivity Networks. IEEE ISBI 2013, accepted, Jan. 14, 2013.

Daianu M, Jahanshad N, Dennis EL, Toga AW, McMahon KL, de Zubicaray GI, Martin NG, Wright MJ, Hickie IB, Thompson PM. 2012a. Left versus right hemisphere differences in brain connectivity: 4-Tesla HARDI tractography in 569 twins. IEEE ISBI 526–529.

Daianu M, Jahanshad N, Nir TM, Dennis E, Toga AW, Jack CR, Jr., et al. Analyzing the structural k-core of brain connectivity networks in normal aging and Alzheimer's disease. In NIBAD' 12 MICCAI Workshop on Novel Imaging Biomarkers for Alzheimer's Disease and Related Disorders, Nice, France, 2012b, pp. 52–62.

de Haan W, Pijnenburg YAL, Strijers RLM, van der Made Y, van der Flier WM, Scheltens P, Stam CJ. 2009. Functional neural network analysis in frontotemporal dementia and Alzheimer's disease using EEG and graph theory. BMC Neurosci 10:101.

Delbeuck X, Van der Linden M, Collette F. 2003. Alzheimer's disease as a disconnection syndrome? Neuropsychology 13:79–92.

Dennis EL, Jahanshad N, Toga AW, Johnson K, McMahon KL, de Zubicaray GI, Martin NG, Hickie IB, Wright MJ, Thompson PM. 2012c. Test-retest reliability of graph theory measures of structural brain connectivity. Med Image Comput Assist Interv 15(Pt 3):305–312.

Dennis EL, Jahanshad N, Toga AW, McMahon KL, de Zubicaray GI, Martin NG, Hickie IB, Wright MJ, Thompson PM. 2012a. Development of brain structural connectivity between ages 12 and 30: a 4-tesla diffusion imaging study in 439 adolescents and adults. NeuroImage 64:671–684.

Dennis EL, Jahanshad N, Toga AW, Rudie JD, Dapretto M, Brown JA, Bookheimer SY, Johnson K, McMahon KL, de Zubicaray GI, Montgomery G, Martin NG, Wright MJ, Thompson PM. 2012b. Abnormal structural brain connectivity in healthy carriers of the autism risk gene, CNTNAP2. Brain Connect 1:447–459.

Dennis EL, Thompson PM. 2012. Mapping connectivity in the developing brain, invited review article (submitted to International Journal of Developmental Neuroscience) Special Issue: "Neuroimaging before and after Birth".

Dennis EL, Thompson PM. 2013. Mapping connectivity in the developing brain. Int J Dev Neurosci 31:525–542.

Desikan RS, Segonne F, Fischl B, Quinn BT, Dickerson BC, Blacker D, Buckner RL, Dale AM, Maguire RP, Hyman BT, Albert MS, Killiany RJ. 2006. An automated labeling system for subdividing the human cerebral cortex on MRI scans into gyral based regions of interest. Neuroimage 31:968–980.

Filippi M, Agosta F, Barkhof F, Dubois B, Fox NC, Frisoni GB, Jack CR, Johannsen P, Miller BL, Nestor PJ, Scheltens P, Sorbi S, Teipel S, Thompson PM, Wahlund LO. 2012. EFNS (European Federation of Neurological Societies) Task Force: the use of neuroimaging in the diagnosis and management of dementia. Eur J Neurol (In press).

Fischl B, Destrieux C, Halgren E, Segonne F, Salat DH, Busa E, Seidman LJ, Goldstein J, Kennedy D, Caviness V, Makris N, Rosen B. 2004. Automatically parcellating the human cerebral cortex. Cereb Cortex 14:11–22.

Geschwind N. 1965. Disconnection syndrome in animals and man. Brain 88:237–294.

Gili T, Cercignani M, Serra L, Perri R, Giove F, Maraviglia B, Caltagirone C, Bozzali M. 2012. Regional brain atrophy and functional disconnection across Alzheimer's disease evolution. J Neurol Neurosurg Psychiatry 82:58–66.

Hagmann P, Cammoun L, Gigander X, Meuli R, Honey CJ, Wedeen VJ, Sporns O. 2008. Mapping the structural core of the human cerebral cortex. PLoS Biol 6:1479–1493.

He Y, Chen Z, Evans A. 2008. Structural insights into aberrant topological patterns of large-scale cortical networks in Alzheimer's disease. J Neurosci 28:4756–5766.

Horwitz B, Grady CL, Sclageter NL, Duara R, Rapoport SI. 1987. Intercorrelations of regional glucose metabolic rates in Alzheimer's disease. Brain Res 407:294–306.

Hua X, Leow AD, Parikshak N, Lee S, Chiang MC, Toga AW, Jack CR, Jr., Weiner MW, Thompson PM, Alzheimer's Disease Neuroimaging Initiative. 2008. Tensor-based morphometry as a neuroimaging biomarker for Alzheimer's disease: an MRI study of 676 AD, MCI and normal subjects. NeuroImage 43:458–469.

Jack CR, Bernstein MA, Borowski BJ, Gunter JL, Fox NC, Thompson PM, Schuff N, Krueger G, Killiany RJ, DeCarli CS, Dale AM, Carmichael OW, Tosun D, Weiner MW. 2010. Update on the magnetic resonance imaging core of the Alzheimer's Disease Neuroimaging Initiative. Alzheimers Dement 6:212–220.

Jahanshad N, Aganj I, Lenglet C, Josh A, Jin Y, Barysheva M, McMahon KL, de Zubicaray GI, Martin NG, Wright MJ, Toga AW, Sapiro G, Thompson PM. 2011. Sex differences in the human connectome: 4-Tesla high angular resolution diffusion imaging (HARDI) tractography in 234 young adult twins. IEEE Xplore 939–943.

Jahanshad N, Valcour VG, Nir TM, Kohannim O, Busovaca E, Nicolas K, Thompson PM. 2012. Disrupted brain networks in the aging HIV+ population. Brain Connect 2:335–344.

Jahanshad N, Zhan L, Bernstein MA, Borowski B, Jack CR, Toga AW, Thompson PM. 2010. Diffusion tensor imaging in seven minutes: determining trade-offs between spatial and directional resolution. IEEE ISBI 1161–1164.

Lazar M, Weinstein DM, Tsuruda JS, Hasan KM, Arfanakis K, Meyerand ME, Badie B, Rowley HA, Haughton V, Field A,

Alexander AL. 2003. White matter tractography using diffusion tensor deflection. Hum Brain Mapp 18:306–321.

Lee H, Kang H, Chung MK, Kim BN, Lee DS. 2012. Persistent brain network homology from the perspective of dendrogram. IEEE Trans Med Imaging 31:2267–2277.

Lichtheim L. 1885. On aphasia. Brain 7:433–484.

Lo CY, Wang PN, Chou KN, Wang J, He Y, Lin CP. 2010. Diffusion tensor tractography reveals abnormal topological organization in structural cortical networks in Alzheimer's disease. J Neurosci 30:16876–16885.

Loewenstein DA, Barker WW, Chang JY, Apicella A, Yoshii F, Kothari P, Levin B, Duara R. 1989. Predominant left hemisphere metabolic dysfunction in dementia. Arch Neurol 46:146–152.

Lustig C, Snyder AZ, Bhakta M, O'Brien KC, McAvoy M, Raichle ME, Morris JC, Buckner RL. 2003. Functional deactivations: change with age and dementia of the Alzheimer type. PNAS 100:14504–14509.

Mesulam MM. 1998. From sensation to cognition. Brain 121:1031–1052.

Mori S, Crain BJ, Chacko VP, van Zijl PC. 1999. Three-dimensional tracking of axonal projections in the brain by magnetic resonance imaging. Ann Neurol 45:265–269.

Nir TM, Jahanshad N, Jack CR, Weiner MW, Toga AW, Thompson PM. 2012a. Small-world network measures predict white matter degeneration in patients with early-stage mild cognitive impairment. IEEE ISBI 1405–1408.

Nir TM, Jahanshad N, Toga AW, Bernstein MA, Borowski BJ, Jack CR, Weiner MW, Thompson PM, Alzheimer's Disease Neuroimaging Initiative (ADNI). 2012b. Connectivity network breakdown predicts imminent volumetric atrophy in early mild cognitive impairment. MICCAI Multi-Modal Workshop (MBIA) 7509:41–50.

Prasad G, Nir TM, Toga AW, Thompson PM and the Alzheimer's Disease Neuroimaging Initiative. 2013. Tractography density and network measure in Alzheimer's disease. IEEE ISBI.

Rose SE, Chen F, Chalk JB, Zelaya FO, Strugnell WE, Benson M, Semple J, Doddrell DM. 2000. Loss of connectivity in Alzheimer's disease: an evaluation of white matter tract integrity with colour coded MR diffusion tensor imaging. J Neurol Neurosurg Psychiatry 69:528–530.

Sanz-Arigita EJ, Schoonheim MM, Damaiseaux JS, Rombouts SA, Maris E, Barkhof F, Scheltens P, and Stam CJ. 2010. Loss of 'Small-World' networks in Alzheimer's disease: graph analysis of fMRI resting-state functional connectivity. PLoS One 5:e13788.

Sporns O. 2011. *Networks of the Brain*. Cambridge, MA: MIT Press, pp. 5–31.

Stam CJ, de Haan W, Daffertshofer A, Jones BF, Nashaden I, van Cappellen van Walsum AM, Montez T, Verbunt JPA, de Munck JC, van Dijk BW, Berendse HW, Scheltens P. 2009. Graph theoretical analysis of magnetoencephalographic functional connectivity in Alzheimer's disease. Brain 132:213–224.

Stam CJ, Jones BE, Nolte G, Breakspear M, Scheltens P. 2007. Small-world networks and functional connectivity in Alzheimer's disease. Cereb Cortex 17:92–99.

Supekar K, Menon V, Rubin D, Musen M, Greicius MD. 2008. Network analysis of intrinsic functional brain connectivity in Alzheimer's disease. PLoS Comput Biol 4:1–11.

Thompson PM, Hayashi KM, de Zubicaray G, Janke AL, Rose SE, Semple J, Herman D, Hong MS, Dittmer SS, Doddrell DM, Toga AW. 2003. Dynamics of gray matter loss in Alzheimer's disease. J Neurosci 23:994–1005.

Thompson PM, Mega MS, Woods RP, Zoumalan CI, Lindshield CJ, Blanton RE, Moussai J, Holmes CJ, Cummings JL, Toga AW. 2001. Cortical change in Alzheimer's disease detected with a disease-specific population-based brain atlas. Cereb Cortex 11:1–16.

Van den Heuvel MP, Sporns O. 2011. Rich club organization of the human connectome. J Neurosci 31:15775–15786.

Wada Y, Nanbu Y, Koshino Y, Yamaguchi N, Hashimoto T. 1998. Reduced interhemispheric EEG coherence in Alzheimer's disease: analysis during rest and photic stimulation. Alzheimer Dis Assoc Disord 12:175–181.

Wang J, Zuo X, Dai Z, Xia M, Zhao Z, Zhao X, Jia J, Han Y, He Y. 2012. Disrupted functional brain connectome in individuals at risk for Alzheimer's disease. Biol Psychiatry 73:472–481.

Wegrzyn M, Hoppner J, Oltmann I, Hauenstein K, Teipel S. 2011. Investigating structural and functional cortical disconnection in Alzheimer's disease, using diffusion tensor imaging and transcranial magnetic stimulation. Alzheimers Dement 7:S746, Abstract.

Wernicke C. 1874/1977. Der aphasische symtomencomplex: Eine psychologische studie auf anatomicher basis. Breslau: Cohn und Weigert: 1874.

Xie T, He Y. 2012. Mapping the Alzheimer's brain with connectomics. Front Psychiatry 2:1–13.

Yao Z, Zhang Y, Lin L, Zhou Y, Xu C, Jiang T, the Alzheimer's Disease Neuroimaging Initiative. 2010. Abnormal cortical networks in mild cognitive impairment and Alzheimer's Disease. PLOS Comput Biol 6:1–11.

Zalesky A. 2009. DTI-derived measure of cortico-cortical connectivity. IEEE 28:1023–1036.

Zhan L, Jahanshad N, Ennis DB, Bernstein MA, Borowski BJ, Jack CR, Toga AW, Leow AD, Thompson PM. 2012. Angular versus spatial resolution trade-offs for diffusion imaging under time constraints. Hum Brain Mapp [Eub ahead of print]; DOI: 10.1002/hbm.22094.

Zhan L, Jahanshad N, Jin Y, Lenglet C, Mueller BA, Sapiro G, Ugurbil K, Harel N, Toga AW, Lim KO, Thompson PM. 2013a. Field strength effects on diffusion measures and brain connectivity networks. Brain Connect 3:72–86.

Zhan L, Jahanshad N, Jin Y, Toga AW, McMahon KL, Martin NG, Wright MJ, Zubicaray GI, Thompson PM. 2013b. Brain network efficiency and topology depend on the fiber tracking method: 11 tractography algorithms compared in 536 subjects. IEEE ISBI.

Address correspondence to:
Paul M. Thompson
Department of Neurology
Laboratory of Neuro Imaging
Imaging Genetics Center
UCLA School of Medicine
635 Charles E. Young Drive South, Suite 225E
Los Angeles, CA 90025-7332

E-mail: thompson@loni.ucla.edu

CHAPTER 3

Network thresholding and the brain's "rich club"

3.1 Effects of network thresholding

This section is adapted from:

Daianu M, et al. Disrupted Brain Connectivity in Alzheimer's Disease: Effects of Network Thresholding. In MMBC'13 MICCAI Workshop on Mathematical Methods for Brain Connectivity, Nagoya, Japan*, accepted,* June 2013.

Disrupted Brain Connectivity in Alzheimer's Disease: Effects of Network Thresholding

Madelaine Daianu[1], Emily L. Dennis[1], Neda Jahanshad[1], Talia M. Nir[1], Arthur W. Toga[1], Clifford R. Jack, Jr.[2], Michael W. Weiner[3,4], Paul M. Thompson[1*]
for the Alzheimer's Disease Neuroimaging Initiative[**]
[1]Imaging Genetics Center, Laboratory of Neuro Imaging,
UCLA School of Medicine, Los Angeles, CA, USA
[2]Department of Radiology, Mayo Clinic, Rochester, Minnesota, USA
[3]Department of Radiology, Medicine, and Psychiatry,
University of California San Francisco, CA, USA
[4]Department of Veterans Affairs Medical Center, San Francisco, CA, USA

Abstract. Diffusion imaging is accelerating our understanding of the human brain. As brain connectivity analyses become more popular, it is vital to develop reliable metrics of the brain's connections, and their network properties, to allow statistical study of factors that influence brain 'wiring'. Here we chart differences in brain structural networks between normal aging and Alzheimer's disease (AD) using 3-Tesla whole-brain diffusion-weighted images (DWI) from 66 subjects (22 AD/44 normal elderly). We performed whole-brain tractography based on the orientation distribution functions. Connectivity matrices were compiled, representing the proportion of detected fibers interconnecting 68 cortical regions. We found clear disease effects on anatomical network topology in the structural backbone – the so-called 'k-core' – of the anatomical network, defined by varying the nodal degree threshold, k. However, the thresholding of the structural networks – based on their nodal degree – affected the pattern and interpretation of network differences discovered between patients and controls.

1. Introduction

Diffusion imaging has recently been added to several large-scale neuroimaging studies, including the Alzheimer's Disease Neuroimaging Initiative (ADNI), to monitor white matter deterioration using metrics not available with standard anatomical MRI. Diffusion MRI yields measures sensitive to fiber integrity and microstructure, such as the mean diffusivity and fractional anisotropy of local water diffusion [1]; in addition, tractography can be used to infer neural pathways and connectivity patterns, yielding additional, more complex mathematical metrics describing fiber networks.

[1*]Corresponding author; email: pthomp@usc.edu

Despite the enthusiasm for using diffusion imaging to map brain connectivity and how it changes with disease, there is a lack of serious groundwork validating these methods to see if the connections they map are correct and how acquisition and analysis protocols affect them. Post-processed connectivity data is also affected by the level of thresholding applied to the brain connectivity matrices; thresholding is commonly applied to retain key information on the most crucial subnetworks, while eliminating false positive fibers or connections inaccurately inferred due to noise and imaging artifacts. There is no consensus about what might be the ideal level of thresholding to retain only the most relevant information in post-processed connectivity data. A common approach filters networks based on the nodal degree, leaving only the most highly connected nodes. As this loses information, some groups advocate defining metrics on the entire set of networks at all thresholds, using concepts such as the *Rips filtration* [2].

Here we studied anatomical fiber networks in 44 controls and 22 identically scanned people with Alzheimer's disease (AD) using novel mathematical network metrics derived from the 'structural backbone' – or k-core – of the human brain. Based on prior studies [3], we were interested in understanding how the different number of nodes, N, in filtered networks from healthy and diseased subjects affects graph theory measures computed from thresholded connectivity matrices. In the end, it would be unwise to infer that AD affects networks in a particular way, if networks filtered differently showed different disease effects. To explore this, we computed the network's structural core using a k-core decomposition [4] to find important sets of nodes that are highly and mutually interconnected. The level of the k-core, k, serves as a threshold to retain nodes in the connectivity matrix with degree k or higher. We systematically varied the values of k (k=1, …, 20) and analyzed the changes in the resulting network measures to understand how they are affected by thresholding the size or degree of the networks (N, k). We calculated global measures sensitive to anatomical network topology: the clustering coefficient (CC), characteristic path length (CPL), efficiency (EFF), and nodal degree (NOD) for all 66 subjects at each of the 20 k-core levels. All network measures showed group differences that depended heavily on the nodal degree and size of the threshold applied to the network. We aimed to find out which network measures are most and least sensitive to variation in the N and k levels, in terms of their ability to resolve differences between the healthy and diseased groups.

2. Methods

2.1. Subjects and Diffusion Imaging of the Brain

We analyzed diffusion-weighted images (DWI) from 66 subjects scanned as part of phase 2 of the Alzheimer's Disease Neuroimaging Initiative (ADNI2), a large multi-site longitudinal study to evaluate biomarkers to assist diagnosis and track disease progression. **Table 1** shows subject demographics and diagnostic information; data collection is ongoing. All 66 subjects underwent whole-brain MRI scanning on 3-Tesla

GE Medical Systems scanners, at a variety of sites across North America, with the same protocol, which had been optimized for SNR. Standard anatomical T1-weighted SPGR (spoiled gradient echo) sequences were collected (256x256 matrix; voxel size = 1.2x1.0x1.0 mm^3; TI = 400 ms, TR = 6.984 ms; TE = 2.848 ms; flip angle = 11°) in the same session as the diffusion-weighted images (DWI; 256x256 matrix; voxel size: 2.7x2.7x2.7 mm^3; scan time = 9 min). 46 separate images were acquired for each DTI scan: 5 T2-weighted mages with no diffusion sensitization (b$_0$ images) and 41 diffusion-weighted images (b = 1000 s/mm^2).

Table 1. Demographic information for 44 controls and 22 AD patients scanned with diffusion MRI as part of ADNI. Their ages ranged from 55.7 to 90.4 years.

	Controls	AD	Total
N	44	22	66
Age	72.7 ± 5.9 SD	75.5 ± 10.0 SD	73.6 ± 7.5 SD
Sex	22M/22F	14M/8F	36M/30F

2.2 Image Analysis

Pre-processing and Co-registration

Non-brain regions were automatically removed from each T1-weighted MRI scan, and from a T2-weighted image from the DWI set using the FSL tool "BET" (http://fsl.fmrib.ox.ac.uk/fsl/). Anatomical scans subsequently underwent intensity inhomogeneity normalization using the MNI "nu_correct" tool (www.bic.mni.mcgill.ca/software/). All T1-weighted images were linearly aligned using FSL (with 6 DOF) to a common space with 1mm isotropic voxels and a 220×220×220 voxel matrix. The DWI were corrected for eddy current distortions using the FSL tools (http://fsl.fmrib.ox.ac.uk/fsl/). For each subject, the 5 images with no diffusion sensitization were averaged, linearly aligned and resampled to a downsampled version of their T1-weighted image (110×110×110, 2×2×2mm). b$_0$ maps were elastically registered to the T1-weighted scan to compensate for susceptibility artifacts or EPI induced distortions.

Tractography and Cortical Extraction

The transformation matrix from linearly aligning the mean b$_0$ image to the T1-weighted volume was applied to each of the 41 gradient directions to properly re-orient the orientation distribution functions (ODFs). We also performed whole-brain tractography as described in [5] on the sets of DWI volumes. We used a method based on the Hough transform to recover fibers, using a constant solid angle orientation density function to model the local diffusion propagator. The angular resolution of the ADNI data

is deliberately limited to avoid long scan times that may increase patient attrition, but the ODF model makes best use of the limited available angular resolution.

Elastic deformations obtained from the EPI distortion correction, mapping the average b_0 image to the T1-weighted image, were then applied to each recovered fiber's 3D coordinates to more accurately align the anatomy. Each subject's dataset contained ~10,000 useable fibers (3D curves) in total. 34 cortical labels per hemisphere, as listed in the Desikan-Killiany atlas [6], were automatically extracted from all aligned T1-weighted structural MRI scans using FreeSurfer (http://surfer.nmr.mgh.harvard.edu/) [7].

NxN Matrices Representing Structural Connectivity

For each subject, a baseline 68x68 connectivity matrix was created, based on 34 right hemisphere ROIs and 34 left hemisphere ROIs. Each element described the estimated proportion of the total number of fibers, in that subject, that passes through each pair of ROIs. We note that various normalizations could be applied (e.g., using the volume or area of the target ROIs, or to turn these counts into densities), but for simplicity we here just used the fiber counts (normalized to the total number of fibers detected in the brain).

2.3   Brain Network Measures

Topological differences in the brain's networks may be analyzed using graph theory, which represents the brain network as a set of nodes and edges. The network's *N* nodes are typically defined as ROIs, usually on the cortex, segmented from anatomical MRI. These network nodes are linked by 'edges' whose weights denote some measure of connectivity between the two regions, such as the density or integrity of fiber tracts in DTI studies [8]. An *NxN* connection matrix may therefore be compiled to describe the network. A square matrix can represent any network of connections, and may also be displayed as a graph, i.e., a discrete set of nodes and edges [8], leading the way for analyses through the branch of mathematics known as graph theory. In our analysis, the matrix entries store the total proportion of fibers connecting each pair of regions (the nodes); these could also be considered as the "weights" of the edges that connect a pair of nodes [8].

From the connection matrices, we applied a threshold by computing the *k*-core for 20 levels of the nodal degree threshold, *k*, using a decomposition algorithm that identifies subsets of graphs (*k*-cores) by recursively removing nodes with degrees lower than *k*, such that *k* serves as a degree threshold for nodes [9]. For a graph $G = (N, E)$ with $|N| = n$ nodes and $|E| = e$ edges, a *k*-core is computed by assigning a subgraph, $H = (B, E|B)$ where set $B \subseteq N$ is a *k*-core of order *k* iff $\forall v \in B$: degree$_H \geq k$, and *H* is the maximal subgraph (most highly connected one) satisfying this property [9]. In other words, to compute the *k*-core of the connectivity matrix, we kept all nodes with a degree *k* or higher. These then become new 68x68 matrices, each being a somewhat thresholded version of the original; weights of nodes that did not satisfy the *k*-cutoff were replaced with zeroes.

We obtained the *k*-core matrices by varying *k* from 1 to 20 for both controls and AD subjects. The global graph theory measures (CC, CPL, EFF, and NOD) were derived from each *k*-core matrix for each subject, to yield four representative network measures at each *k*-level (i.e., each subject had 20 global metrics for CC, CPL, EFF and NOD). These are the most common topological network measures used to describe the integrity of the healthy or diseased human brain (Sporns, 2011), although their use in brain connectivity and AD research is yet to be extensively explored. The degree of a node *i*, measures the number of edges connected to a node:

$$k_i = \sum_{j \in N} a_{ij} \qquad \text{(Eq. 1)}$$

where a_{ij} is a connections status between nodes *i* and *j*; $a_{ij} = 1$ when there is a link (*i,j*) interconnecting nodes *i* and *j* and $a_{ij} = 0$ otherwise.

CPL, a measure of integration, is the average shortest path length in a network:

$$L = \frac{1}{n}\sum_{i \in N} L_i = \frac{\sum_{j \in N, j \neq i} d_{ij}}{n-1} \qquad \text{(Eq. 2)}$$

where L_i is the average distance between node *i* and all other nodes in the networks, d_{ij} is the shortest path length, *(i,j)* is a link between nodes *i* and *j* and *n* is the number of nodes (Sporns, 2011).

EFF is a global and generally robust measure, and is the inverse of the average of the characteristic path length:

$$E = \frac{1}{n}\sum_{i \in N} \frac{\sum_{j \in N, j \neq i} d_{ij}^{-1}}{n-1} \qquad \text{(Eq. 3)}$$

CC, a measure of segregation, is the fraction of a node's neighbors that are neighbors of each other:

$$C = \frac{1}{n}\sum_{i \in N} C_i = \frac{1}{n}\sum_{i \in N} \frac{\frac{1}{2}\sum_{j,h \in N} a_{ij}a_{ih}a_{jh}}{k_i(k_i-1)} \qquad \text{(Eq. 4)}$$

where C_i is the clustering coefficient of node *i* ($C_i = 0$, $k_i < 2$), k_i is the degree of a node *i*, $k_i = \sum_{j \in N} a_{ij}$ where a_{ij} is the connection status between nodes *i* and *j* when a link between *(i,j)* exists (Sporns, 2011).

NOD was computed as a nodal measure first, and then averaged overall all 70 cortical regions for each subject to output a global measure. CC and CPL measures were normalized based on 100 randomized networks of equal size and similar connectivity distribution. Path length should be normalized using appropriately constructed random networks, as the absolute (unnormalized) value of the path length provides limited information on the integration in the brain network (Sporns, 2011); the path length varies greatly with the size and density of individual graphs, whereas efficiency is a more robust measure - the average of the inverse of the distance matrix (Sporns, 2011), and was not normalized here. We tested for between-group differences using a linear regression, controlling for age and sex, with AD coded as 1 and controls as 0. We tested for differences between groups of controls and AD subjects for CC, CPL, EFF and NOD at each *k*-core value for the brain network. We also tested for within-group differences for network measures EFF and NOD, which were found to be "most significant" in the between-group comparison. For this, we compared every *k*-level across subjects within

one diagnostic group with every other k-level in that group (i.e., EFF for controls at $k1$=1,2…19 was compared to EFF for controls at $k2$=($k1$+1)…20) using a 2-tailed paired t-test. We applied an FDR correction on all (20*20-20)/2 comparisons.

3. Results

The variation in the k-core levels (k=1, …, 20) affected the networks and, as expected, resulted in changing graph theory measures (CC, CPL, EFF and NOD) in each diagnostic group.
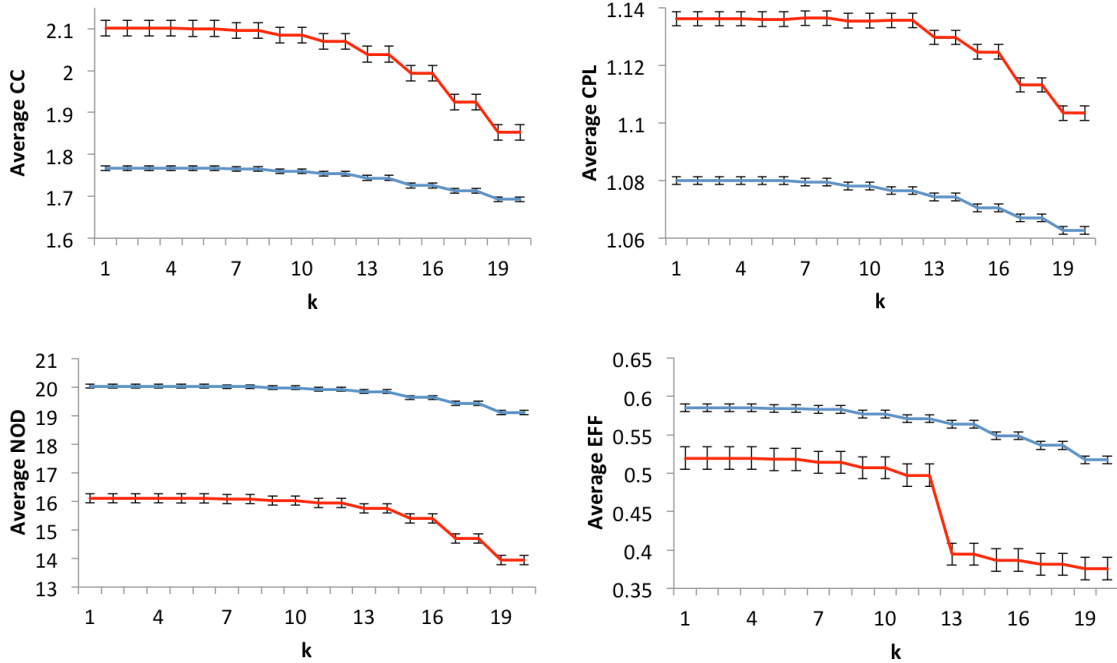
Figure 1. Average and global CC, CPL, EFF and NOD for the whole brain in 44 controls (*blue*) and 22 AD subjects (*red*), based on thresholding the network at k=1, …, 20. Error bars show the standard errors.

We performed *between* group comparisons to find out how effect sizes for group differences depended on the network degree threshold. Relative to controls, the AD group had a higher global CC (FDR critical p-value=6.26E-03) for the entire range of k-core values (k=1-20) and a higher global CPL (p-value=5.72E-3) for k-cores in the range k=1-18. Obtaining a higher CC in AD, relative to controls, may not be entirely intuitive, but the CC can be disproportionately influenced by nodes with low degree [8]. NOD (FDR critical p-value=3.65E-05) and EFF (FDR critical p-value=6.21E-05) were lower in AD over the whole range of k-core values (k=1-20), relative to controls. Averaged network measures (**Figure 1**) and p-values (**Figure 2**) are plotted.

Furthermore, we tested for *within* group differences in all subjects for NOD and EFF, as these measures showed greatest effect sizes in the diagnostic group comparisons. The results are shown in a 20x20 matrix, where the EFF was calculated from matrices thresholded at each k-level. We compared the EFF network measure to the same network

measure calculated from the other *k*-levels – always within the same diagnostic group, to avoid incorporating disease effects (**Figure 3)**. EFF changed significantly as *k* varied in both controls and AD (FDR critical *p*-value=1.42E-02 for controls and 1.27E-02 for AD). Within-group measures for NOD were not significantly different across any *k*-levels in either group.
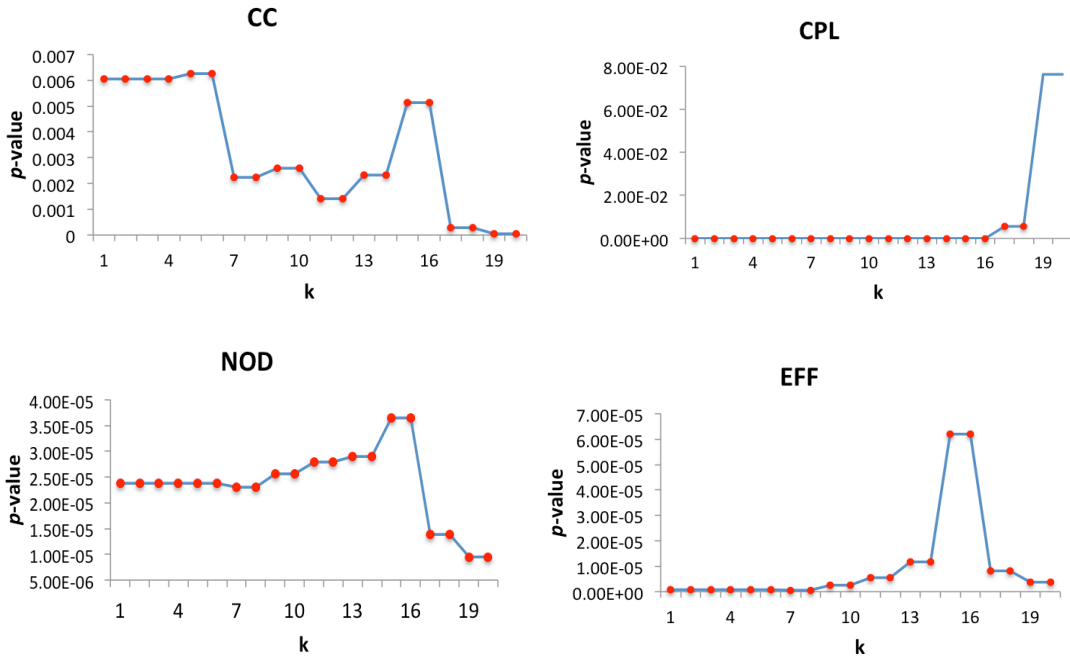
Figure 2. *p*-values from a regression controlling for age and sex, testing for significant differences between AD subjects and controls for whole-brain global CC, CPL, EFF and NOD in AD subjects versus controls. Red points highlight *p*-values that are less than the *p*-value threshold (CC *p*-value=6.26E-03, EFF *p*-value=6.21E-05, NOD *p*-value=3.65E-05 and CPL *p*-value=5.72E-03) that controls the FDR at 5%. This FDR correction allows us to state that the groups truly differ, even though multiple thresholds were tested.
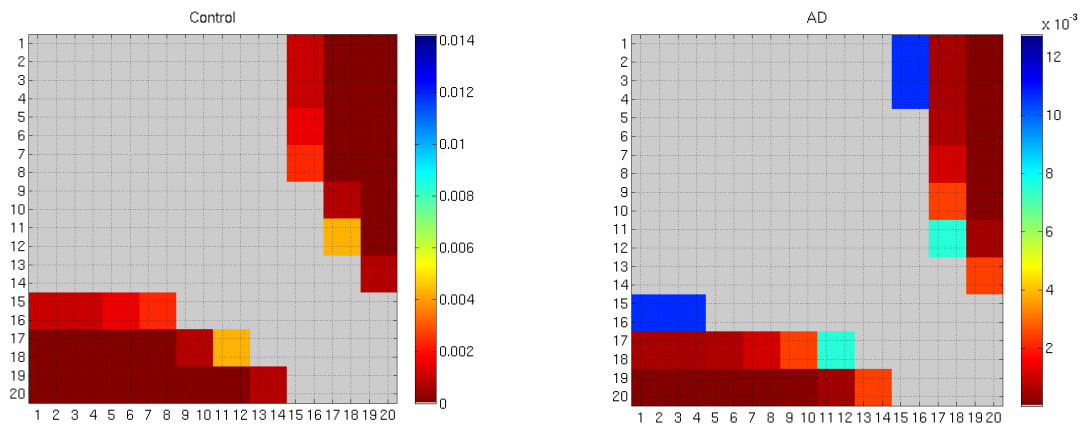
Figure 3. Matrix (20x20) representing the *p*-values from the *within* group comparisons for EFF across all *k*-levels within each group (FDR critical *p*-value=1.42E-02 for controls and 1.27E-02 for AD). A given cell (*x,y*) in this matrix gives the *p*-value for the *t*-test comparing the value of EFF

between *k*-cores where the minimum nodal degree is x and y, respectively. As expected, greatest differences in network measures were found between lowest and highest *k*-levels (red *p*-values).

4. Discussion

Graph theory has been widely used to assess functional and anatomical networks in the brain, but not nearly so much attention has been paid to analyzing network variations due to choices made in analysis methods (i.e., network thresholding) and how they impact network topology comparisons. With the growing interest in connectivity analyses, it is important to understand how stable network measures are, and develop reliable guidelines when applying them to study disease. The interpretation of network breakdown in disease may be somewhat different depending on the criteria used to compare or filter networks.

Here we analyzed brain connectivity in cognitively impaired patients with AD and matched normal controls. We varied the nodal degree threshold applied to the connectivity matrices for both groups by using a wide range of *k*-core values (*k*=1, …, 20). Some network measures - CC, CPL, EFF and NOD - *declined* across all subjects as nodal degree threshold levels were increased. Network measures that showed the greatest differences between diagnostic groups over *k* levels ranging from 1 to 20 are in the following order (i.e., with the greatest size effect and smallest *p*-values): NOD, EFF, CPL, and CC. NOD and EFF were found to have greatest size effects among all measures (FDR critical *p*-value=3.65E-05 and 6.21E-05) (**Figures 1** and **2**). This led us to analyze within-group differences for NOD and EFF; we found that increasing levels of *k* significantly affects the apparent efficiency of the overall network in both controls and AD, while NOD was not affected by varying *k* levels (**Figure 3**).

The decline in all network measures with increasing *k* levels is expected in both diagnostic groups. This is because networks thresholded at higher *k* levels required a greater number of nodes to be connected (e.g., at *k*=20, approximately 30% of the nodes are connected). Similarly, AD is known to disrupt the overall network topology of the brain [2,3] leading to fewer nodes when compared to controls. This is why NOD had the greatest effect size in the between-group comparisons. Also, the loss of nodes in the network can disproportionately influence other network metrics, such as the CC – found to be greater in AD than in controls [10], which otherwise would indicate a densely interconnected and coherent brain system [3, 8].

An ideal network threshold for this data is in the range of *k*=15-18. This includes at least 22-26% of the nodes in each brain network, yielding the 'most significant' effects in both *between* and *within* group comparisons. Ideally, this threshold would tend to suppress noise and some imaging artifacts, removing weak connections while emphasizing stronger connections altered in disease. This range may vary with study-specific parameters.

We studied the effect sizes for the group differences here, to clarify how network filtering parameters influence the differentiation of diseased versus normal groups based on graph theory metrics. Although there is no universal method and no definitive answer as to how networks of different sizes and connectivity densities should be accurately compared and analyzed [11], maintaining these measures consistent across study groups is crucial for obtaining comparable results. Normalizing the network measures using

randomized networks with the same number of nodes and connections may make graph metrics more stable with respect to differences in N and k [11]. In the end, methods based on network filtrations may supersede those applied to thresholded networks, if they better detect disease effects on brain connectivity.

References

1. Clerx, P., et al., *New MRI markers for Alzheimer's disease: a meta-analysis of diffusion tensor imaging and a comparison with medial temporal lobe measurements*. **J Alzheimer's Dis.** 2012; 29(2):405-29.
2. Lee H., et al., *Persistent Brain Network Homology from the Perspective of Dendrogram*. **IEEE Transactions on Medical Imaging** 31(12):2267-77.
3. Daianu M., et al., *Breakdown of Brain Connectivity between Normal Aging and Alzheimer's Disease: A Structural k-core Network Analysis*. **Brain Connect.** 2013 [Epub ahead of print].
4. Hagmann, P., et al., *Mapping the structural core of the human cerebral cortex*. **PLoS Biology** 2008;6(7):1479-1493
5. Aganj, I., et al., *A Hough transform global probabilistic approach to multiple-subject diffusion MRI tractography*. **Med Image Analysis** 2011;15(4):414-25.
6. Desikan, R. S., et al., *An automated labeling system for subdividing the human cerebral cortex on MRI scans into gyral based regions of interest*. **NeuroImage** 2006; 31(3):968-80.
7. Fischl B., et al., *Automatically parcellating the human cerebral cortex*. **Cerebral Cortex** 2004;14:11-22.
8. Sporns, O., *Networks of the Brain*. Cambridge, MA, 2011;5-31.
9. Alvarez-Hamelin, J. I., et al., *Large scale networks fingerprinting and visualization using k-core decomposition*. Weiss Y, Scholkopf B, Platt J. editors. Cambridge (Massachusetts) 2006; MIT Press 44-55.
10. Yao Z., Zhang Y., Lin L., Zhou Y., Xu C., Jiang T. *Alzheimer's Disease Neuroimaging Initiative. Abnormal cortical networks in mild cognitive impairment and Alzheimer's disease.* **PLoS Comput Biol.** 2010 18;6(11):e1001006.
11. Wijk, B. C. M., et al., *Comparing Brain Networks of Different Size and Connectivity Density Using Graph Theory*. **PLoS One** 2010; 5(10):e13701.

3.2 Disruptions of the "rich club" network

This section is adapted from:

Daianu M, et al. Structural brain network and rich club disruptions in mild cognitive impairment and Alzheimer's disease. Neurobiology of Aging, *submitted*, January 7 2014.

Structural brain network and rich club disruptions in mild cognitive impairment and Alzheimer's disease

Madelaine Daianu [a,b], Neda Jahanshad [b], Talia M. Nir [b], Emily L. Dennis [b], Cassandra D. Leonardo [b],

Clifford R. Jack, Jr.[c], Michael W. Weiner [d,e], Matthew Bernstein [c], Paul M. Thompson [a,b,f,g]*

and the Alzheimer's Disease Neuroimaging Initiative[**]

[a] Department of Neurology, UCLA School of Medicine, Los Angeles, CA, USA

[b] Imaging Genetics Center, Institute for Neuroimaging & Informatics, University of Southern California, Los Angeles, CA, USA

[c] Department of Radiology, Mayo Clinic, Rochester, Minnesota, USA

[d] Department of Radiology, Medicine, and Psychiatry, University of California San Francisco, CA, USA

[e] Department of Veterans Affairs Medical Center, San Francisco, CA, USA

[f] Departments of Neurology, Psychiatry, Radiology, Engineering, Pediatrics, and Ophthalmology, USC

[g] Department of Psychiatry, Semel Institute, UCLA, Los Angeles, CA, USA

Submitted to ***Neurobiology of Aging***: January 7, 2014

Please address correspondence to:

Paul Thompson, Professor of Neurology, Psychiatry, Engineering, Radiology, Pediatrics, and Ophthalmology

Imaging Genetics Center, and Institute for Neuroimaging and Informatics

Keck School of Medicine of USC, University of Southern California

2001 N. Soto Street, SSB1-102, Los Angeles, CA 90032

Tel: (323) 442-7246

Email: pthomp@usc.edu

Abstract

Diffusion imaging can assess white matter deterioration in the brain, revealing the breakdown of neural pathways in Alzheimer's disease (AD). We analyzed 3-Tesla whole-brain diffusion-weighted images from 202 subjects scanned by the Alzheimer's Disease Neuroimaging Initiative (ADNI) – 50 healthy controls, 72 with early- and 38 with late-stage mild cognitive impairment (eMCI/lMCI) and 42 AD patients. Based on whole-brain tractography, we reconstructed structural brain connectivity networks to map connections between cortical regions. We tested whether AD disrupts the 'rich club' – a network property where high-degree network nodes are more interconnected than expected by chance. We evaluated additional network topology measures including global degree, clustering coefficient, path length and efficiency. The rich club effect increased with cognitive impairment, as network complexity degenerated. Fewer network connections led to a more densely interconnected 'rich club'. With disease, global degree and efficiency declined, but the clustering coefficient and path length increased – measures more sensitive to disease effects than the rich club coefficient. As connections degenerate brain network properties are disrupted, offering additional biomarkers of AD.

Keywords: Alzheimer's disease, Mild Cognitive Impairment, MRI, DTI, structural network, biomarker, rich club, efficiency, global degree, path length, clustering coefficient

Acronyms

AD – Alzheimer's disease; ADNI –Alzheimer's Disease Neuroimaging Initiative; DTI – Diffusion tensor imaging; DWI – Diffusion weighted image; E – number of edges in network; eMCI – Early mild cognitive impairment; EEG – Electroencephalography; FDR – False discovery rate; FLAIR – Fluid-attenuated inversion-recovery; fMRI – Functional MRI; LH – Left hemisphere; lMCI – Late mild cognitive impairment; MEG – Magnetoencephalography; MMSE – Mini Mental State Examination; MRI – Magnetic resonance imaging; NS – Not significant; N – number of nodes in network; PET – Positron emission tomography; R – rich club coefficient; R_n – normalized rich club; R_{rand} – randomized rich club; RH – Right hemisphere; rs-fMRI – Resting state functional magnetic resonance imaging; SNR – Signal-to-noise ratio; SPGR – Spoiled gradient echo; WB – Whole brain

2

1. Introduction

Alzheimer's Disease (AD) is a progressive, degenerative brain disease and is the 6th leading cause of death in the US (Alzheimer's Association, 2013). Over 5 million Americans live with the disease and this number is expected to triple by 2050 (Alzheimer's Association, 2013) increasing health care costs by as much as 85% (Bruner and Jacobs, 2013). Worldwide, 44 million people have the disease. As the elderly population increases, over 115 million people may have AD by 2050 (Alzheimer's Association, 2013).

AD leads to a severe decline in multiple cognitive domains, particularly memory (Filippi et al., 2012). Progressive deposition of beta-amyloid and tau proteins in the brain lead to inflammation, neural atrophy and cell death (Wang et al., 2012). These processes affect the brain's gray matter, leading to extensive cortical and subcortical gray matter atrophy.

Recent studies with diffusion tensor imaging (DTI) reveal widespread disease effects on the brain's white matter (Clerx et al., 2012, Nir et al., 2013, Jahanshad et al., 2012). The spread of white matter degeneration may be due in part to Wallerian or 'backward' neurodegeneration, in which gray matter atrophy leads to axonal degeneration (Coleman, 2005; Ewers et al., 2012). White matter changes such as myelin degeneration (Braak and Braak, 1996), neuroinflammation and abnormal axonal transport are found in AD patients (Rowley et al., 2013). As white matter fiber tracts lose axons and myelin degenerates, T2-weighted MRI scans are often used to evaluate white matter hyperintensities – a sign of cerebrovascular disease. The breakdown of the brain's fiber networks may also explain some of the symptoms as AD progresses.

To better understand these fiber networks and microstructural white matter changes in AD, DTI (Mori and van Zijl, 2002; Basser and Jones, 2002) is increasingly used. DTI is sensitive to fiber integrity and microstructure, based on indices such as the mean diffusivity and fractional anisotropy of local water diffusion (Clerx et al., 2012). Diffusion-based tractography can infer neural pathways and patterns of structural connectivity. Cortical connectivity networks, reflecting the extent and degree to which various cortical regions are connected to each other, may be represented as a graph of nodes describing cortical regions and the neural pathways (or "edges") that connect them; the same data may be stored in a 2D matrix. This allows mathematical metrics to be used to describe the topology of the brain's networks, and the connectedness of key nodes. Network measures can assess the breakdown of white matter tracts with disease and have only been recently studied in AD (Buckner et al., 2009; Daianu et al., 2012; Nir et al., 2012a, b; Daianu et al., 2013; Prasad et al., 2013a, b)**.**

3

Recently, DTI has been added to several large-scale neuroimaging studies, including the Alzheimer's Disease Neuroimaging Initiative (ADNI) (Jack et al., 2010), to monitor white matter deterioration using metrics not available with standard anatomical MRI. Here we analyzed brain networks in 50 healthy controls, 72 people with eMCI, 38 with lMCI and 42 AD patients using recently proposed mathematical metrics, such as the rich club coefficient (van den Heuvel and Sporns, 2011). As far as we know, this is the first study to assess the rich club effect in MCI and AD. To better interpret our results, we assessed additional metrics: nodal degree, the clustering coefficient, characteristic path length and efficiency – some of which have network components involved in computing the rich club coefficient. The motivation for the study was the notion that the brain functions as an integrative network at micro- and macro-structural levels, where we can examine the integrity or dysfunction of white matter bundles using network measures. The rich club coefficient, among other connectivity metrics, may become potential biomarkers of AD, in additional to standard, more widely accepted measures.

Network models of the brain suggest that there is a 'rich club' effect – i.e., a core of nodes with a high degree (k) – that are more densely interconnected among themselves than lower-degree nodes in the network. In other words, the high-degree, 'richly-connected' nodes form a club. The nodal degree means the number of edges (or connections) that each node in a network has. A network's k-core is the subnetwork that remains after deleting all nodes of degree $< k$. The rich club coefficient, $R(k)$, is the ratio of the number of connections among nodes of degree k or higher versus the total possible number of connections if those nodes were fully connected. As higher-degree nodes are more likely to be interconnected with each other, simply by chance, $R(k)$ is typically normalized relative to R calculated on a set of simulated random networks with the same degree distribution, and the same edge distribution, as a function of the nodal degree, k. If $R_n > 1$ (i.e., $R(k) > R_{rand}$, for some k), then there is evidence of rich club organization (tests of the rich club effect use randomized networks to create a reference null distribution; van den Heuvel and Sporns, 2011).

To understand how networks break down in MCI and AD, we assessed how the rich club changes at each stage of cognitive impairment, and how more standard measures such as the nodal degree, clustering coefficient, characteristic path length and efficiency are affected as the brain degenerates. Intuition might suggest that the rich club effect might be affected in AD – but not in a direction known *a priori*. As we will show later, the normalized rich club coefficient *increased* with age and with greater cognitive impairment. To better understand how this could arise, we also detected a decline in the network's global degree and efficiency as disease progressed, and an overall

4

increase in the global normalized clustering coefficient and characteristic path length, consistent with a loss of key network connections. Finally, we analyzed how the normalized and unnormalized rich club coefficients provide information on network changes in AD in relation to the most sensitive network measures for detecting differences between diagnostic groups – efficiency and global degree. We ranked all network measures in the order of their effect size for detecting white matter alterations between the brain networks of all diagnostic groups.

2. Methods

2.1 Subjects and diffusion-weighted imaging of the brain

We analyzed diffusion-weighted images (DWI) from 202 subjects scanned as part of the Alzheimer's Disease Neuroimaging Initiative (ADNI). ADNI is a large multi-site longitudinal study to evaluate biomarkers of AD. **Table 1** shows the demographics of the subjects we studied including age, sex, and the mini-mental state exam (MMSE) scores, broken down by diagnosis; at the time of writing (November 2013), data collection for ADNI is ongoing. All 202 subjects underwent whole-brain MRI on 3-Tesla GE Medical Systems scanners, at a variety of sites across North America. Standard anatomical T1-weighted SPGR (spoiled gradient echo) sequences were collected (256x256 matrix; voxel size = 1.2x1.0x1.0 mm^3; TI = 400 ms, TR = 6.984 ms; TE = 2.848 ms; flip angle = 11°) in the same session as the DWI (128x128 matrix; voxel size: 2.7x2.7x2.7 mm^3; scan time = 9 min). 46 separate images were acquired for each scan: 5 T2-weighted images with no diffusion sensitization (b_0 images) and 41 diffusion-weighted images (b = 1000 s/mm^2). This protocol was chosen after comparing several different DWI protocols for ADNI, to optimize the signal-to-noise ratio in a fixed scan time (Jahanshad et al., 2010; Zhan et al., 2013a; Zhan et al., 2013b; Zhan et al., 2013c).

	Controls	eMCI	lMCI	AD	Total
N	50	72	38	42	202
Age	72.6 ± 6.1 SD	72.4 ± 7.9 SD	72.6 ± 5.6 SD	75.5 ± 8.9 SD	73.1 ± 7.4 SD
MMSE	28.9 ± 1.4 SD	28.1 ± 1.5 SD	26.9 ± 2.1 SD	23.3 ± 1.9 SD	27.1 ± 2.7 SD
Sex	22M/28F	45M/27F	25M/13F	28M/14F	120M/82F
Site	10	16	12	12	16

Table 1. Demographic information from 50 controls, 72 eMCI, 38 lMCI and 42 AD subjects scanned with diffusion MRI as part of the ADNI project. Their ages ranged from 55.2 to 90.4 years. The mean age and Mini Mental State Exam (MMSE) scores are listed for each diagnostic group. Subjects were scanned at 16 sites.

2.2 Image analysis and structural connectivity

Tractography based on diffusion-weighted images may be performed and used in conjunction with an automatically labeled set of brain regions from anatomical MRI to map connectivity and perform network analysis of the brain's fiber connections. Many analyses of brain connectivity have been conducted in this way (Jahanshad et al., 2012; Jahanshad et al., 2011; Ingalhalikar et al., 2013; Zhan et al., 2013a). Connectivity matrices were compiled using a processing pipeline described before (Jahanshad et al., 2011, Braskie et al., 2012; Jahanshad et al., 2012; Nir et al., 2012a; Nir et al., 2012b), which are described in detail in the *Supplementary Information*.

Briefly, we performed whole-brain tractography using the Hough voting method on orientation distribution functions (ODFs) reconstructed using the constant-solid angle method (Aganj et al., 2010) as described in (Aganj et al., 2011) on the sets of linearly registered DWI volumes. Each subject's dataset contained ~10,000 useable fibers (3D curves) in total. Then, 34 cortical labels per hemisphere, from the Desikan-Killiany atlas (Desikan et al., 2006) (**Table S1**), were automatically extracted from all aligned T1-weighted structural MRI scans using FreeSurfer version 5.0 (http://surfer.nmr.mgh.harvard.edu/) (Fischl et al., 2004). The resulting T1-weighted images and cortical models were aligned to the original T1-weighted input image space and down-sampled to the space of the DWIs (we assume that the anatomical scan serves as a relatively undistorted anatomical reference).

Considering the white matter tractography and the cortical parcellations, fiber bundles connecting each pair of ROIs were detected. From this, a 68x68 connectivity matrix was created, 34 right hemisphere ROIs and 34 left hemisphere ROIs (**Table S1**), for each subject. Each element described the estimated proportion of the overall set of detected fibers (streamlines), in that subject, passing through each pair of ROIs. In this paper, we use the word *fiber* to denote a single curve, or streamline, extracted via tractography; if no subjects had detected fibers connecting two regions (i.e., all subjects had a 0 count at a specific matrix element), then that connection was considered invalid, or not consistent enough in the population, and was not included in the analysis.

2.3 Brain network measures

Topological changes in the brain's networks may be analyzed using graph theory, which represents the brain's connections as a set of nodes and edges. The network's nodes are typically defined as ROIs, in our case on the cortex, segmented from anatomical MRI. In DTI studies, these network nodes are linked by 'edges' whose weights denote some measure of connectivity between the two regions, such as the density or integrity of fiber tracts (Sporns, 2011) connecting the regions. In graph theory, an *NxN* connection matrix may be compiled to describe the network. A square matrix can represent any network of connections, and may also be displayed as a graph, i.e., a discrete set of nodes and edges (Sporns, 2011). In our analysis, matrix entries are proportional to the total number of detected fibers connecting each pair of regions (the nodes); these values are considered as the "weights" of the edges that connect a pair of nodes (Sporns, 2011).

The most basic measure to describe the connectedness of the connectivity matrix is the *nodal degree* - the number of edges (unweighted) that connect to a node. Here, the nodal degree was averaged over all cortical areas to output the global degree. The nodal degree is one factor involved in calculating the *k*-core network and rich club coefficient, and is important to consider when interpreting other measures that depend on it. The nodal degree serves as a threshold for defining the mutually and highly interconnected central structural cores in the brain network, using a *k*-core decomposition algorithm. In other words, to compute the "16-core" (*k*=16, for example) of the connectivity matrix, all nodes with a degree 16 or higher would be retained while all connections to other nodes would be set to zero. These would be output in a 68x68 matrix (the same size as the whole brain's connectivity matrix); nodes that do not satisfy this condition are replaced with zeroes. Setting a threshold of 16 requires that at least 23.5% of the nodes in a 68-node matrix to be connected to at least one remaining node (as 100%*(16/68)=23.5%). On the other hand, it is not required that the remaining nodes in a *k*-core must form one single totally connected graph, in which one could travel from any node to any other via a continuous connected path of edges.

Next, we computed the rich club coefficient for each subject's anatomical network at a range of *k*-core thresholds (i.e., *k*=1-22). As noted earlier, the rich club coefficient is the fraction of edges ($E_{>k}$) that connect nodes of degree *k* or higher ($N_{>k}$) over a range of *k*-core values:

$$R(k) = \frac{E_{>k}}{N_{>k}(N_{>k}-1)} \qquad \textbf{(Eq. 1)}$$

The rich club coefficient was normalized relative to its value in 100 randomized networks of equal size and similar connectivity distribution. Random networks are constructed from a disconnected set of nodes (Sporns, 2011) with

similar nodal degree as the *k*-core network being randomized. It is important to normalize the rich club coefficient as the absolute value of the coefficient varies greatly with the size and density of individual graphs, so it provides only limited information on network integration (Sporns, 2011).

Here, we analyzed the whole-brain network as well as the left and right hemisphere networks in all subjects separately. As noted earlier, if $R_n>1$, then there is evidence of rich club organization. To be consistent throughout the study, we only reported *k*-core levels at which the rich club effect was detected in all diagnostic groups across most subjects – *k*=1-22 for the whole brain networks and *k*=1-19 for the left and right hemispheres. For certain subjects, the normalized rich club coefficient was not detectable at all *k*-core levels 1-22 in the whole brain and 1-19 in the left and right hemispheres (**Table S2**), and therefore, was marked as zero, which eventually decreased the average normalized rich club coefficient below 1. A rich club can be undetectable at high levels of *k* due to noisy data or a low number of connections, which is a phenomenon observed in diseased subjects (Daianu et al., 2013). At higher levels of *k* (i.e., *k*>22 for the whole brain, and *k*>19 for the left and right hemispheres), most subjects, especially in the diseased groups, did not have enough nodal connections to form a network of degree *k* or higher. In the single-hemisphere analyses, we did not evaluate fibers that crossed between the hemispheres, as they are present in the whole-brain network; for simplicity, we focused on the sub-networks of nodes and edges that remain entirely within a specific hemisphere[1].

First, we assessed if normalized rich club coefficients relate to age or Mini Mental State Examination (MMSE) scores across all 202 subjects, covarying for sex and using site as a random effects variable. Using a similar set up, we tested for any association of age and MMSE scores with the global degree at *k*-core values *k*=1-22 in the whole brain, and *k*=1-19 for the left and right hemispheres of all subjects (at *k*=1-22 and *k*=1-19 is where a rich club effect was detectable in the whole brain and left/right hemispheres of most subjects). We tested for diagnostic group differences between normalized and unnormalized rich club coefficients at each *k*-core value, between controls and AD subjects, as well as between controls and eMCI and lMCI subjects. Then, we also tested for the same diagnostic group differences for the rich club effect components – *N*, the total number of nodes and *E*, the total number of

---

[1] The rich club effect was also computed on the interhemispheric connections within each diagnostic group and we found that, due to the low number of nodal connections, the highest rich club coefficient in the interhemispheric connections shared among all controls was at *k*=7, *k*=4 in eMCI and AD and *k*=2 in lMCI subjects. Due to the small rich club effect, we did not investigate this further.

8

edges between nodes, computed within each brain network. For the statistical analyses, we used a random effects regression, with controls coded as 0 and eMCI, lMCI or AD coded as 1. We controlled for age and sex and used scanning site as the grouping variable. This tested for connection differences in the whole brain matrix, then separately for the left and right hemisphere matrices. We used the false discovery rate procedure (FDR) to correct for the multiple tests performed at each k-core level. We report the critical FDR p-value, or the highest p-value, which ensures control of the false discoveries at 0.05. The higher the critical p-value (the closer to 0.05), the greater the effect of the test as a whole, and often the more tests can be reported as significant. Once we found that the rich club effect detected network differences among healthy and diseased subjects, we also wanted to determine whether it was sensitive enough to detect network differences between healthy elderly and all MCI subjects (eMCI and lMCI combined), as well as more subtle differences, between eMCI and lMCI, eMCI and AD and finally, lMCI and AD in the whole brain, left and right hemisphere brain networks. To do this we used a similar random regression set up as described above where the least impaired diagnostic group (i.e., controls, eMCI), in each setup, was coded as 0 and the more impaired diagnostic group (i.e., lMCI, AD) was coded as 1.

As the rich club effect has not been previously computed for networks in the diseased brain, we interpreted the connectivity alterations in the cognitively impaired subjects by also computing more basic network measures for the whole brain, left and right hemisphere matrices including global degree, normalized clustering coefficient, characteristic path length and efficiency. To normalize the measures, we compared the observed values to an average calculated from 50 randomized networks of equal size and similar connectivity distribution. For comparable results, we reported these measures on the same range of k-core values as used to compute the rich club coefficient, k=1-22 for the whole brain and k=1-19 for the left and right hemispheres in all diagnostic groups. Depending on the total number of nodal connections in each brain network, some subjects (but not all) had global measures computed at higher k-core levels than reported here (i.e., >22). The *normalized clustering coefficient* is a measure of segregation and describes how densely interconnected a node's neighboring nodes are. The *clustering coefficient* is a nodal measure and was averaged here, over all 68 nodes in the whole brain or 34 nodes in the left and right hemispheres, to output the global normalized clustering coefficient. Furthermore, the path length is a measure of network integration, computed as the total number of edges that need to be traversed to get from one node to the other. It can help to normalize these rather unstable graph theory metrics, such as the clustering coefficient, path length and rich club coefficient, as their absolute value provides limited information on network integration in the

9

brain (Sporns, 2011). Statistically, we performed the same analyses as described above for the rich club effect. We ran a random effects regression to test for differences for each graph theory metric between healthy elderly and the diseased groups, then separately between healthy elderly and all MCI subjects, lMCI and eMCI subjects, eMCI and AD and lMCI and AD.

3. Results

The results are presented in the order they were performed. Below, we discuss how the rich club effect depended on age and cognitive decline among all 202 subjects and then we present the differences between diagnostic groups. Then, we present the network alterations detected by the rich club effect and its components among healthy and AD subjects, as well as controls and the MCI disease groups, accompanied by more subtle alterations detected by the same measures between the disease groups only. And to better understand the rich club findings, we applied basic brain connectivity metrics, global degree, normalized clustering coefficient, normalized characteristic path length and efficiency in similar fashion as the rich club was applied, respectively, at each k-core level where a rich club effect was detected.

3.1 Rich club effect changes with advancing age and cognitive decline

Age and MMSE scores were associated with the rich club coefficients, for both raw and normalized measures. The unnormalized rich club coefficient decreased with age at certain k-core values indicated in **Table 2**, but the normalized rich club coefficient increased with age (**Table 2**). As MMSE scores declined, the unnormalized rich club coefficient also declined, but the normalized rich club coefficient *increased* at particular k-core levels (**Table 2**). As the rich club effect depends on the network degree, we also assessed if there was a general trajectory of the association of age and MMSE scores and global degree at all corresponding k-core values and found that global degree decreased with increasing age in the right hemisphere only in all subjects at k-core thresholding levels listed in **Table 3**. Also, as MMSE scores declined, global degree decreased in the whole brain, left and right hemispheres of all subjects at k-core values (**Table 3**). Next, we analyzed differences in the rich club effect between healthy elderly and the diseased groups, and separately between diseased groups.

3.2 Effect of normalizing the rich club coefficient

The unnormalized rich club coefficient increased over an increasing range of k-core values in the whole brain, left and right hemispheres of all subjects (**Fig. 1**). This was computed at k-core values ranging from 1-22 in the whole brain and 1-19 in the left and right hemispheres of all subjects. The normalized rich club coefficient was

increasingly greater than 1 for a stable range of k-core levels, which indicates that a rich club effect was detectable in most subjects (**Fig. 2**). The number of subjects who did not have a rich club effect at high levels of k is presented in **Table S2** for the diagnostic groups that showed significant differences in their brain network architecture. The normalized rich club coefficients are plotted for all values of the nodal degree threshold, k, including at the first k-core value where a rich club effect was no longer detectable (<1). All significant p-values are listed in **Tables 4** and **5**.

In the whole brain network, the unnormalized rich club coefficients were significantly lower in AD subjects, than in controls, at k=1-15 k-core levels (FDR critical p-value=0.03), but no significant differences were detected in the unnormalized rich club coefficients between controls and eMCI, or lMCI subjects at any k levels (**Fig. 1**). In the left hemisphere, the unnormalized rich club coefficient was significantly lower in AD subjects, than in controls, at k-core levels k=1-10 (FDR critical p-value=0.014) but no significant differences were detected in the unnormalized rich club between controls and eMCI, or lMCI subjects at any k-core levels. Finally, in the right hemisphere, the unnormalized rich club coefficient was significantly higher in AD subjects relative to controls, at k=1-4, 6, 16, 18, 19 (FDR critical p-value=0.021), and again no differences were found between controls and eMCI, or lMCI. At very high values of k, there is a large loss of nodal connections in the network, and therefore, properties can greatly differ from those seen at lower k. There were no differences detected in the unnormalized rich club coefficient between controls and all MCI subjects (eMCI + lMCI combined), eMCI and lMCI, eMCI and AD, and lastly lMCI and AD.

Interestingly, the main terms involved in the rich club coefficient formula, N and E, also showed group differences. The number of nodes, N, declined and was lower in AD subjects, relative to controls, in the whole brain at k=1-22 (FDR critical p-value=0.001), left hemisphere at k=1-19 (FDR critical p-value=0.006) and right hemisphere at k=3-5, 7-19 (FDR critical p-value=0.02). N was also found to decline and lower in left hemisphere of eMCI, relative to controls, at k=1, 3-19 (FDR critical p-value=0.045) but not in their whole brain or right hemisphere (**Fig. 1**). For lMCI subjects, N declined and was lower in the left hemisphere at k=4, 6, 8-10, 15-19, relative to controls (FDR critical p-value=0.02). The number of edges, E, declined and was lower in AD subjects, relative to controls, in the whole brain networks at k=1-22 (FDR critical p-value=4.9x10^{-5}), left hemisphere at k=1-19 (FDR critical p-value=1.2x10^{-4}) as well as right hemisphere (FDR critical p-value=0.006). Furthermore, E was also lower and declining in the left hemisphere of eMCI at k=1-19 (FDR critical p-value=0.042) and lMCI subjects,

11

relative to controls (FDR critical *p*-value=0.026). No significant differences were detected for *E* between eMCI and lMCI, relative to controls in the whole brain and right hemisphere (**Fig. 1**).
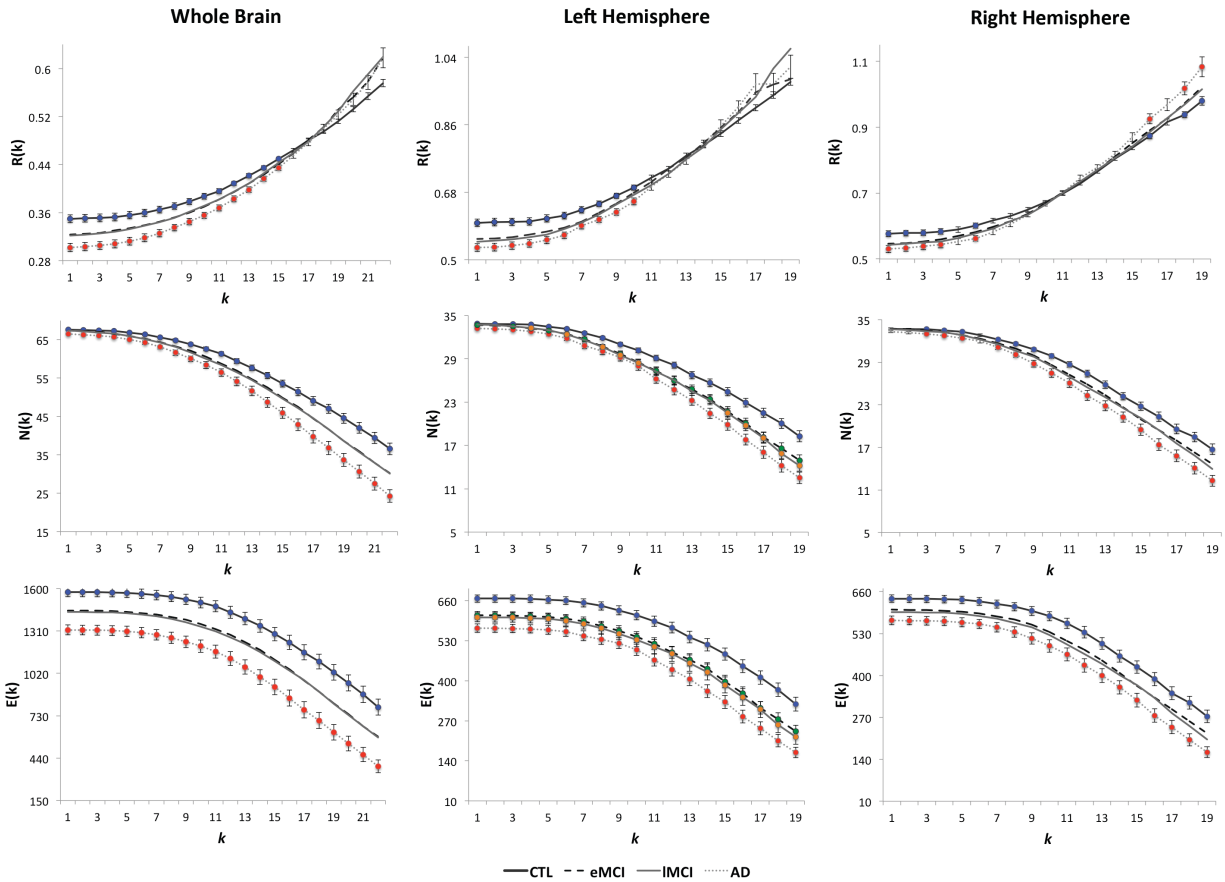
Figure 1. Average unnormalized rich club coefficient (*R(k)*), average number of nodes (*N(k)*) and average number of edges (*E(k)*), in brain networks for groups of healthy controls (CTL), eMCI, lMCI and AD subjects at nodal degree thresholds *k*=1-22 for the whole brain (WB), and for *k*=1-19 in the left and right hemispheres (LH, RH). *R(k)* is significantly lower and declining in AD subjects (*red*), relative to controls (*blue*) in the whole brain, left and right hemispheres at the plotted *k*-core levels (colored dots). The unnormalized rich club coefficient curves cross at mid *k*-core levels because as thresholding levels increase more nodal connections are removed leading to highly sparse networks and modified network properties compared to what is seen at lower *k*-core values. *N(k)* and *E(k)* were lower and declining in AD subjects in the whole brain, left and right hemispheres, relative to controls, as plotted. *N(k)* was also lower and found to decline in left hemisphere of eMCI (*green*), relative to controls, at select *k* levels and in lMCI subjects (*orange*). The number of edges, *E(k)*, declined and was lower in AD subjects, relative to controls, in the whole brain networks, left and right hemispheres. *E(k)* was also lower and declining in the left hemisphere of eMCI and lMCI subjects, relative to controls. The colored dots indicate where significant differences were found. Error bars are the standard error computed at each *k*-core level for all subjects. FDR corrected *p*-values are shown in **Table 5**.

Unlike the rich club coefficient, N and E detected network differences between all MCI subjects and controls (**Fig. 4**). N was lower and declined in the whole brain networks in MCI subjects at $k=4$ (FDR critical p-value=0.002) and in the left hemisphere networks in MCI subjects at $k=1$, 3-10, 12, 15-19 (FDR critical p-value=0.02) and at $k=1$-19 (FDR critical p-value=0.03), but not in the right hemisphere. Similarly, E was lower and declined in the whole brain of MCI at $k=1$-22 (FDR critical p-value=0.047) and left hemisphere at $k=1$-19 (FDR critical p-value=0.047), relative to controls.

In **Figure 2**, we illustrate the normalized rich club coefficients, which were significantly higher in AD subjects, relative to controls, at a range of k-core levels, $k=1$-9, 11, in the whole brain (FDR critical p-value=0.021). The normalized rich club coefficient was also higher in eMCI subjects at $k=3$ and 4 in the whole brain, relative to controls (FDR critical p-value=0.003). No significant differences were found between the rich club in the whole brain networks of controls and the other diagnostic groups. In the left hemisphere, we found the normalized rich club coefficient to be higher in AD subjects, relative to controls, at $k=1$, 3, 4, 7 k-core levels (FDR critical p-value=0.001) and in eMCI subjects at $k=4$ (FDR critical p-value=0.002). No significant differences were found between controls and any of the diseased groups for the normalized rich club coefficient in the right hemisphere. Meanwhile, the normalized rich club coefficient increased and was higher in the whole brain network of all MCI subjects (eMCI and lMCI combined) at $k=3$ and 4, relative to controls (FDR critical p-value=0.003) and left hemisphere at $k=3$ and 4 (FDR critical p-value=0.004). Furthermore, we did not detect differences in the normalized rich club coefficient between eMCI and lMCI groups, eMCI and AD and lMCI and AD.

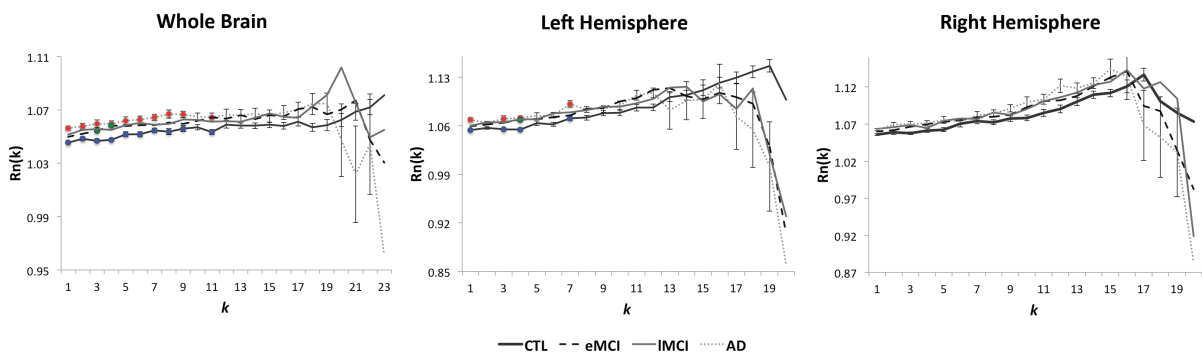**Figure 2.** Average normalized rich club coefficients, $R_n(k)$, for controls (CTL), eMCI, lMCI and AD subjects plotted at nodal degree thresholds $k=1$-23 for the whole brain (*left panel of the figure*), and at $k=1$-20 in left and right hemispheres. At $k=23$ and 20 we did not detect an average rich club effect >1 in the whole brain, left and right hemispheres of all diagnostic groups, so we

13

only analyzed the range of rich club coefficients computed at k=1-22 and k=1-19 (where R_n>1)). This occurs when metrics are unstable at very high nodal degree thresholds, where very few nodes remain the network. $R_n(k)$ increased in AD, relative to controls, in the whole brain for k-cores ranging between k=1-9, 11 (*red*, FDR critical *p*-value=0.021), and in the left hemisphere at k=1, 3, 4, 7 k-core levels (FDR critical *p*-value=0.001). Also, $R_n(k)$ was higher in eMCI, relative to controls, in the whole brain (*green*, FDR critical *p*-value=0.003), and at k=4 in the left hemisphere (*green*, FDR critical *p*-value=0.002). No other significant differences were found for $R_n(k)$. Error bars are the standard error computed at each k-core level for all subjects.

3.3 Other brain metrics: global degree, global normalized rich club coefficient, global normalized clustering coefficient and efficiency applied at a range of thresholding levels, *k*

To interpret the rich club effects in the diagnostic groups, we computed some of the most commonly used, more basic graph theory metrics on the k-cores of each subject. These metrics are the global degree, normalized global clustering coefficient, normalized path length and efficiency and are plotted in **Figures 3** and **S1**. The measures were computed for the same range of k-core levels as for the rich club coefficients, 1-22 for the whole brain of all subjects and 1-19 for the left and right hemispheres of all subjects. Measures computed for each diagnostic group, eMCI, lMCI and AD, were compared to measures in healthy elderly and due to our significant findings between diagnostic groups, we further compared these measures between controls and all MCI subjects (eMCI and lMCI combined), as well as between eMCI and lMCI, eMCI and AD and separately, lMCI and AD. Differences in measures not reported below did not significantly differ among diagnostic groups and are marked not significant in **Tables 4** and **S1**.

Global degree: As the network threshold (k) increased and removed more low degree nodes, the global degree declined in all diagnostic groups in the whole brain for all k-core levels, k=1-22, relative to healthy elderly. In diagnostic group comparisons, the global degree declined and was significantly lower at all k-core levels, k=1-19, in AD subjects, relative to healthy elderly, in the left hemisphere and right hemisphere, however, not in eMCI, or lMCI, relative to healthy elderly. Global degree declined (with increasing k) in all MCI subjects (eMCI and lMCI combined) and was lower than in controls for all k-core levels, k=1-22, in the whole brain. Lastly, the global degree also distinguished the disease groups, indicating a decreasing and lower global degree in the left hemisphere of AD subjects, relative to eMCI subjects at k=1-16.

Global normalized clustering coefficient: The global normalized clustering coefficient was also indicative of disease differences in the network architecture of the whole brain, left and right hemispheres. This measure is expected to be disrupted with disease progression as the nodal connections in the network drop drastically and is expected to be

14

lower in disease when unnormalized and greater when normalized, relative to healthy subjects. Here, we showed that the global normalized clustering coefficient was higher in eMCI at k=1-18 and AD subjects at k=1-20 in the whole brain, relative to controls. Furthermore, the normalized clustering coefficient was significantly higher in the left hemisphere of AD subjects at k=1-16, relative to controls, and in the right hemisphere of AD subjects at k=1-8, 10, 13-14, relative to controls. The normalized clustering coefficient was also higher in all MCI subjects compared to healthy elderly in the whole brain for k-core levels k=1-16.

Global normalized characteristic path length: The normalized characteristic path length is expected to be longer in disease, relative to controls, as the diseased networks of the brain lose complexity. Here, we found that the normalized characteristic path length was significantly higher in the whole brain networks at k=1-20 in eMCI and AD subjects, relative to controls. Even so, it was only significantly higher in AD at k=1-16 in the left and right hemispheres, relative to controls, but not in eMCI or lMCI subjects. The global normalized path length was significantly higher in all MCI subjects, relative to controls, for all k-core levels at k=1-20 in the whole brain.

Efficiency: With disease progression, a decline in the overall network efficiency is expected, as the characteristic path length increases (efficiency is an approximate inverse of the network path length). Efficiency declined (as the network threshold, k, increased) in all diagnostic groups and was significantly lower in the whole brain at k=1-22 in eMCI, lMCI and AD, relative to controls and in the left and right hemispheres of AD subjects at k=1-19, relative to controls, but not in eMCI and lMCI subjects. Efficiency also declined in all MCI and was lower than in controls for all k-core levels, k=1-22, in the whole brain. Finally, we found a declining and lower efficiency in AD subjects, relative to eMCI, for k=1-16 in the left hemisphere.

3.4 Ranking of the 8 brain network measures

We ranked the 8 brain network measures in the order of their effect size (**Table 6**) to indicate which measures were the most sensitive to detecting brain network alteration with disease progression. Efficiency, followed by global degree detected most alterations among diagnostic groups with most significant differences (lowest *p*-value, highest FDR critical *p*-value). These two measures were found significantly different when analyzing the topology of controls and AD, eMCI and lMCI for the whole brain networks; they also detected differences between controls and AD in their left and right hemispheres (**Table 4**) and importantly, they were the only two measures to detect differences between the left hemisphere of eMCI and AD (**Table 5**). The most sensitive thresholding levels, k, where differences in the network were detected were at levels, k=9-10, 13, 14, optimal for the left and right

15

hemisphere and higher levels, k=17-20, optimal for the whole brain networks. This suggests that a certain amount of thresholding is necessary to detect network alterations in the brain using network measures efficiency and global degree, with increasing thresholding levels for larger networks (i.e., k=17-20 for the whole brain), to eliminate noisy connections that may prevent the detection of alterations caused by disease. The next most sensitive measures to detect network alterations in disease are the rich club factors – the total number of edges, E, as well as the total number of nodes, N. E and N detected differences between healthy elderly and all diagnostic groups in the left hemisphere as well as between healthy elderly and all MCI, and AD subjects in their whole brain, and healthy elderly and AD in the right hemisphere. The k-core levels where most significant differences were detected were at either low k levels, k=4, or high k-levels, k=18, 19 and 22 in all brain regions – suggesting that, perhaps, N and E are sensitive enough to overcome the effects of noisy connections present at low levels of thresholding and still be able to pick up network alterations. Normalized characteristic path length and clustering coefficient are the next measures to detected most differences between healthy elderly and AD subjects in their whole brain, left and right hemisphere networks. These two measures also detected differences between the whole brain networks of healthy elderly and eMCI, and all MCI subjects. The thresholding levels where most significant differences were detected are rather scattered, k =1, 2, 4, 5, 7, 8, 16, so these measures might be rather unstable even after being normalized. Finally, the unnormalized and normalized rich club coefficients detected differences in the whole brain networks of healthy and diseased subjects. The unnormalized rich club coefficient was significantly different between the whole brain of controls and all MCI, and AD subjects and between the left hemisphere networks of controls and eMCI, all MCI and AD subjects. The normalized rich club coefficient was significantly different between the whole brain networks of controls and AD subjects and did not distinguish network alterations among other diagnostic groups. The thresholding levels most optimal for the detection of disease effects using the rich club effect were found to be at k=1, 2, 4 and 18, with most differences detected in the left hemisphere, indicating that this part of the brain might be the most affected in AD. Some studies attribute left hemisphere findings in AD to reflect that cognitive testing overall is heavily weighted toward verbal function; 10 AD subjects assessed with near-infrared spectroscopy showed decreased left hemispheric functional activity during a verbal fluency test, relative to 10 healthy subjects (Fallgatter et al., 1997). Finally, no measure detected differences among eMCI and lMCI diagnostic groups, or lMCI and AD.

16

Figure 3. Average global degree, normalized clustering coefficient, normalized characteristic path length and efficiency computed in all diagnostic groups, controls (CTL, *blue*), eMCI (*green*), lMCI (*orange*) and AD subjects (*red*) over *k*-core levels *k*=1-22 in the whole brain networks and *k*=1-19 in the left and right hemisphere networks. The colored dots on the curves indicate that a group difference between CTL and the diseased subjects is detectable at that value of *k*. As expected from the definition of nodal degree thresholds, all network measures declined, with increasing values of the network threshold, *k*, in the whole brain (WB) networks of eMCI (*green*), lMCI (*orange*) and AD subjects (*red*), relative to controls (*blue*) at all *k*-core levels. Global degree and efficiency declined in the left and right hemisphere (LH, RH) networks of AD, relative to controls, while normalized clustering coefficient and normalized path length increased in AD, relative to controls in the left and right

55

hemisphere networks at the plotted k-core levels. Error bars are the standard error computed at each k-core level for all subjects. FDR corrected p-values are shown in **Table 4**.

4. Discussion

Here we analyzed structural brain connectivity in cognitively healthy elderly, eMCI, lMCI and AD subjects from the ADNI study. We assessed the rich club effect in MCI and AD, and to help interpret our results, we analyzed a range of more standard and widely-used brain connectivity meas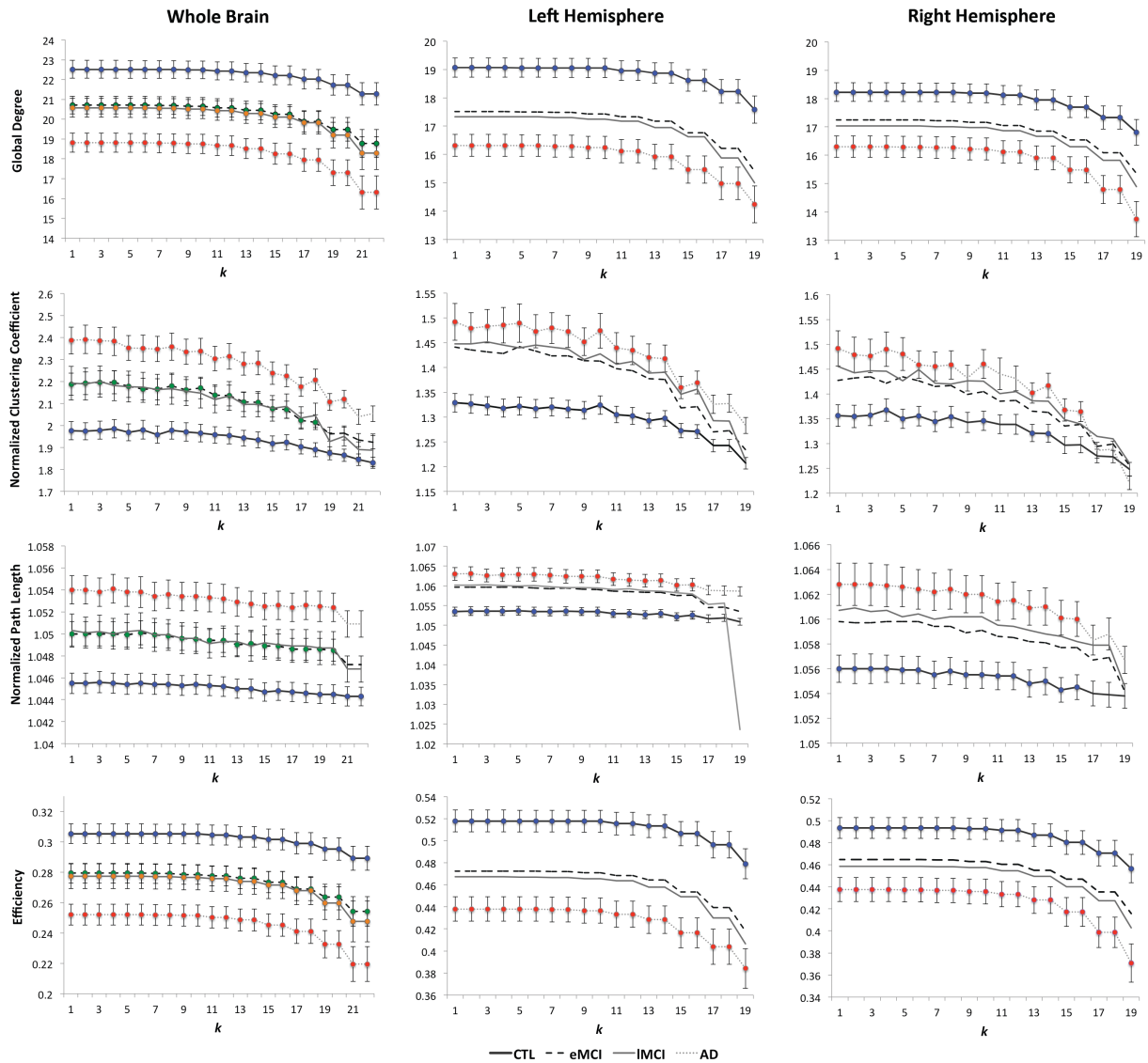ures: the global degree, global normalized clustering coefficient, normalized characteristic path length and efficiency, in the same diagnostic groups. We ranked the brain network metrics based on their effect sizes for distinguishing structural differences between healthy and diseased subjects, but also between the different disease groups separately. Our study had 3 main findings: 1) the rich club coefficient is disrupted in AD; 2) connectivity analyses can reveal network breakdown at different stages of dementia; 3) the rich-club coefficient is not as sensitive as a measure as more standard network measures, but can offer complementary information in understanding network disruptions.

4.1 The rich club effect is disrupted in the AD

We have two key results about the rich club in AD. First, the unnormalized rich club coefficient decreased with age and with declining MMSE scores, but the normalized rich club coefficient increased with age and with declining MMSE scores (**Table 2**). Intuitively, the rich club is an emerging property in the network that is presumably functionally beneficial, and does not arise at random as its value is computed by accounting for randomized networks with similar nodal distribution. Second, there was a lower unnormalized rich club coefficient in the diseased groups (**Fig. 1**), relative to healthy or less impaired subjects, but the normalized coefficient higher in the impaired groups, relative to the coefficients in healthy or less impaired subjects (**Fig. 2**).

The rich club coefficient describes the density of connections for subnetworks, or k-cores, created by thresholding the network at a range of nodal degrees, k, starting with $k=1$ until no more nodes of degree k or higher remain. High values of k only leave the primary core of the network, keeping the highly connected nodes and removing low degree nodes, including inaccurate nodes obtained from tractography errors. In this study, the rich club coefficient increased over all k-core levels regardless of disease status. Defined as the ratio of the total number of edges, E, to the total number of nodes, $N(N-1)$, this property of the rich club effect is explained by its rapidly decreasing denominator, $N(N-1)$. Although the brain networks lose approximately more edges than nodes throughout

the k-core thresholding process, the denominator, $N(N\text{-}1)$, decreases approximately at double the rate the nodal degree, N, does, leading to a greater loss in the denominator than numerator – hence an increase in the rich club coefficient.

Intuition might suggest that the rich club effect might be disrupted or reduced in AD, if we assume that rich club organization is functionally beneficial although there are no prior findings to show the rich club phenomenon in disease. However, at high thresholds, very few network nodes remain, especially in disease, so paradoxically, some rich club measures are higher in disease. When we studied simpler measures of numbers of nodes and edges, we confirmed that the changes in the rich club were still consistent with what is expected in degenerative brain disease – there was a rapid loss in nodal connections in the networks. For example, in the right hemisphere networks (**Table 3**), there were fewer nodes but the remaining network tended to be, on average, more interconnected, as disease progressed. This is possible if there is a preferential loss of low-degree nodes.

For low k-levels, k=1-15, in the whole brain and k=1-10 in the left hemisphere (**Fig. 1**), the unnormalized rich club coefficient was significantly lower in AD subjects than in controls. Interestingly, for higher k values (k>15, k>10), the rich club coefficient was not found to be significantly different between controls and AD subjects in the whole brain and left hemisphere networks. This could be explained by the catastrophic alterations that may occur with higher thresholding levels of the network, leading to a large loss of nodes and edges, and therefore, fewer distinguishable features between the two diagnostic groups. In the right hemisphere, the unnormalized rich club coefficient in AD was lower at k=1-4 and 6 and higher at k=16, 18, 19, relative to controls. The structural topology of the right hemisphere in AD has been shown to retain more connections than the left hemisphere (Daianu et al., 2013), and therefore, this could explain why we were able to pick up structural differences at higher levels of k in the right hemisphere but not in the left. For the eMCI and lMCI groups, their unnormalized rich club coefficient was not detectably different from that in the healthy elderly group.

When normalized, the rich club coefficient describes a more coherent integration in the network by adjusting the coefficient using randomized networks of same size and similar nodal distribution. As the unnormalized rich club coefficient (but with a smaller effect size), the normalized rich club detected differences between AD and healthy elderly at low levels of k, however was found to be higher (not lower) at k=1-9, 11 in the whole brain of AD and k=1, 3, 4, 7 in the left hemisphere of AD (**Fig. 2**) only. Unlike the unnormalized rich club coefficient, the normalized rich club was also found to be higher at k=3, 4 in the whole brain of eMCI and at k=4 in their left

19

hemisphere, relative to controls. It is not intuitive to find a higher rich club in disease, and it would not have been predicted in advance. One plausible explanation is that the node counts and edge counts, N and E, fall off more rapidly with increasing k in AD subjects (**Fig. 1**), than controls. This leads to a smaller denominator in the calculation of the rich club coefficient, and a more pronounced rich club phenomenon in AD, even for the same k, as a smaller fraction of nodes are left (**Fig. 3**). In general, for both AD and controls, the rich club coefficient is higher when a smaller percentage of nodes is retained. Applying the same numerical threshold to the nodal degree will retain a smaller fraction of nodes from AD networks, making their rich club coefficient appear higher as less of the network is left. Even so, at low k, the higher unnormalized rich club coefficient in controls fits with the hypothesis that some aspects of normal network organization are lost or impaired in disease.

4.2 Interpreting of the rich club effect using brain network measures computed at the same range of thresholding levels, *k*

To better understand our rich club coefficient findings, we assessed the most standard and well-studied topological metrics describing brain networks – the global degree, global normalized clustering coefficient, normalized path length and global efficiency. To our knowledge, these measures were not previously applied on a range of thresholding levels, k (i.e., k=1-22 for the whole brain), as studied here, other than by colleagues in our group (Daianu et al., 2014).

The global degree and efficiency declined with stricter thresholding levels at all k values in the whole brain in all diagnostic groups, and in the left hemisphere and right hemisphere of AD subjects, relative to controls. All these measures were significantly lower in the diseased groups than in controls. This is in line with recent studies that showed decreased local efficiency in structural networks of 32 AD subjects, relative to 50 healthy elderly, however, no significant patterns were found for global efficiency (Reijmer et al., 2013). Also, the same study showed decreased unnormalized clustering coefficient and no significant changes in the unnormalized shortest path length and (Reijmer et al., 2013). Here we showed that the characteristic path length and the clustering coefficient tend to be rather unstable, so we normalized them. These specific measures were higher in the disease groups at all k-core levels in the whole brain, and were greater in the left and right hemispheres of AD subjects, relative to controls, at only select k-core levels. This can help to understand why there is a higher rich club phenomenon in AD subjects, relative to controls, based on the mathematical definition of the rich club coefficient. A higher normalized characteristic path length means that a higher number of edges must be traversed to get from one node to another.

Presumably, a shorter path length is preferred, along with a high clustering coefficient, to form the small-world networks that characterize the topology of the brain (Sporns, 2011). However, a greater normalized path length, especially as fibers are lost in disease, may suggest that more paths are needed for the transfer of information between two cortical regions of the brain. Also, one might expect to obtain longer (higher) characteristic path lengths in disease (Daianu et al., 2014), relative to controls, as the organization of the diseased network tends to become less optimal, which may suggest a loss of complexity (Stam et al., 2007). Furthermore, the greater normalized clustering coefficient in the diseased groups, relative to healthy elderly, is another example of the disproportionate influence the decrease in global degree has on the network. As a function of degree, the clustering coefficient, normally describing a densely interconnected network (Daianu et al., 2013; Sporns, 2011), is left with fewer nodal connections, and therefore, fewer neighboring nodes to form clusters among – possibly increasing the average level of interconnectedness for the remaining nodes.

Some prior studies show that the left hemisphere in AD may have greater disruptions in connectivity than the right hemisphere, and, in some AD cohorts, there may even be more left than right hemisphere cortical atrophy (Thompson et al., 2003). We were able to pick up AD vs. control differences in the left hemisphere – but not in their right hemisphere - for the normalized and unnormalized rich club coefficients and for the normalized clustering coefficient and path length (**Figs. 1, 2** and **3**). Meanwhile, changes in connectivity in eMCI and lMCI diagnostic groups, relative to controls, might be too subtle to be detected by the rich club coefficient (**Figs. 1** and **2**), but they were detected by the global degree, global normalized clustering coefficient, normalized path length and efficiency in the whole brain, but not in their left and right hemispheres considered on their own (**Fig. 3**). Furthermore, the overall disrupted brain connectivity metrics with disease progression observed in this study are linked to prior structural studies that showed similar findings. Jahanshad et al. (2012) showed that, relative to HIV- controls, HIV+ subjects had weaker connection strengths (lower fiber density) for many cortical regions where strength was defined as the sum of edge weights for edges connected to a node. For HIV+ subjects who were also ApoE4 carriers (a genetic risk factor for AD), the authors also found impaired nodal efficiency in multiple cortices. Other studies have also shown impaired network communication efficiency, quantified by local interconnectivity and global interaction of the brain networks of ApoE4 carriers. One study reported an accelerated age-related loss of connectivity in the brain overall and specifically in several cortices (Brown et al., 2011).

4.3 Most sensitive brain network measures to detect white matter alterations in MCI and AD

Efficiency and global degree detected most white matter alterations among diagnostic groups with greatest effect sizes (lowest p-values). In this study, these were the two measures that detected network differences between controls and all disease groups as well as between eMCI and AD subjects – differences not detectable by other network measures. Next, rich club factors – the total number of edges, E, as well as the total number of nodes, N, were the most sensitive measures to detect network differences between controls and all diagnostic groups. As efficiency and global degree, these two measures are functions of the network's most basic components – nodes and edges – which, in this study, picked up network alterations most sensitively. Slightly more complex measures (in the order specified), clustering coefficient, path length and rich club coefficient, are measures that are stabilized by normalization with random networks of the same size and degree distribution. Even so, they detected the least network alterations between diagnostic groups, and were ranked as the least sensitive measures. Overall, as the network measures detected topological differences between groups at a variety of threhsolding k-core levels, therefore, the most optimal thresholding of the brain network might to use a range of k-core levels (i.e., k=1-22) as opposed to at a specific thresholding level, k.

The rich club phenomenon takes into account the fiber density for the white matter connections (van den Heuvel and Sporns, 2011) and has not previously been assessed in people with AD. Here we show that the unnormalized rich club coefficient decreased with age and declining MMSE, but the normalized rich club coefficient changed in the opposite direction. The unnormalized rich club coefficient was lowest in the most affected disease groups and the normalized rich club coefficient was highest in the most affected disease groups. Based on its mathematical definition, the rich club coefficient increases with increasing k and decreasing nodal degree (when a smaller percentage of nodes are retained). AD reduces the fraction of connections in the brain network and this can induce a higher rich club coefficient leading to a loss in network complexity. This phenomenon complements and is supported by the decline in global degree and efficiency, and increase in global normalized clustering coefficient and normalized characteristic in disease. Basic network measures, efficiency, global degree and the rich club factors – total number of edges (E) and nodes (N), were the most sensitive measures to detecting white matter topological alteration between diagnostic groups, while the normalized clustering coefficient, path length and rich club coefficient were the least sensitive.

22

Disclosure statement

ADNI is partially funded by public and private agencies. One of the authors, Michael Weiner, has private funding unrelated to the content of this paper.

References:

1. Alzheimer's Association Colorado. 2011 Fact Sheet Alzheimer's Disease. http://www.alz.org/co/in_my_community_11039.asp. Accessed, Dec. 7, 2013.

2. Aganj, I., Lenglet, C., Sapiro, G., Yacoub, E., Ugurbil, K., Harel, N., 2010. Reconstruction of the Orientation Distribution Function in Single and Multiple Shell Q-Ball Imaging within Constant Solid Angle. Magn Reson Med. 64(2), 554-466.

3. Alvarez-Hamelin, J.I., Dall'Asta, L., Barrat, A., Vespignani, A., 2006. Large scale networks fingerprinting and visualization using k-core decomposition. Weiss Y, Scholkopf B, Platt J. editors. Cambridge (Massachusetts); MIT Press 44-55.

4. Basser, P.J., Jones, D.K., 2002. Diffusion-tensor MRI: theory, experimental design and data analysis - a technical review NMR Biomed. 15(7-8):456-67.

23

5. Braak, H., Braak, E., 1996. Development of Alzheimer-related neurofibrillary changes in the neocortex inversely recapitulates cortical myelogenesis. Acta Neuropathol. 67, 677-685.

6. Braskie, M.N., Jahanshad, N., Stein, J.L., Barysheva, M., McMahon, K.L., de Zubicaray, G.I., Martin, N.G., Wright, K.L., Ringman, J.M., Toga, A.W., Thompson, P.M., 2012. Common Alzheimer's Disease risk variant within the CLU gene affect white matter microstructure in young adults. J Neurosci. 31(18):6764-6770.

7. Brown, J.A., Terashima, K.H., Burggren, A.C., Ercoli, L.M., Miller, K.J., Small, G.W., Bookheimer, S.Y., 2011. Brain network local interconnectivity loss in aging APOE-4 allele carriers. PNAS. 108(51), 20760-20765.

8. Bruner, E. and Jacobs, H.I., 2013. Alzheimer's disease: the downside of a highly evolved parietal lobe?. J Alzheimers Dis. 35(2):227-40.

9. Clerx, L., Visser, P.J., F. Verhey, F., Aalten, P., 2012. New MRI markers for Alzheimer's disease: a meta-analysis of diffusion tensor imaging and a comparison with medial temporal lobe measurements. J Alzheimer's Dis. 29(2), 405-29.

10. Coleman, M., 2005. Axon degeneration mechanisms: commonality amid diversity. Nat Rev Neurosci. 6(11):889-98.

11. Daianu, M., Jahanshad, N., Nir, T.M., Dennis, E., Toga, A.W., Jack, C.R., Jr., Weiner, M.W., Thompson, P.M., and the Alzheimer's Disease Neuroimaging Initiative, 2012. Analyzing the structural k-core of brain connectivity networks in normal aging and Alzheimer's disease. In NIBAD' 12 MICCAI Workshop on Novel Imaging Biomarkers for Alzheimer's Disease and Related Disorders, Nice, France, 52–62.

12. Daianu, M., Jahanshad, N., Nir, T.M., Toga, A.W., Jack, C.R., Jr., Weiner, M.W., Thompson, P.M. and the Alzheimer's Disease Neuroimaging Initiative. Breakdown of Brain Connectivity between Normal Aging and Alzheimer's Disease: A Structural *k*-core Network Analysis. *Brain Connectivity 2013*;3(4):407-22.

13. Daianu, M., Dennis, E.L., Jahanshad, N., Nir, T.M., Toga, A.W., Jack, C.R., Jr., Weiner, M.W., Thompson P.M., 2014. Disrupted Brain Connectivity in Alzheimer's Disease: Effects of Network Thresholding. T. Schultz et al. (eds.), Computational Diffusion MRI and Brain Connectivity, Mathematics and Visualization, 199-207.

14. Desikan RS.. Segonne F, Fischl B, Quinn BT, Dickerson BC, Blacker D, Buckner RL, Dale AM, Maguire RP, Hyman BT, Albert MS, Killiany RJ. 2006. An automated labeling system for subdividing the human cerebral cortex on MRI scans into gyral based regions of interest. Neuroimage 31(3):968-80.

15. Ewers, M., Insel, P., Jagust, W.J., Shaw, L., Trojanowski, J.Q., Aisen, P., Petersen, R.C., Schuff, N., Weiner, M.W., Alzheimer's Disease Neuroimaging Initiative (ADNI). CSF biomarker and PIB-PET-derived beta-amyloid signature predicts metabolic, gray matter, and cognitive changes in nondemented subjects. Cereb Cortex. 22(9):1993-2004.

16. Fallgatter, A.J., Roesler, M., Sitzmann, L., Heidrich, A., Mueller, T.J., Strik, W.K., 1997. Loss of functional hemispheric asymmetry in Alzheimer's dementia assessed with near-infrared spectroscopy. Brain Res Cogn Brain Res. 6(1):67-72.

17. Filippi, M., Agosta, F., Barkhof, F., Dubois, B., Fox, N.C., Frisoni, G.B., Jack, C.R., Johannsen, P., Miller, B.L., Nestor, P.J., Scheltens, P., Sorbi, S., Teipel, S., Thompson, P.M., Wahlund, L.O., 2012. EFNS (European Federation of Neurological Societies) Task Force: The use of neuroimaging in the diagnosis and management of dementia, European Journal of Neurology. 19 (12), 1487-1501.

18. Fischl B, Destrieux C, Halgren E, Segonne F, Salat DH, Busa E, Seidman LJ, Goldstein J, Kennedy D, Caviness V, Makris N, Rosen B. 2004. Automatically parcellating the human cerebral cortex. Cerebral Cortex 14:11-22.

19. Ingalhalikar, M., Smith, A., Parker, D., Satterthwaite, T.D., Elliott, M.A., Ruparel, K., Hakonarson, H., Gur, R.E., Gur, R.C., Verma, R., 2013. Sex differences in the structural connectome of the human brain. PNAS. Published online before print December 2, 2013, doi: 10.1073/pnas.1316909110 PNAS December 2, 2013.

20. Jack, C.R., Bernstein, M.A., Borowski, B.J., Gunter, J.L., Fox, N.C., Thompson, P.M., Schuff, N., Krueger, G., Killiany, R.J., DeCarli, C.S., Dale, A.M., Carmichael, O.W., Tosun, D., Weiner, M.W., 2010. Update on the Magnetic Resonance Imaging core of the Alzheimer's Disease Neuroimaging Initiative. Alzheimers Dement. 6(3):212-20.

21. Jahanshad, N., Zhan, L., Bernstein, M.A., Borowski, B., Jack, C.R., Toga, A.W., Thompson, P.M., 2010. Diffusion Tensor Imaging in Seven Minutes: Determining Trade-Offs Between Spatial and Directional Resolution. IEEE ISBI 1161-1164.

22. Jahanshad, N., Aganj, I., Lenglet, C., Josh, A., Jin, Y., Barysheva, M., McMahon, K.L., de Zubicaray, G.I., Martin, N.G., Wright, M.J., Toga, A.W., Sapiro, G., Thompson, P.M., 2011. Sex differences in the human connectome: 4-Tesla high angular resolution diffusion imaging (HARDI) tractography in 234 young adult twins. IEEE Xplore 939-943.

23. Jahanshad, N., Valcour, V.G., Nir, T.M., Kohannim, O., Busovaca, E., Nicolas, K., Thompson, P.M., 2012. Disrupted Brain Networks in the Aging HIV+ Population Brain Connectivity. 2(6), 335-344.

24. Mori, S., van Zijl, P.C., 2002. Fiber tracking: principles and strategies - a technical review. NMR Biomed. 15(7-8):468-80.

25. Nir, T.M., Jahanshad, N., Villalon-Reina, J.E., Toga, A.W., Jack, C.R., Weiner, M.W., Thompson, P.M., 2013. Effectiveness of regional DTI measures in distinguishing Alzheimer's disease, MCI, and normal aging. NeuroImage:Clinical. 3,180–195.

26. Nir, T.M., Jahanshad, N., Jack, C.R., Weiner, M.W., Toga, A.W., Thompson P.M., and the Alzheimer's Disease Neuroimaging Initiative 2012a. Small world network measures predict white matter degeneration in patients with early-stage mild cognitive impairment. International Symposium on IEEE 10th Biomedical Imaging (ISBI). 1405-1408.

27. Nir, T.M., Jahanshad, N., Toga, A.W., Bernstein, M.A., Jack, C.R., Weiner, M.W., Thompson, P.M., 2012b. ADNI Connectivity network breakdown predicts imminent volumetric atrophy in early mild cognitive impairment MBIA Lect. Notes Comput. Sci., 7509: 41–50.

28. Prasad, G., Nir, T.M., Toga, A.W., Thompson, P.M., 2013a. Tractography density and network measures in Alzheimer's Disease. International Symposium on IEEE 10th Biomedical Imaging (ISBI). 692 - 695.

25

29. Prasad, G., Burkart, J., Joshi, S.H., Nir, T.M., Toga, A.W., Thompson, P.M., 2013b. A Dynamical Clustering Model of Brain Connectivity Inspired by the N-Body Problem. Multimodal Brain Image Analysis, Lecture Notes in Computer Science. 8159, 129-137.

30. Reijmer, Y.D., Leemans, A., Caeyenberghs, K., Heringa, S.M., Koek, H.L., Biessels, G.J., 2013. Disruption of cerebral networks and cognitive impairment in Alzheimer disease. Neurology. 80(15), 1370-7.

31. Rowley, J., Fonov, V., Wu, O., Eskildsen, S.F., Schoemaker, D., Wu, L., Mohades, S., Shin, M., Sziklas, V., Cheewakriengkrai, L., Shmuel, A., Dagher, A., Gauthier, S., Rosa-Neto, P., Alzheimer's Disease Neuroimaging Initiative, 2013. White Matter Abnormalities and Structural Hippocampal Disconnections in Amnestic Mild Cognitive Impairment and Alzheimer's Disease. PLoS ONE. 8(9): e74776. doi:10.1371/journal.pone.0074776.

32. Sporns, O., 2011. Networks of the Brain. Cambridge, MA, 2011, pp. 5-31.

33. Stam, C.J., Jones, B.F., Nolte, G., Breakspear, M., Scheltens, Ph., 2007. Small-World Networks and Functional Connectivity in Alzheimer's Disease. Cereb. Cortex. 17(1), 92-99.

34. Thompson PM, Hayashi KM, de Zubicaray G, Janke AL, Rose SE, Semple J, Herman D, Hong MS, Dittmer SS, Doddrell DM, Toga AW. 2003. Dynamics of Gray Matter Loss in Alzheimer's Disease, J Neuroscience 23(3):994-1005.

35. van den Heuvel, M.P. and Sporns, O., 2011. Rich-club organization of the human connectome. J Neurosci. 31(44), 15775-15786.

36. Zhan, L., Jahanshad, N., Jin, Y., Lenglet, C., Mueller, B.A., Sapiro, G., Ugurbil, K., Harel, N., Toga, A.W., Lim, K.O., Thompson, P.M., 2013a. Magnetic resonance field strength effects on diffusion measures and brain connectivity networks. Brain Connect. 3(1):72-86.

37. Zhan, L., Bernstein, M.A., Borowski, B., Jack Jr., C.R., Thompson, P.M., 2013b. Evaluation of Diffusion Imaging Protocols for the Alzheimer's Disease Neuroimaging Initiative. International Symposium on IEEE 11th Biomedical Imaging (ISBI). *In press*.

38. Zhan, L., Jahanshad, N., Jin, Y., Nir, T.M., Leonardo, C., Bernstein, M., Borowski, B., Jack Jr C.R., Thompson, P.M., 2013c. Understanding Scanner Upgrade Effects on Brain Integrity and Connectivity Measures. International Symposium on IEEE 11th Biomedical Imaging (ISBI). *In press*.

39. Wang, J., Zuo, X., Dai, Z., Xia, M., Zhao, Z., Zhao, X., Jia, J., Han, Y., He, Y., 2012. Disrupted functional brain connectome in individuals at risk for Alzheimer's disease. Biological psychiatry *73*(5):472–81.

Tables

	Controls	eMCI	lMCI	AD	Total
N	50	72	38	42	202
Age	72.6 ± 6.1 SD	72.4 ± 7.9 SD	72.6 ± 5.6 SD	75.5 ± 8.9 SD	73.1 ± 7.4 SD
MMSE	28.9 ± 1.4 SD	28.1 ± 1.5 SD	26.9 ± 2.1 SD	23.3 ± 1.9 SD	27.1 ± 2.7 SD
Sex	22M/28F	45M/27F	25M/13F	28M/14F	120M/82F
Site	10	16	12	12	16

Table 1. Demographic information from 50 controls, 72 eMCI, 38 lMCI and 42 AD subjects scanned with diffusion MRI as part of the ADNI project. Their ages ranged from 55.2 to 90.4 years. The mean age and Mini Mental State Exam (MMSE) scores are listed for each diagnostic group. Subjects were scanned at 16 sites.

R, WB	**R, LH**	**R, RH**	**R_n, WB**	**R_n, LH**	**R_n, RH**
Age Associations					
p-value=0.026 age $\Uparrow$, R(k)$\Downarrow$, for $\underline{k}$=1-11 age $\Uparrow$, R(k) $\Uparrow$, for k=19-22 min p-value=4.9e-05	p-value=0.009 age $\Uparrow$, R(k)$\Downarrow$, for $\underline{k}$=1-8 age $\Uparrow$, R(k) $\Uparrow$, for k=17 min p-value=3.1e-04	p-value=0.021 age $\Uparrow$, R(k)$\Downarrow$, for $\underline{k}$=1-5 age $\Uparrow$, R(k) $\Uparrow$, for k=15-19 min p-value=5.1E-04	p-value=0.031 age $\Uparrow$, Rn(k) $\Uparrow$, for $\underline{k}$=1-12 min p-value=1.3E-06	p-value=0.023 age $\Uparrow$, Rn(k) $\Uparrow$, for $\underline{k}$=1-5, 7, 9-12 min p-value= 1.2E-04	p-value=0.036 age $\Uparrow$, Rn(k) $\Uparrow$, for $\underline{k}$=1-10, 12, 14-16 min p-value= 2.5E-04
MMSE Score Associations					
p-value=0.019 MMSE $\Uparrow$, R(k) $\Uparrow$, for $\underline{k}$=1-13 min p-value=0.000137	p-value=0.013 MMSE $\Uparrow$, R(k) $\Uparrow$, for $\underline{k}$=1-10 min p-value=0.00014	p-value=0.025 MMSE $\Uparrow$, R(k) $\Uparrow$, for $\underline{k}$=1-8, 12, 13, 16-19 min p-value=0.00021	p-value=0.018 MMSE $\Uparrow$, Rn(k) $\Downarrow$, for $\underline{k}$=1-5, 7, 8 min p-value=8.96e-05	p-value=0.0073 MMSE $\Uparrow$, Rn(k) $\Downarrow$, for $\underline{k}$=1-5, 7 min p-value=7.91e-06	p-value=0.0097 MMSE $\Uparrow$, Rn(k) $\Downarrow$, for $\underline{k}$=3, 2, 5, 9 min p-value=0.0014

Table 2. Differences in the unnormalized, *R,* and normalized, *R_n,* coefficients with age and Mini Mental State Examination scores (MMSE) using a random effects regression in the whole brain (WB), left and right hemispheres (LH, RH) in all 202 subjects (controls, eMCI, lMCI and AD). We covaried for sex and used site as a random effects regression coefficient. *R*

decreased with age for the listed k-core levels and $R_n(k)$ increased with age for the listed k-core levels. Also, R decreased with lower MMSE scores and R_n increased with declining MMSE scores. All p-values were FDR corrected.

Global Degree, WB	**Global Degree, LH**	**Global Degree, RH**
Age Association		
NS	NS	p-value=0.001 age ⇑, GD(k)⇓, for $\underline{k}$=1-19 min p-value=3.2e-06
MMSE Score Association		
p-value=6.6E-06 MMSE ⇑, GD(k) ⇑, for $\underline{k}$=1-22 min p-value=5.3e-06	p-value=8.7E-04 MMSE ⇑, GD(k) ⇑, for $\underline{k}$=1-19 min p-value=3.6e-05	p-value=0.01 MMSE ⇑, GD(k) ⇑, for $\underline{k}$=1-19 min p-value=2.5e-04

Table 3. Differences in the global degree (GD) as a function of k-core with age and Mini Mental State Examination scores (MMSE) using a random effects regression in the whole brain (WB), left and right hemispheres (LH, RH) in all 202 subjects (controls, eMCI, lMCI and AD). We covaried for sex and used site as a random effects regression coefficient. Global degree decreased with age and increased with MMSE scores for k-core levels listed above. All p-values were FDR corrected.

	p-values, WB			**p-values, LH**			**p-values, RH**		
Brain Connectivity Measures	eMCI vs. CTL	lMCI vs. CTL	AD vs. CTL	eMCI vs. CTL	lMCI vs. CTL	AD vs. CTL	eMCI vs. CTL	lMCI vs. CTL	AD vs. CTL
R	NS	NS	0.03 k=1-15 min p-val =6.6E-05 same, k=1	NS	NS	0.014 k=1-10 min p-val =2.1E-04, k=2	NS	NS	0.021 k=1-4, 6, 16, 18, 19 min p-val =1.0E-03, k=18

28

N	NS	NS	0.001 $k=1$-22 min p-val $=1.2$E-05, $k=22$	0.045 $k=1$, 3-19 min p-val $=0.0031$, $k=4$	0.018 $k=4$, 6, 8-10, 15-19 min p-val $=0.0016$, $k=18$	0.006 $k=1$-19 min p-val $=1.6$e-05, $k=18$	NS	NS	0.027 $k=3$-5, 7-19 min p-val$=$ 0.00027, $k=18$
E	NS	NS	4.9E-05 $k=1$-22 min p-val $=4.3$E-06, $k=4$	0.042 $k=1$-19 min p-val $=0.0081$, $k=4$	0.026 $k=1$-19 min p-val $=0.0028$, $k=18$	1.2E-04 $k=1$-19 min p-val $=6.7$ e-06, $k=4$	NS	NS	0.006 $k=1$-19 min p-val$=$ 0.00029, $k=19$
R_n	0.0034 $k=3$, 4 min p-val$=3.3$E-04., $k=4$	NS	0.021 $k=1$-9, 11 min p-val $=2.2$E-06, $k=1$	0.002 $k=4$ min p-val $=0.0021$, $k=4$	NS	1.2E-03 $k=1$, 3, 4, 7 min p-val $=3.2$E-05, $k=4$	NS	NS	NS
Global Degree	0.028 $k=1$-22 min p-val$=$ 0.018, $k=17$, 18	0.033 $k=1$-22 min p-val$=$ 0.020, $k=19$, 20	5.6E-05 $k=1$-22 min p-val$=$ 4.3e-06, $k=9$, 10	NS	NS	6.1E-04 $k=1$-19 min p-val$=6.7$E-06, $k=9$, 10	NS	NS	4.5E-03 $k=1$-19 min p-val$=0.001$, $k=9$, 10
Normalized Clustering Coefficient (γ)	0.038 $k=1$-18 min p-val$=$	NS	1.4E-04 $k=1$-20 min p-	NS	NS	0.012 $k=1$-16 min p-	NS	NS	0.027 $k=1$-8, 10, 13-14

29

67

	0.0039. *k*=2		val= 6.1e-06, *k*=5			val=2.0E-04, *k*=8			min *p*-val=0.0054, *k*=1, 16
Normalized Characteristic Path Length (λ)	0.018 *k*=1-20 min *p*-val= 0.008, *k*=2	NS	6.3E-05 *k*=1-20 min *p*-val= 1.45e-05, *k*=5	NS	NS	8.5E-04 *k*=1-16 min *p*-val=4.9E-05, *k*=1	NS	NS	0.017 *k*=1-16 min *p*-val=0.003, *k*=7
Efficiency	0.028 *k*=1-22 min *p*-val= 0.019, *k*=17, 18	0.033 *k*=1-22 min *p*-val= 0.020, *k*=19, 20	4.8E-05 *k*=1-22 min *p*-val= 4.8e-06, *k*=9, 10	NS	NS	5.0E-04 *k*=1-19 min *p*-val=7.7E-06, *k*=9, 10	NS	NS	0.0049 *k*=1-19 min *p*-val=0.0017 *k*=9, 10

Table 4. FDR corrected *p*-values are shown from fitting a random effects regression model to the network measure, rich club coefficient (*R*), normalized rich club coefficient (*R*ₙ), total number of nodes (*N*), and edges (*E*), global degree, global normalized clustering coefficient, normalized characteristic path length and efficiency, computed on *k*-core levels *k*=1-22 in the whole brain and *k*=1-19 in the left and right hemispheres to test for diagnostic group differences between controls (CTL) and eMCI, lMCI and AD subjects (with controls coded at 0 and AD subjects coded at 1). We covaried for sex and age and used site as a random regression variable. *k*-core levels where significant differences were found are included or are marked as not significant (NS); also, *k*-core levels where minimum *p*-values were detected are listed. Please see **Figure 3** for the plotted results.

Brain Connectivity Measures	***p*-values, WB**	***p*-values, LH**	***p*-values, RH**
	CTL vs. MCI		
N	0.0019 *k*=4	0.037 *k*=1, 3-10, 12, 15-19 min *p*-val= 0.0021, *k*=4	NS
	0.047, *k*=1-22	0.047	NS

E		k=1-19	
	min p-val=0.019, k=4	min p-val= 0.0068, k=4	
R_n	0.0032 k=3, 4 min p-val=0.0011, k=4	0.0041 k=3, 4 min p-val=0.0024, k=4	NS
Global Degree	0.035, k=1-22 min p-val=0.019, k=9,10	NS	NS
Normalized Clustering Coefficient (γ)	0.023, k=1-16 min p-val=0.0065, k=2	NS	NS
Normalized Characteristic Path Length (λ)	0.028, k=1-20 min p-val=0.012, k=4	NS	NS
Efficiency	0.034, k=1-22 min p-val=0.020, k=9,10	NS	NS
	eMCI vs. AD		
Global Degree	NS	0.039, k=1-16 min p-val=0.033, k=13, 14	NS
Efficiency	NS	0.034, k=1-16 min p-val=0.029, k=13, 14	NS

Table 5. FDR corrected p-values are shown from fitting a random effects regression model independently to every network measures, normalized rich club coefficient (R_n), total number of nodes (N), total number of edges (E), global degree, normalized clustering coefficient, normalized path length and efficiency. We covaried for age and sex and used site as a random effects regression. Here, we only show measures that detected significant structural differences between the diagnostic groups. For plotted results details, please see **Figure 1S**. *NS=not significant.*

#	Brain network measure in order of effect size	FDR critical p-value	Diagnostic groups between which difference was detected	Brain region where network differences were detected	Thresholding levels, k, with most significant between diagnostic group differences (lowest p-values)
1	**Efficiency**	4.8E-05 0.033	CTL vs. AD CTL vs. lMCI	Whole brain	k=9, 10 k=17-20

		0.028	CTL vs. eMCI		
		0.034	CTL vs. MCI (eMCI + lMCI)		
		5.0E-04	CTL vs. AD	Left hemisphere	k=9, 10
		0.034	eMCI vs. AD		k=13, 14
		0.0049	CTL vs. AD	Right Hemisphere	k=9, 10
2	**Global degree**	5.6E-05	CTL vs. AD	Whole Brain	k=9, 10
		0.033	CTL vs. lMCI		k=17-20
		0.028	CTL vs. eMCI		
		0.035	CTL vs. MCI		
		6.1E-04	CTL vs. AD	Left hemisphere	k=9, 10
		0.039	eMCI vs. AD		k=13, 14
		4.5E-03	CTL vs. AD	Right Hemisphere	k=9, 10
3	*E*	4.9E-05	CTL vs. AD	Whole brain	k=4
		0.047	CTL vs. MCI		
		1.2E-04	CTL vs. AD	Left hemisphere	k=4, 18
		0.026	CTL vs. lMCI		
		0.042	CTL vs. eMCI		
		0.037	CTL vs. MCI		
		0.006	CTL vs. AD	Right hemisphere	k=19
4	*N*	0.0012	CTL vs. AD	Whole brain	k=22
		0.0019	CTL vs. MCI		
		0.00648	CTL vs. AD	Left hemisphere	k=4, 18
		0.0181	CTL vs. lMCI		
		0.045	CTL vs. eMCI		
		0.037	CTL vs. MCI		
		0.0279	CTL vs. AD	Right hemisphere	k=18
5	**Normalized Characteristic Path Length (λ)**	6.3E-05	CTL vs. AD	Whole Brain	k= 2, 4, 5
		0.018	CTL vs. eMCI		
		0.028	CTL vs. MCI		

		8.5E-04	CTL vs. AD	Left hemisphere	k=1
		0.017	CTL vs. AD	Right hemisphere	k=7
6	**Normalized Clustering Coefficient (γ)**	1.4E-04	CTL vs. AD	Whole brain	k=2, 5
		0.038	CTL vs. eMCI		
		0.23	CTL vs. MCI		
		0.012	CTL vs. AD	Left hemisphere	k=8
		0.027	CTL vs. AD	Right hemisphere	k=1, 16
7	**R_n**	0.021	CTL vs. AD	Whole brain	k=1
		0.0032	CTL vs. MCI		
		1.2E-03	CTL vs. AD	Left hemisphere	k=4
		0.0021	CTL vs. eMCI		
		0.0041	CTL vs. MCI		
8	**R**	0.03	CTL vs. AD	Whole brain	k=1
		0.014	CTL vs. AD	Left hemisphere	k=2
		0.021	CTL vs. AD	Right hemisphere	k=18

Table 6. All brain network metrics listed in the order of their size effect (lowest FDR critical p-value) based on results listed in **Tables 4** and **5.** The measures were also ranked based on how many diagnostic groups they were able to detect significant alterations among. Thresholding levels, k, where minimum p-values were detected are also listed.

Supplementary Information

Methods

Image Analysis

Diffusion-weighted imaging may be combined with an automatically labeled set of brain regions from anatomical MRI to map connectivity and perform network analysis of the brain's fiber connections. Many analyses of brain connectivity have been conducted in this way (Jahanshad et al., 2012, Jahanshad et al., 2011a, Zhan et al., 2012a; Ingalhalikar et al., 2013). Connectivity matrices were compiled using a processing pipeline described before (Jahanshad et al., 2011a, Braskie et al., 2012; Jahanshad et al., 2012; Nir et al., 2012a; Nir et al., 2012b), which is summarized briefly below.

33

Pre-processing and co-registration

Non-brain regions were automatically removed from each T1-weighted MRI scan, and from a T2-weighted image from the DWI set using the FSL tool "BET" (http://fsl.fmrib.ox.ac.uk/fsl/). Anatomical scans underwent intensity inhomogeneity normalization using the MNI "nu_correct" tool (www.bic.mni.mcgill.ca/software/). All T1-weighted images were linearly aligned using FSL (with 6 DOF) to a common space with 1mm isotropic voxels and a 220×220×220 voxel matrix. The DWIs were corrected for eddy current distortions using the FSL tools (http://fsl.fmrib.ox.ac.uk/fsl/). For each subject, the 5 images with no diffusion sensitization were averaged, linearly aligned and resampled to a downsampled version of their T1-weighted image (110×110×110, 2×2×2mm). b_0 maps were elastically registered (Leow et al., 2005) to the T1-weighted scan to compensate for susceptibility artifacts (EPI distortions). Images were visually inspected and there were no misalignments or cases where the field of view did not cover the full brain (i.e., cropping).

Tractography and cortical extraction

The transformation matrix from linearly aligning the mean b_0 image to the T1-weighted volume was applied to each of the 41 gradient directions to re-orient the orientation distribution functions (ODFs). We also performed whole-brain tractography as described in (Aganj et al., 2011) on the sets of DWI volumes. Only linear registration was performed before tractography, as nonlinear registration before tractography could introduce processing artifacts. Gradient directions for each DWI volume were adjusted using the transformation matrix obtained from the linear registration. The tractography method uses a fiber detection approach based on the Hough transform (Aganj et al., 2011).

1	Banks of the superior temporal sulcus	19	*Pars orbitalis*
2	Caudal anterior cingulate	20	*Pars triangularis*
3	Caudal middle frontal	21	Peri-calcarine
4	-N/A-	22	Postcentral
5	Cuneus	23	Posterior cingulate
6	Entorhinal	24	Precentral
7	Fusiform	25	Precuneus
8	Inferior parietal	26	Rostral anterior cingulate
9	Inferior temporal	27	Rostral middle frontal
10	Isthmus of the cingulate	28	Superior frontal
11	Lateral occipital	29	Superior parietal
12	Lateral orbitofrontal	30	Superior temporal
13	Lingual	31	Supra-marginal
14	Medial orbitofrontal	32	Frontal pole
15	Middle temporal	33	Temporal pole
16	Parahippocampal	34	Transverse temporal
17	Paracentral	35	Insula
18	*Pars opercularis*		

Table S1. Index of cortical labels extracted from FreeSurfer. Cortical areas are derived from the Desikan-Killiany brain atlas (Desikan et al., 2006).

To detect crossing fibers, the method uses a constant solid angle orientation density function (CSA-ODF; Aganj et al., 2010) rather than a diffusion tensor, to model the local diffusion propagator. The angular resolution of the ADNI data is deliberately limited to avoid long scan times that may tend to increase patient attrition. Even so, this ODF model makes best use of the limited angular resolution (even if the protocol is not ideal for resolving fiber crossing).

Elastic deformations obtained from the EPI distortion correction, mapping the average b_0 image to the T1-weighted image, were then applied to each recovered fiber's 3D coordinates to more accurately align the anatomy (we assume that the anatomical scan serves as a relatively undistorted anatomical reference). Each subject's dataset contained ~10,000 useable fibers (3D curves) in total.

34 cortical labels per hemisphere, listed in the Desikan-Killiany atlas (Desikan et al., 2006), were automatically extracted from all aligned T1-weighted structural MRI scans using FreeSurfer version 5.0 (http://surfer.nmr.mgh.harvard.edu/) (Fischl et al., 2004). The resulting T1-weighted images and cortical models were aligned to the original T1-weighted input image space and down-sampled using nearest neighbor interpolation (to avoid intermixing of labels) to the space of the DWIs. To ensure tracts would intersect labeled cortical regions, labels were dilated with an isotropic box kernel of width 5 voxels (Jahanshad et al., 2011).

NxN Matrices Representing Structural Connectivity

For each subject, a 68x68 connectivity matrix was created, 34 right hemisphere ROIs and 34 left hemisphere ROIs (tabulated in Daianu et al., 2013). Each element described the estimated proportion of the overall set of detected fibers (streamlines), in that subject, passing through each pair of ROIs. In this paper, we use the word fiber to denote a single curve, or streamline, extracted via tractography; if no subjects had detected fibers connecting two regions (i.e., all subjects had a 0 count at a specific matrix element), then that connection was considered invalid, or not consistent enough in the population, and was not included in the analysis.

Brain network measures

Topological changes in the brain's networks may be analyzed using graph theory, which represents the brain's connections as a set of nodes and edges. The network's nodes are typically defined as ROIs, in our case on the cortex, segmented from anatomical MRI. In DTI studies, these network nodes are linked by 'edges' whose weights

35

denote some measure of connectivity between the two regions, such as the density or integrity of fiber tracts (Sporns, 2011) connecting the regions. In graph theory, an *NxN* connection matrix may be compiled to describe the network. A square matrix can represent any network of connections, and may also be displayed as a graph, i.e., a discrete set of nodes and edges (Sporns, 2011). In our analysis, matrix entries are proportional to the total number of detected fibers connecting each pair of regions (the nodes); these values are considered as the "weights" of the edges

BCT measures	Whole Brain	Left Hemisphere	Right Hemisphere
R	All CTL, eMCI and AD subjects	All CTL All but 1 AD (k=19)	All CTL and all AD
R_n	All CTL and eMCI All but 2 AD subjects at k=20-22) All but 3 eMCI (k=19-22)	All CTL All but 6 AD (k=13-19) *only one subject was missing Rn for 13-19; 5 were missing it k=17-19	All but 2 CTL (k=17-19) All but 5 AD (k=16-19)
N	All CTL and AD	All CTL, eMCI, lMCI and AD	All CTL and AD
E	All CTL and AD	All CTL, eMCI, lMCI and AD	All CTL and AD
Global Degree	All CTL, eMCI, lMCI, AD	All CTL All but 1 lMCI (k=19) All AD	All but 1 AD (k=17-19)
Normalized Clustering Coefficient (γ)	All CTL All but 2 eMCI (k=21-22) All but 1 lMCI (k=21-22) All but 1 AD (k=21-22)	All CTL All but 1 AD (k=17-19)	All CTL All but 1 AD (k=17-19)
Normalized Characteristic Path Length (λ)	All CTL All but 2 eMCI (k=21-22) All but 1 lMCI (k=21-22) All but 1 AD (k=21-22)	All CTL All but 1 AD (k=17-19)	All but 1 AD (k=17-19)
Efficiency	All CTL, eMCI, lMCI, AD	All CTL and all AD	All CTL and eMCI All but 1 AD (k=17-19)

36

Table S2. Number of subjects who did not have detectable brain network measures at high levels of thresholding, *k*, due to the rapidly decreasing number of nodal connections.
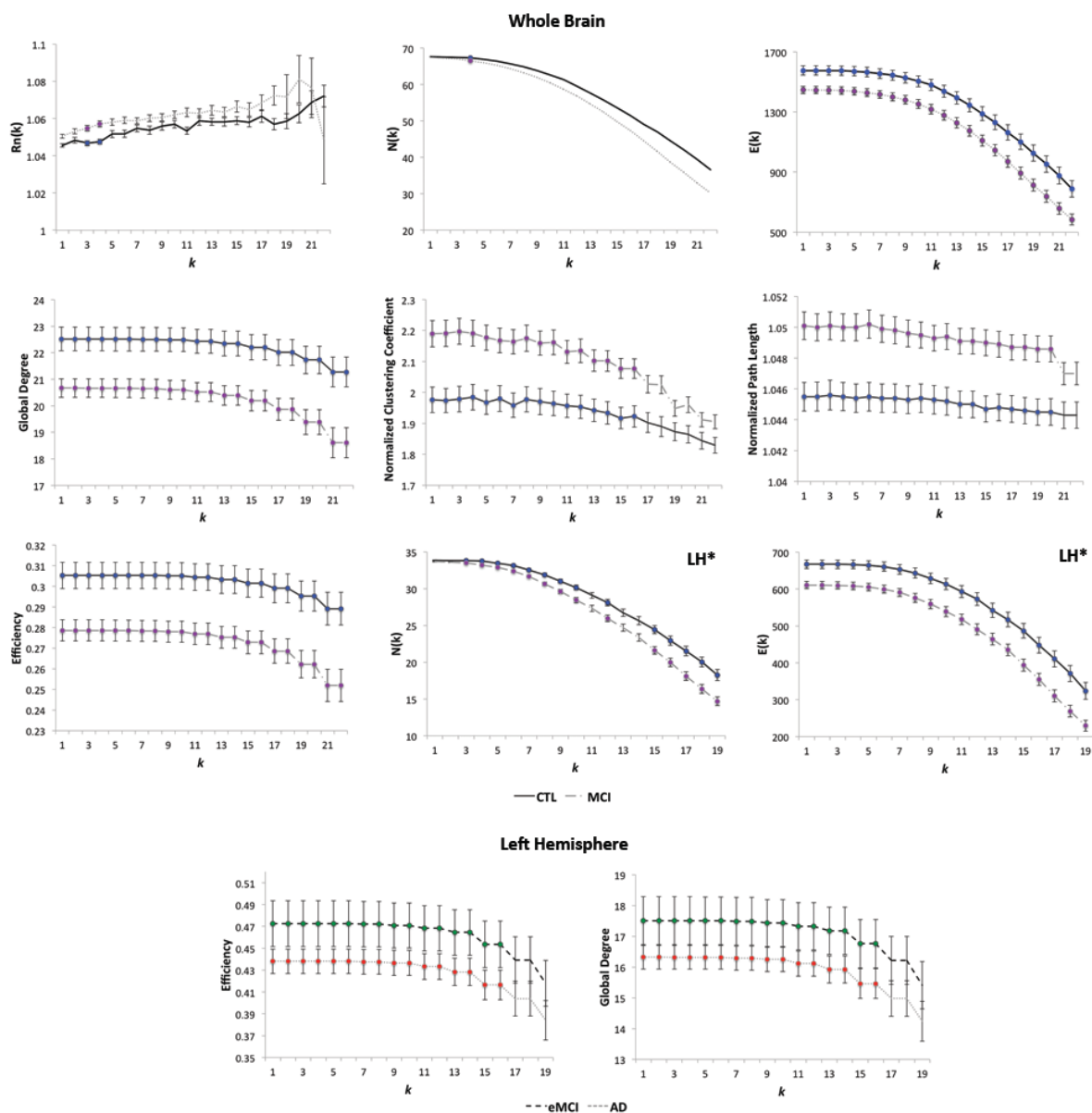
Figure S1. Average normalized rich club coefficient ($R_n(k)$), total number of nodes ($N(k)$), total number of edges ($E(k)$), global degree, normalized clustering coefficient, normalized characteristic path length and efficiency computed in controls (CTL, *blue*), eMCI (*green*), AD subjects (*red*) and all MCI subjects (*purple*, eMCI+lMCI combined) over *k*-core levels *k*=1-22 in the whole brain networks and *k*=1-19 in the left and right hemisphere networks. The colored dots on the curves indicate that a group difference between the diagnostic groups was detectable at that value of *k*. $R_n(k)$ was higher in the whole brain of MCI than of controls while $N(k)$ and $E(k)$ were lower in the whole brain and left hemispheres of MCI than in controls. Global degree and efficiency declined as a function of *k* in MCI subjects, relative to controls in the whole brain only, while the normalized

37

clustering coefficient and path length were higher in MCI subjects in the whole brain, relative to controls. The bottom panels show a declining efficiency and global degree in AD subjects than in eMCI at k-core levels. Error bars are the standard error computed at each k-core level for all subjects. FDR corrected p-values are shown in **Table 5**.

that connect a pair of nodes (Sporns, 2011).

The nodal degree is one factor involved in calculating the k-core network and rich club coefficient, and is important to consider when interpreting other measures that depend on it. The nodal degree serves as a threshold for defining the mutually and highly interconnected central structural cores in the brain network, using a k-core decomposition algorithm. For a graph $G = (N, E)$ with $|N| = n$ nodes and $|E| = e$ edges, a k-core is computed by assigning a subgraph, $H = (B, E|B)$ where set $B \subseteq N$ is a k-core of order k iff $\forall v \in B$: $\text{degree}_H \geq k$, and H is the maximum subgraph satisfying this property (Alvarez-Hamelin et al., 2006).

Supplementary reference:

1. Leow, A., Huang, S.C., Geng, A., Becker, J., Davis, S., Toga, A., Thompson, P., 2005. Inverse consistent mapping in 3D deformable image registration: its construction and statistical properties. Inf Process Med Imaging. 19: 493-503.

CHAPTER 4

Brain network cost and algebraic connectivity

4.1 Inefficient network cost in dementia

This section is adapted from:

Daianu M, et al. Cost inefficient structural brain networks in frontotemporal dementia and Alzheimer's disease. Brain. *To be submitted,* March 2014.

Cost inefficient structural brain networks in behavioral variant frontotemporal dementia and early-onset Alzheimer's disease

Madelaine Daianu [a,b], Neda Jahanshad [b], Julio E. Villalon-Reina[b], Cassandra D. Leonardo [b], Mario F. Mendez[c],

George Bartzokis[a], Elvira Jimenez[c], Paul M. Thompson [a,b,d,f]*

[a] Department of Neurology, UCLA School of Medicine, Los Angeles, CA, USA

[b] Imaging Genetics Center, Institute for Neuroimaging & Informatics, University of Southern California, Los Angeles, CA, USA

[c] Alzheimer's Disease Research Center, Department of Neurology, UCLA School of Medicine, Los Angeles, CA, USA

[d] Departments of Neurology, Psychiatry, Radiology, Engineering, Pediatrics, and Ophthalmology, USC

[f] Department of Psychiatry, Semel Institute, UCLA, Los Angeles, CA, USA

Submitted to **Brain**: March 2014

Please address correspondence to:

Paul Thompson, Professor of Neurology, Psychiatry, Engineering, Radiology, Pediatrics, and Ophthalmology

Imaging Genetics Center, and Institute for Neuroimaging and Informatics

Keck School of Medicine of USC, University of Southern California

2001 N. Soto Street, SSB1-102, Los Angeles, CA 90032

Tel: (323) 442-7246

Email: pthomp@usc.edu

Abstract

Diffusion imaging and brain connectivity analyses can assess white matter deterioration in the brain, revealing underlying patterns in how brain structure declines. Fiber tractography methods can infer neural pathways and connectivity patterns, yielding sensitive mathematical metrics of network integrity. Cortical atrophy patterns differ between Alzheimer's Disease and behavioral variant frontotemporal dementia, but differences in network connectivity have not yet been studied. Here, we analyzed 1.5-Tesla whole-brain diffusion-weighted images from 64 participants –15 patients with behavioral variant frontotemporal dementia, 19 with early-onset Alzheimer's disease, and 30 healthy elderly controls. Using whole-brain tractography, we reconstructed structural brain connectivity networks to map connections between cortical regions. We evaluated the brain's networks focusing on the most highly central and connected regions, also known as *hubs*, in each diagnostic group – specifically the "high-cost" structural backbone used in global and regional communication. We assessed the contribution of the cortico-cortico pathways to the high-cost network hubs using network topology measures. In all diagnostic groups, the brain's hubs alone accounted for over 50% of the "communication capacity" of the network. Compared to healthy elderly, early-onset Alzheimer's disease patients showed alterations in pathways linking hub regions on the cortex, indicating early abnormalities in the highly connected core connections of the brain. Relative to healthy controls, behavioral variant frontotemporal dementia patients showed alterations in numerous connections, with the majority of them located in the hub communities but also in more remote cortical regions (*i.e.*, non-hub regions). Behavioral variant frontotemporal dementia patients were overall more structurally impaired, especially in frontal cortex. Central hubs in the brain network transfer information between neural pathways in the hub, and other regions. Disruption of this major network core of the brain may impair neural communication and functional integrity in characteristic ways typical of each subtype of dementia.

2

1. Introduction

Brain connectivity studies are becoming increasingly popular for investigating the integrity of the normal and diseased brain. Connectivity analyses combine concepts from neuroscience and engineering to characterize the brain in terms of its structural and functional connections. The brain can be thought of as a network at multiple scales. It can be described at elementary level, in terms of its synaptic connections, and at a more macroscopic level, in terms of its connections between cortical areas and deep nuclei, including bundles of white matter tracts (Mori et al., 1999; Petrella, 2011). The rapidly emerging field of "connectomics" (Toga et al., 2013; Engel et al., 2013) employs data from structural imaging, such as diffusion weighted imaging (DWI), or functional imaging, such as resting state functional MRI (rs-fMRI), as well as methods of analysis such as graph theory – a branch of mathematics that models the topological organization of the brain's networks. These forms of analysis have recently been applied to neurological diseases, for instance to test the long-standing hypothesis that each focal neurodegenerative syndrome targets specific large-scale networks (Seeley, 2010).

DWI is used in structural brain connectivity studies to assess the global and local breakdown of network integration in degenerative disease. Over 50 years ago, Norman Geschwind argued that some forms of neuropsychological deficits arose as a "disconnection syndrome"; and later theories further expanded the model to consider consequences of white matter hyperconnectivity and cortical "hyperfunction" (Catani et al., 2005). These later theories suggest that degeneration of neural pathways interconnecting cortical areas could lead to higher brain activity or diminish the activity of the function of the affected cortical areas (Catani et al., 2005). Advanced imaging techniques such as diffusion imaging (Basser et al., 1994) combined with tractography (Mori et al., 1999) may also reveal the basis of structural dysfunction in patients with various forms of neurological disease.

Behavioral variant frontotemporal dementia (bvFTD) and early-onset Alzheimer's disease (EOAD) are the two highly common forms of early onset dementia in patients less than 65 years of age (Rosenmann and Meiner, 2013; Zhou et al., 2010), and are often characterized by dysfunctional connectivity (Zhou et al., 2010). Here we studied 15 bvFTD participants and 19 early-onset amnestic AD (EOAD) participants, and compared them to 30 healthy age-matched participants using advanced structural connectivity measures to define some of the differentiating factors between the diagnostic groups. bvFTD is a neurodegenerative disease that affects mainly areas in the anterior cingulate cortex and frontoinsular regions, and this leads to dramatic changes in socio-emotional processing (Seeley, 2010); even so, the occipital and parietal lobes are often spared in the disease progression (de Hann et al., 2009).

3

Amnestic AD is a neurodegenerative disease with dysfunctions predominantly in the hippocampal-cingulo-temporal parietal network (Greicius et al., 2003; Zhou et al., 2010). AD has specific atrophic patterns that differentiate it from frontotemporal dementia; for example, AD patients tend not to show frontal, sensorimotor and primary visual cortex atrophy until later in the disease progression (Thompson et al., 2003; Zhou et al., 2010). At autopsy, bvFTD participants tend to show greater atrophy in the anterior insula, anterior cingulate cortex and ventral striatum compared to AD (Rabinovici et al., 2007; Thompson and Vinters, 2012).

Here we analyzed bvFTD and EOAD neural networks in terms of their structural network efficiency. To do this, we defined densely and mutually interconnected networks in the brain – also known as *hubs* – consisting of "nodes", represented by segmented regions of interest (ROIs), and edges, interconnecting these ROIs. Often, edges, or connections that link a pair of ROIs can be assigned a 'weight', for instance, the density of fibers extracted from tractography or the shortest fiber path between the ROIs. These two weights can be multiplied together to define a measure of the *communication cost,* which provides information about a network's spatial layout in the brain. Previous studied showed that densely connected pathways of connections in the brain's network are expected to highly contribute to a network cost and communication capacity of cortico-cortico connections (van den Heuvel et al., 2012). Here, we hypothesized that (1) relative to healthy controls, degenerative disease would impair the communication cost networks in bvFTD and EOAD participants, and (2) there would be different patterns of disruption among network components, with greater frontal lobe disruption in bvFTD.

2. Methods

2.1 Participants and diffusion-weighted imaging of the brain

We analyzed diffusion-weighted images (DWI) from 30 healthy controls and 34 dementia patients – 15 patients with bvFTD and 19 with EOAD (**Table 1**). All 64 participants underwent whole-brain MRI scanning on a 1.5-Tesla Siemens Avanto scanner, at the MRI Center at the University of California, Los Angeles. Standard anatomical T1-weighted sequences were collected (256x256 matrix; voxel size=1x1x1 mm^3; TI=900, TR=2000 ms; TE=2.89 ms; flip angle=40 degrees), along with diffusion-weighted images (DWI) using a single-shot multi-section spin-echo echo-planar pulse sequence with the following parameters: 144x144 matrix; voxel size: 2x2x3 mm^3; TR=9800 ms; TE=97 ms; flip angle=90; scan time=5 min 38 s. 31 separate images were acquired for each DWI sequence: 1 T2-weighted image with no diffusion sensitization (b_0 image) and 30 diffusion-weighted images (b=1000 s/mm^2).

	CTL	bvFTD	EOAD	Total
Age	59.5 ± 9.6 SD	61.3 ± 10.8 SD	57.9 ± 4.3 SD	59.5 ± 8.7 SD
Sex	13M/17F	7M/8F	7M/12F	27M/37F
MMSE	29.2 ± 0.8	24.1 ± 4.8	23.5 ± 4.5	26.3 ± 4.3

Table 1. Demographic information from the 30 healthy controls, 15 bvFTD and 19 EOAD patients with brain imaging. The mean age, sex and Mini Mental State Exam (MMSE) scores are listed for each diagnostic group.

2.2 Image Analysis

Tractography from diffusion-weighted images was combined with an automatically labeled set of brain regions from the high-resolution T1-weighted MRI to map the brain's fiber connections and create the cortical connectivity networks. Several studies of brain connectivity have been conducted in this way (Jahanshad et al., 2012, Jahanshad et al., 2011a, Zhan et al., 2012a; Ingalhalikar et al., 2013). Connectivity matrices were compiled using a processing pipeline described previously (Jahanshad et al., 2011a, Braskie et al., 2012; Jahanshad et al., 2012; Nir et al., 2012a; Nir et al., 2012b), which are described in detail in the *Supplementary Information.*

Briefly, we performed whole-brain tractography using the Hough voting method on orientation distribution functions (ODFs) reconstructed using the constant-solid angle method (Aganj et al., 2010) as described in (Aganj et al., 2011) on the sets of linearly registered DWI volumes. Each subject's dataset contained ~10,000 useable fibers (3D curves) in total. Then, 34 cortical labels per hemisphere, from the Desikan-Killiany atlas (Desikan et al., 2006) (**Table S1**), were automatically extracted from all aligned T1-weighted structural MRI scans using FreeSurfer version 5.0 (http://surfer.nmr.mgh.harvard.edu/) (Fischl et al., 2004). The resulting T1-weighted images and cortical models were aligned to the original T1-weighted input image space and down-sampled to the space of the DWIs (we assume that the anatomical scan serves as a relatively undistorted anatomical reference).

Considering the white matter tractography and the cortical parcellations, fiber bundles connecting each pair of ROIs were detected. From this, a 68x68 connectivity matrix was created for each subject with 34 ROIs in each hemisphere (**Table 1S**). In this paper, we use the word *fiber* to denote a single curve, or "streamline", extracted via tractography; if no participants had detected fibers connecting two regions (*i.e.*, all participants had a 0 count at a specific matrix element), then that connection was considered invalid, or not consistent enough in the population, and was not included in the analysis.

2.3 Brain network measures computed on the NxN connectivity matrices

Topological changes in the brain's networks may be analyzed using graph theory, which represents the brain's connections as a set of nodes and edges. The network's nodes are typically defined as ROIs, in our case on the cortex, segmented from anatomical MRI. These network nodes are linked by 'edges' whose weights denote some measure of connectivity between the two regions. In DTI studies, the edges can be represented by the density or integrity of fiber tracts connecting the regions (Sporns, 2011). Often, the edges connecting a pair of ROIs are denoted by binary measures, *i.e.,* 1 if an edge exists or 0 if an edge does not exist between two ROIs. In graph theory, an *NxN* connection matrix may be compiled to describe the network (either weighted or binarized). A square matrix can represent any network of connections, and may also be displayed as a graph, *i.e.*, a discrete set of nodes and edges (Sporns, 2011).

The most basic measure to describe the connectedness of the connectivity matrix is the nodal degree – the number of edges (binary) that connect to a node. The nodal degree is one main factor involved in calculating the *k*-core network – to define the hubs of the network, and was used here to model the basic architecture of the neural networks. For this, we used a *k*-core decomposition algorithm that reveals hierarchical structure by defining 'central cores' of the network (Alvarez-Hamelin et al., 2006). The *k*-core decomposition outputs a network core that consists of highly and mutually interconnected nodes (Hagmann et al., 2008). This is done by identifying subsets of graphs (*k*-cores) by recursively removing nodes with degrees lower than *k*, such that *k* serves as a degree threshold for nodes (Alvarez-Hamelin et al., 2006). For a graph $G = (N, E)$ with $|N| = n$ nodes and $|E| = e$ edges, a *k*-core is computed by assigning a subgraph, $H = (B, E|B)$ where set $B \subseteq N$ is a *k*-core of order *k* iff $\forall v \in B$: degree$_H \geq k$, and *H* is the maximum subgraph satisfying this property (Alvarez-Hamelin et al., 2006; Hagmann et al., 2008; Daianu et al., 2013). The *k*-core was computed on binarized connectivity matrices, so regardless of the weighting schemes, all *k*-core matrices used in this study, within each diagnostic group, were equivalent. A thresholding level of *k*=12 requires one node to be connected to at least 18% of the other nodes in the 68x68 connectivity matrix (as 100%*(12/68)=17.6%). This level of thresholding was used to remove unreliable tracts that may arise from tractography; removed connections are further described under *Results*.

To define the most interconnected hubs, we computed the maximum *k*-cores to preserve the highest degree nodes that are most densely interconnected among themselves. To do this, we iteratively increased the level of *k* in each diagnostic group until all connections among nodes were removed. Then, we selected the *k* level prior to the one

6

where all connections were purged. Network nodes that were not included in the hubs are referred to as non-hub networks (or remote networks) through the remainder of the paper. To confirm the presence of a high degree hub in the brain of each subject, we computed 68x68 randomized networks of the same size and nodal degree distribution as the original subject's network. Next, the subset of nodes of degree k or higher were computed for the randomized networks at the corresponding k-core values within the diagnostic groups where the hubs were found (k=26 for controls and EOAD, k=22 for bvFTD). A global value, R, describing the fraction of edges that connect nodes of nodal degree k, $R(k) = \frac{E_{>k}}{N_{>k}(N_{>k}-1)}$, was computed for each hub for both the non-randomized and randomized networks in each subject. Finally, the ratio between the non-random and random global values, R, was computed to indicated that at a ratio greater than 1, the hub-like organization in the brain network did not occur by chance. This concept is similar to the "rich-club" coefficient that compares the density of connections among nodes in a non-random network to density found in random network at a range of thresholding values, k (Sporns, 2011; van den Heuvel, 2012). Instead, here we confirmed the existence of rich-club networks at one maximum thresholding value, k, (not a whole range) pertaining to each diagnostic group.

To understand organizational differences in the networks of the diseased groups versus the healthy elderly – specifically, why the existing hubs were created at varying thresholding levels, k, we separately computed brain network metrics, nodal degree and nodal efficiency within each diagnostic group on the minimally thresholded connectivity matrices (at k=12). Nodal efficiency is a form of global efficiency (the approximate inverse of path length), and is computed on the neighborhood of a node and therefore, relates to clustering coefficient (Sporns, 2011).

2.4 Connectivity matrices representing communication cost within the brain network

For each subject's connectivity matrix we assessed the communication cost among a pair of ROIs in the form of a 68x68 matrix, where each element of the matrix reflected the multiplication between the total number of fibers (*i.e.*, fiber density) connecting two ROIs and the minimum physical fiber length among those fibers (**Figure 1**). To do this, we traced all the fibers that connected all pairs of nodes (ROIs) in the network and saved the total counts of fibers connecting the regions under an element-wise 68x68 fiber density connectivity matrix. From the fiber counts interconnecting a pair of ROIs, we selected the fiber with the minimum physical length and saved it under a separate element-wise 68x68 connectivity matrix; this connectivity matrix described the length of the shortest fiber, extracted directly from tractography that allows communication between two ROIs via the shortest fiber path. Therefore, a

7

total of three connectivity matrices were computed for each subject containing information related to the connections between each pair of ROIs to estimate the 1) fiber density, 2) minimum physical fiber length, and 3) local communication cost – which is intended to describe an aspect of communication related to the network's spatial embedding (van den Heuvel et al., 2009). By estimating the cost as the product of the fiber density and its minimum length, some have argued that that the cost is proportional to axonal volumes (van den Heuvel et al., 2009):

$$C_{ij} = \sum_{i,j \in N} L_{ij}\rho_{ij}$$

where C_{ij} is the total minimum communication cost between nodes i and j, L_{ij} is the shortest physical fiber bundle length between nodes i and j, and ρ_{ij} is the density of the edges used for information transfer between nodes i and j (van den Heuvel et al., 2012).
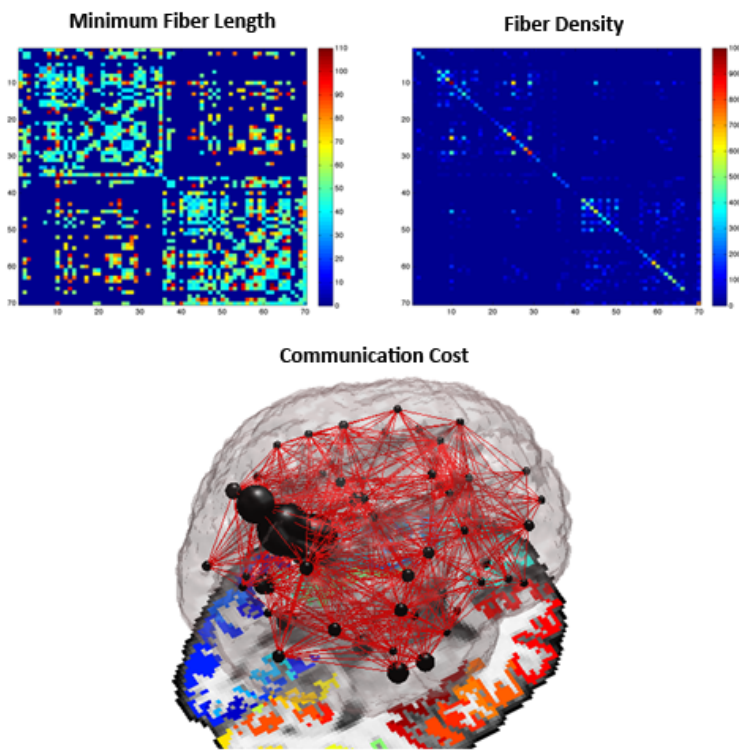

Figure 1. A local network "communication cost" can be defined between a pair of ROIs. Here we define the cost as the number of fibers (*i.e.*, fiber density) intersecting each ROI multiplied by the minimum physical fiber length among a set of white matter bundles connecting ROIs, thus describing an aspect of communication related to the network's spatial embedding.

8

2.8 Statistical analyses: Permutations

To explain the differences in hub network densities (at varying k-values) between the diagnostic groups, we tested for group differences in nodal degree and separately, efficiency, by running a linear regression using age and sex as covariates. Controls were coded as 0 and diseased participants as 1. As we cannot assume data normality for connectivity measures, nonparametric methods may be more appropriate. For this, we performed 10,000 permutations, permuting the coded value of 0 and 1 while keeping sex and age true for each subject. Next, we generated permutation corrected p-values using the following formula: $p=(b+1)/(m+1)$, where b is the number of test statistics t_{perm} found to be more significant than the observed test statistic t_{obs}, and m is the total number of permutations (i.e., 10,000). We further used the false discovery rate (FDR; Benjamini and Hochberg, 1995) to correct for multiple comparisons across all permuted p-values. For all analyses, the independent variables were permuted 10,000 times.

We further assessed group network differences for element-wise connectivity matrices describing the communication cost, and then separately, fiber density and minimum fiber length, between bvFTD and healthy controls in a linear regression, covarying for age and sex, with controls coded as 0 and bvFTD coded as 1. Similarly, we tested for group differences in communication cost between EAOD and controls. Then, to determine how the diseased groups differed in their brain network architectures, we compared the communication cost between bvFTD and EAOD in the same way. Permutations were run as above. We assessed the resulting connections in terms of their participation in the densely interconnected hubs, or rather in the more remote components of the brain networks.

3. Results

We outline the results in the order they were performed. First, we analyzed the most densely interconnected hubs in the brain for each diagnostic group. Brain hub communities in healthy controls have a centrally positioned, efficient and high-cost communication that is disrupted in both bvFTD and EAOD groups. Network components in EAOD that showed disruptions in the form of relative decreases and increases of the cost and fiber density, relative to healthy elderly, were all among the hub community of the brain network; meanwhile, in bvFTD, 72% of the impaired components were among hub connections, while the remaining 28% impairments were part of the non-hub

(remote) regions of the brain. In bvFTD and EAOD, there were both relative increases and decreases in communication cost and fiber density within the brain connectome.

3.1 Assessment of the densely interconnected hubs of the brain

Hubs in controls and EAOD participants were defined at thresholding levels $k=26$, and in bvFTD, at $k=22$; these were the maximum degree hubs with a nodal degree of 26 (in controls and EAOD) and 22 (in bvFTD); nodal degrees 27 and 23 did not exist among the corresponding diagnostic groups. Next, to determine if the highly interconnected hubs in the brain occurred by chance, we assessed the ratio between the density of connections among nodes in random networks to the density found in real networks at $k=26$ in controls and AD patients and at $k=22$ in bvFTD patients. All ratios were greater than 1, indicating that the hubs within the brain existed and were not interconnected by chance.

The network hub at $k=26$ in controls accounted for 64% of the communication cost of the entire network (unthresholded connectivity matrix at $k=0$), 65% of the fiber density and 48% of the short-distance connections (<40mm), 53% of the medium-distance connections (40-60 mm) and 82% of the long-distance connections (>60 mm). 2% of the cost and 4% of the fiber density were removed as part of the low degree nodes in the network using a consistent and minimal thresholding at $k=12$ across all diagnostic groups (**Figure 2**). In bvFTD, the network hub contained 70% of the communication cost of the whole network, 71% of the fiber density, 56% of the short-distance connections, 65% of the medium-distance connections and 100% of the long-distance connections. 4% of the cost and fiber density were removed from each subject's network. Finally, the EAOD network hub contained 57% communication cost of the whole unthresholded network, 59% fiber density, 45% of the short-distance connections, 44% of the medium-distance connections and 100% of the long distance connections. Less than 1% of the low degree network nodes were removed from the whole brain network in each subject (**Figure 2**).

To understand the less densely connected networks in bvFTD participants, we compared them to controls. We tested for nodal degree and efficiency differences between the two diagnostic groups. All nodal degree measures that were significantly different (critical FDR p-value=0.0087) between the two groups were lower in bvFTD. The bvFTD group showed decreases in the following hub regions: in the left precentral, superior temporal and middle temporal regions, and the right insula, posterior cingulate, and precentral ROIs. In non-hub regions, the decreases were in the left *pars opercularis*, left caudal middle frontal, right caudal middle frontal, and right *pars opercularis*. Meanwhile, nodal efficiency was also found significantly different between bvFTD and controls (critical FDR p-value=0.0061).

10

Nodal efficiency was higher in the following hub regions: left and right inferior, middle and superior temporal. Moreover, nodal efficiency was lower in the following non-hub regions: left and right rostral anterior cingulate and the right medial orbitofrontal; and an increase in the non-hub left rostral middle frontal, relative to controls. We also tested for differences in nodal degree and nodal efficiency between the EAOD and controls but found no significant differences.

3.2 Diagnostic group differences for communication cost, fiber density and minimum fiber length

Communication cost was lower in the left hemisphere of bvFTD patients, relative to controls, between the insula and superior frontal, rostral middle frontal and caudal middle frontal, superior frontal and *pars opercularis*, and higher cost between the insula and postcentral, and precentral and postcentral. In the right hemisphere of bvFTD participants, relative to controls, we found a lower communication cost between the posterior cingulate and superior frontal, and an increase between the precuneus and paracentral, insula and postcentral, insula and superior parietal, insula and supra-marginal and postentral and paracentral (FDR p-value=1.0×10^{-4}; **Figure 3A**). We also analyzed the components of the communication cost – the fiber density and the minimum fiber length. Significant differences in fiber density generally supported the findings in the communication cost. However, bvFTD participants had an additional decrease in density in the left hemisphere of between the insula and fusiform gyrus, and an increase in fiber density between the paracentral and postcentral regions, relative to controls. The overall critical FDR p-value for fiber density was 0.0029. Meanwhile, the minimum fiber lengths between regions were not detectably different between bvFTD and controls.

Relative to controls, in EAOD patients, communication cost was lower in the left hemisphere between the superior frontal and caudal anterior cingulate, posterior cingulate and superior frontal, and higher between the insula and precentral. A decrease in cost was found in the right hemisphere between the insula and postcentral and insula and superior parietal (FDR p-value=0.0018; **Figure 3B**). In addition to these, fiber density was lower in the left hemisphere posterior cingulate and the caudal anterior cingulate, and higher between the insula and postcentral gyrus in EAOD, relative to controls. Also, lower fiber density was found between the inferior parietal and precentral in the right hemisphere of the EAOD group, relative to controls (FDR p-value=1.0×10^{-4}). Minimum fiber length was significantly lower in the interhemispheric connection of the isthmus of the cingulate in EAOD, relative to healthy participants (FDR p-value=1.0×10^{-4}).
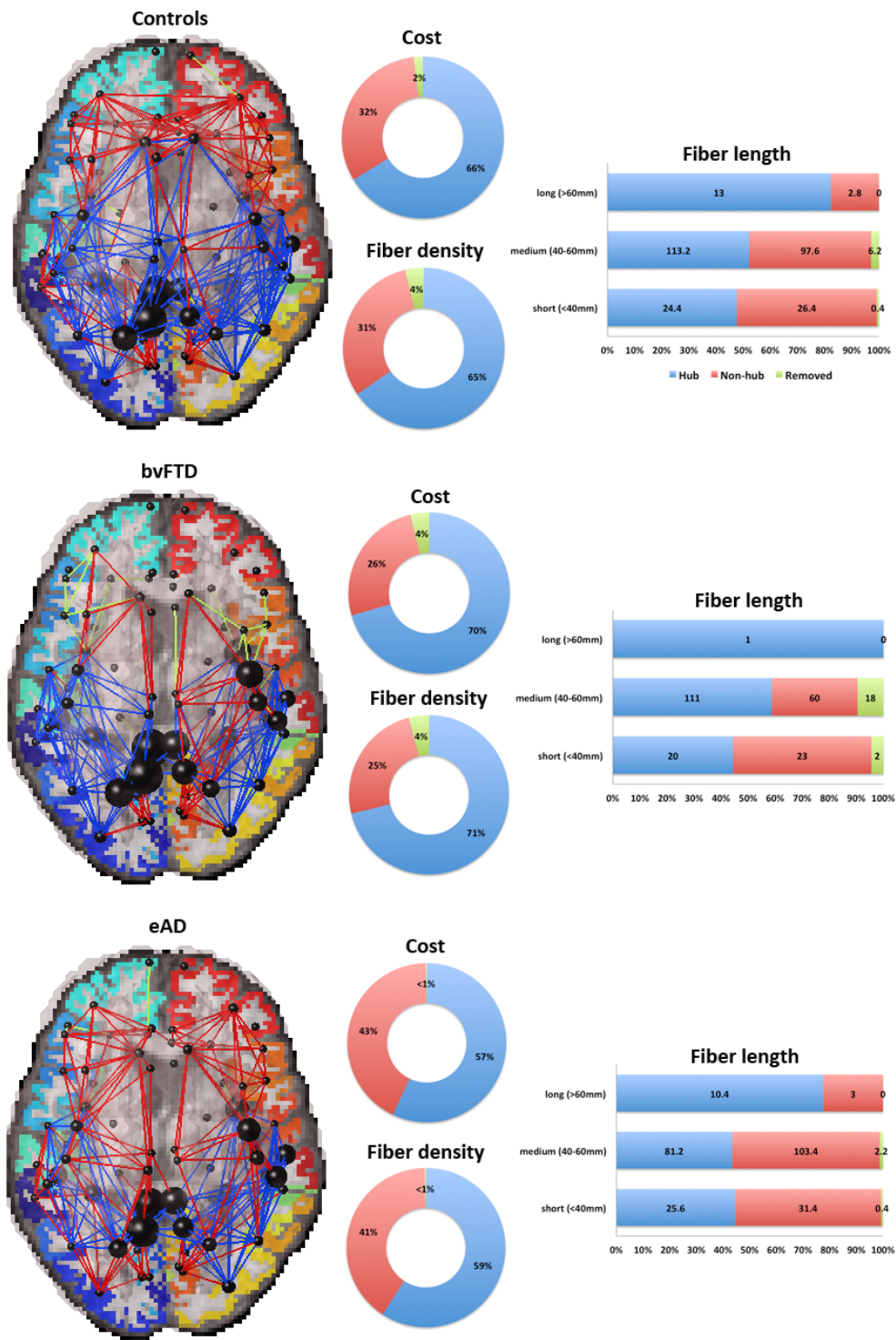
Figure 2. Set of nodes illustrating the structural backbone averaged for groups of healthy controls, bvFTD and EAOD participants. Blue edges indicate connections part of the network hub in each diagnostic group (*k*=26 for controls and EAOD,

k=22 for bvFTD), while red edges indicate non-hub connections and green edges connect low degree nodes that were removed from the network (at *k*=12). The cost, fiber density and minimum fiber length were computed for each type of network (hub, non-hub and removed connections) in all groups. The hub-like networks account for more than 50% of the whole brain network's cost, fiber density and number of connections. The size of the black nodes is proportional to the communication cost, with larger nodes having higher communication cost.

When testing for network differences between bvFTD and EAOD, bvFTD participants showed lower communication cost between the insula and superior frontal, and between the insula and *pars opercularis*, relative to EAOD; they also showed higher cost between the precuneus and cuneus, and between the cuneus and peri-calcarine, relative to EAOD (FDR *p*-value=6.0x10^{-4}; **Figure 4**). We further examined the fiber density and minimum fiber length and found overlapping differences in fiber density as compared to the communication cost, as well as a decrease in fiber density in the left hemisphere rostral middle frontal and caudal anterior cingulate regions in bvFTD, relative to EAOD, and an increase in the right hemisphere cuneus and a decrease in the superior frontal in bvFTD, relative to EAOD (FDR *p*-value=0.0012). The minimum fiber length was not found significantly different between the two disease groups. Finally, all connections were categorized as either part or not part of the set of densely connected hubs in controls (*k*=26), bvFTD participants (*k*=22) and EAOD (*k*=26) in **Table 3**.

	Connections of significance	Hub/Non-hub
	Communication Cost (*k*=12)	**Communication Cost (*k*=12)**
	(FDR *p*-value=1.0E-04)	
	Left Hemisphere	*Left Hemisphere*
	Caudal middle frontal and rostral middle frontal, ⇓	Non-hub CTL, bvFTD
	Superior frontal and *pars opercularis*, ⇓	Hub CTL, non-hub bvFTD
	Superior frontal and insula, ⇓	Hub CTL, bvFTD
	Postcentral and precentral ⇑	Hub CTL, bvFTD
	Insula and postcentral, ⇑	Hub CTL, bvFTD
	Right Hemisphere	*Right Hemisphere*
bvFTD vs. Controls	Superior frontal and posterior cingulate, ⇓	Hub CTL, non-hub bvFTD
	Insula and postcentral, ⇑	Hub CTL, bvFTD
	Insula and superior parietal, ⇑	Hub CTL, bvFTD
	Insula and supra-marginal, ⇑	Hub CTL, bvFTD
	Precuneus and paracentral, ⇑	Hub CTL, bvFTD
	Paracentral and postcentral, ⇑	Hub CTL, bvFTD

13

	Fiber Density (*k*=12) (FDR *p*-value=0.0029) *In addition to connections listed under cost:* *Left Hemisphere* Insula and fusiform, ⇓ Paracentral and postcentral, ⇑	**Fiber Density (*k*=12)** *Left Hemisphere* Hub CTL, bvFTD Hub CTL, bvFTD
	Minimum fiber length (*k*=12) NS	**Minimum fiber length (*k*=12)** NS
EAOD vs Controls	**Communication Cost (*k*=12)** (FDR *p*-value=1.8E-03) *Left Hemisphere* Posterior cingulate and superior frontal, ⇓ Caudal anterior cingulate and superior frontal, ⇓ Insula and precentral, ⇑ *Right Hemisphere* Insula and postcentral, ⇑ Insula and superior parietal, ⇑	**Communication Cost (*k*=12)** *Left Hemisphere* Hub CTL, EAOD Hub CTL, EAOD Hub CTL, EAOD *Right Hemisphere* Hub CTL, EAOD Hub CTL, EAOD
	Fiber Density (*k*=12) (FDR *p*-value=1.0E-04) *In addition to connections listed under cost:* *Left Hemisphere* Caudal anterior cingulate, ⇓ Posterior cingulate, ⇓ Insula and postcentral, ⇑	**Fiber Density (*k*=12)** *Left Hemisphere* Hub CTL, EAOD Hub CTL, EAOD Hub CTL, EAOD
	Minimum fiber length (*k*=12) (FDR *p*-value=1.0E-04) *Interhemispheric* Isthmus of the cingulate, long distance connection, ⇓	**Minimum fiber length (*k*=12)** *Interhemispheric* Hub CTL, EAOD
bvFTD vs. EAOD	**Communication Cost (*k*=12)** (FDR *p*-value=6.0E-04) *Left Hemisphere* Insula and superior frontal, ⇓ Insula and *pars opercularis,* ⇓ *Right Hemisphere* Precuneus and cuneus, ⇑ Cuneus and peri-calcarine, ⇑	**Communication Cost (*k*=12)** *Left Hemisphere* Non-hub bvFTD, hub EAOD Non-hub bvFTD, EAOD *Right Hemisphere* Hub bvFTD, non-hub EAOD Hub bvFTD, non-hub EAOD

14

	Fiber Density (*k*=12)	Fiber Density (*k*=12)
	(FDR *p*-value=1.2E-03)	
	In addition to connections listed under cost:	
	Left Hemisphere	*Left Hemisphere*
	Caudal anterior cingulate, ⇓	Non-hub bvFTD, hub EAOD
	Rostral middle frontal, ⇓	Non-hub bvFTD, EAOD
	Right Hemisphere	
	Superior frontal, ⇓	Non-hub bvFTD, hub EAOD
	Cuneus, ⇑	Hub bvFTD, non-hub EAOD
	Minimum fiber length (*k*=12)	**Minimum fiber length (*k*=12)**
	NS	NS

Table 3. Connections that were found significantly different between controls and bvFTD, controls and EAOD, and bvFTD and EAOD for minimally thresholded connectivity matrices (*k*=12) for measures of communication cost, fiber density and minimum fiber length. The arrows indicate increases (⇑) and decreases (⇓) in the diseased group measures (*i.e.*, cost), relative to healthy; they also indicate increases or decreases for measures in bvFTD, relative to EAOD. *NS=not significant.
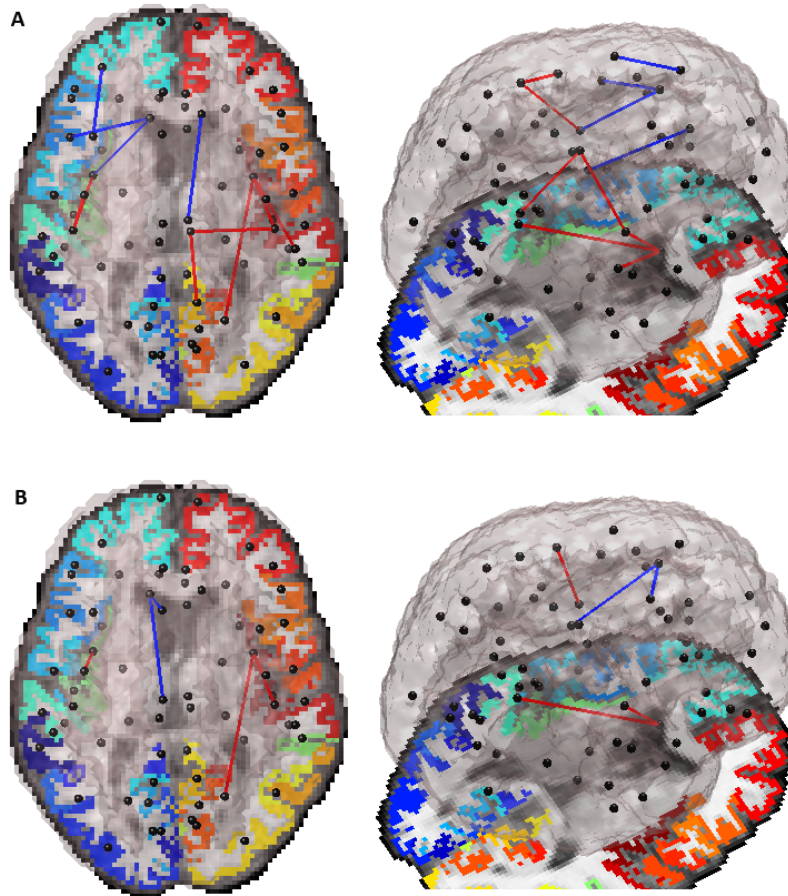
Figure 3. A. Group differences in network communication cost between bvFTD and healthy controls. Cost was lower (*blue edges*) in the left hemisphere of the FTD group, relative to controls, between the caudal middle frontal and rostral middle frontal, *pars opercularis* and superior frontal, insula and superior frontal, and was higher (*red edges*) between the postcentral and precentral gyrus, and the postcentral gyrus and insula. Cost was higher in the right hemisphere of FTD, relative to controls, between the postentral and paracentral, precuneus and paracentral, insula and postcentral, insula and superior parietal and insula and supra-marginal region (FDR *p*-value=1.0x10^{-4}). **B.** Group differences in network communication cost between EAOD and healthy controls. Cost was lower in the left hemisphere of EAOD, relative to controls, between the caudal anterior cingulate and superior frontal, posterior cingulate and superior frontal, and increased between the insula and precentral. In the right hemisphere of EAOD, cost was higher between the insula and postcentral gyrus, and between the insula and the superior parietal region (FDR *p*-value=0.0018).
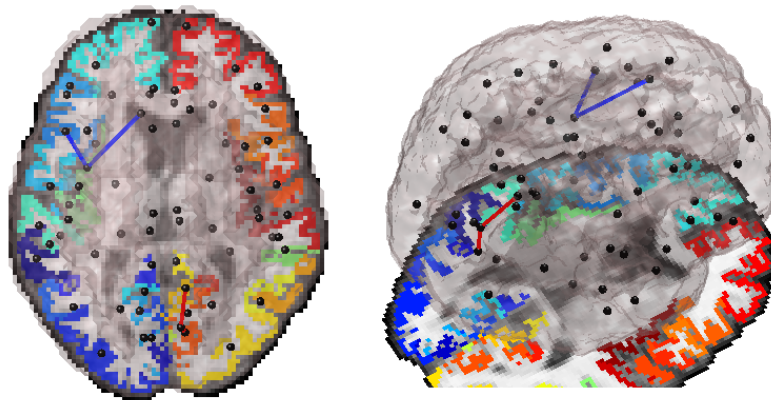
Figure 4. Group differences in network communication cost between bvFTD and EAOD participants. Cost was lower in bvFTD participants, relative to EAOD, between the insula and superior frontal, and insula and *pars opercularis*. Cost was higher in bvFTD, relative to EAOD, between the cuneus and precuneus, and cuneus and peri-calcarine (FDR *p*-value=6.0x10^{-4}). Fiber density was different between the two disease groups and had the same directionality between the described ROIs as the network cost (FDR *p*-value=0.0012), while minimum fiber length did not show a distinguishing pattern.

4. Discussion

Here we analyzed white matter pathways that formed central and high-cost hubs in the networks of healthy elderly people, and groups of patients with bvFTD and EAOD. We assessed how these networks differed in their communication cost, fiber density and fiber length assignments among ROIs on the cortex. Our study had 3 main findings: **1)** most densely interconnected hubs account for over 50% of the total communication cost and fiber

density of the overall brain network; these are centrally-positioned, high-cost communities that process and disseminate information among all connections in the brain; **2)** in the EAOD group, compared to healthy elderly controls, all communication cost network disruptions were located within the hub community of the brain, indicating that disease strikes the dense core structure of the brain in the early-onset AD; for the bvFTD group, 72% of network abnormalities were in hubs and the rest (28%) were in their remote connections. **3)** bvFTD and EAOD showed different patterns of network disruptions; bvFTD participants were overall more structurally impaired than EAOD, especially in frontal regions, as might be expected.

4.1 Densely interconnected hubs uptake more that 50% of the brain's network cost and fiber density

We also divided the whole brain network of each subject into densely interconnected "hub" nodes and non-hub nodes. Each hub node was connected to at least 38% of the other nodes in the network by having a nodal degree of k=26 or higher. These criteria were fulfilled by brain networks in the healthy and EAOD groups, while the bvFTD group formed a network hub at k=22 where one hub node was connected to only 32% of the other network nodes. Significant reductions in nodal degree within 10 regions of the brain in bvFTD, relative to healthy controls, explain the less interconnected hub in this particular diagnostic group. These reductions in nodal degree were located in hub regions of both bvFTD and CTL and were: 20% in the frontal lobe, 20% in the temporal lobe as well as the right insula and posterior cingulate; more reductions were categorized as non-hub regions and were located 40% in the frontal lobe.

The communication cost is a network measure related to the network's spatial embedding (van den Heuvel et al., 2012; Achard and Bullmore, 2007). In other words, it depends on the length of fibers, not just their topology. In the network hubs of the brain, we showed higher-cost and higher-capacity structures for global brain communications than in the non-hub nodes. The hubs in the brain were more costly than predicted by their fiber density alone and they accounted for 66% of the total communication cost in the whole brain of healthy elderly, 70% in bvFTD and 57% in EAOD participants. Most edges (75%) interconnecting these hubs were of medium length (40-60mm) – only 16% short and 9% long in the hubs of controls; 15% short, 84% medium and <1% long in the hubs of bvFTD, and 22.5% short, 71% medium and 6.5% long in the whole brain hubs of EAOD participants. We note that the length of fibers in the brain's connectome may depend on the tractography method used – for instance, the Hough method is known to trace longer fibers, on average, than many other methods.

17

4.2 Interpreting network disruptions in the diseased brain

Significant differences in network cost and fiber density were found among the disease groups, relative to healthy elderly, and were mostly located in the densely interconnected hubs of the brain (**Table 3; Figure 3A**). In bvFTD, the insula has shows early network degeneration (Seeley et al., 2010). Here, the insula was a major hub projecting connections to nodes in the network that significantly increased and decreased in cost and fiber density, relative to controls. Pathways that connected the left insula to more frontal ROIs (*i.e.,* superior frontal, fusiform) and were part of the hub networks in both bvFTD and controls, showed a declining communication cost and fiber density. Pathways that connected the left and right insula to more posterior regions of the cortex (*i.e.*, postcentral, superior parietal), as part of the hub networks in both groups, showed increasing cost and fiber density in bvFTD, relative to healthy elderly. In the meantime, hub regions were lost in bvFTD (became non-hubs), relative to controls, between the left superior frontal and *pars opercularis* and the right superior frontal and posterior cingulate, where both cost and fiber density declined – potentially inducing the loss in hub nodes.

Compared to controls, EAOD showed consistent differences in cost, fiber density and minimum fiber length (**Table 3**; **Figure 3B**). First, all the connections that differed between the two groups were part of the hub networks. This indicates that disease, in its early stages, strikes the core structure of the brain – composed of highly interconnected nodes that account for more than 50% of the whole brain's structural capacity. Furthermore, communication cost and fiber density declined between the left posterior cingulate and superior frontal regions. Meanwhile, different patterns of degeneration were seen, as expected, in AD versus bvFTD, as sensorimotor and frontal regions tend to be relatively spared until later in the disease (Thompson et al., 2003). In line with this, we found increases in cost and fiber density for pathways connecting the left insula to the precentral and the right insula to the postcentral and superior parietal regions. These connections may provide further evidence for the patterns of altered connectivity previously shown in functional studies – associated with dysfunctions in episodic memory (Buckner et al., 2005) shown as reductions in the Default Mode Network (DMN), and enhancement of the Salience Network (SN), with preservation of socio-emotional functioning (Seeley at al., 2007; Zhou et al., 2010).

When compared to each other, groups of patients with bvFTD and EAOD showed similar but more prominent differences than when comparing the dementia groups to the healthy elderly. The bvFTD group showed drastic connectivity reductions, compared to EAOD, between the insula and the superior frontal and *pars opercularis*. Connections between the insula and superior frontal region are part of the network hub in EAOD, but not in bvFTD,

and connections between the insula and *pars opercularis* are non-hub connections in both diagnostic groups. The EAOD group showed dramatic connectivity reductions between the precuneus and cuneus, peri-calcarine and cuneus– connections that were both categorized as hubs in bvFTD, but not in EAOD. In no region did the bvFTD group show an increase in connectivity to the insula, relative to EAOD – and this is a region known to degenerate more anteriorly in bvFTD (Seeley et al., 2010). In no regions did the EAOD participants show an increase in connectivity of the precunes, relative to bvFTD, shown to atrophy in early onset AD (Karas et al., 2007).

Although it is sometimes difficult to differentiate between bvFTD and EAOD as some of their symptoms overlap (Young et al., 2009), there has been an ongoing effort to understand the differentiating factors between the two neurodegenerative diseases, especially with functional imaging. In structural studies, bvFTD patients have signs of atrophy in the frontal lobe and anterior regions in general (*i.e.*, anterior insula, anterior cingulate) and with disease progression, extending into more posterior areas including the posterior insula, temporal and anterior parietal regions (Seeley et al., 2008; Rohrer, 2012). Functional imaging studies show different patterns of connectivity in bvFTD versus AD, particularly, intrinsic connectivity network reductions in the SN and enhancement in the DMN in bvFTD participants, relative to AD (Zhou et al., 2010).

References

1. Aganj I, Lenglet C, Sapiro G. Yacoub E, Ugurbil K, Harel N, 2010. Reconstruction of the Orientation Distribution Function in Single and Multiple Shell Q-Ball Imaging within Constant Solid Angle. Magn Reson Med.;64(2), 554-466.

2. Alvarez-Hamelin JI, Dall'Asta L, Barrat A, Vespignani A, 2006. Large scale networks fingerprinting and visualization using k-core decomposition. Weiss Y, Scholkopf B, Platt J. editors. Cambridge (Massachusetts); MIT Press 44-55.

3. Benjamini Y, Hochberg Y, 1995. Controlling the False Discovery Rate: A Practical and Powerful Approach to Multiple Testing. Journal of the Royal Statistical Society. Series B (Methodological), Vol. 57, No. 1, pp. 289-300.

4. Braak H, Braak E. 1991. Neuropathological staging of Alzheimer-related changes. Acta Neuropathol;82(4):239-59.

5. Clerx L, Visser PJ, Verhey F, Aalten, P, 2012. New MRI markers for Alzheimer's disease: a meta-analysis of diffusion tensor imaging and a comparison with medial temporal lobe measurements. J Alzheimer's Dis.; 29(2), 405-29.

6. Daianu M, Jahanshad N, Nir TM, Toga AW, Jack CR, Jr., Weiner MW, Thompson PM and the Alzheimer's Disease Neuroimaging Initiative, 2013. Breakdown of Brain Connectivity between Normal Aging and Alzheimer's Disease: A Structural *k*-core Network Analysis. Brain Connectivity;3(4):407-22.

7. Daianu M, Jahanshad, N Nir, TM, Dennis E, Toga AW, Jack CR, Jr., Weiner MW, Thompson PM, and the Alzheimer's Disease Neuroimaging Initiative, 2012. Analyzing the structural k-core of brain connectivity networks in normal aging and

19

Alzheimer's disease. In NIBAD' 12 MICCAI Workshop on Novel Imaging Biomarkers for Alzheimer's Disease and Related Disorders, Nice, France, 52–62.

8. Desikan RS, Segonne F, Fischl B, Quinn BT, Dickerson BC, Blacker D, Buckner RL, Dale AM, Maguire RP, Hyman BT, Albert MS, Killiany RJ, 2006. An automated labeling system for subdividing the human cerebral cortex on MRI scans into gyral based regions of interest. Neuroimage;31(3):968-80.

9. Dopper EG, Rombouts SA, Jiskoot LC, Heijer Td, de Graaf JR, Koning Id, Hammerschlag AR, Seelaar H, Seeley WW, Veer IM, van Buchem MA, Rizzu P, van Swieten JC, 2013. Structural and functional brain connectivity in presymptomatic familial frontotemporal dementia. Neurology;80(9):814-23.

10. Engel JP, Thompson PM, Stern JM, Staba RJ, Bragin A, Mody I, 2013. Connectomics and Epilepsy, Current Opinion in Neurology, invited paper, *in press*.

11. Fischl B, Destrieux C, Halgren E, Segonne F, Salat DH, Busa E, Seidman LJ, Goldstein J, Kennedy D, Caviness V, Makris N, Rosen B, 2004. Automatically parcellating the human cerebral cortex. Cerebral Cortex;14:11-22.

12. Greicius MD, Krasnow B, Reiss AL, Menon V, 2013. Functional connectivity in the resting brain: a network analysis of the default mode hypothesis. Proc Natl Acad Sci.;100(1):253-8.

13. Karas G, Scheltens P, Rombouts S, van Schijndel R, Klein M, Jones B, van der Flier W, Vrenken H, Barkhof F, 2007. Neuroradiolog;,49(12):967-76.. Precuneus atrophy in early-onset Alzheimer's disease: a morphometric structural MRI study.

14. Mendez MF and Lim GTH, 2004.Alterations of the Sense of "Humanness' in Right Hemisphere Predominant Frontotemporal Dementia Patients. Cog Behav Neurol;17(3):133-138.

15. Minoshima S, Giordani B, Berent S, Frey KA, Foster NL, Kuhl DE, 1997. Ann Neurol. 42(1):85-94.Metabolic reduction in the posterior cingulate cortex in very early Alzheimer's disease.

16. Mori S, van Zijl PC, 2002. Fiber tracking: principles and strategies - a technical review. NMR Biomed. 15(7-8):468-80.

17. Thompson PM, Hayashi KM, de Zubicaray G, Janke AL, Rose SE, Semple J, Herman D, Hong MS, Dittmer SS, Doddrell DM, Toga AW, 2003. *Dynamics of Gray Matter Loss in Alzheimer's Disease,* J Neuroscience;23(3):994-1005.

18. Thompson PM, Vinters HV, 2012. Pathologic Lesions in Neurodegenerative Diseases, Prog Mol Biol Transl Sci. 2012;107:1-40; also printed as a book chapter in the Elsevier Book (edited by David Teplow), "The Molecular Biology of Neurodegenerative Diseases."

19. Toga AW, Thompson PM, 2013. Connectomics Sheds New Light on Alzheimer's Disease, Biological Psychiatry, 1;73(5):390-2.

20. van den Heuvel, MP and Sporns, O, 2011. Rich-club organization of the human connectome. J Neurosci. 31(44), 15775-15786.

21. van den Heuvel, MP, Kahn RS, Goni J, Sporns O, 2012. High-cost, high-capacity backbone for brian communication. PNAS 109(28):11372-11377.

22. Seeley WW, 2010. Anterior insula degeneration in frontotemporal dementia. Brain Struct. Funct., vol. 214(5-6), pp. 465-75.

23. Seeley WW, Allman JM, Carlin DA, Crawford RK, Macedo MN, Greicius MD, DeArmond SJ, Miller BL, 2007. Divergent Social Functioning in Behavioral Variant Frontotemporal Dementia and Alzheimer Disease: Reciprocal Networks and Neuronal Evolution. Alzheimer Dis Assoc Disord.;21(4):S50-7.

24. Seeley WW, Menon V, Schatzberg AF, Keller J, Glover GH, Kenna H, Reiss AL, Greicius MD, 2007. Dissociable Intrinsic Connectivity Networks for Salience Processing and Executive Control. J Neurosci.;28;27(9):2349-56.

25. Seeley WW, 2010. Anterior insula degeneration in frontotemporal dementia. Brain Struct Funct. 2010 Jun;214(5-6):465-75.

26. Rohrer JD, 2012. Structural brain imaging in frontotemporal dementia . Imaging Brain Aging and Neurodegenerative Disease;1822(3):325–332

27. Rosenmann H, Meiner Z, 2013. Frontotemporal dementia: clinical features, genetics, pathogenesis and treatment. Harefuah;152(11):661-6, 687.

28. Sporns O, 2011. Networks of the Brain. Cambridge, MA, pp. 5-31.

29. Young K, Du AT, Kramer J, Rosen H, Miller B, Weiner M, Schuff N, 2009. Patterns of structural complexity in Alzheimer's disease and frontotemporal dementia. Hum Brain Mapp.;30(5):1667-77.

Supplementary Information

Pre-processing and co-registration

Non-brain regions were automatically removed from each T1-weighted MRI scan, and from a T2-weighted image from the DWI set using the FSL tool "BET" (http://fsl.fmrib.ox.ac.uk/fsl/). Anatomical scans underwent intensity inhomogeneity normalization using the MNI "nu_correct" tool (www.bic.mni.mcgill.ca/software/). All T1-weighted images were linearly aligned using FSL (with 6 degrees-of-freedom; DOF) to a common space with 1mm isotropic voxels and a 220×220×220 voxel matrix. The DWIs were corrected for eddy current distortions using the FSL toolkit (http://fsl.fmrib.ox.ac.uk/fsl/). For each subject, the image with no diffusion sensitization was linearly aligned and resampled to match a downsampled version of the corresponding T1-weighted image (110×110×110, 2×2×2mm). b_0 maps for each subject were elastically registered (Leow et al., 2005) to the corresponding T1-weighted scan to compensate for susceptibility artifacts (EPI distortions). Images were visually inspected and there were no misalignments or cases where the field of view did not cover the full brain (i.e., cropping).

Tractography and cortical extraction

The transformation matrix from linearly aligning the mean b_0 image to the T1-weighted volume was applied to each of the 31 gradient directions to re-orient the orientation distribution functions (ODFs). We also performed whole-brain tractography as described in (Aganj et al., 2011) on the sets of DWI volumes. Only linear registration was performed before tractography, as nonlinear registration before tractography could introduce processing artifacts. Gradient directions for each DWI volume were adjusted using the transformation matrix obtained from the linear registration. The tractography method uses a fiber detection approach based on the Hough transform (Aganj et al., 2011). To detect crossing fibers, the method uses a constant solid angle orientation density function (CSA-ODF; Aganj et al., 2010) rather than a diffusion tensor, to model the local diffusion propagator. The angular resolution of our data is deliberately limited to avoid long scan times that may tend to increase patient attrition. Even so, this ODF model makes best use of the limited angular resolution (even if the protocol is not ideal for resolving fiber crossing).

Elastic deformations obtained from the EPI distortion correction, mapping the average b_0 image to the T1-weighted image, were then applied to each recovered fiber's 3D coordinates to more accurately align the anatomy (we assume that the anatomical scan serves as a relatively undistorted anatomical reference). Each subject's dataset contained ~10,000 useable fibers (3D curves) in total.

34 cortical labels per hemisphere, listed in the Desikan-Killiany atlas (Desikan et al., 2006), were automatically extracted from all aligned T1-weighted structural MRI scans using FreeSurfer version 5.0 (http://surfer.nmr.mgh.harvard.edu/) (Fischl et al., 2004). The resulting T1-weighted images and cortical models were aligned to the original T1-weighted input image space and down-sampled using nearest neighbor interpolation (to avoid intermixing of labels) to the space of the DWIs. To ensure tracts would intersect labeled cortical regions, labels were dilated with an isotropic box kernel of width 5 voxels (Jahanshad et al., 2011).

1	Banks of the superior temporal sulcus	19	*Pars orbitalis*
2	Caudal anterior cingulate	20	*Pars triangularis*
3	Caudal middle frontal	21	Peri-calcarine
4	-N/A-	22	Postcentral
5	Cuneus	23	Posterior cingulate
6	Entorhinal	24	Precentral
7	Fusiform	25	Precuneus
8	Inferior parietal	26	Rostral anterior cingulate
9	Inferior temporal	27	Rostral middle frontal
10	Isthmus of the cingulate	28	Superior frontal
11	Lateral occipital	29	Superior parietal
12	Lateral orbitofrontal	30	Superior temporal
13	Lingual	31	Supra-marginal
14	Medial orbitofrontal	32	Frontal pole
15	Middle temporal	33	Temporal pole
16	Parahippocampal	34	Transverse temporal
17	Paracentral	35	Insula
18	*Pars opercularis*		

Table 1S. Index of cortical labels extracted from FreeSurfer (Desikan et al., 2006).

23

4.2 Algebraic connectivity

This section is adapted from:

Daianu M, et al. Algebraic connectivity of brain networks shows patterns of segregation leading to reduced network robustness in Alzheimer's disease. MICCAI 2014, Boston, MA, USA, *submitted*, February 28 2014.

Algebraic connectivity of brain networks shows patterns of segregation leading to reduced network robustness in Alzheimer's disease

Madelaine Daianu [a,b], Neda Jahanshad [b], Talia M. Nir [b], Cassandra D. Leonardo [b], Clifford R. Jack, Jr.[c], Michael W. Weiner [d,e], Matthew Bernstein [c], Paul M. Thompson[a,b,f,g]* and the Alzheimer's Disease Neuroimaging Initiative**

[a] Department of Neurology, UCLA School of Medicine, Los Angeles, CA, USA
[b] Imaging Genetics Center, Institute for Neuroimaging & Informatics, University of Southern California, Los Angeles, CA, USA
[c] Department of Radiology, Mayo Clinic, Rochester, Minnesota, USA
[d] Department of Radiology, Medicine, and Psychiatry, University of California San Francisco, CA, USA
[e] Department of Veterans Affairs Medical Center, San Francisco, CA, USA
[f] Departments of Neurology, Psychiatry, Radiology, Engineering, Pediatrics, and Ophthalmology, USC

Abstract. Measures of network topology and connectivity aid the understanding of network breakdown as the brain degenerates in Alzheimer's disease (AD). We analyzed 3-Tesla diffusion-weighted images from 202 patients scanned by the Alzheimer's Disease Neuroimaging Initiative – 50 healthy controls, 72 with early- and 38 with late-stage mild cognitive impairment (eMCI/lMCI) and 42 with AD. Using whole-brain tractography, we reconstructed structural connectivity networks representing connections between pairs of cortical regions. We examined for the first time the network's Laplacian matrix and its corresponding Fiedler value, describing the network's *algebraic connectivity*, and the Fiedler vector, used to partition a graph. We assessed algebraic connectivity and four additional supporting metrics, revealing a decrease in network robustness and increasing disarray among nodes as dementia progressed. Network components became more disconnected and segregated, and their modularity increased. These novel measures are sensitive to diagnostic group differences, and may help understand the complex brain changes in AD.

Keywords: brain network, algebraic connectivity, Fiedler value, modularity, Alzheimer's disease

1. Introduction

Brain connectivity analyses are increasingly popular, and combine concepts from neuroscience and engineering to characterize the brain in terms of its structural and functional connections. Diffusion weighted imaging (DWI) and advanced tractography methods are used for mapping structural brain connectivity. This may offer new insights into how the brain changes in degenerative diseases such as Alzheimer's disease (AD), and its precursor, mild cognitive impairment (MCI).

Topological changes in the brain's networks may be analyzed using graph theory, which represents the brain's connections as a set of nodes and edges. The network's nodes are typically defined as regions of interest (ROIs) - in our case on the cortex, segmented from anatomical MRI. These nodes are considered to be linked by 'edges' whose weights denote some measure of connectivity between the two regions, such as the density or integrity of fiber tracts.

There is an increasing interest in analyzing the brain using graphs, *i.e.*, as a set of interconnected nodes and edges, which can be studied using network analysis toolboxes [1]. However, as the field is still in its formative stages, we do not yet know which graph theoretic measures best differentiate disease states or change the most with disease progression. Here, we computed some novel graph measures - not previously examined in the context of dementia. We applied ideas from algebraic graph theory: specifically, we computed the second smallest eigenvalue of the Laplacian matrix (Fiedler value) for each subject to describe their algebraic connectivity – *i.e.*, the higher the magnitude of the Fiedler value, the more interconnected a graph is. The Fiedler value, accompanied by a measure of link density (interconnectedness of nodes) can further describe the robustness of a graph – the denser the connections, the less vulnerable the brain network is to being disconnected. Similarly, based on the set of eigenvalues, we determined the number of disconnected network components (ROIs that do not have connections to other ROIs, or where network connections are not detected). To expand our analysis of brain connectivity, we computed more standard measures of modularity – a measure that the degree to which a network may be subdivided to significantly delineated groups of nodes [1,2]. Our overall goal was to develop unusual network metrics from algebraic graph theory and apply them for the first time to the study of dementia.

To determine whether the network changes were behaviorally and clinical relevant, we related the network measures to the Mini Mental Status Examination score – a simple but widely-used test to evaluate patients and help in diagnosis of dementia. We hypothesized that with disease progression, the graph representation of the brain would becomes more modular (*i.e.*, segregated), reducing the density of connections among its ROIs and eventually, leading to disconnections among its nodes. We expected to see changes predominantly in the entorhinal areas and temporal cortices, areas affected first by structural atrophy in Alzheimer's disease. In diagnostic group comparisons, we also aimed to show that the algebraic connectivity is disrupted. The overall goal of our work is to mathematically describe how the brain network changes in disease. Although all measures were sensitive to disease effects in the ADNI cohort, we found that the Fielder value was most sensitive to picking up topological effects among AD patients as well as lMCI patients.

2. Methods

2.1 Participants and diffusion-weighted brain imaging

We analyzed diffusion-weighted images (DWI) from 202 participants scanned as part of the Alzheimer's Disease Neuroimaging Initiative (ADNI). ADNI is a large multi-site longitudinal study to evaluate biomarkers of AD. **Table 1** shows the demographics of the participants included here, including age, sex, and mini-mental state exam (MMSE) scores, broken down by diagnosis. All 202 participants underwent whole-brain MRI on 3-Tesla GE Medical Systems scanners, at 16 sites across North America. Standard anatomical T1-weighted SPGR (spoiled gradient echo) sequences were collected (256x256 matrix; voxel size = 1.2x1.0x1.0 mm^3; TI = 400 ms, TR = 6.984 ms; TE = 2.848 ms; flip angle = 11°) in the same session as the DWI (128x128 matrix; voxel size: 2.7x2.7x2.7 mm^3; scan time = 9 min). 46 separate images were acquired for each scan: 5 T2-weighted images with no diffusion sensitization (b_0 images) and 41 diffusion-weighted images (b = 1000 s/mm^2). Image preprocessing was performed as described previously in [3]. This was not included here due to space limitations.

	Controls	eMCI	lMCI	AD	Total
N	50	72	38	42	202
Age (mean ± SD in years)	72.6 ± 6.1	72.4 ± 7.9	72.6 ± 5.6	75.5 ± 8.9	73.1 ± 7.4
MMSE (mean ± SD)	28.9 ± 1.4	28.1 ± 1.5	26.9 ± 2.1	23.3 ± 1.9	27.1 ± 2.7
Sex	22M/28F	45M/27F	25M/13F	28M/14F	120M/82F

Table 1. Demographic information from 50 controls, 72 eMCI, 38 lMCI and 42 AD participants scanned with diffusion MRI as part of the ADNI project. Their ages ranged from 55.2 to 90.4 years. The mean age and mini mental state exam (MMSE) scores are listed for each diagnostic group.

2.2 NxN Connectivity Matrix Creation

We performed whole-brain tractography as described in [3]. We used a method based on the Hough transform to recover fibers, using a constant solid angle orientation distribution function to model the local diffusion propagator.

Each subject's dataset contained ~10,000 useable fibers (3D curves) in total. 34 cortical labels per hemisphere, as listed in the Desikan-Killiany atlas [4], were automatically extracted from all aligned T1-weighted structural MRI scans with FreeSurfer (http://surfer.nmr.mgh.harvard.edu/).

For each subject, a 68x68 connectivity matrix was created whereby each element represented the total number of fibers, in that subject, that passes through each pair of ROIs. For simplicity, all connectivity matrices were binarized to describe whether any connection was detected between a pair of cortical ROIs (marked as 1), or otherwise (marked as 0). Weighted networks will be considered in future work.

2.3 Algebraic connectivity and supporting network metrics

Algebraic graph theory is a branch of mathematics that uses linear algebra and matrix theory to study the properties of graphs [5]. In algebraic graph theory, the Laplacian matrix is used to study the *spectrum* of a graph, which is the topic of study in another

branch of mathematics known as *spectral graph theory* [6]. Recently, spectral theory has been applied to better reconstruct brain activity by considering the edges of a graph describing anatomical connectivity [7]. Other applications of algebraic graph theory are in the fields of circuit design, parallel and distributive computing, data representation [8] and the online web [9]. Here, we are the first to introduce the application of algebraic graph theory to extract graph properties from human brain connectivity networks to better understand the structural changes in Alzheimer's disease.

Structural networks are usually modeled as undirected and symmetric graphs, *G(N,E)* containing a set of nodes, *N*, and edges, *E*. Here we computed an adjacency matrix for each graph, *A(G)=a_{ij}*, where a_{ij} was 1 if a connection linked a pair of nodes and 0 otherwise. Next, we computed the Laplacian matrix of graph *G* (**Fig. 1**), *L(G)=l_{ij}*, where *L(G)=D(G)-A(G)*. *D(G)* is the *NxN* diagonal degree adjacency matrix (*i.e.,* diag(sum(*G*))). Then, the eigenvalues, λ_i, were computed on the Laplacian matrix, where 0=*det(L-λI)* and *I* is an *NxN* identity matrix. In this study, we were interested in the second smallest eigenvalue, also called the Fiedler value, and its corresponding eigenvector, *x*, computed from *(L-λI)x=0* [10].

	2	−1	−1	0	0	0	−0.4647
	−1	2	−1	0	0	0	−0.4647
	−1	−1	3	−1	0	0	−0.2610
	0	0	−1	3	−1	−1	0.2610
	0	0	0	−1	2	−1	0.4647
	0	0	0	−1	−1	2	0.4647

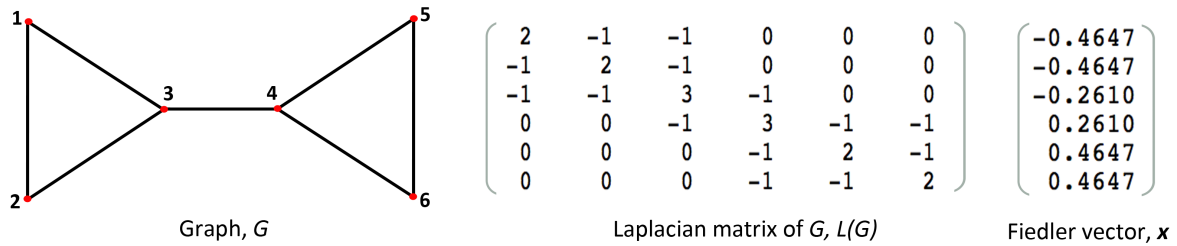Graph, *G*   Laplacian matrix of *G*, *L(G)*   Fiedler vector, *x*

Figure 1. Illustration of a graph *G*, its corresponding Laplacian matrix, *L(G)*, and the Fiedler vector, *x*. The algebraic connectivity of *G* is approximately 0.43.

The magnitude of the Fiedler value describes the *algebraic connectivity* among the elements of a network; a Fiedler value of zero indicates that the network is disconnected [12]. The Fiedler value may be used in conjunction with the number of edges and nodes to further describe the robustness of a network [11]. To evaluate robustness, we also computed the number of edges in each brain network, *E*, and the link (edge) density defined as *d=2E/N(N-1)*, because a decreasing edge density may indicate decreased robustness.

Another measure obtained from the eigenvalues of *L(G),* the number of λ_i=0, which reflects the number of disconnected components in the brain network [9]. The number of network components was further assessed with *modularity* computed using Newman's equations [2]. The algorithm efficiently defines an optimal community structure into non-overlapping sets of nodes such that the within group edges are maximized and the between-group edges are minimized. Essentially, modularity is a statistical evaluation of the degree to which the network may be subdivided to significantly delineated groups of nodes, $Q = \sum_{u\epsilon M}(E_{uu} - (\sum_{v\in M} E_{uv})^2)$, where *M* is a nonoverlapping module that the network is subdivided into, and E_{uv} is the proportion of links that connects nodes in module *u* to nodes in modules *v* [1, 2]. If *Q<0.3*, the community structure formed is not

significant as the within-community edges are close or equal to what would be expected by chance; however, $Q \geq 0.3$ signifies significant community structures [2].

To plot the algebraic connectivity we sorted brain network nodes as a function of the Fiedler vector; components in the brain were assigned to groups based on the magnitude of the eigenvector's corresponding component. This method is similar to *spectral partitioning* [6], however, in this study no partitions were added. Tools from the MIT Strategic Engineering website (http://strategic.mit.edu) were used for all calculations [9] excluding the modularity measure implemented from Newman [2] in the brain connectivity toolbox [1].

2.4 Statistical analyses

First, we assessed if the graph metrics (Fiedler value, total number of nodes, link density, the number of disconnected components and modularity) related to Mini Mental State Examination (MMSE) scores across all 202 participants using a random-effects regression, covarying for sex and using site as a grouping variable. As we cannot assume statistical normality for the network measures, nonparametric methods may be more appropriate. We performed $m=10,000$ permutations of the independent variable of interest (*i.e.*, MMSE or disease status), while maintaining covariates (sex and age and imaging site) true to the subject. Next, we generated permutation-corrected p-values using the following formula: $p=(b+1)/(m+1)$, where b is the number of randomized test statistics t_{perm} found to have a greater magnitude than the observed test statistic t_{obs}. By performing 10,000 permutations, the smallest possible permutation corrected p-value is 10^{-4}, so even if the observed p-value was much less than 10^{-4}, the lowest corrected p-value was 10^{-4}.

Next, we tested if any of the graph theory metrics that closely describe algebraic connectivity (*i.e.*, Fiedler value, link density and modularity) detected group differences between controls and the diseased groups by running a random-effects regression with controls coded as 0 and diseased participants coded as 1, covarying for age and sex and using the imaging site as a random-effects grouping variable, to eliminate confounding effects of the scan site. Then, 10,000 permutations of the independent value were performed as described above.

3. Results

MMSE scores – a measure of clinical decline – were significantly related to 5 of the network measures across all 202 participants. To adjust for multiple statistical tests, the significance threshold was set to 0.05/5 when testing associations of MMSE with 5 network measures. MMSE scores declined with a decreasing Fielder value ($p_{perm}<10^{-4}$) decreasing total number of edges ($p_{perm}<10^{-4}$) and decreasing link density ($p_{perm}<10^{-4}$). Meanwhile, as hypothesized, MMSE scores declined with an increasing number of disconnected components ($p_{perm}=3.2 \times 10^{-3}$) in the network and increasing modularity among network communities ($p_{perm}=3.4\times10^{-4}$). These disruptions led to a less robust and inefficient distribution of the brain's network components with advancing disease, and

were sorted here as a function of the eigenvectors corresponding to the Fiedler eigenvalue (**Fig. 1**). Also, brain regions that showed most frequent disconnections (0 eigenvalues) among diseased participants were those of the entorhinal, temporal and frontal poles bilaterally, in line with the sites that typically show the earliest AD pathology.
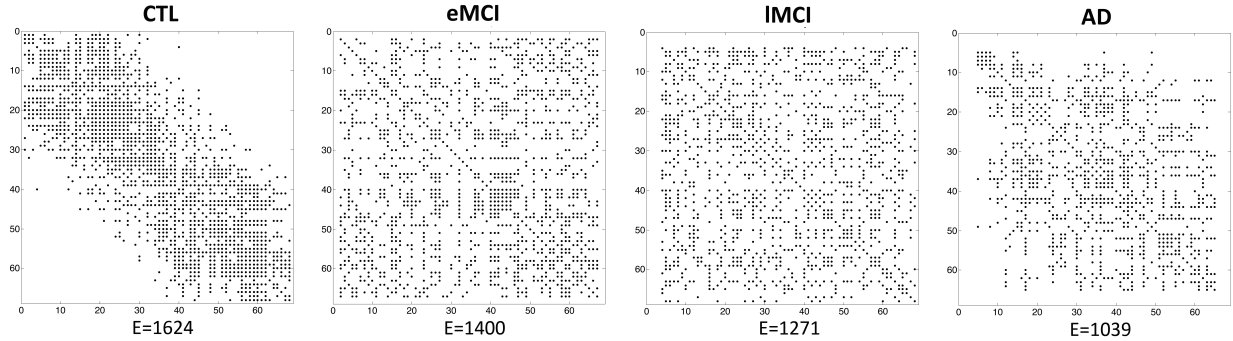

Figure 2. Sorted connectivity matrix as a function of the eigenvector corresponding to the Fiedler value (*i.e.*, second smallest eigenvalue) in one participant from each diagnostic group. E is the number of edges within each network. The plots indicate patterns of disarray with increasing numbers of disconnected components with disease progression; no completely disconnected components are shown in controls (CTL), but there are 2 in early MCI, 3 in late MCI and 5 disconnected components in AD.
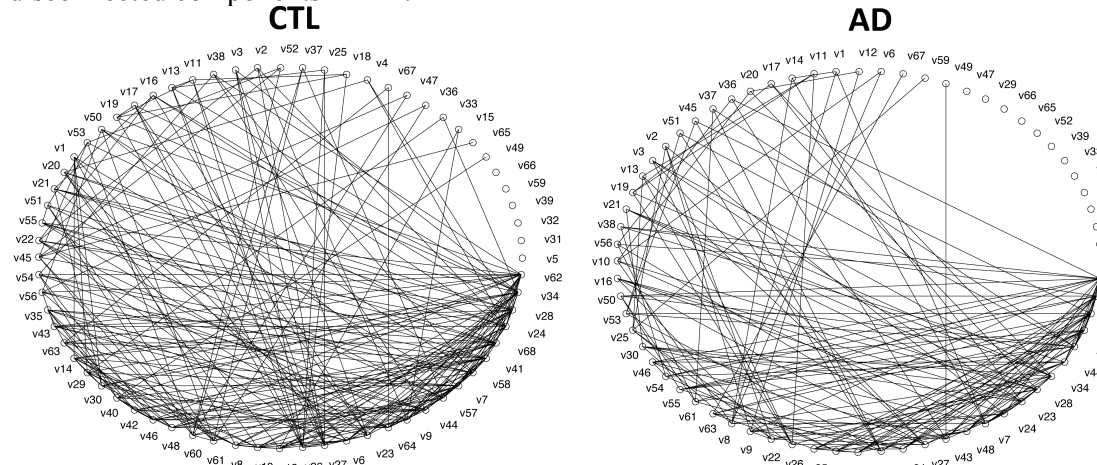

Figure 3. Circle drawings of nodes (*v1* through *v68*) interconnected by averaged edges across 50 controls (CTL) and 42 AD participants. The loss in link (edge) density across the nodes indicates decreased interconnectedness.

For the group comparisons, AD participants showed a significantly decreasing algebraic connectivity and a topological organization of the brain network that was different overall, relative to controls. Here, the significance threshold was set to 0.05/3, to adjust for testing 3 network metrics in the group comparison. The Fiedler value ($p_{perm}<10^{-4}$) and link density ($p_{perm}<10^{-4}$) was lower in AD, than in controls. Meanwhile, modularity increased in AD, relative to healthy elderly ($p_{perm}<10^{-4}$).

For group comparisons between lMCI and controls, the Fiedler value was the only measure to be significantly decreasing in lMCI, relative to healthy elderly (permuted *p-*

value=0.012). No significant differences were detected between eMCI and controls, although that group comparison is typically the most challenging among those we tested.

The average link density was 0.360 across all healthy elderly, 0.331 in eMCI and 0.333 in lMCI participants, and 0.304 in AD. This indicates that eMCI and lMCI had an 8.2-8.8% "less" interconnected network, under this metric, while the AD patients had a 15.7% less interconnected network.

4. Discussion

This study introduces the application of algebraic connectivity, with additional supporting neural metrics, to the analysis of brain connectivity. Here, we treated the networks as sets of nodes and edges and analyzed their interconnectedness based on associations with cognitive decline scores (*i.e.*, MMSE) and diagnostic group differences. We fused all steps of analysis together and reported an overall assessment of how and where in the brain Alzheimer's strikes.

The decline in algebraic connectivity, as indicated by the decreased Fiedler values with disease progression (as indicated by decreased MMSE scores), accompanied by the reductions in the density of connections among brain regions, highlights the loss of interconnectedness within the brain network. The diseased brains may be more vulnerable to losses in connections that allow communication between cortical regions, leading to a less robust neural network, at least according to these mathematical metrics. If brain connections were to be purged (lost altogether), eMCI and lMCI brain networks would disconnect approximately 8-9% more readily than healthy networks, while AD brain networks would disconnect approximately 16% more readily than controls. Cortical regions that contributed the most to the loss of nodes were located in the entorhinal areas – regions that typically degenerate early in AD [12, 13], and the temporal pole progressing into the frontal pole in the more impaired – also supported by previous studies [12]. Disconnections in these nodes may in turn impair connected nodes, as information transfer may be reduced accordingly.

Modularity computed on the original graphs (not the Laplacian) was used to verify the changes in network component assignments in disease. Modularity increased with disease progression indicating that the brain networks became more segregated (formed more modular structures) with a loss in connections between modules, leading to a less efficient distribution of the network overall (**Fig. 2**). Modular networks were less defined in controls at an average Q=0.34, with Q=0.36 in eMCI and lMCI and 0.39 in AD participants – leading to readily detectable disease differences.

The Fiedler value, link density, and modularity were sensitive to group differences in eMCI, lMCI and AD, versus controls (except for the Fiedler value that did not detect differences in eMCI, relative to controls). The direction of change for all these measures indicated an overall lower interconnectness for the diseased connectomes (**Fig. 3**).

Discovering changes in brain network organizational properties allows us to understand disease progression with additional detail. Most of these network algorithms have been successfully developed and applied for non-medical applications such as online

social interactions [9]; our study used these properties to study disease progression. We found that measures such as the Fiedler value - a measure of algebraic connectivity - was the most sensitive measure to detecting differences between disease groups and controls. Supporting network metrics, such as the number of edges, link density, the number of disconnected components, and modularity, validate and strengthen the results indicating a less robust and more segregated brain with increased cognitive impairment. As a limitation, we acknowledge that future studies should compare these new metrics with standard DTI-derived measures such as FA and MD, and other non-DTI or non-imaging biomarkers of AD, to determine what added predictive value they contain. At the same time, the network disruptions in disease are so complex that the added mathematical descriptors are likely to enhance our understanding of network dysfunction in the living brain.

References

1. Rubinov, M., Sporns, O.: Complex network measures of brain connectivity: uses and interpretations. **Neuroimage**. 52(3):1059-69. (2010)
2. Newman, M.E.: Fast algorithm for detecting community structure in networks. **Phys Rev E Stat Nonlin Soft Matter Phys**. 69(6 Pt 2):066133 (2004)
3. [Anonymous]

4. Desikan, R.S., Segonne, F., Fischl B., Quinn, B.T., Dickerson, B.C., Blacker, D., Buckner, R.L., Dale, A.M., Maguire, R.P., Hyman, B.T., Albert, M.S., Killiany, R.J..: An automated labeling system for subdividing the human cerebral cortex on MRI scans into gyral based regions of interest. **Neuroimage** 31(3):968-80 (2006)
5. Norman, B.: Algebraic Graph Theory (2nd ed.), Cambridge: Cambridge University Press (1993)
6. Mohar. B. The Laplacian spectrum of graphs. **Graph Theory, Combinatorics, and Applications**, 1991, Vol. 2: 1-28. (1991)
7. Hammond, D.K., Scherrer, B, Warfield, S.K.: Cortical graph smoothing: a novel method for exploiting DWI-derived anatomical brain connectivity to improve EEG source estimation. **IEEE Trans Med Imaging**. 32(10):1952–1963 (2013)
8. Chung, F.R.K., Faber, V., Manteuffel, T. A.: **SIAM J. Discrete Math**. 7, 443 (1994)
9. Bounova, G., de Weck, O.L.: Overview of metrics and their correlation patterns for multiple-metric topology analysis on heterogeneous graph ensembles. **Phys. Rev. E** 85, 016117 (2012).
10. Fiedler, M.: Algebraic connectivity of graphs, **Czechoslovak Math**. J. 23:298-305 (1973)
11. Jamakovic, A, van Mieghem, P.: On the Robustness of Complex Networks by Using the Algebraic Connectivity. Networking, Network ad-hoc and sensor networks, wireless networks, next generation Internet, Lecture Notes in Computer Science, vol. 4982, pp. 183-194 (2008)
12. [Anonymous]

13. Devanand, D.P., Pradhaban, G., Liu, X., Khandji, A., De Santi, S., Segal, S., Rusinek, H., Pelton, G.H., Honig, L.S., Mayeux, R., Stern, Y., Tabert, M.H., de Leon, M.J: Hippocampal and entorhinal atrophy in mild cognitive impairment: prediction of Alzheimer. **Neurology**. 13;68(11):828-36 (2007)

CHAPTER <u>5</u>

HARDI and brain asymmetry

5.1 Lateralization in the developmental connectome

This section is adapted from:

Daianu M, et al. Lateralization in the Developmental Human Connectome: 4-Tesla High Angular Resolution Diffusion Imaging (HARDI) Tractography in 576 Twins. IEEE ISBI 2012, pp. 526–529.

LEFT VERSUS RIGHT HEMISPHERE DIFFERENCES IN BRAIN CONNECTIVITY:
4-TESLA HARDI TRACTOGRAPHY IN 569 TWINS

*Madelaine Daianu[1], Neda Jahanshad[1], Emily L. Dennis[1], Arthur W. Toga[1], Katie L. McMahon[2],
Greig I. de Zubicaray[3], Nicholas G. Martin[4], Margaret J. Wright[2,4], Ian B. Hickie[5], Paul M. Thompson[1]*

[1]Laboratory of Neuro Imaging, Department of Neurology, UCLA School of Medicine, Los Angeles, CA
[2]Centre for Advanced Imaging, and [3]School of Psychology, University of Queensland, Brisbane, Australia
[4]Queensland Institute of Medical Research, Brisbane, Australia
[5]University of Sydney, Brain and Mind Research Institute, Australia

ABSTRACT

Diffusion imaging can map anatomical connectivity in the living brain, offering new insights into fundamental questions such as how the left and right brain hemispheres differ. Anatomical brain asymmetries are related to speech and language abilities, but less is known about left/right hemisphere differences in brain wiring. To assess this, we scanned 457 young adults (age 23.4±2.0 SD years) and 112 adolescents (age 12-16) with 4-Tesla 105-gradient high-angular resolution diffusion imaging. We extracted fiber tracts throughout the brain with a Hough transform method. A 70x70 connectivity matrix was created, for each subject, based on the proportion of fibers intersecting 70 cortical regions. We identified significant differences in the proportions of fibers intersecting left and right hemisphere cortical regions. The degree of asymmetry in the connectivity matrices varied with age, as did the asymmetry in network topology measures such as the small-world effect.

***Index terms** –* tractography, high angular resolution diffusion imaging (HARDI), small-world effect, connectome, laterality

1. INTRODUCTION

Diffusion MRI, and its extensions such as high angular diffusion imaging (HARDI), can be used to infer patterns of anatomical connectivity in the living brain [10]. Connectivity studies are now being extended to even larger populations, offering ever-increasing power to identify characteristic patterns of brain wiring in psychiatric and neurological disorders [6]. Surprisingly, many fundamental questions are still unanswered, such as whether the left and right brain hemispheres differ in connectivity. By contrast, morphometric brain asymmetry has been intensively studied [3].

Graph theory [10] is a powerful branch of mathematics that is increasingly applied to study how neural networks are organized. Several network topology measures have identified highly connected hubs in the brain [3]. Its anatomical and functional connections are organized as "small-world" networks and are highly modular [3]. Signs of network efficiency - such as a high clustering coefficient and short average path length - are related to intellectual function in high-density resting state EEG [7]. Full-scale IQ is also related to small-world properties in networks derived from diffusion tensor tractography [9]. Network connectivity measures may therefore offer insights into efficient information transfer in the brain [9].

Morphometric asymmetries are widely recognized for Sylvian fissure morphology and the volumes of language-related cortices such as the *planum temporale* [14]. Given these known asymmetries, which may also influence neural connectivity, we set out to use HARDI in a large cohort to find areas with left/right hemisphere differences in fiber density. We also aimed to identify

left/right differences in global network properties, such as clustering coefficient, characteristic path lengths and nodal strength. Some models of Alzheimer's disease suggest that the hemispheres may degenerate at different rates due to differences in network connectivity [13], but data on this question has been lacking.

To address this, we scanned 569 subjects (112 adolescents and 457 young adults) with HARDI and extracted tracts throughout the brain using a HARDI tractography algorithm based on the Hough transform [1]. The tractography method used orientation density functions to provide higher order models of the diffusion process, capturing fiber crossings that might be missed if a single-tensor diffusion model is assumed [6]. Connection matrices were created to represent the proportion of brain connections interconnecting 70 cortical regions of interest, defined automatically in co-registered anatomical scans. Patterns of interhemispheric (left/right) asymmetries in the connection matrices were assessed statistically.

Furthermore, we used a set of MATLAB toolbox functions (BCT; https://sites.google.com/a/brain-connectivity-toolbox.net/) to analyze network topology for the right and left hemispheres, separately. We also tested if brain laterality depended on age, as the gross anatomical asymmetry of the brain increases with age, well into adolescence [12].

2. METHODS

2.1. Subjects and image acquisition

We scanned 457 right-handed young adults (mean age, 23.4±2.0 SD years) and 112 right-handed adolescents (age 12-16) with 4T HARDI and standard T1-weighted structural MRI. The participants were all twins, but genetic aspects are not considered further here. MR images were collected at the Center for Magnetic Resonance (University of Queensland) with a 4-Tesla Bruker Medspec MRI scanner (Ettingen, Germany) using a transverse electromagnetic (TEM) headcoil. T1-weighted imaging used an inversion recovery rapid gradient echo sequence with parameters: TI/TR/TE=700/1500/3.35 ms, flip angle=8°, slice thickness = 0.9 mm, and a 256x256 acquisition matrix. Diffusion-weighted images were acquired using single-shot echo planar imaging with a twice-refocused spin echo sequence to reduce eddy-current induced distortions with imaging parameters: TR/TE 6090/91.7 ms, 23 cm FOV, with a 128×128 acquisition matrix. Each 3D volume consisted of 55 2-mm thick axial slices with no gap, and a 1.79×1.79 mm^2 in-plane resolution.

We acquired 105 images per subject: 11 with no diffusion sensitization (i.e., T2-weighted b_0 images) and 94 diffusion-weighted (DW) images (b = 1159 s/mm^2) with gradient directions

evenly distributed on the hemisphere, for unbiased directional sampling of the diffusion propagator. Scan time was 14.2 minutes.

2.2. DWI preprocessing, cortical surface extraction and registration

We preprocessed the data by automatically removing non-brain tissue from each T1-weighted MRI scan, using ROBEX [5] as well as from a T2-weighted image from the DWI set, using the FSL tool "BET" (http://fsl.fmrib.ox.ac.uk/fsl/). T1-weighted images were linearly aligned using FSL (with 9 DOF) to a common space [9] with 1mm isotropic voxels and a 220×220×220 voxel matrix. Raw diffusion-weighted images were corrected for eddy current distortions using FSL's "eddy_correct" (http://fsl.fmrib.ox.ac.uk/fsl/). For each subject, the 11 eddy-corrected images with no diffusion sensitization were averaged, linearly aligned and resampled to a downsampled version of their corresponding T1 image (110×110×110, 2×2×2mm). Averaged b_0 maps were elastically registered to the structural scan using a mutual information cost function [8] to compensate for EPI-induced susceptibility artifacts.

2.3. HARDI tractography

The transformation matrix from linearly aligning the mean b_0 image to the T1-weighted volume was applied to each of the 94 gradient directions to properly re-orient the orientation distribution functions (ODFs). At each HARDI voxel, ODFs were computed using the normalized and dimensionless ODF estimator, derived for QBI in [13]. This approach considers the Jacobian factor r^2 to compute the constant solid angle (CSA) ODF:

$$\underset{\text{in CSA-QBI}}{ODF}(\hat{u}) \approx \frac{1}{4\pi} + \frac{1}{16\pi^2}\text{FRT}\left\{\nabla_b^2 \ln\left(-\ln\frac{S(\hat{u})}{S_0}\right)\right\}$$

Here $S(\hat{u})$ is the diffusion signal, and S_0 is the baseline image. FRT is the Funk-Radon transform and ∇_b^2 is the Laplace-Beltrami operator. We used this ODF reconstruction scheme as it improves the resolution of multiple fiber orientations [13] relative to the original QBI definition [14]. With this set of ODFs, we performed HARDI tractography on the linearly aligned DWI volumes.

Tractography was performed by seeding voxels with a prior probability based on the fractional anisotropy (FA) value derived from the single-tensor model [2]. All curves passing through a seed point receive a score estimating the probability of the existence of the fiber, computed from the ODFs. A voting process provided by the Hough transform determined the best fitting curves through each point [1].

Elastic deformations obtained from the EPI distortion correction, mapping the average b_0 image to the T1-weighted image, were then applied to the tract's 3D coordinates. Fibers with fewer than 15 points were filtered out. Each subject's dataset contained 5000-10,000 useable fibers (3D curves).

2.4 Left and right hemisphere matrix analysis

A 70x70 connectivity matrix was created for each subject. The elements of this matrix represented the proportion of fibers connecting all cortical regions, within and across hemispheres; the key to these 70 regions is in [6]. To avoid applying statistical analysis to unreliable or incorrectly extracted connections, any connection was considered *invalid* if it was only found in less than 95% of the subjects.

We analyzed the left and right hemispheres individually for all 569 subjects and computed several network measures (clustering coefficient, characteristic path length, directed strengths and small-world effects) for each hemisphere using the BCT. We fitted a random effects regression model to all subjects testing for differences between the left and right hemispheres and age effects between the left and right hemisphere connectivity matrices and scalar measures of brain connectivity. Correlated samples may arise in the tractography maps as individuals in the same family are related; therefore, we used random effects regression to correctly account for kinship and group the subjects by family. A random intercept was included for each family. Hemispheric differences were assessed after covarying for any effect of age and sex at each valid matrix connection. Moreover, we computed the element-wise difference matrix between the left and right hemispheres. In this case, BCT measures can still be applied but have a different meaning; they can identify the direction of the asymmetry (i.e., L>R or R>L) for all valid connections.

2.5 Clustering coefficient, characteristic path length, nodal strength and small-world effect

In graph theory, a connection matrix may be compiled that describes the topology of a network and consists of nodes and edges [11]. Nodes are represented as matrix rows and columns and the edges are the matrix entries [11]. The degree of a node, i, can be derived from the connection matrix:

$$k_i = \sum_{j \in N} a_{ij}$$

Here, (i,j) represents a link between nodes i and j, while a_{ij} is the connection status between nodes i and j.

The functional contribution of a node, and its interactions with neighboring nodes, is determined by computing the network's *clustering coefficient*. This measures the density of the interconnected neighbors of individual nodes [11]:

$$C = \frac{1}{n}\sum_{i \in N} C_i = \frac{1}{n}\sum_{i \in N} \frac{2t_i}{k_i(k_i - 1)}$$

C_i is the clustering coefficient of node i (C_i=0 for k_i<2) and t_i is the number of triangles around node, i:

$$t_i = \frac{1}{2}\sum_{j,h \in N} a_{ij}a_{ih}a_{jh}$$

The 'triangles' around node i, are the fraction of fully connected 3-nodes, which is equivalent to the clustering coefficient [11]. The clustering coefficient was computed from the left hemisphere 35x35 matrix, $C_L(x,y)$, and right hemisphere 35x35 matrix, $C_R(x,y)$. The left and right hemisphere matrices are undirected graphs and the difference between the two is defined by the laterality matrix, $A(x,y)=C_L(x,y)-C_R(x,y)$. If this matrix is thresholded to retain only connections exceeding some positive laterality threshold, then it becomes a directed graph. In directed networks, such as the asymmetry matrix $A(x,y)$, the incoming and outgoing edges make up the indegree ($k_i^{IN} = \sum_{j \in N} a_{ji}$) and outdegree ($k_i^{OUT} = \sum_{j \in N} a_{ij}$) of the network. The nodal strength is the sum of all edge weights of a node [11].

The characteristic path length, where L_i is the average distance between node, i, and all other nodes, is the number of distinct edges [11] in a network.

$$L = \frac{1}{n}\sum_{i \in N} L_i = \frac{1}{n}\sum_{i \in N} \frac{\sum_{j \in N, j \neq i} d_{ij}}{n - 1}$$

The small-world effect, S, is the ratio between the clustering coefficient and the characteristic path length after both measures are normalized relative to corresponding values obtained from randomized networks [11]. A small-world effect measure significantly greater than one indicates the coexistence of a high clustering coefficient and short path length [11].

$$S = \frac{\frac{C}{C_{rand}}}{\frac{L}{L_{rand}}}$$

3. RESULTS

We fitted a random effects regression model to all 569 subjects testing for differences between left vs. right hemispheres (using zeros for the left hemisphere and ones for the right hemisphere) to determine any differences between the left and right hemisphere connectivity matrices and the scalar measures of brain connectivity (clustering coefficient, nodal strength, characteristic path length and small-world effect). This set-up essentially served as a paired *t*-test as the random effects model accounts for the family relatedness between the twin subjects. We first tested the difference between the left, $C_L(x,y)$, and right, $C_R(x,y)$, hemisphere connectivity matrices in all 569 subjects using random effects regression (**Fig. 1**). The test returned significant differences between the left and right hemispheres at almost all cortical connections (FDR critical *p*-value=0.043). Some of the significant differences were between cortical regions 18, *pars opercularis*, 19, *pars orbitalis*, and 20, *pars triangularis*. These regions are of note as they form part of Broca's area, which is functionally specialized for speech production in the left hemisphere, and has known morphometric asymmetries. Even so, regions with connectivity differences extended well beyond the systems most typically studied for morphometric asymmetries. These results led us to further analyze left-right differences in the scalar measures of brain connectivity.

To determine the differences between the left and right hemisphere brain connectivity measures in all 569 subjects, we ran the random effects regression as described above and found left-right differences in the clustering coefficient ($p<0.034$), characteristic path length ($p<2.42\times10^{-10}$) and nodal strength ($p<0.041$). The differences between the left and right hemispheres were seen in 28 cortical regions for the nodal clustering coefficient measure, 1 cortical region for the characteristic path length and 30 cortical regions for the nodal strength. Of all these, cortical region 18, the *pars opercularis*, was significant for all measures.

The Pearson correlation between the clustering coefficients of the left and right hemispheres was significant (see above) but not high: 0.21 in adolescents and 0.33 in adults. Interestingly, the characteristic path length showed much higher correlations between left and right hemispheres: 0.49 in adolescents and 0.78 in adults. The global clustering coefficient and characteristic path length jointly determine the small-world effect. For this, a global clustering coefficient was computed by taking the mean of all local clustering coefficients for each of the adolescents and adults respectively. The ratio of the global clustering coefficient to the characteristic path length for the left and high hemisphere connection matrices is the small-world effect and is shown in **Figure 3**.

To see if the laterality matrix, $A(x,y)$, depended on age, a random effects regression was run across all subjects and an FDR critical *p*-value of 0.017 was found. We analyzed the beta maps to determine the asymmetry shift between the left and right hemisphere. *Beta*-values (or the slope of the regression) for significant age effects are plotted element-wise in **Figure 2**, which was masked by the significant and thresholded *p*-values obtained from the random effects regression between the left and right connectivity matrices (**Fig. 1**). The masked *beta*-value map consisted of 235 negative values and 229 positive values showing that the right hemisphere has more fibers with age. Significant age

effects were also found when analyzing the laterality matrix between left and right hemisphere nodes. Within these connections, many (but not all) nodes were within regions with acknowledged morphometric asymmetry, such as the *pars triangularis* and *pars opercularis*.
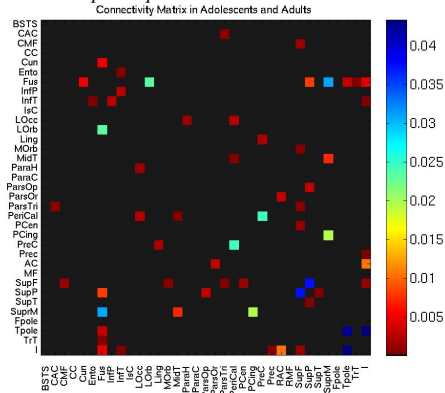

Figure 1. *P*-values from the random effects regression model (using zeroes for the left hemisphere and ones for the right hemisphere) comparing the left, $C_L(x,y)$, and right, $C_R(x,y)$, hemisphere connectivity matrices in 112 adolescents and 457 adults (FDR critical *p*-value=0.0433; higher critical values denote stronger effects).
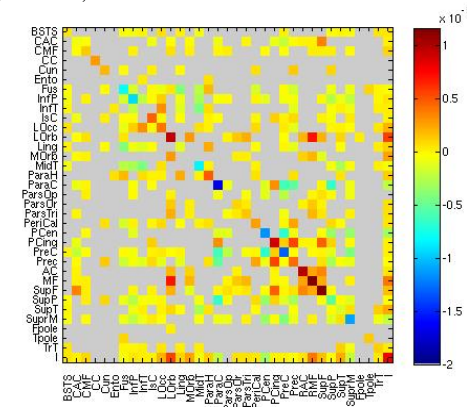

Figure 2. *B*-values from a random effects regression at each element of the difference matrix between the left and right connectivity matrices, $A(x,y)= C_L(x,y) - C_R(x,y)$, masked by the significant *p*-values from the random effects regression between the left and right hemispheres (**Fig. 1**). The gray values denote non-significant *b*-values. There are more significant negative *b*-values (235) than positive *b*-values (229), suggesting that the relative density of fibers in the right hemisphere increases with age.

1	Banks of the superior temporal sulcus	19	*Pars orbitalis*
2	Caudal anterior cingulate	20	*Pars triangularis*
3	Caudal middle frontal	21	Peri-calcarine
4	Corpus callosum	22	Postcentral
5	Cuneus	23	Posterior cingulate
6	Entorhinal	24	Pre-central
7	Fusiform	25	Precuneus
8	Inferior parietal	26	Rostral anterior cingulate
9	Inferior temporal	27	Rostral middle frontal
10	Isthmus of the cingulate	28	Superior frontal
11	Lateral occipital	29	Superior parietal
12	Lateral orbitofrontal	30	Superior temporal
13	Lingual	31	Supra-marginal
14	Medial orbitofrontal	32	Frontal pole
15	Middle temporal	33	Temporal pole
16	Parahippocampal	34	Transverse temporal
17	Paracentral	35	Insula
18	*Pars opercularis*		

Table 1. Index of cortical areas extracted from FreeSurfer.

Significant age effects were found for the clustering coefficient (the overall summary measure) in both the left and right hemispheres. In the left hemisphere, there were effects of age on fiber organization of the clustering coefficient measures at 17 nodes: 2, 3, 8, 9, 10, 11, 14, 16, 17, 18, 20, 22, 23, 24, 27, 29, and 31 (**Table 1**). Similarly, in the right hemisphere, the age effects were found at 14 nodes: 3, 5, 11, 12, 14, 15, 19, 20, 21, 22, 23, 26, 27 and 28.

Age differences were found in the analysis of the characteristic path length measure for the right and left hemispheres in cortical region 1. For the nodal strength measure, age effects were found at 22 nodes in the left hemisphere at regions: 1, 2, 3, 7, 8, 9, 11, 12, 14, 15, 16, 17, 18, 20, 22, 23, 24, 27, 29, 31, 34 and 35, and at 16 nodes in the right hemisphere at regions: 2, 3, 5, 9, 11, 12, 14, 19, 20, 21, 22, 23, 26, 27, 28 and 35. The banks of the superior temporal sulcus are part of this list (region 1), consistent with our prior findings of changing perisylvian asymmetry in adolescence [12].
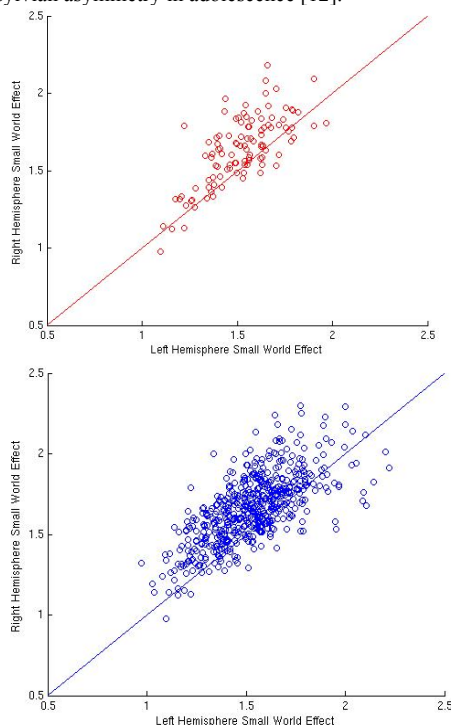

Figure 3. The level of "smallworldness" for the left and right hemispheres is shown for 112 adolescents (*top, red*) and 457 adults (*bottom, blue*). This measure is the ratio of the global clustering coefficient to the characteristic path length, computed from binarized connectivity matrices for the left and right hemispheres. As expected, network topology measures are highly correlated between left and right hemispheres. Small-world organization is more evident in the right hemisphere.

The directional matrix between the left and right hemisphere, $A(x,y)$, also showed sex differences, so sex may interact with the level of brain asymmetry (in line with prior reports of small but detectable sex differences in asymmetry and connectivity [6]). These results are omitted due to space limits.

4. DISCUSSION

We used 94-direction high-angular resolution images (HARDI) in 569 individuals at 4 Tesla to trace fiber tracts throughout the brain, with orientation distribution function (ODF) based tractography. This allowed valid pursuit of the diffusion propagator where fibers mix or cross. After cortical labels were extracted automatically from co-registered surface models the interhemispheric connections were studied using statistical analysis of the binary directed connection matrices extracted from each brain.

Regions with connectional asymmetry, or with significant age effects on this asymmetry, are scattered all over the brain. Regions with well-known morphometric asymmetry, such as the *pars opercularis* (a region specialized for speech in the left hemisphere) also showed asymmetric connections, but the connectional asymmetry was by no means limited to well-studied temporal and parietal language areas where morphometric asymmetry is widely documented [14]. Based on the results shown by the *beta*-map (**Fig. 2**) there is an increase in the relative fiber density favoring the right hemisphere over time (or the brain becomes more asymmetric towards the right hemisphere with age). Also, the small world effect was more evident in the right hemisphere (**Fig. 3**).

REFERENCES:

[1] Aganj I, *et al*. "A Hough transform global probabilistic approach to multiple-subject diffusion MRI tractography." *Med Image Anal* 2011;15(4): 414-25.

[2] Basser PJ and Pierpaoli C, "Microstructural and physiological features of tissues elucidated by quantitative-diffusion-tensor MRI." *J Magn Reson B* 1996;111:209-19.

[3] Bullmore E and Sporns O. "Complex brain networks: graph theoretical analysis of structural and functional systems." *Nature* 2009;10:186-198.

[4] Fischl B, *et al*. "Automatically parcellating the human cerebral cortex." *Cereb Cortex* 2004;14:11-22.

[5] Iglesias JE, Liu CY, Thompson PM *et al*. "Robust brain extraction across datasets and comparison with publicly available methods." *IEEE Trans Med Imaging* 2011;30(9):1617-34.

[6] Jahanshad N, *et al*. "Sex differences in the human connectome: 4-Tesla high angular resolution diffusion imaging (HARDI) tractography in 234 young adult twins." *IEEE Xplore* 2011;939-943.

[7] Langer N, *et al*. "Functional Brain Network Efficiency Predicts Intelligence." *Human Brain Mapping* 2011 May 9. doi: 10.1002/hbm.21297.

[8] Leow A, *et al.*, "Inverse consistent mapping in 3D deformable image registration: its construction and statistical properties." *Inf Proc Med Imaging* 2005;19:493-503.

[9] Li Y, *et al*. "Brain Anatomical Network and Intelligence." *PLoS Computational Biology* 2009;5(5):1-17.

[10] Rubinov M and Sporns O. "Complex network measures of brain connectivity: Uses and interpretations." *NeuroImage* 2010;52:1059–1069.

[11] Sporns O. *Networks of the Brain*. Cambridge, MA, 2011;5-31.

[12] Sowell ER *et al*. (2002). "Mapping Sulcal Pattern Asymmetry & Local Cortical Surface Gray Matter Distribution In Vivo: Maturation in Perisylvian Cortices." *Cereb. Cortex* 2002;12(1):17-26.

[13] Thompson PM *et al*. "Dynamics of Gray Matter Loss in Alzheimer's Disease." *J. Neurosci*. 2003;23(3):994-1005.

[14] Toga AW, Thompson PM (2003). "Mapping Brain Asymmetry." *Nature Reviews Neurosci.* 2003;4(1):37-48.

CHAPTER 6

Disease risk genes and altered connectivity

6.1 Multi-modal imaging and the Alzheimer' disease risk genes

This section is adapted from:

Neuroimaging and genetic risk for Alzheimer's disease and addiction-related degenerative brain disorders

Florence F. Roussotte · Madelaine Daianu ·
Neda Jahanshad · Cassandra D. Leonardo ·
Paul M. Thompson

Abstract Neuroimaging offers a powerful means to assess the trajectory of brain degeneration in a variety of disorders, including Alzheimer's disease (AD). Here we describe how multi-modal imaging can be used to study the changing brain during the different stages of AD. We integrate findings from a range of studies using magnetic resonance imaging (MRI), positron emission tomography (PET), functional MRI (fMRI) and diffusion weighted imaging (DWI). Neuroimaging reveals how risk genes for degenerative disorders affect the brain, including several recently discovered genetic variants that may disrupt brain connectivity. We review some recent neuroimaging studies of genetic polymorphisms associated with increased risk for late-onset Alzheimer's disease (LOAD). Some genetic variants that increase risk for drug addiction may overlap with those associated with degenerative brain disorders. These common associations offer new insight into mechanisms underlying neurodegeneration and addictive behaviors, and may offer new leads for treating them before severe and irreversible neurological symptoms appear.

Keywords Alzheimer's disease · Imaging genetics · Multi-modal imaging · Neurodegeneration · Addiction

Florence F. Roussotte and Madelaine Daianu contributed equally to this work.

F. F. Roussotte · M. Daianu · N. Jahanshad · C. D. Leonardo ·
P. M. Thompson (✉)
Imaging Genetics Center, Laboratory of Neuro Imaging, Department of Neurology, David Geffen School of Medicine at UCLA, 635 Charles E. Young Drive South, Suite 225E, Los Angeles, CA 90095-7332, USA
e-mail: thompson@loni.ucla.edu

P. M. Thompson
Department of Psychiatry and Biobehavorial Sciences, Semel Institute, David Geffen School of Medicine at UCLA, Los Angeles, CA, USA

Introduction

Alzheimer's disease (AD) is a progressive, degenerative brain disease affecting around 1 in 8 people (13 %) aged 65 or older (Alzheimer's Association 2011). AD has alarming consequences for society: the number of AD patients is expected to triple by 2050, increasing health care costs by an estimated 85 % (Bruner and Jacobs 2013). A century after the first reports of AD, we still do not fully understand what causes it, nor what is needed to treat it successfully (Hua et al. 2008; Braskie et al. 2012; Bruner and Jacobs 2013).

In AD, many cognitive domains progressively decline, including memory (Filippi et al. 2012). This cognitive decline is promoted by a combination of age-related brain changes and by progressive deposition of beta-amyloid and tau proteins in the brain. The beta-amyloid aggregate can induce inflammation and neurotoxicity (Wang et al. 2012a) while tau proteins can lead to neuronal atrophy and finally, cell death (Fasulo et al. 2002). As neurons are lost, the brain's gray matter shows widespread atrophy, visible on a structural T1-weighted MRI scan (also referred to as structural MRI). At the same time, the white matter volume is reduced, reflecting loss of myelin and axons in the neural fiber tracts (Braak and Braak 1996).

Many neuroimaging studies have assessed brain degeneration in AD by scanning patients and healthy elderly controls, and, in many cases, people with early or late mild cognitive impairment (MCI)—an intermediate state with heightened risk of developing AD. Changes in cognitive performance correlate with characteristic patterns of change in brain structure and function, making it possible to characterize typical patterns of disease progression based on in vivo scans. With high-resolution structural MRI, we can quantify brain atrophy; software tools can map the profile of cortical gray matter thinning, and volume loss in subcortical structures. PET scans can reveal

Ⓐ Springer

the pattern of plaques and tangles in the living brain, based on using specialized radiotracer ligands, sensitive to amyloid or tau proteins (Wong et al. 2010; Teng et al. 2011; Mathis et al. 2012; Wolk et al. 2012). A progressive breakdown of the brain's fiber networks may also contribute to cognitive decline in AD. In the most common approach for assessing the white matter, "FLAIR" or T2-weighted MRI scans are used to evaluate the volume or distribution of white matter hyperintensities—a radiological sign of stroke or cerebrovascular disease. More recently, newer methods, such as diffusion-weighted imaging (DWI) and resting-state functional MRI (fMRI), have emerged to assess brain connectivity. These methods reveal how anatomical and functional networks reorganize and break down in degenerative diseases (Delbeuck et al. 2003; Buckner et al. 2005; Gili et al. 2011; Wegrzyn et al. 2012; Daianu et al. 2012; Daianu et al. 2013).

Over half of our risk for developing AD is due to genetic factors, with heritability estimates in the range of 58–74 % (Bergem et al. 1997; Gatz et al. 1997; Braskie et al. 2011a). Many specific genetic markers have been discovered that are associated with Alzheimer's disease risk (Naj et al. 2011). Historically, these genetic discoveries have been made through genome-wide association scans, or linkage studies, in groups of patients and cognitively healthy controls. Association studies, in particular, are designed to identify common genetic variants that are over- or under- represented in diseased populations.

Case–control genome-wide association studies (GWAS) have revealed a large number of genetic variants that have now been consistently associated with AD, and have held up in meta-analyses of a large number of studies worldwide (Nussbaum 2013). These studies typically use widely-agreed GWAS practices that include quality control of genotyping, testing for population stratification and imputation—merging data collected using different genotyping platforms with different sets of variants (Nussbaum 2013); these approaches help to avoid false positive and false negative associations, and improve the design of the case–control association studies. As with other GWAS studies of complex diseases, large sample sizes are needed to ensure adequate power to detect genetic associations. Successful studies often require tens of thousands or even upwards of a hundred thousand subjects (Rietveld et al. 2013, Speliotes et al. 2010), which can be difficult to amass for more costly phenotypes. Therefore, one alternative approach to discover genetic variants that affect disease risk is to use the endophenotype approach (Gottesman and Gould 2003); endophenotypes are indicators of brain structure or function that index genetic liability for disease (Glahn et al. 2007). For example, one can use neuroimaging biomarkers as quantitative traits to search the genome for variants that affect them (Glahn et al. 2007); this is one

key line of work in the promising field of *imaging genetics*. Imaging genetics may also offer a better understanding of the pathways and mechanisms involved in the dynamic interplay of genes, brain, and environment to shape variability in behavior and disease risk (Munoz et al. 2010). A logical and effective initial screen would be to determine which brain measures serve as good endophenotypes based on the heritability of the trait and how it associates with disease (see Glahn et al. (2012) for an endophenotype ranking method). While much work is still being conducted in the field, improved endophenotypes can be discovered by first identifying novel biomarkers for disease and secondly using these and existing biomarkers for genetic discoveries.

Another less explored approach is to understand how brain differences are associated with carrying genetic variants that are associated with multiple disorders, as our group did in (Roussotte et al. 2013). The patterns of brain tissue loss and atrophy are quite similar, at least at the gross anatomical level, in people who abuse drugs and in AD patients, as Fig. 1 illustrates. In recent years, it was found that some genes that affect our risk for neurodegeneration are also implicated in risk for substance abuse (as discussed below). This discovery led some investigators to challenge the more traditional assumption (supported by a range of studies, e.g., Thompson et al. 2004) that brain atrophy in drug addicts only results from chronic exposure to drugs of abuse. A provocative hypothesis is that those at genetic risk for addiction may also harbor latent processes that contribute to neurodegeneration later in life, whether or not those people do abuse drugs.

Several neurotransmitter transporters and receptors are now known to be involved in the etiology or pathophysiology of both degenerative brain disorders such as Alzheimer's disease and substance abuse disorders. Examples include the delta opioid receptors. These receptors involved in drug addiction are coded by the *OPRD1* gene, which also harbors several single-nucleotide polymorphisms (common genetic variants) that are associated with risk for substance abuse disorders (Levran et al. 2012). Delta opioid receptors also play important roles in learning and memory, and are down-regulated in specific regions of the brain in Alzheimer's disease (Thathiah and De Strooper 2011). In a mouse model of AD, administration of a selective DOR antagonist improved spatial learning and reference memory, and reduced amyloid plaque burden (Teng et al. 2010). Similarly, in vivo knock-down of the DOR reduced amyloid-β_{40} accumulation in the hippocampus of an AD mouse model (Teng et al. 2010).

There are other examples of neurotransmitter transporters and receptors involved in the etiology of both Alzheimer's
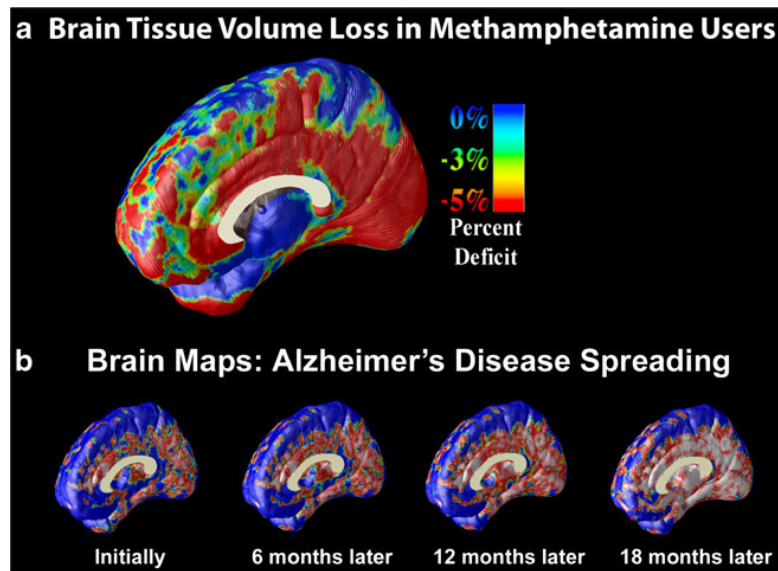
Fig. 1 Similarities in brain tissue loss between stimulant abusers and Alzheimer's patients. **a** Brain tissue (*gray* matter) deficits in methamphetamine abusers, relative to healthy adults, mapped using T1-weighted MRI scans. Frontal and limbic brain regions involved in drug craving, emotion and reward, and hippocampal regions involved in learning and memory, show deficits of up to 5 % in gray matter density. Red colors denote brain regions with greatest deficits, blue colors regions that remain relatively intact. [Adapted, with permission of the authors, Thompson et al. 2004—and publishers]. **b** Brain tissue loss in Alzheimer's disease patients, relative to average healthy elderly over time, interpolated and inferred using longitudinal T1-weighted MRI scans. These are frames from a time-lapse film computed from MRI; by contrast with Panel A, the maps in this panel represent *p*-values (showing the significance of the group difference) between a group of AD patients and controls. *Red colors* denote brain regions with greatest tissue loss. The deficits in temporo-parietal and hippocampal territory spread into the cingulate and frontal lobes over time, with some apparent similarities with brain tissue deficits associated with drug abuse. [Adapted, with permission of the authors, Thompson et al. 2003—and publishers]

disease and drug addiction, including SLC1 glutamate transporters. These include excitatory amino-acid transporters (EAATs), whose role is to terminate the excitatory signal by re-uptake of glutamate from the neuronal synapse into neuroglia and neurons. Dysfunction of EAATs can cause abnormal excitatory synaptic transmission and excitotoxicity, and they have been implicated in the etiology of Alzheimer's disease and drug dependence (Nakagawa and Kaneko 2013). Another instance is the human sigma-1 receptor (S1R), which was once thought to be a type of opioid receptor, but is now considered to belong to a separate class of receptors. S1R activity and dysfunction is implicated in several diseases of the central nervous system including Alzheimer's disease and drug abuse (Ortega-Roldan et al. 2013). These receptors play important roles in plasticity underlying reinforcement and addictive processes (Maurice and Su 2009). Moreover, S1R receptor ligands show some neuroprotective activity against amyloid toxicity (Marrazzo et al. 2005). Understanding commonalities in the genetic and neuroanatomical pathways of these genetically modulated disorders may help shed light on the pathogenesis of neurological disease and drug addiction.

In this review, we describe a range of biomarkers of Alzheimer's disease, including newer methods that examine and quantify structural brain connectivity. We show how these new biomarkers (brain measures) can be used to discover genetic markers that associate with neuroanatomical variations, and then their role in disease risk can also be evaluated. Next, we review the role that neuroimaging has played in mapping out effects of specific AD-associated genes on the brain, highlighting brain regions where risk gene carriers may first begin to show signs of derailment. Finally, we discuss some neurodegenerative risk genes related to addiction, how they affect brain structure, and how this line of research may help us understand the neurodegenerative process and the genes that put us all at risk.

Multi-modal neuroimaging for the study of Alzheimer's disease

AD was called a "disconnection syndrome" by Geschwind (1965) as patients often show neuropsychological deficits that suggest a worsening anatomical and functional disconnection between brain regions (Wernicke 1874/1977; Lichtheim 2006). Evidence for this disconnection is evident from a variety of structural and functional imaging methods including structural MRI, fMRI, DWI, PET, electrophysiology (EEG) and more. In structural MRI studies, AD patients have widespread cortical atrophy, severe tissue loss in

the hippocampus and medial temporal lobes (often by 10–20 %) and expansion of the ventricular and sulcal cerebrospinal fluid spaces (Ewers et al. 2011). To better understand degenerative brain changes, combined structural and functional information is helpful, as well as other multi-modal analyses. Multi-modal imaging can confirm links between brain changes and other blood or CSF biomarkers (Braskie et al. 2010). Neuroimaging can also be used to help predict disease progression in individuals or groups of subjects (Zhang et al. 2012), study treatments effects on the brain (Schmidt et al. 2008) and how genetic and anatomical variations relate to brain function (Wang et al. 2012a, b).

The cumulative effects of neural shrinkage and cell death, as well as intracortical myelin reduction and neuropil loss can be measured with cortical thickness mapping methods and high-resolution 3D volumetric MRI (Duyckaerts and Dickson 2003). One of the more sophisticated techniques, *cortical pattern matching* (Thompson et al. 2003), relies on aligning cortical sulci and gyri identified by hand to a reference template. Subsequently, statistical modeling can reveal the 3D pattern of group differences in cortical thickness, or cognitive differences—such as memory decline or apathy—that statistically relate to some of the changes. Cortical thinning is arguably a reflection, although not a perfect one, of how beta-amyloid burden and tau pathology spread in the living brain, as well as vascular and other forms of pathology that contribute to dementia. In one study, healthy elderly subjects and people with MCI and AD were scanned with both MRI and a novel PET molecular probes sensitive to amyloid-beta, neurofibrillary tangle pathology, or both (Braskie et al. 2010). As seen in Fig. 2b, AD pathology is generally low or undetectable in controls and higher in those with impaired cognition; the trajectory of pathology, seen here in scans of the living brain (Fig. 2b), is fairly consistent with the known trajectory of neurofibrillary tangle accumulation (Braak and Braak 1995, 1996). Amyloid PET changes are correlated with subclinical cognitive decline in normal controls (Braskie et al. 2010) and some have argued that they may be detected earlier in the disease process than cortical thinning (Jack et al. 2010a; Fjell and Walhovd 2011). Nonetheless, the pattern of brain alterations detected on MRI and amyloid PET is anatomically similar, despite a possible lag between the detection of changes in each modality (Fig. 2).

A number of recent studies have shown that the use of multi-modal imaging for AD or MCI classification offered improved performance compared to studies that used single-modality imaging (Fan et al. 2008; Hinrichs et al. 2011; Vemuri et al. 2009; Walhovd et al. 2010 and Zhang et al. 2012). This is not surprising, as biomarkers from distinct modalities can provide complementary information that is sensitive to AD. Zhang et al. developed a multi-modal
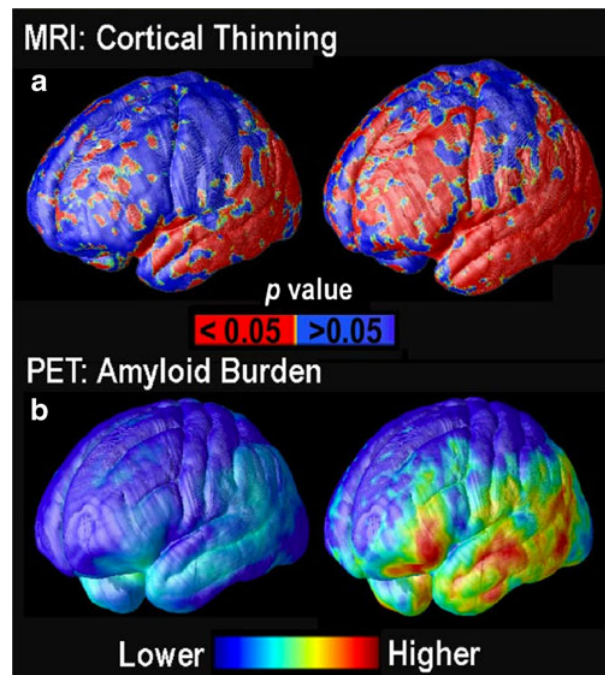

Fig. 2 Cortical thinning and changes in apparent cerebral amyloid and tau burden as AD progresses. **a** In mild AD (*left*), cortical gray matter deficits are most severe in the temporal lobes but tend to progress to the frontal lobes in moderate AD (*right*); these maps compare patients to controls and are constructed using T1-weighted MRI and a method known as "cortical pattern matching" in a longitudinal dataset. **b** The apparent profile of amyloid and tau burden based on PET scans—with the ligand [^{18}F] FDDNP—tends to be low in controls (*left*) and higher in cognitively impaired subjects (*right*). [Adapted, with permission of the authors—Braskie et al. 2010; Thompson et al. 2003—and publishers]

multi-task learning method using baseline MRI, FDG-PET, and cerebrospinal fluid data (CSF) in AD, MCI and healthy subjects to estimate a continuous clinical variable from multi-modal neuroimaging data (imaging-based regression), rather than predicting categorical variables as in classification. This method may help to evaluate the stage of AD pathology as a "disease burden score" and predict future progression. Using it, the authors successfully estimated clinical scores (MMSE, ADAS-Cog) and the correct diagnostic classification when distinguishing both AD vs. controls and MCI vs. controls, and predicted 2-year changes in the scores and diagnostic classifications in people who converted from MCI to AD as well as non-converters.

To study the effects of medication on the brain in AD, the multi-modal approach can reveal numerous treatment effects, including changes in brain structure, function and metabolism—which cannot be mapped with a single modality (unless of course MRI, fMRI and MRS are considered submodalities of MRI; Schmidt et al. 2008). Schmidt et al. used structural MRI, PET and chemical shift imaging (CSI) in a longitudinal study in patients with moderate AD and found a

reduction in total brain volume, hippocampal volume and in glucose metabolism after 52 weeks of the administration of memantine. However, their CSI results were not conclusive due to patient-related artifacts. Based on this study and others, there is a clear need to understand factors that affect long-term changes in various imaging measures. We also need to assess the variability and reproducibility of methods used in treatment trials for both MCI and AD (Schmidt et al. 2008).

Genetic data can also be integrated with other multimodality imaging data, using machine learning methods to generate new disease-sensitive biomarkers of AD (Wang et al. 2012a, b). Wang et al. (2012a, b) studied the statistical dependencies among neuroimaging measures, cognitive scores and disease status—which are often ignored in traditional association studies. Wang et al. found that voxel-based morphometry (VBM) and FreeSurfer measures from structural MRI were associated with disease status and cognitive scores, and glucose metabolism from PET as well as the *APOE ε4* SNPs were also found to have strong links to disease status and cognitive measures. These results led to fairly accurate predictions of both disease status and cognitive function and helped elucidate biological pathways from gene to brain structure, function, cognition and disease (Wang et al. 2012a, b).

Recent advances in multimodal imaging provide exciting new opportunities to understanding brain structure and function and how genetic variations affect them. Furthermore, multi-modal imaging may also help explain why there appear to be similarities at the systems level between detrimental effects of drug abuse and alterations that occur with AD (Thompson et al. 2004).

Brain connectivity and risk genes

Diffusion weighted imaging (DWI) has recently been added to several large studies of AD, including the Alzheimer's Disease Neuroimaging Initiative (ADNI), (Jack et al. 2010b). The benefit of adding DWI to the more standard imaging approaches is to better monitor aspects of white matter deterioration that are not detectable with standard anatomical MRI. Some recent studies using ADNI DWI data (including our own) have employed network analyses, based on graph theory, to better understand the pattern of connections, their properties, and how the disease disrupts them.

Connectivity analyses typically consider the connections among a large number of brain regions as a *graph* consisting of *nodes* (e.g., cortical regions) linked by *edges* (which may represent densities of fibers inferred based on whole-brain tractography). These topological networks may be used to understand how neural pathways break down with disease; they have only recently been studied in AD (Buckner et al.

2009; Daianu et al. 2012; Toga and Thompson 2013; Daianu et al. 2013).

Early reports suggest that the brain's anatomical "core" structure is highly disrupted in AD relative to normal aging. Some analyses focus on the most highly connected regions in the brain, which are severely affected in AD. Some methods define the brain's "core" anatomical network by "thresholding" the fiber density connectivity matrices so that only a subset (e.g., 50 %) of the network's nodes (cortical regions) remain connected. This method identifies "core" regions of the network that are most highly connected. In one of our studies (Daianu et al. 2012), the effect of retaining only highly connected nodes in the network led to a loss of all core connections in the left hemisphere network in AD (Fig. 3). Furthermore, AD patients had lower fiber density than controls for the connections between the following brain regions: the *pars triangularis* and caudal middle frontal regions, the precentral gyrus and the caudal middle frontal gyrus, the rostral middle frontal gyrus and the *pars opercularis*, and the superior parietal area and lingual gyrus. On average, AD patients also had a lower proportion of fibers emanating to and from the fusiform gyrus, precuneus and rostral anterior cingulate gyrus and higher proportion of fibers in the supra-marginal region (as a fraction of the total number of fibers detected in the brain), relative to controls (Fig. 3) (Daianu et al. 2013).

Little is known about which genetic factors account for inter-subject differences in brain connectivity, but a recent study by Jahanshad and colleagues discovered a connectome-wide, genome-wide significant association between a genetic variant in F-spondin (*SPON1*) and connectivity in 59 brain regions (all connectome-wide connections pre-screen to include only those with a detectable genetic influence in a twin study). This same genetic variant was associated with dementia severity in the ADNI cohort (Jahanshad et al. 2013a). The effect of the genetic variant was also replicated in an independent subsample at the same nodes of the brain's connectivity network. *SPON1* encodes F-spondin, a developmentally regulated protein that is attached to the extracellular matrix. SPON1 is induced in neuronal injury and interacts with receptors for Apolipoprotein E (*APOE4*)—a robust AD genetic risk factor. Also, SPON1 modulates amyloid-beta protein cleavage (Ho and Sudhof 2004) and binds to cholesterol (Barrett et al. 2012), an important component of myelin. Intriguingly, the overexpression of *SPON1* in mice improves memory performance and reduces amyloid-beta levels (Hafez et al. 2012). Therefore, the *SPON1* variant may have a protective impact on dementia regardless of the *APOE* risk genotype; the same protective variant was associated with stronger white matter fiber connections. In an independent sample (ADNI) the clinical dementia rating (CDR) was found to be lower in carriers of the protective variant of *SPON1* (Jahanshad et al. 2013a; where a higher CDR indicates increased levels of impairment). Additionally, another variant within the same

Fig. 3 Structural "core" of anatomical connectivity in healthy controls and AD subjects, reconstructed using DWI scans of the brain. Set of nodes present in the weighted k-core (A "weighted k-core" is a technical term that aims to define the core anatomical network in the brain. It is defined as a set of network nodes (cortical regions) that are highly and mutually interconnected (Hagmann et al. 2008; Sporns 2011).) networks of 28 controls (*top left panel*), and 15 AD subjects (*top right panel*). In healthy controls, the structural core was defined to include at least half of the detectable connected nodes per hemisphere. In AD, the left hemisphere loses its k-core connections (FDR critical p-value=0.0015). The *bottom panel* shows connections that survived FDR when comparing the k-cores (k=18) of AD subjects to controls, using age and sex as covariates, and the scanning site as a random effect. *Figures follow anatomical convention (where the left hemisphere is on the left and the right hemisphere is on the right).* [Adapted, with permission of the authors—Daianu et al. 2013— and publishers]
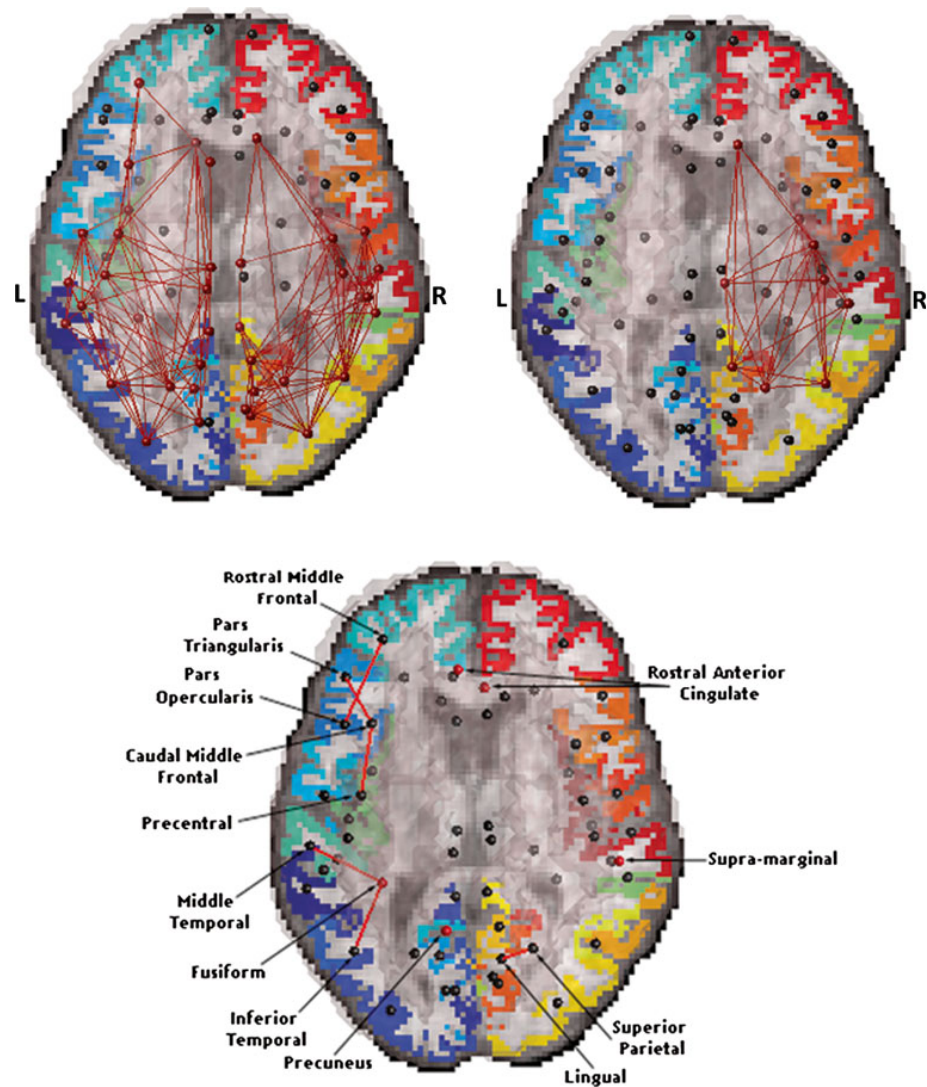
SPON1 gene was found to play a role in cognitive decline (Sherva et al. 2013).

While connectivity measures have been shown to associate with known AD risk genes including *APOE4* (Brown et al. 2011; Jahanshad et al. 2012a), recent findings from connectome-wide genome-wide association studies (Jahanshad et al. 2013a; Thompson et al. 2013a, b) suggest that diffusion-based connectome measures help in discovering genetic factors that affect the wiring and degeneration of the brain.

Late-Onset Alzheimer's disease risk genes and neuroimaging measures

Early-onset familial AD (fAD) is relatively rare, and represents about 5 % of AD cases [reviewed in: (Tanzi 2012)]. fAD follows an autosomal dominant, highly penetrant mode of inheritance. Rare mutations in the presenilin 1 and presenilin 2 genes (*PSEN1* and *PSEN2*), and in the amyloid precursor protein gene (*APP*) lead to a much higher risk of developing early-onset familial AD. In recent years, we have learned a great deal about how fAD affects the brain. Patterns of structural atrophy are more widespread in fAD, without the strong predilection for medial temporal lobes as in late-onset AD (Frisoni et al. 2007; Benzinger et al. 2013; Cash et al. 2013). By contrast, the more common, late-onset form of AD— known as LOAD or sporadic AD—is moderately heritable. Many common genetic polymorphisms have been identified that are associated with increased risk for LOAD (Braskie et al. 2011a provide an in-depth review). Here, as a brief overview, we will discuss 10 of these genetic variants that have been consistently associated not only with increased risk for developing LOAD, but also with specific brain measures in neuroimaging studies (Table 1). For many of these variants,

Table 1 List of several major Alzheimer's disease risk genes that have been studied using neuroimaging. Here we list a range of studies that have found associations between brain imaging measures and common variants in major Alzheimer's disease risk genes. Note that the prevalence of the risk-associated variant is different for each gene. Some of the AD risk alleles are fairly rare—the one in *TREM2* is carried by only about 1 % of the healthy population. Other risk alleles (e.g., for *CLU*) are carried by more than half of the healthy population, meaning that carriers of the rarer form are at lower risk for the disease, if other factors were equal. For other in-depth reviews of neuroimaging studies of common genetic variants, see Thompson et al. 2013b, and Shen et al. 2013 (*this issue*)

Publication	Gene	Reference number, or location, of the common genetic variant (SNP) that is associated with risk for Alzheimer's disease	Minor Allele (i.e., the least prevalent form)	Minor Allele Frequency (MAF) [%]	Imaging Modality	Brain Regions Assessed	Results	Affected Regions	Population
O'Dwyer et al. 2012	*APOE*	rs7412 and rs429358; for *APOE*, the genotype E2, E3 or E4 depends on the genetic variants at two locations on the chromosome	T and C, respectively	7.4 and 14.9, respectively[a,b]; around 25 % of healthy people, but 40–65 % of AD patients, carry at least one APOE4 allele	T1-weighted MRI	Hippocampal morphometry	ApoE4 carriers have smaller hippocampal volumes	Greater effects on the right than the left hippocampus	Not stated
Braskie et al. 2011b	*CLU*	rs11136000	T	35[a] (T-allele); for *CLU*, the minor allele is associated with lower risk, and the more common allele is associated with higher risk	Diffusion tensor imaging (DTI); tested voxel-wise association with FA	Full white matter FA	Carriers of the *CLU-C* variant (major allele) had lower white matter integrity	Strongest effects in the splenium, bilateral posterior and anterior corona radiata, bilateral perithalamic tracts, and posterior thalamic radiation, left SLF, ILF/IFO	Caucasian
Bralten et al. 2011	*CRI*	rs6656401	A	24[a]	Voxel-based morphometry	Regional gray matter volume	*CRI* minor allele is negatively associated with local gray matter volume	Lower local gray matter volume in entorhinal cortex and hippocampus	Caucasian
Hibar et al. 2011, 2012	*GAB2*	rs7101429	G	13[a]	T1 weighted MRI/ voxelwise gene based test (PCR)	Whole brain voxel based morphometry (VBM)	In the right parietal lobe, *GAB2* loading is negatively correlated with overall tissue volume; in the temporal lobe sulci, there was a positive correlation between CSF volume and *GAB2* loading	Significant differences in the right parietal lobe, additional smaller clusters in left parietal, along CSF boundary, and in the temporal lobe	Caucasian
Jahanshad et al. 2012b	*HFE*	rs1799945	G	18[a]	Diffusion tensor imaging (DTI); tested voxel-wise association with FA	Full white matter FA	*HFE* minor allele has a negative correlation between transferrin levels and FA measures	Mainly in the external capsule and portions of the genu of the corpus callosum	Caucasian
Furney et al. 2011	*PICALM*	rs3851179	T	41[a]	T1-weighted MRI/cortical thickness and volume	Entorhinal cortex	*PICALM* major allele carriers have thinner entorhinal cortical volume than minor allele carriers	Increased entorhinal cortical thickness in minor allele carriers	Participants in the AddNeuroMed study and ADNI

125

Table 1 (continued)

Publication	Gene	Reference number, or location, of the common genetic variant (SNP) that is associated with risk for Alzheimer's disease	Minor Allele (i.e., the least prevalent form)	Minor Allele Frequency (MAF) [%]	Imaging Modality	Brain Regions Assessed	Results	Affected Regions	Population
Rajagopalan et al. 2013	TREM2	Rajagopalan et al. assessed rs9394721, a close proxy for the newly discovered risk variant, rs75932628, in TREM2	A allele for rs7593268; T allele for rs75932628 in the Jonsson et al. paper	Around 1 %, but more common in AD patients	T1-weighted MRI	Tensor-based morphometry, focusing on the temporal lobes	Carriers of the (rare) TREM2 minor allele have faster rates of brain atrophy	TREM2 mutation carriers annually lose brain tissue up to 1.4–3.3 % faster than non-carriers, in a pattern that mirrors the profile of AD pathology in the brain	Caucasian participants in the ADNI
Rajagopalan et al. 2012a	MTHFR	rs1801133	A	31[a]	T1-weighted MRI	Whole brain morphometry	MTHFR-T (major allele) is negatively associated with regional brain volume	Significant volume deficits in the bilateral periventricular fronto-parietal white matter, periventricular parietal white matter, and posterior parieto-occipital white matter	Caucasian
Johnson et al. 2011	TOMM40	rs1054523; this is a SNP, but some studies focus on a poly-T repeat in the same gene	NA	NA	MRI; voxel-based morphometry	Gray matter morphometry	Risk-associated variant in TOMM40 is negatively correlated with brain volume	Significant effects seen in the left ventral posterior cingulate and the cuneus	Participants of WRAP
Stein et al. 2010	GRIN2B	rs10845840	T	46[a]	MRI; voxel-based association testing	Tensor-based morphometry, focusing on the temporal lobes	GRIN2B minor allele has wide ranging effects across the temporal lobe	Strongest effects in the bilateral temporal poles and medial temporal lobes	Caucasian participants in the ADNI

[a] MAF obtained from the CEU database in http://hapmap.ncbi.nlm.nih.gov/

[b] MAF obtained from http://www.ncbi.nlm.nih.gov/SNP/

differences in brain structure are observable not only in AD patients, but also in asymptomatic carriers of risk alleles, including groups of young and healthy carriers. In this review, we summarize some key findings (for a more in-depth review of all neuroimaging genetics studies in one large-scale initiative, ADNI, please refer to Shen et al. 2013, *this issue*).

Common variants in the apolipoprotein E (*APOE ε2/3/4*) gene confer the highest known odds ratio for developing LOAD. On average, around 25 % of the world's population has at least one copy of the ε4 risk allele and each copy of this risk allele is associated with around threefold increased odds of developing AD (Bertram et al. 2007). There are ethnic differences among carriers of the ε4 allele. The association between the ε4 allele and AD appears stronger in Asian and Caucasian populations than in individuals of African or Hispanic descent (Farrer et al. 1997). Even so, brain structure and function are altered in AD patients and controls who carry *APOE* ε4. Temporal lobe atrophy rates are faster in AD patients with a greater number of ε4 alleles (Lehtovirta et al. 1995; Filippini et al. 2009), and medial temporal lobe volumes are reduced in healthy middle-aged and elderly *APOE* ε4 carriers (Barboriak et al. 2000; den Heijer et al. 2002; Wishart et al. 2006). Recently, a study showed reduced hippocampal volume in healthy young *APOE* ε4 carriers, especially in the right hemisphere, suggesting that possession of the *APOE* ε4 allele may lead to greater risk for brain atrophy even in healthy young subjects in their 20s and 30s, long before the average age of onset of AD (O'Dwyer et al. 2012).

Another common risk gene for LOAD is clusterin (*CLU*), whose risk allele is carried by 88 % of Caucasians (Harold et al. 2009; Lambert et al. 2009). Intriguingly, the more prevalent form of this disease risk gene confers greater risk; in a sense, the less commonly carried version of *CLU* may be considered a protective form of the gene. Our group recently showed that the risk variant in *CLU* is associated with differences in white matter microstructure, even in healthy young adults (Braskie et al. 2011b). Each copy of the risk allele is associated with lower white matter integrity in multiple brain regions, including several areas known to degenerate in AD. This distinct profile of lower white matter integrity is observable in healthy individuals in their early 20s, and may therefore help predict vulnerability for AD later in life—a topic in need of further exploration. Consistent with the possibility of lower white matter integrity, the same risk variant has been associated with faster cognitive decline in asymptomatic and presymptomatic elderly individuals (Thambisetty et al. 2013).

The erythrocyte complement receptor 1 (*CR1*) is another risk gene for which a commonly-carried variant is associated with risk for developing LOAD (Lambert et al. 2009, Naj et al. 2011). A risk allele in *CR1* is significantly associated with AD in both Caucasians and Chinese populations (Jin et al. 2012). As with *APOE* and *CLU*, young healthy risk allele carriers, as a group, appear to show structural brain abnormalities long

before possible AD symptoms appear. Carriers of the *CR1* risk allele have lower gray matter volumes in the entorhinal cortex, one of the core structures for AD pathology (Bralten et al. 2011). An intragenic functional copy number variation in *CR1* may explain the association between *CR1* and AD (Van Cauwenberghe et al. 2013).

The growth factor receptor-bound protein 2-associated protein, or *GAB2*, encodes the growth factor receptor bound protein 2-associated protein. *GAB2* is well characterized as a risk gene for the development of LOAD, with a moderate effect on disease risk (Reiman et al. 2007; Chapuis et al. 2008). In a recent study, our group found *GAB2* was significantly associated with alterations in brain structure (Hibar et al. 2011). In a follow-up study, we investigated *GAB2*'s effects on brain structure in healthy young adults (Hibar et al. 2012). In line with expectation, subjects with fewer mutations (or minor alleles) in the *GAB2* gene had greater tissue volumes in the parietal lobe, while participants with less common alleles in *GAB2* showed CSF space expansion in the temporal lobe sulci (Hibar et al. 2012). The mechanism by which the *GAB2* gene affects neurodegeneration is quite well understood. The normally functioning GAB2 protein suppresses the phosphorylation of tau protein, whose accumulation results in neurofibrillary tangles promoting AD (Reiman et al. 2007). We do not yet know how changes in the efficiency of the GAB2 protein might lead to morphological differences in young adult brains. Even so, morphological differences associated with an AD risk gene such as *GAB2* appear to be detectable in healthy young adults. This may indicate an early vulnerability to LOAD, long before the onset of Alzheimer's disease. However, long term longitudinal studies would be needed to determine whether the carriers with greater brain abnormalities are at heightened risk of AD, beyond what might be predicted from their genotype alone.

Another interesting line of work concerns genes involved in iron regulation, a mechanism disrupted in many neurodegenerative disorders including AD (Ke et al. 2003). Hemochromatosis, for example, is the most common genetic disorder in the world, and involves an inability of the body to regulate iron levels. Genetic studies of those affected found that the human hemochromatosis protein is encoded by the *HFE* gene, in which common variants explain a large part of the risk for hemochromatosis (see Thompson and Jahanshad 2012; Jahanshad et al. 2013b, for a review).

The HFE protein regulates iron absorption by modulating the interaction of transferrin with its receptor. The H63D polymorphism in the *HFE* gene is well-known for its association with iron overload (Aguilar-Martinez et al. 2001). Patients with AD who carried the H63D polymorphism had increased plasma iron and transferrin levels, but this pattern was not found in healthy control subjects with the variant (Giambattistelli et al. 2012). A meta-analysis found that the H63D polymorphism may actually be *protective* against AD

(Lin et al. 2012). In a recent investigation, our group found that the *HFE* H63D polymorphism influences both serum transferrin levels and white matter microstructure in the external capsule in young healthy adults (Jahanshad et al. 2012b). This finding links blood serum-related genomic variation to brain structure, and suggests that iron may be beneficial (e.g., for myelination) at a young age; however, the effect of the variant on brain integrity in old age has yet to be studied, and it is possible the same variant has a detrimental effect later in life, and may exacerbate disease risk. The role of other metal ions in neurodegeneration is a key target of study, as many of the molecular pathways regulating them are fairly well-understood (Jahanshad et al. 2013b).

Another gene associated with susceptibility for LOAD codes for the phosphatidylinositol binding clathrin assembly protein (*PICALM*) (Harold et al. 2009). This gene likely contributes to the pathogenesis of AD via its effect on amyloid beta metabolism (Xiao et al. 2012) and also through its association with neurofibrillary tangles and the development of tau pathology (Ando et al. 2013). A recent study integrating structural MRI measures and genome-wide common variant data reported that a variant in the *PICALM* gene was most strongly associated with entorhinal cortical thickness (Furney et al. 2011). The *PICALM* variant identified earlier in the large case–control studies (Harold et al. 2009) was associated with less atrophy in the entorhinal cortex, suggesting a protective effect against neurodenegerative diseases (Furney et al. 2011).

A recently discovered rare variant in *TREM2*, which encodes the Triggering receptor expressed on myeloid cells 2 protein, almost triples the lifetime risk of AD (Benitez et al. 2013; Guerreiro et al. 2013; Jonsson et al. 2013). If the odds ratio for this variant holds up in future studies and meta-analyses, it is the variant with the second strongest known effect (in terms of odds ratio) on the risk of late-onset AD, following *APOE4*. A missense mutation in *TREM2* is associated with a significantly higher risk of Alzheimer's disease in diverse human populations (Benitez et al. 2013; Guerreiro et al. 2013; Jonsson et al. 2013). Our group recently reported that elderly *TREM2* mutation carriers in the ADNI cohort appear to lose temporal lobe brain tissue around twice as fast as elderly individuals who lack the mutation (Rajagopalan et al. 2013). The risk allele was associated with smaller hippocampal volumes, higher levels of cerebrospinal fluid biomarkers of neurodegeneration, and poorer cognitive performance (Rajagopalan et al. 2013). Given the anti-inflammatory role of *TREM2* in the brain, the mutation may lead to an increased predisposition to AD through impaired containment of inflammatory processes (Jonsson et al. 2013), possibly leading to a dysfunction in the microglial phagocytosis pathway (Neumann and Daly 2013). This may lead to the inability of the brain to clear amyloid plaques (Jones 2013). If these findings regarding *TREM2* are corroborated in future studies, the selective

enrollment of carriers (or *post hoc* stratification by *TREM2* status) may empower clinical trials, by selecting a population more likely to decline.

Another gene associated with increased risk for LOAD is *MTHFR*, which encodes the methylenetetrahydrofolate reductase enzyme. Some common variants in this gene are associated with reduced enzyme activity and result in increased serum homocysteine levels (Mansoori et al. 2012). A moderate elevation of plasma homocysteine is considered a potential risk factor for AD. Homocysteine has garnered significant interest recently, as vitamin B supplementation can lower homocysteine levels, and some studies report that such supplements may reduce the rate of brain atrophy (Douaud et al. 2013). The involvement of *MTHFR* in the pathogenesis of AD is somewhat controversial. Some *MTHFR* polymorphisms may confer greater susceptibility for developing AD in Asian populations, but not in Caucasians (Zhang et al. 2010; Hua et al. 2011). Even so, our group recently reported an association between a common *MTHFR* variant and brain structure in elderly Caucasian individuals with mild cognitive impairment (Rajagopalan et al. 2012a). Carriers of the *MTHFR* risk allele had significant brain volume deficits in the white matter locally at baseline. These subjects also showed accelerated brain atrophy at 1-year follow-up. These brain volume deficits were replicated in an independent elderly cohort with mild cognitive impairment (Rajagopalan et al. 2012a). An earlier report also confirmed a link between brain atrophy and homocysteine levels in the ADNI cohort, with higher levels appearing to have an adverse effect (Rajagopalan et al. 2011).

Variants in the *TOMM40*, which codes for the translocase of the outer mitochondrial membrane 40 homolog protein, was recently associated with an increased risk of developing LOAD at an earlier age (Roses et al. 2010). Downregulation of *TOMM40* expression has been found in the blood of AD subjects compared to healthy controls in Asian populations (Lee et al. 2012). A study of middle-aged subjects with *APOE* ε3/ε3 genotype showed that carriers of a risk allele in *TOMM40* had poorer cognitive performance than non-carriers. A dose-dependent increase in the risk variant was also associated with decreased gray matter volumes in regions of the brain that are affected early on in LOAD, such as the medial ventral precuneus (Johnson et al. 2011). In addition, there are poly-T "repeats" in the *TOMM40* gene, and some studies have begun to relate the length of the expansion to AD risk and to brain measures (Babakchanian et al. 2011). Nonetheless, the involvement of *TOMM40* in the pathogenesis of AD is somewhat controversial, mainly because *TOMM40* is in strong linkage disequilibrium with *APOE*. Several authors have tried to tease apart an *APOE*-independent role for *TOMM40* in the risk for developing

AD and the age of onset (Guerreiro and Hardy 2012; Rajagopalan et al. 2012b).

In a genome-wide association study of temporal lobe degeneration, our group identified a risk variant for lower temporal lobe volume in the *GRIN2B* gene, which encodes the *N*-methyl-*D*-aspartate (NMDA) glutamate receptor NR2B subunit. This risk variant was significantly over-represented in subjects with AD and mild cognitive impairment than in healthy elderly controls, and was also associated with poorer performance on the Mini Mental Status Exam (MMSE) (Stein et al. 2010). The NR2B subunit of the NMDA receptor is involved in learning and memory, structural plasticity of the brain, and in characteristic features of AD and neurodegeneration. NMDA receptors are an evolving target for the treatment of dementia. The genetic association of *GRIN2B* variants with neuroimaging and cognitive phenotypes supports the relevance of these receptors as therapeutic targets in AD.

Neurodegenerative risk genes related to addiction

The 10 genes described above only begin to paint a picture of how AD related genes exert their effects on the brain. Intriguingly, as discussed in the introduction, some genetic variants associated with neurodegeneration may *also increase our risk for substance abuse.* Understanding how these pleiotropic genes influence differences in the brain, would not only shed light on the neuroanatomical pathways altered by the gene, but may allow us to detect which common pathways are affected by both conditions. For instance, the *COL25A1* gene encoding Collagen XXV alpha 1, also known as collagen-like Alzheimer's amyloid plaque component precursor, is a transmembrane protein specifically expressed in neurons. It colocalizes with amyloid-beta in senile plaques, in the brains of AD patients (Hashimoto et al. 2002; Tong et al. 2010). *COL25A1* may also be associated with substance dependence (Li et al. 2012).

To our knowledge, very few neuroimaging studies have examined how some of the genes affecting both our risk for neurodegeneration and for substance abuse influence brain structure. We discuss three of them below. Two of these studies examined the *BDNF* gene encoding the brain derived neurotrophic factor. The most studied polymorphism in this gene has been the Val66Met mutation. Several older studies already showed that Val/Val individuals were at greater risk of developing AD (Ventriglia et al. 2002; Harris et al. 2006). A recent imaging genetics study demonstrated that healthy elderly Val/Val individuals had diminished entorhinal cortex thickness, lower white matter tract integrity, and poorer episodic memory performance, providing a compelling picture of the effect of the Val66Met polymorphism on an intermediate phenotype related to AD (Voineskos et al. 2011). Interestingly,

BDNF also plays important and diverse roles in addiction-related behaviors [reviewed in (Autry and Monteggia 2012)]. Val/Val carriers may also be at higher risk for methamphetamine abuse (Heinzerling and Shoptaw 2012). In previous work from our group, the *BDNF* polymorphism was a significant but weak predictor of white matter integrity in young adulthood (Chiang et al. 2010)—its predictive value was weaker than that of several other genes so far discussed, including *CLU* and *HFE* (Kohannim et al. 2012).

Another neuroimaging study focused on the *OPRD1* gene encoding delta opioid receptors, mentioned earlier. These receptors are involved in neurodegeneration and promote the processing of amyloid-beta precursor protein (APP). Knockdown or antagonization of delta receptors ameliorates amyloid-beta-related pathology and amyloid-beta-dependent behavioral deficits in mice (Teng et al. 2010). In particular, one *OPRD1* polymorphism (rs1042114) changes the evolutionarily conserved phenylalanine to cysteine in the *N*-terminus of the receptor. In human cell lines, this change in the amino-acid sequence of the delta receptors leads to a detrimental accumulation of one type of APP, which is degraded less efficiently (Sarajarvi et al. 2011). Interestingly, this same variant is strongly associated with opioid dependence (Zhang et al. 2008). Thus the same allele, which seems to promote neurodegeneration (Sarajarvi et al. 2011), also confers a predisposition to drug addiction (Zhang et al. 2008).

In a recent study, our group used imaging genetics tools to investigate the relationship between another *OPRD1* polymorphism implicated in addiction, rs678849 (Crist et al. 2013) and regional brain volumes in two large independent samples in early and late adulthood (Roussotte et al. 2013). The first sample was an elderly cohort including multiple diagnostic groups: AD, MCI, and healthy elderly controls. The second cohort consisted of young healthy adults. We discovered that carriers of this *OPRD1* variant have identifiable differences in brain structure. The brain regions affected differed between the two samples, but the same minor allele (previously implicated in addiction, Crist et al. 2013) in the same gene (which encodes receptors known to be involved in the processing of amyloid-beta precursor protein and neurodegeneration, Teng et al. 2010; Sarajarvi et al. 2011) was associated with reduced volumes in two very different cohorts (Roussotte et al. 2013). Indeed, we detected these brain abnormalities not just in the elderly (Fig. 4), but also in healthy young adults without any history of substance abuse or cognitive impairments (Fig. 5).

The association of these addiction-related variants with greater risk for developing degenerative brain disorders (Tong et al. 2010; Sarajarvi et al. 2011), decline in cognitive performance (Voineskos et al. 2011) and differences in brain structure (Voineskos et al. 2011; Roussotte et al. 2013) are key discoveries. This field of study is in its infancy and further research is needed to follow through with these findings and

Fig. 4 Effects of the minor allele at the rs678849 locus in the delta opioid receptor gene, on regional brain volumes in the elderly cohort. The intronic *OPRD1* polymorphism rs678849 was significantly associated with regional frontal, temporal, and occipital brain volumes. Negative beta values (*warm colors*) show regions where minor allele carriers had lower tissue volumes. The color bar encodes the average percentage of volume difference relative to the template for the subjects carrying at least one minor allele, versus noncarriers. Tests for associations are adjusted for age and sex; maps are corrected for multiple comparisons with the searchlight false discovery rate (FDR) method. Images are in radiological convention (left side of the brain shown on the right) (Roussotte et al. 2013)
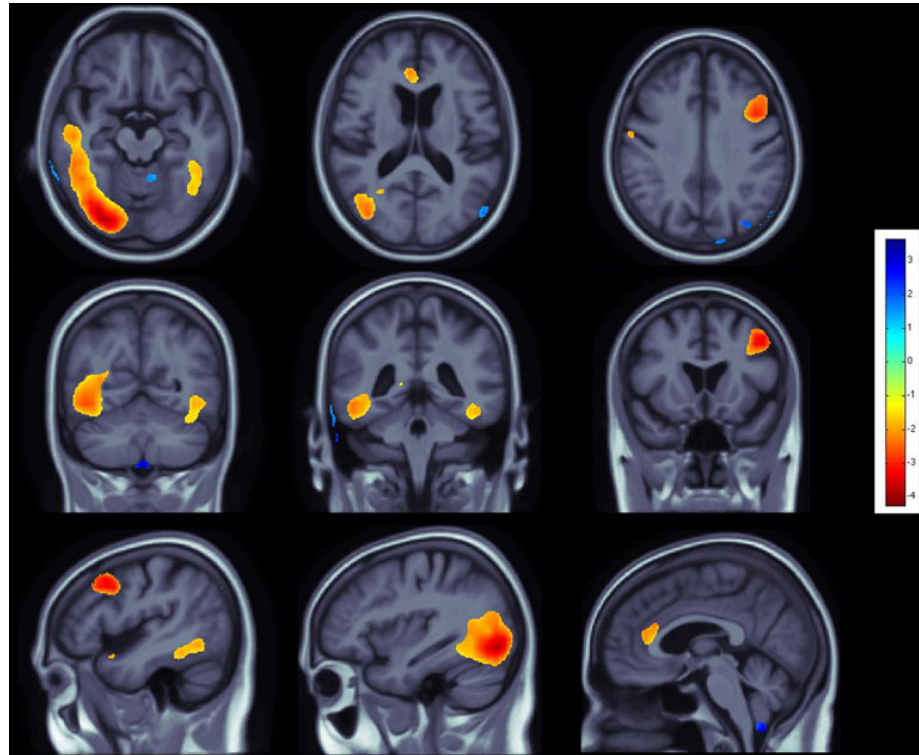
better characterize how genetic polymorphisms associated with addiction affect brain structure, function, and networks in the brain. Currently, many pharmacological agents targeting neurotransmitter receptors and transporters involved in the etiology or pathophysiology of both AD and drug addiction are being investigated as potential therapeutic agents for
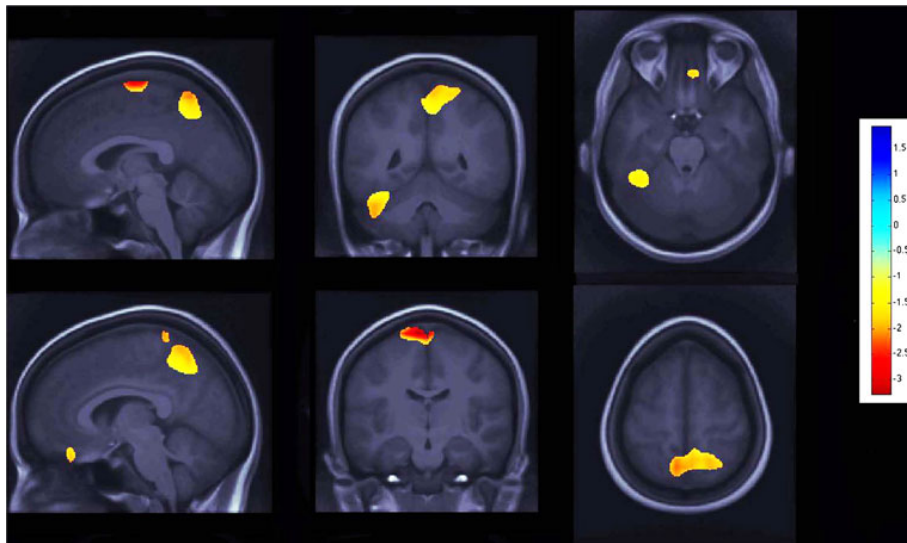

Fig. 5 Effects of the minor allele at the rs678849 locus in the delta opioid receptor gene, on regional brain volumes in the young healthy cohort. The same *OPRD1* polymorphism, rs678849, was significantly associated with regional frontal, temporal, and occipital brain volumes. Negative beta values (*warm colors*) show regions where minor allele carriers had lower tissue volumes. The color bar encodes the average percentage of volume difference relative to the template for the subjects carrying at least one minor allele, versus noncarriers. Tests for associations are adjusted for age and sex; maps are corrected for multiple comparisons with the searchlight false discovery rate (FDR) method. Images are in radiological convention (left side of the brain shown on the right) (Roussotte et al. 2013)

treating these brain disorders, including EAATs (Nakagawa and Kaneko 2013), S1Rs (Guitart et al. 2004), and delta opioid receptors (Pradhan et al. 2011). Further investigations outside the field of macroscopic brain imaging could also reveal possible genetic and biological pathways that may underlie specific mechanisms for these gene-brain associations. Gene therapy has become more common and many clinical trials are being conducted for the management of various brain disorders, including AD and those resulting in part from drug addiction. Effective development of gene therapy requires not only the identification of specific molecular and anatomic targets but also specific brain regions or networks to modulate with genetic intervention (Gelfand and Kaplitt 2012). Therefore, this line of research may help in devising more targeted and effective treatments for degenerative brain disorders.

Conclusion

The pathology of degenerative brain diseases, specifically AD, may progress along structural and functional connections in brain networks. Common genetic variations may also affect a whole host of biological processes that contribute to atrophy, amyloid processing, and vascular integrity. As we have seen in this brief overview, a variety of brain imaging modalities provide complementary information on how the disease progresses in the brain. To fully understand the effects of AD, discoveries must be integrated from a range of imaging methods, and a variety of processing algorithms and statistical analyses, surveying atrophy, dysfunction, and network breakdown, to name a few. Moreover, there is growing evidence of some overlap between genes that promote neurodegeneration and risk for substance abuse; this offers important new avenues for research. Degenerative disorders are typically diagnosed only after severe brain changes have occurred, so it is vital to discover genetic variants that may influence brain volume or atrophy, as well as addictive behaviors in young and healthy individuals. Understanding these associations is within our reach. It may offer new directions for understanding promoters of brain degeneration, and ultimately intervention, many decades before symptoms appear.

References

Aguilar-Martinez, P., Bismuth, M., Picot, M. C., Thelcide, C., Pageaux, G. P., Blanc, F., et al. (2001). Variable phenotypic presentation of iron overload in H63D homozygotes: are genetic modifiers the cause? *Gut, 48*(6), 836–842.

Alzheimer's Association Colorado. 2011 fact Sheet Alzheimer's Disease. (2011). from www.alz.org/co/in_my_community_11039.asp

Ando, K., Brion, J. P., Stygelbout, V., Suain, V., Authelet, M., Dedecker, R., et al. (2013). Clathrin adaptor CALM/PICALM is associated with neurofibrillary tangles and is cleaved in Alzheimer's brains. *Acta Neuropathologica, 125*(6), 861–878.

Autry, A. E., & Monteggia, L. M. (2012). Brain-derived neurotrophic factor and neuropsychiatric disorders. *Pharmacological Reviews, 64*(2), 238–258.

Babakchanian, S., Hwang, K. S., Coppola, G., Johnson, S., Thompson P. M., Lee, J. J., Cummings, J. L., Apostolova, L. G. (2011). *TOMM40* rs2075650 and *TOMM40* PolyT Polymorphism effects on ventricular enlargement in individuals with and without mild cognitive impairment, *International Conference on Alzheimer's Disease (ICAD)* 2011, July 16–21, Paris, France.

Barboriak, D. P., Doraiswamy, P. M., Krishnan, K. R., Vidyarthi, S., Sylvester, J., & Charles, H. C. (2000). Hippocampal sulcal cavities on MRI: relationship to age and apolipoprotein E genotype. *Neurology, 54*(11), 2150–2153.

Barrett, P. J., Song, Y., Van Horn, W. D., Hustedt, E. J., Schafer, J. M., Hadziselimovic, A., et al. (2012). The amyloid precursor protein has a flexible transmembrane domain and binds cholesterol. *Science, 336*(6085), 1168–1171.

Benitez, B. A., Cooper, B., Pastor, P., Jin, S. C., Lorenzo, E., Cervantes, S., et al. (2013). TREM2 is associated with the risk of Alzheimer's disease in Spanish population. *Neurobiology of Aging, 34*(6), e15–e17.

Benzinger, T. L. S., Blazey, T., Jack, Jr., C. R., Koeppe, R. A., Su, Y., Raichle, M. E., Snyder, A. Z., Ances, B. M., Bateman, R. J., Cairns, N. J., Fagan, A. M., Goate, A., Marcus, D. S., Xiong, C., Aisen, P. S., Aldea, P., Christensen, J. J., Ercole, L., Hornbeck, R. C., Farrar, A. M., Jasielec, M. S., Owen, C. J., Xie, X., Mayeux, R. Brickman, A. M., McDade, E., Klunk, W. E., Mathis, C. A., Ringman, J. M., Thompson, P. M., Ghetti, B., Saykin, A. J., Sperling, R. A., Johnson, K. A., Salloway, S., Correia, S., Schofield, P. R., Masters, C. L., Rowe, C. C., Villemagne, V. L., Martins, R. N., Rossor, M. N., Fox, N. C., Cash, D. M., Weiner, M. W., Holtzman, D. M., Buckles, V. D., Moulder, K., Morris, J. C., for the Dominantly Inherited Alzheimer Network (2013). Regional variability of imaging biomarker changes in autosomal dominant Alzheimer's Disease, submitted to *PNAS*, April 26 2013.

Bergem, A. L., Engedal, K., & Kringlen, E. (1997). The role of heredity in late-onset Alzheimer disease and vascular dementia. A twin study. *Archives of General Psychiatry, 54*(3), 264–270.

Bertram, L., McQueen, M. B., Mullin, K., Blacker, D., & Tanzi, R. E. (2007). Systematic meta-analyses of Alzheimer disease genetic association studies: the AlzGene database. *Nature Genetics, 39*(1), 17–23.

Braak, H., & Braak, E. (1995). Staging of Alzheimer's disease-related neurofibrillary changes. *Neurobiology of Aging, 16*(3), 271–278. discussion 278–284.

Braak, H., & Braak, E. (1996). Development of Alzheimer-related neurofibrillary changes in the neocortex inversely recapitulates cortical myelogenesis. *Acta Neuropathologica, 92*(2), 197–201.

Bralten, J., Franke, B., Arias-Vasquez, A., Heister, A., Brunner, H. G., Fernandez, G., et al. (2011). CR1 genotype is associated with entorhinal cortex volume in young healthy adults. *Neurobiology of Aging, 32*(11), e7–e11.

Braskie, M. N., Klunder, A. D., Hayashi, K. M., Protas, H., Kepe, V., Miller, K. J., et al. (2010). Plaque and tangle imaging and cognition in normal aging and Alzheimer's disease. *Neurobiology of Aging, 31*(10), 1669–1678.

Braskie, M. N., Ringman, J. M., & Thompson, P. M. (2011a). Neuroimaging measures as endophenotypes in Alzheimer's disease. *International Journal of Alzheimer's Disease, 2011*, 490140.

Braskie, M. N., Ringman, J. M., & Thompson, P. M. (2011b). Common Alzheimer's disease risk variant within the CLU gene affects white

matter microstructure in young adults. *Journal of Neuroscience, 31*(18), 6764–6770.

Braskie, M. N., Jahanshad, N., Stein, J. L., Barysheva, M., Johnson, K., McMahon, K. L., et al. (2012). Relationship of a variant in the NTRK1 gene to white matter microstructure in young adults. *Journal of Neuroscience, 32*(17), 5964–5972.

Brown, J. A., Terashima, K. H., Burggren, A. C., Ercoli, L. M., Miller, K. J., Small, G. W., et al. (2011). Brain network local interconnectivity loss in aging APOE-4 allele carriers. *Proceedings of the National Academy of Sciences of the United States of America, 108*, 20760–20765.

Bruner, E., & Jacobs, H. I. (2013). Alzheimer's disease: the downside of a highly evolved parietal lobe? *Journal of Alzheimer's Disease, 35*(2), 227–240.

Buckner, R. L., Snyder, A. Z., Shannon, B. J., LaRossa, G., Sachs, R., Fotenos, A. F., et al. (2005). Molecular, structural, and functional characterization of Alzheimer's disease: evidence for a relationship between default activity, amyloid, and memory. *Journal of Neuroscience, 25*(34), 7709–7717.

Buckner, R. L., Sepulcre, J., Talukdar, T., Krienen, F. M., Liu, H., Hedden, T., et al. (2009). Cortical hubs revealed by intrinsic functional connectivity: mapping, assessment of stability, and relation to Alzheimer's disease. *Journal of Neuroscience, 29*(6), 1860–1873.

Cash, D. M., Ridgway, G. R., Ryan, N. S., Kinnunen, K. M., Yeatman, T., Malone, I., Benzinger, T. L. S., Koeppe, R., Jack, C. R., Raichle, M., Marcus, D., Ringman, J., Thompson, P. M., Saykin, A. J., Salloway, S., Correia, S., Johnson, K., Sperling, R., Schofield, P., Rowe, C., Brickman, A. M., Mayeux, R., Mathis, C., McDade, E., Klunk, W., Weiner, M., Bateman, R., Goate, A., Xiong, C., Buckles, V., Moulder, K., Morris, J. C., Rossor, M. N., Ourselin, S., Fox, N. C. (2013). The pattern of volumetric atrophy in familial Alzheimer's disease: Results from the DIAN Study, submitted to Neurology, April 2013.

Chapuis, J., Hannequin, D., Pasquier, F., Bentham, P., Brice, A., Leber, I., et al. (2008). Association study of the GAB2 gene with the risk of developing Alzheimer's disease. *Neurobiology of Disease, 30*(1), 103–106.

Chiang, M. C., Barysheva, M., Toga, A. W., Medland, S. E., Hansell, N. K., James, M. R., et al. (2010). *BDNF* gene effects on brain circuitry and intelligence replicated in 455 Twins. *NeuroImage, 55*(2), 448–454.

Crist, R. C., Ambrose-Lanci, L. M., Vaswani, M., Clarke, T. K., Zeng, A., Yuan, C., et al. (2013). Case–control association analysis of polymorphisms in the delta-opioid receptor, OPRD1, with cocaine and opioid addicted populations. *Drug and Alcohol Dependence, 127*(1–3), 122–128.

Daianu, M., Jahanshad, N., Nir, T. M., Dennis, E., Toga, A. W., Jack, C. R. J., et al. (2012). Analyzing the structural k-core of brain connectivity networks in normal aging and Alzheimer's Disease. Paper presented at the MICCAI NIBAD, Nice, France, 2012.

Daianu, M., Jahanshad, N., Nir, T. M., Toga, A. W., Jack Jr, C. R., Weiner, M. W., et al. (2013). Breakdown of brain connectivity between normal aging and Alzheimer's Disease: a structural k-core network analysis. *Brain Connectivity, 3*(4), 407–422.

Delbeuck, X., Van der Linden, M., & Collette, F. (2003). Alzheimer's disease as a disconnection syndrome? *Neuropsychology Review, 13*(2), 79–92.

den Heijer, T., Oudkerk, M., Launer, L. J., van Duijn, C. M., Hofman, A., & Breteler, M. M. (2002). Hippocampal, amygdalar, and global brain atrophy in different apolipoprotein E genotypes. *Neurology, 59*(5), 746–748.

Douaud, G., Refsum, H., de Jager, C. A., Jacoby, R., Nichols, T. E., Smith, S. M., Smith, A. D. (2013). Preventing Alzheimer's disease-related gray matter atrophy by B-vitamin treatment. *Proceedings of the National Academy of Sciences of the United States of America, 110*(23), 9523–9528.

Duyckaerts, C., & Dickson, D. W. (2003). *Neurodegeneration: the molecular pathology of dementia and movement disorders* (pp. 46–65). Basel: Neurpath Press.

Ewers, M., Frisoni, G. B., Teipel, S. J., Grinberg, L. T., Amaro, E., Jr., Heinsen, H., et al. (2011). Staging Alzheimer's disease progression with multimodality neuroimaging. *Progress in Neurobiology, 95*(4), 535–546.

Fan, Y., Resnick, S. M., Wu, X., & Davatzikos, C. (2008). Structural and functional biomarkers of prodromal Alzheimer's disease: a high-dimensional pattern classification study. *NeuroImage, 41*(2), 277–285.

Farrer, L. A., Cupples, L. A., Haines, J. L., Hyman, B., Kukull, W. A., Mayeux, R., et al. (1997). Effects of age, sex, and ethnicity on the association between apolipoprotein E genotype and Alzheimer disease. A meta-analysis. APOE and Alzheimer disease meta analysis consortium. *JAMA, 278*(16), 1349–1356.

Fasulo, L., Ugolini, G., Visintin, M., Bradbury, A., Brancolini, C., Verzillo, V., et al. (2002). The neuronal microtubule-associated protein Tau is a substrate for caspase-3 and an effector of apoptosis. *Journal of Neurochemistry, 75*(2), 624–633.

Filippi, M., Agosta, F., Barkhof, F., Dubois, B., Fox, N. C., Frisoni, G. B., et al. (2012). EFNS task force: the use of neuroimaging in the diagnosis of dementia. *European Journal of Neurology, 19*(12), e131–e140. 1487–1501.

Filippini, N., Rao, A., Wetten, S., Gibson, R. A., Borrie, M., Guzman, D., et al. (2009). Anatomically-distinct genetic associations of APOE ε4 allele load with regional cortical atrophy in Alzheimer's disease. *NeuroImage, 44*(3), 724–728.

Fjell, A. M., & Walhovd, K. B. (2011). Neuroimaging results impose new views on Alzheimer's dIsease—the role of amyloid revised. *Molecular Neurobiology, 45*, 153–172.

Frisoni, G. B., Pievani, M., Testa, C., Sabattoli, F., Bresciani, L., Miniussi, M., et al. (2007). The topography of gray matter involvement in early and late-onset Alzheimer's disease. *Brain, 130*, 720–730.

Furney, S. J., Simmons, A., Breen, G., Pedroso, I., Lunnon, K., Proitsi, P., et al. (2011). Genome-wide association with MRI atrophy measures as a quantitative trait locus for Alzheimer's disease. *Molecular Psychiatry, 16*(11), 1130–1138.

Gatz, M., Pedersen, N. L., Berg, S., Johansson, B., Johansson, K., Mortimer, J. A., et al. (1997). Heritability for Alzheimer's disease: the study of dementia in Swedish twins. *Journals of Gerontology. Series A, Biological Sciences and Medical Sciences, 52*(2), M117–M125.

Gelfand, Y., & Kaplitt, M. G. (2012). Gene therapy for psychiatric disorders. *World Neurosurgery*. doi:10.1016/j.wneu.2012.12.028.

Geschwind, N. (1965). Disconnection syndrome in animals and man. *Brain, 88*, 237–294.

Giambattistelli, F., Bucossi, S., Salustri, C., Panetta, V., Mariani, S., Siotto, M., et al. (2012). Effects of hemochromatosis and transferrin gene mutations on iron dyshomeostasis, liver dysfunction and on the risk of Alzheimer's disease. *Neurobiology of Aging, 33*(8), 1633–1641.

Gili, T., Cercignani, M., Serra, L., Perri, R., Giove, F., Maraviglia, B., et al. (2011). Regional brain atrophy and functional disconnection across Alzheimer's disease evolution. *Journal of Neurology, Neurosurgery, and Psychiatry, 82*(1), 58–66.

Glahn, D. C., Thompson, P. M., & Blangero, J. (2007). Neuroimaging endophenotypes: strategies for finding genes influencing brain structure and function. *Human Brain Mapping, 28*, 488–501.

Glahn, D. C., Curran, J. E., Winkler, A. M., Carless, M. A., Kent, J. W., Jr., Charlesworth, J. C., et al. (2012). High dimensional endophenotype ranking in the search for major depression risk genes. *Biological Psychiatry, 71*, 6–14.

Gottesman, I. I., & Gould, T. D. (2003). The endophenotype concept in psychiatry: etymology and strategic intentions. *The American Journal of Psychiatry, 160*(4), 636–645.

Guerreiro, R. J., & Hardy, J. (2012). TOMM40 association with Alzheimer disease: tales of APOE and linkage disequilibrium. *Archives of Neurology, 69*(10), 1243–1244.

Guerreiro, R., Wojtas, A., Bras, J., Carrasquillo, M., Rogaeva, E., Majounie, E., et al. (2013). TREM2 variants in Alzheimer's disease. *New England Journal of Medicine, 368*(2), 117–127.

Guitart, X., Codony, X., & Monroy, X. (2004). Sigma receptors: biology and therapeutic potential. *Psychopharmacology, 174*(3), 301–319.

Hafez, D. M., Huang, J. Y., Richardson, J. C., Masliah, E., Peterson, D. A., & Marr, R. A. (2012). F-spondin gene transfer improves memory performance and reduces amyloid-beta levels in mice. *Neuroscience, 223*, 465–472.

Hagmann, P., Cammoun, L., Gigander, X., Meuli, R., Honey, C. J., Wedeen, V. J., et al. (2008). Mapping the structural core of the human cerebral cortex. *PLoS Biology, 6*(7), 1479–1493.

Harold, D., Abraham, R., Hollingworth, P., Sims, R., Gerrish, A., Hamshere, M. L., et al. (2009). Genome-wide association study identifies variants at CLU and PICALM associated with Alzheimer's disease. *Nature Genetics, 41*(10), 1088–1093.

Harris, S. E., Fox, H., Wright, A. F., Hayward, C., Starr, J. M., Whalley, L. J., et al. (2006). The brain-derived neurotrophic factor Val66Met polymorphism is associated with age-related change in reasoning skills. *Molecular Psychiatry, 11*(5), 505–513.

Hashimoto, T., Wakabayashi, T., Watanabe, A., Kowa, H., Hosoda, R., Nakamura, A., et al. (2002). CLAC: a novel Alzheimer amyloid plaque component derived from a transmembrane precursor, CLAC-P/collagen type XXV. *EMBO Journal, 21*(7), 1524–1534.

Heinzerling, K. G., & Shoptaw, S. (2012). Gender, brain-derived neurotrophic factor Val66Met, and frequency of methamphetamine use. *Gender Medicine, 9*(2), 112–120.

Hibar, D. P., Stein, J. L., Kohannim, O., Jahanshad, N., Saykin, A. J., Shen, L., et al. (2011). Voxelwise gene-wide association study (vGeneWAS): multivariate gene-based association testing in 731 elderly subjects. *NeuroImage, 54*(4), 1875–1891.

Hibar, D. P., Jahanshad, N., Stein, J. L., Kohannim, O., Toga, A. W., Medland, S. E., et al. (2012). Alzheimer's disease risk gene, GAB2, is associated with regional brain volume differences in 755 young healthy twins. *Twin Research and Human Genetics, 15*(3), 286–295.

Hinrichs, C., Singh, V., Xu, G., Johnson, S. C., & Alzheimer's disease neuroimaging initiative. (2011). Predictive markers for AD in a multi-modality framework: an analysis of MCI progression in the ADNI population. *NeuroImage, 55*(2), 574–589.

Ho, A., & Sudhof, T. C. (2004). Binding of F-spondin to amyloid-beta precursor protein: a candidate amyloid-beta precursor protein ligand that modulates amyloid-beta precursor protein cleavage. *Proceedings of the National Academy of Sciences of the United States of America, 101*(8), 2548–2553.

Hua, X., Leow, A. D., Parikshak, N., Lee, S., Chiang, M. C., Toga, A. W., et al. (2008). Tensor-based morphometry as a neuroimaging bio-marker for Alzheimer's disease: an MRI study of 676 AD, MCI, and normal subjects. *NeuroImage, 43*(3), 458–469.

Hua, Y., Zhao, H., Kong, Y., & Ye, M. (2011). Association between the MTHFR gene and Alzheimer's disease: a meta-analysis. *International Journal of Neuroscience, 121*(8), 462–471.

Jack, C. R., Jr., Knopman, D. S., Jagust, W. J., Shaw, L. M., Aisen, P. S., Weiner, M. W., et al. (2010a). Hypothetical model of dynamic bio-markers of the Alzheimer's pathological cascade. *Lancet Neurology, 9*(1), 119–128.

Jack, C. R., Jr., Bernstein, M. A., Borowski, B. J., Gunter, J. L., Fox, N. C., Thompson, P. M., et al. (2010b). Update on the magnetic resonance imaging core of the Alzheimer's disease neuroimaging initiative. *Alzheimers Dement, 6*, 212–220.

Jahanshad, N., Valcour, V. G., Nir, T. M., Kohannim, O., Busovaca, E., Nicolas, K., et al. (2012a). Disrupted brain networks in the aging HIV+ population. *Brain Connect, 2*, 335–344.

Jahanshad, N., Kohannim, O., Hibar, D. P., Stein, J. L., McMahon, K. L., de Zubicaray, G. I., et al. (2012b). Brain structure in healthy adults is related to serum transferrin and the H63D polymorphism in the HFE gene. *Proceedings of the National Academy of Sciences of the United States of America, 109*(14), E851–E859.

Jahanshad, N., Rajagopalan, P., Hua, X., Hibar, D. P., Nir, T. M., Toga, A. W., et al. (2013a). Genome-wide scan of healthy human connectome discovers SPON1 gene variant influencing dementia severity. *Proceedings of the National Academy of Sciences of the United States of America, 110*(12), 4768–4773.

Jahanshad, N., Rajagopalan, P., Thompson, P. M. (2013b). Neuroimaging, Nutrition, and Iron-Related Genes, Invited Review for *Cellular Molecular and Life Science Reviews* (CMLS Reviews), in press.

Jin, C., Li, W., Yuan, J., Xu, W., & Cheng, Z. (2012). Association of the CR1 polymorphism with late-onset Alzheimer's disease in Chinese Han populations: a meta-analysis. *Neuroscience Letters, 527*(1), 46–49.

Johnson, S. C., La Rue, A., Hermann, B. P., Xu, G., Koscik, R. L., Jonaitis, E. M., et al. (2011). The effect of TOMM40 poly-T length on gray matter volume and cognition in middle-aged persons with APOE epsilon3/epsilon3 genotype. *Alzheimers Dement, 7*(4), 456–465.

Jones, B. (2013). Alzheimer disease: TREM2 linked to late-onset AD. *Nature Reviews Neurology, 9*(1), 5.

Jonsson, T., Stefansson, H., Steinberg, S., Jonsdottir, I., Jonsson, P. V., Snaedal, J., et al. (2013). Variant of TREM2 associated with the risk of Alzheimer's disease. *New England Journal of Medicine, 368*(2), 107–116.

Ke, Y., & Ming Qian, Z. (2003). Iron misregulation in the brain: a primary cause of neurodegenerative disorders. *Lancet Neurology, 2*(4), 246–253.

Kohannim, O., Jahanshad, N., Braskie, M. N., Stein, J. L., Chiang, M. C., Reese, A. H., et al. (2012). Predicting white matter integrity from common genetic variants. *Neuropsychopharmacology*. doi:10.1038/npp.2012.49.

Lambert, J. C., Heath, S., Even, G., Campion, D., Sleegers, K., Hiltunen, M., et al. (2009). Genome-wide association study identifies variants at CLU and CR1 associated with Alzheimer's disease. *Nature Genetics, 41*(10), 1094–1099.

Lee, T. S., Goh, L., Chong, M. S., Chua, S. M., Chen, G. B., Feng, L., et al. (2012). Downregulation of TOMM40 expression in the blood of Alzheimer disease subjects compared with matched controls. *Journal of Psychiatric Research, 46*(6), 828–830.

Lehtovirta, M., Laakso, M. P., Soininen, H., Helisalmi, S., Mannermaa, A., Helkala, E. L., et al. (1995). Volumes of hippocampus, amygdala and frontal lobe in Alzheimer patients with different apolipoprotein E genotypes. *Neuroscience, 67*(1), 65–72.

Levran, O., Yuferov, V., & Kreek, M. J. (2012). The genetics of the opioid system and specific drug addictions. *Human Genetics, 131*(6), 823–842.

Li, D., Zhao, H., Kranzler, H. R., Oslin, D., Anton, R. F., Farrer, L. A., et al. (2012). Association of COL25A1 with comorbid antisocial personality disorder and substance dependence. *Biological Psychiatry, 71*(8), 733–740.

Lichtheim, L. (2006). On aphasia. *Brain, 129*(6), 1347–1350.

Lin, M., Zhao, L., Fan, J., Lian, X. G., Ye, J. X., Wu, L., et al. (2012). Association between HFE polymorphisms and susceptibility to Alzheimer's disease: a meta-analysis of 22 studies including 4,365 cases and 8,652 controls. *Molecular Biology Reports, 39*(3), 3089–3095.

Mansoori, N., Tripathi, M., Luthra, K., Alam, R., Lakshmy, R., Sharma, S., et al. (2012). MTHFR (677 and 1298) and IL-6-174 G/C genes in pathogenesis of Alzheimer's and vascular dementia and their epistatic interaction. *Neurobiology of Aging, 33*(5), e1–e8.

Marrazzo, A., Caraci, F., Salinaro, E. T., Su, T. P., Copani, A., & Ronsisvalle, G. (2005). Neuroprotective effects of sigma-1 receptor

agonists against β-amyloid-induced toxicity. *Neuroreport, 16*(11), 1223–1226.

Mathis, C. A., Kuller, L. H., Klunk, W. E., Snitz, B. E., Price, J. C., Weissfeld, L. A., et al. (2012). In vivo assessment of amyloid-β deposition in nondemented very elderly subjects. *Annals of Neurology*. doi:10.1002/ana.23797.

Maurice, T., & Su, T. P. (2009). The pharmacology of sigma-1 receptors. *Pharmacology and Therapeutics, 124*(2), 195–206.

Munoz, K. E., Hype, L. W., & Hariri, A. R. (2010). Imaging genetics. *Journal of the American Academy of Child and Adolescent Psychiatry, 48*(4), 356–361.

Naj, A. C. (+over 100 authors) (2011). Common variants at MS4A4/MS4A6E, CD2AP, CD33 and EPHA1 are associated with late-onset Alzheimer's disease. *Nature Genetics,* 43, 436–441.

Nakagawa, T., & Kaneko, S. (2013). SLC1 glutamate transporters and diseases: psychiatric diseases and pathological pain. *Current Molecular Pharmacology, 6*(2), 66–73.

Neumann, H., & Daly, M. J. (2013). Variant TREM2 as risk factor for Alzheimer's disease. *New England Journal of Medicine, 368*(2), 182–184.

Nussbaum, R. L. (2013). Genome-wide association studies, Alzheimer disease, and understudied populations. *JAMA, 309*(14), 1527–1528.

O'Dwyer, L., Lamberton, F., Matura, S., Tanner, C., Scheibe, M., Miller, J., et al. (2012). Reduced hippocampal volume in healthy young ApoE4 carriers: an MRI study. *PLoS One, 7*(11), e48895. doi:10.1371/journal.pone.0048895.

Ortega-Roldan, J. L., Ossa, F., & Schnell, J. R. (2013). Characterization of the human sigma-1 receptor chaperone domain structure and Binding Immunoglobulin Protein (BiP) interactions. *Journal of Biological Chemistry, 288*(29), 21448–21457.

Pradhan, A. A., Befort, K., Nozaki, C., Gaveriaux-Ruff, C., & Kieffer, B. L. (2011). The delta opioid receptor: an evolving target for the treatment of brain disorders. *Trends in Pharmacological Sciences, 32*(10), 581–590.

Rajagopalan, P., Hua, X., Jack, C. R., Weiner, M. W., Toga, A. W., Thompson, P. M., et al. (2011). Homocysteine levels are associated with regional brain volumes in 732 elderly subjects. *NeuroReport, 22*(8), 391–395.

Rajagopalan, P., Jahanshad, N., Stein, J. L., Hua, X., Madsen, S. K., Kohannim, O., et al. (2012a). Common folate gene variant, MTHFR C677T, is associated with brain structure in two independent cohorts of people with mild cognitive impairment. *NeuroImage: Clinical, 1*(1), 179–187.

Rajagopalan, P., Hua, X., Kohannim, O., Toga, A. W., Jack, Jr., C. R., Weiner, M. W., Thompson, P. M., and the Alzheimer's Disease Neuroimaging Initiative (2012b). Mapping the interaction between *APOE*-epsilon4 and *TOMM40* SNPs and Brain Atrophy: An N=705 ADNI study, *Organization for Human Brain Mapping (OHBM)* 2012, Beijing, China, June 10–14, 2012.

Rajagopalan, P., Hibar, D. P., Thompson, P. M. (2013). *TREM2* risk variant and loss of brain tissue. *The New England Journal of Medicine*, in press.

Reiman, E. M., Webster, J. A., Myers, A. J., Hardy, J., Dunckley, T., Zismann, V. L., et al. (2007). GAB2 alleles modify Alzheimer's risk in APOE epsilon4 carriers. *Neuron, 54*(5), 713–720.

Rietveld, C. A. (+over 100 authors) (2013). GWAS of 126,559 Individuals Identifies Genetic Variants Associated with Educational Attainment. Science, doi: 10.1126/science.1235488

Roses, A. D., Lutz, M. W., Amrine-Madsen, H., Saunders, A. M., Crenshaw, D. G., Sundseth, S. S., et al. (2010). A TOMM40 variable-length polymorphism predicts the age of late-onset Alzheimer's disease. *Pharmacogenomics Journal, 10*(5), 375–384.

Roussotte, F. F., Jahanshad, N., Hibar, D. P., Sowell, E. R., Kohannim, O., Barysheva, M., et al. (2013). A commonly carried genetic variant in the delta opioid receptor gene, *OPRD1*, is associated with smaller regional brain volumes: Replication in elderly and young populations. *Human Brain Mapping*. doi:10.1002/hbm.22247.

Sarajarvi, T., Tuusa, J. T., Haapasalo, A., Lackman, J. J., Sormunen, R., Helisalmi, S., et al. (2011). Cysteine 27 variant of the delta-opioid receptor affects amyloid precursor protein processing through altered endocytic trafficking. *Molecular and Cellular Biology, 31*(11), 2326–2340.

Schmidt, R., Ropele, S., Pendl, B., Ofner, P., Enzinger, C., Schmidt, H., et al. (2008). Longitudinal multimodal imaging in mild to moderate Alzheimer's disease: a pilot study with memantine. *Journal of Neurology, Neurosurgery, and Psychiatry, 79*(12), 1312–1317.

Shen, L., Thompson, P. M., Potkin, S. G., Bertram, L., Farrer, L. A., Foroud, T. M., Green, R. C., Hu, X., Huentelman, M. J., Kim, S., Kauwe, J. S. K., Li, Q., Liu, E., Moore, J. H., Munsie, L., Nho, K., Ramanan, V. K., Stone, D. J., Swaminathan, S., Toga, A. W., Weiner, M. W., Saykin, A. J., for the Alzheimer's Disease Neuroimaging Initiative (2013). Genetic analysis of quantitative phenotypes in AD and MCI: Imaging, Cognition and Biomarkers, to be submitted to *Brain Imaging & Behavior*, Special Issue on Imaging Genetics (ed. John D. van Horn), June 13 2013.

Sherva, R., Tripodis, Y., Bennett, D. A., Chibnik, L. B., Crane, P. K., de Jager, P. L., et al. (2013). Genome-wide association study of the rate of cognitive decline in Alzheimer's disease. *Alzheimer's Dement*. doi:10.1016/j.jalz.2013.01.008.

Speliotes, E. K. (+over 100 authors) (2010). Association analyses of 249, 796 individuals reveal 18 new loci associated with body mass index. *Nature Genetics,* 42, 937–948.

Sporns O. (2011). Neworks of the brain. Cambridge, MA, p. 5–31.

Stein, J. L., Hua, X., Morra, J. H., Lee, S., Hibar, D. P., Ho, A. J., et al. (2010). Genome-wide analysis reveals novel genes influencing temporal lobe structure with relevance to neurodegeneration in Alzheimer's disease. *NeuroImage, 51*(2), 542–554.

Tanzi, R. E. (2012). The genetics of Alzheimer disease. *Cold Spring Harbor Perspectives in Medicine, 2*(10).

Teng, L., Zhao, J., Wang, F., Ma, L., & Pei, G. (2010). A GPCR/secretase complex regulates beta- and gamma-secretase specificity for Abeta production and contributes to AD pathogenesis. *Cell Research, 20*(2), 138–153.

Teng, E., Kepe, V., Frautschy, S. A., Liu, J., Satyamurthy, N., Yang, F., et al. (2011). [F-18] FDDNP microPET imaging correlates with brain Aβ burden in a transgenic rat model of Alzheimer disease: effects of aging, in vivo blockade, and anti-Aβ antibody treatment. *Neurobiology of Disease, 43*(3), 565–575.

Thambisetty, M., Beason-Held, L. L., An, Y., Kraut, M., Nalls, M., Hernandez, D. G., et al. (2013). Alzheimer risk variant CLU and brain function during aging. *Biological Psychiatry, 73*(5), 399–405.

Thathiah, A., & De Strooper, B. (2011). The role of G protein-coupled receptors in the pathology of Alzheimer's disease. *Nature Review Neuroscience, 12*(2), 73–87.

Thompson, P. M., & Jahanshad, N. (2012). Ironing out neurodegeneration: is iron intake important during the teenage years? *Expert Review of Neurotherapeutics, 12*(6), 629–631.

Thompson, P. M. (+over 150 authors) for the ENIGMA Consortium (2013b). The ENIGMA Consortium: Large-scale Collaborative Analyses of Neuroimaging and Genetic Data, to be submitted to *Brain Imaging & Behavior*, Special Issue on Imaging Genetics (ed. John D. van Horn), June 15 2013.

Thompson, P. M., Hayashi, K. M., de Zubicaray, G., Janke, A. L., Rose, S. E., Semple, J., et al. (2003). Dynamics of gray matter loss in Alzheimer's disease. *Journal of Neuroscience, 23*(3), 994–1005.

Thompson, P. M., Hayashi, K. M., Simon, S., Geaga, J., Hong, M. S., Sui, Y., et al. (2004). Structural abnormalities in the brains of human subjects who use methamphetamine. *Journal of Neuroscience, 24*(26), 6028–6036.

Thompson, P. M., Glahn, D., Ge, T., Jahanshad, N., Nichols, T. E. (2013a). Genetics of the Connectome, Invited Review Paper for the Special Issue on the Connectome, *NeuroImage*, in press, May 8 2013.

Toga, A. W., & Thompson, P. M. (2013). Connectomics sheds new light on Alzheimer's disease. *Biological Psychiatry, 73*(5), 390–392.

Tong, Y., Xu, Y., Scearce-Levie, K., Ptacek, L. J., & Fu, Y. H. (2010). COL25A1 triggers and promotes Alzheimer's disease-like pathology in vivo. *Neurogenetics, 11*(1), 41–52.

Van Cauwenberghe, C., Bettens, K., Engelborghs, S., Vandenbulcke, M., Van Dongen, J., Vermeulen, S., et al. (2013). Complement receptor 1 coding variant p.Ser1610Thr in Alzheimer's disease and related endophenotypes. *Neurobiol Aging*.

Vemuri, P., Wiste, H. J., Weigand, S. D., Shaw, L. M., Trojanowski, J. Q., Weiner, M. W., et al. (2009). MRI and CSF biomarkers in normal, MCI, and AD subjects: predicting future clinical change. *Neurology, 73*(4), 294–301.

Ventriglia, M., Bocchio Chiavetto, L., Benussi, L., Binetti, G., Zanetti, O., Riva, M. A., et al. (2002). Association between the BDNF 196 A/G polymorphism and sporadic Alzheimer's disease. *Molecular Psychiatry, 7*(2), 136–137.

Voineskos, A. N., Lerch, J. P., Felsky, D., Shaikh, S., Rajji, T. K., Miranda, D., et al. (2011). The brain-derived neurotrophic factor Val66Met polymorphism and prediction of neural risk for Alzheimer disease. *Archives of General Psychiatry, 68*(2), 198–206.

Walhovd, K. B., Fjell, A. M., Brewer, J., McEvoy, L. K., Fennema-Notestine, C., Hagler, D. C., Jr., et al. (2010). Combining MR imaging, positron-emission tomography, and CSF biomarkers in the diagnosis and prognosis of Alzheimer disease. *AJNR—American Journal of Neuroradiology, 31*(2), 347–354.

Wang, S. W., Wang, Y. J., Su, Y. J., Zhou, W. W., Yang, S. G., Zhang, R., et al. (2012a). Rutin inhibits beta-amyloid aggregation and cytotoxicity, attenuates oxidative stress, and decreases the production of nitric oxide and proinflammatory cytokines. *Neurotoxicology, 33*(3), 482–490.

Wang, H., Nie, F., Huang, H., Risacher, S. L., Saykin, A. J., Shen, L., et al. (2012b). Identifying disease sensitive and quantitative trait-relevant biomarkers from multidimensional heterogeneous imaging genetics data via sparse multimodal multitask learning. *Bioinformatics, 28*(12), i127–i136.

Wegrzyn, M., Teipel, S. J., Oltmann, I., Bauer, A., Thome, J., Grossmann, A., et al. (2012). Structural and functional cortical disconnection in Alzheimer's disease: A combined study using diffusion tensor imaging and transcranial magnetic stimulation. *Psychiatry Research, 212*(3), 192–200.

Wernicke, C. (1874/1977). *Der aphasische symtomencomplex: Eine psychologische studie auf anatomicher basis*. Breslau: Cohn und Weigert, 1874.

Wishart, H. A., Saykin, A. J., McAllister, T. W., Rabin, L. A., McDonald, B. C., Flashman, L. A., et al. (2006). Regional brain atrophy in cognitively intact adults with a single APOE ε4 allele. *Neurology, 67*(7), 1221–1224.

Wolk, D. A., Price, J. C., Madeira, C., Saxton, J. A., Snitz, B. E., Lopez, O. L., et al. (2012). Amyloid imaging in dementias with atypical presentation. *Alzheimers Dement, 8*(5), 389–398.

Wong, D. F., Rosenberg, P. B., Zhou, Y., Kumar, A., Raymont, V., Ravert, H. T., et al. (2010). In vivo imaging of amyloid deposition in Alzheimer disease using the radioligand 18F-AV-45 (florbetapir [corrected] F 18). *Journal of Nuclear Medicine, 51*(6), 913–920.

Xiao, Q., Gil, S. C., Yan, P., Wang, Y., Han, S., Gonzales, E., et al. (2012). Role of phosphatidylinositol clathrin assembly lymphoid-myeloid leukemia (PICALM) in intracellular amyloid precursor protein (APP) processing and amyloid plaque pathogenesis. *Journal of Biological Chemistry, 287*(25), 21279–21289.

Zhang, H., Kranzler, H. R., Yang, B. Z., Luo, X., & Gelernter, J. (2008). The OPRD1 and OPRK1 loci in alcohol or drug dependence: OPRD1 variation modulates substance dependence risk. *Molecular Psychiatry, 13*(5), 531–543.

Zhang, M. Y., Miao, L., Li, Y. S., & Hu, G. Y. (2010). Meta-analysis of the methylenetetrahydrofolate reductase C677T polymorphism and susceptibility to Alzheimer's disease. *Neuroscience Research, 68*(2), 142–150.

Zhang, D., Shen, D., & Alzheimer's The Alzheimer's Disease Neuroimaging Initiative. (2012). Multi-modal multi-task learning for joint prediction of multiple regression and classification variables in Alzheimer's disease. *NeuroImage, 59*(2), 895–907.

CHAPTER 7

Future works

The work presented herein sheds light on white matter integrity in health and disease, however, is only the beginning of this line of research, leaving many questions unanswered. Some of the next aims are already in progress, and entail: ***Aim 7.1*** – the linkage between imaging signals to cellular and biochemical correlates in mouse models of Alzheimer's disease.

Aim 7.1 Novel protocol for processing DWIs in mouse

Nowadays, engineered animal models can be used to mimic human disease (*i.e.,* human Tau mutant). Also, these can be studied using both advanced imaging techniques and histological assessments to tackle a more complex notion – the validation of neuroimaging techniques using connectivity patterns developed with histological information. Preliminary work was done to aid the understanding of structural patterns of disruptions in the white matter in DWIs acquired at high-field 11.6 T in 7 hTau mice and 6 wild types. This work is in preparation for large-scale connectivity analyses that will ultimately lead to correlations with histological data.

In the same line of work, we will be able to design data scanning protocols by analyzing how scans vary using protocols in mice, compared to those used in humans. Similarly, we will be able to aid the understanding of the limitation of DTI for therapeutic quantifications and finally, aid the diagnosis and treatment of Alzheimer's disease.

Aim 7.1

This section is adapted from:

Daianu M, Jahanshad N, Eschenburg KM, Villalon-Reina JE, Nir TM, Jacobs R, Dong H, Zlokovic BV, Thompson PM. Mapping Brain Connectivity with Diffusion Tensor Imaging in Human Tau Mutant Mice. Organization of Human Brain Mapping (OHBM), *submitted*, January 2014.

Mapping Brain Connectivity with Diffusion Tensor Imaging

in Human Tau Mutant Mice

Madelaine Daianu[1,2], Neda Jahanshad[2], Kristian M. Eschenburg[2], Julio Villalon[2], Talia M. Nir[2],

Hongwei Dong[2] , Russell Jacobs[3], Berislav V. Zlokovic[4], Paul M. Thompson[1, 2, 5]

[1] Department of Neurology, UCLA School of Medicine, Los Angeles
[2] Imaging Genetics Center, Institute for Neuroimaging & Informatics,
University of Southern California, Los Angeles
[3] Biological Imaging Center, California Institute of Technology
[4] Zilhka Neurogenetic Institute, Keck School of Medicine, University of Southern California, Los Angeles
[5] Departments of Neurology, Psychiatry, Radiology, Engineering, Pediatrics, and Ophthalmology, USC

Introduction

Brain mapping is crucial for understanding the effects of disease, genetics and therapeutic interventions on the living brain, but the underlying cellular basis of the signals is easier to investigate in experimental animal models. Here we describe *in vivo* imaging and connectivity analysis in mutant mice. We developed and tested an analysis protocol to process high-field diffusion-weighted MRI in the hTau (human Tau mutant) mouse model acquired at 11.7 Tesla. Results from this preliminary data will aid the assessment of DWI data in mice, in preparation for larger scale brain connectivity analyses and correlations with histological information that link imaging signals to their cellular and biochemical correlates.

Methods

All 13 mice (7 hTau and 6 wild type) were scanned with an 11.7 Tesla Bruker BioSpin MRI scanner at the California Institute of Technology. Diffusion weighted images (DWI) were acquired using a spin echo pulse sequence (256x170x128 matri*x;* voxel size: 0.1x0.1x0.1 mm^3, TE= 16 ms; TE= 300 ms, δ=3 ms, Δ=8 ms). 7 separate volumes were acquired for each DWI scan: 1 T2-weighted volume with no diffusion sensitization (b_0 image) and 6 diffusion-weighted images (b=3000 s/mm^2). The mice were sacrificed at 6 months, fixed brains remained within the skull and were soaked in 5mM Prohance for 4 days prior to imaging; resulting in DWI volumes acquired with high precision and no motion artifacts. To correct for eddy current distortions we used the "eddy correct FSL" tool (www.fmrib.ox.ac.uk/fsl) and aligned each DWI volume to the b_0 image. We removed extra cerebral tissue using the "skull-stripping" Brain Extraction Tool (BET) from FSL (Smith, 2002). All resulting volumes were visually inspected and manually edited as needed. Then, all images were linearly aligned to one individual hTau DWI scan using FLS's *flirt* function (Jenkinson et al., 2002) with 12 degrees of freedom to allow rotations and translations in 3D; linearly aligned images were adjusted to a cubic image size of 180x180x180.

We elastically registered the skull-stripped b_0 images to a minimum deformation template (Gutman et al., 2010) created using all 13 linearly registered images, to ensure that all scans were in the same space. We applied the resulting 3D deformation fields to the remaining 6 DWI volumes and as a final step, a corrected gradient table was calculated to account for the linear registrations between the b_0 images.

Fractional anisotropy (FA) and mean diffusivity (MD) maps were computed using the FSL *dtifit* tool, for which a single diffusion tensor was modeled at each voxel in the brain (Basser et al., 1994). The diffusion tensor was computed using the eddy corrected and elastically registered DWI scans.

We applied a Gaussian lowpass filter of size 5 to the FA and MD images and then ran a voxel-wise linear regression with hTau mice coded as 1 and wild-type mice coded as 0. A regional FDR correction (Langers et al., 2007) was used to correct for multiple comparisons across voxels. Additionally, we performed searchlight statistics on the resulting *p*-value outputs from the regression.

As a proof of concept, tractography was performed on the eddy corrected DWI scans using a deterministic method, *Trackvis* (http://trackvis.org/, **Fig. 1d**).

Figure 1. Workflow indicating a.) 3D mouse brain; b.) axial DWI map; c.) axial FA map and, d.) tractography of mouse corpus callosum computed using Trackvis overlaid on the FA map. Brainsuite and FSL were used for visualization purposes.

Results

We found an increase in MD in hTau, relative to the wildtype mice, in the corpus callosum (corrected *p*-value<0.044; **Fig. 2**). No significant differences were found between FA maps of hTau and wild type. Increases in MD in the white matter of Alzheimer's disease (AD) subjects were also detected in a recent study assessing structural changes in the AD brain (Nir et al., 2013).

Conclusion

This pilot study is aimed to design scanning and image processing protocols for mice, soon to be linked with histological information. For future studies, a larger number of subjects will be assessed scanned with a higher number of diffusion gradients
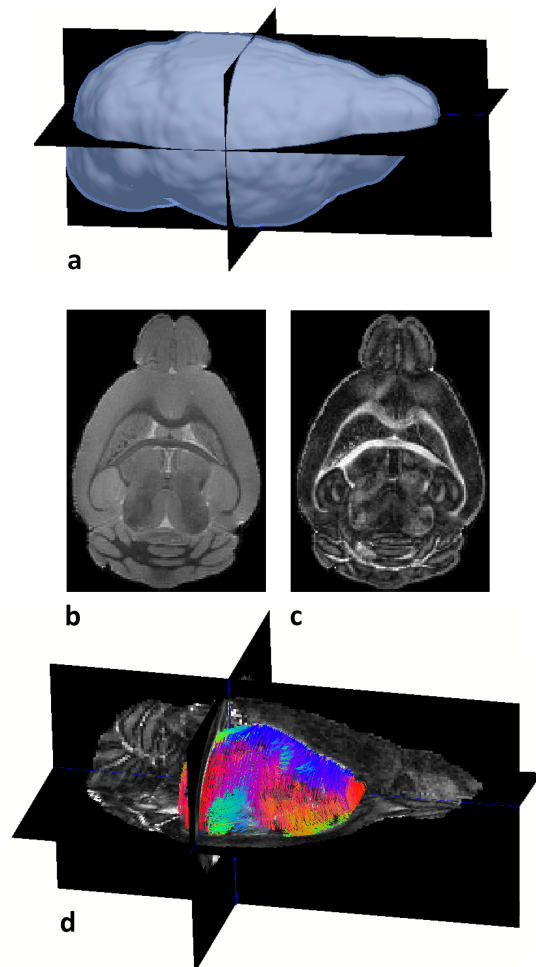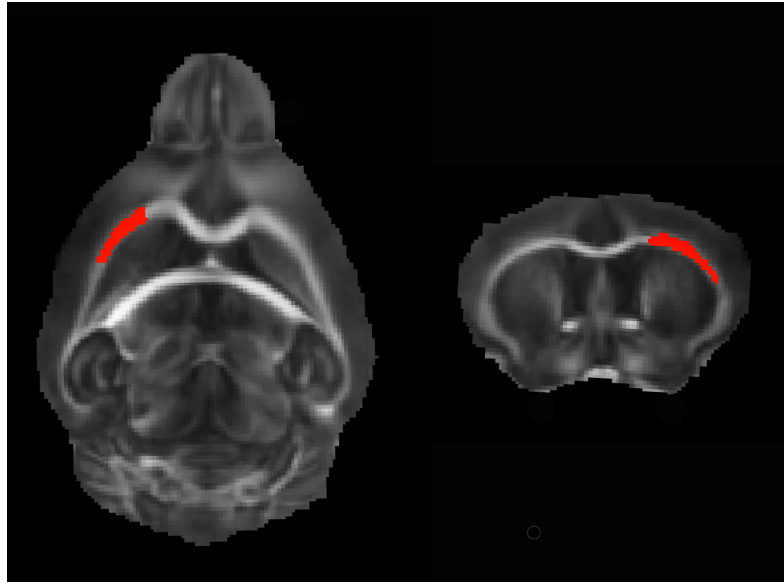
Figure 2. Positive *beta*-map showing an elevation in MD in the corpus callosum of hTau mice, relative to wild type mice, from a voxel-wise linear regression with hTau coded at 1 and wild type coded as 0 (corrected *p*-values<0.044).

References:

1. Basser, P.J., Mattiello, J., LeBihan, D. (1994), 'MR Diffusion Tensor Spectroscopy and Imaging', Biophysical Journal, vol. 66, pp. 259-267.
2. Gutman, B., Svarer, C., Leow, A.D., Yanovsky, I., Toga, A.W., Thompson, P.M. (2010), 'Creating unbiased minimal deformation templates for brain volume registration', OHBM 2010. http://scholar.google.com/citations?view_op=view_citation&hl=en&user=s10OwfIAAAAJ&citation_for_view=s10OwfIAAAAJ:YsMSGLbcyi4C
3. Langers, D.R., Jansen, J.F., Backes, W.H. (2007), 'Enhanced signal detection in neuroimaging by means of regional control of the global false discovery rate', Neuroimage, vol. 38, no. 1, pp. 43-56.
4. Jenkinson, M., Bannister, P., Brady, M., Smith, S. (2002), 'Improved optimization for the robust and accurate linear registration and motion correction of brain images', Neuroimage, vol. 17, pp. 825-841.
5. Nir, T.M., Jahanshad, N., Villalon-Reina, J.E., Toga, A.W., Jack, C.R., Weiner, M.W., Thompson, P.M., (2013), 'Effectiveness of regional DTI measures in distinguishing Alzheimer's disease, MCI, and normal aging', NeuroImage:Clinical, vol. 3, pp. 180–195.
6. Smith, S.M., (2002), 'Fast robust automated brain extraction', Hum Brain Mapp, vol. 17, pp. 143-155.

REFERENCES

Aganj, I., Lenglet, C., Sapiro, G., Yacoub, E., Ugurbil, K., Harel, N. (2010). Reconstruction of the orientation distribution function in single- and multiple-shell q-ball imaging within constant solid angle. Mag Res Med, 64:554-566.

Aganj, I., Lenglet, C., Jahanshad, N., Yacoub, E., Harel, N., Thompson, P.M., Sapiro G. (2011). A Hough transform global probabilistic approach to multiple-subject diffusion MRI tractography. Med Image Analysis, 15:414-425.

Basser, P.J. & Pierpaoli, C. (1996). Microstructural and physiological features of tissues elucidated by quantitative diffusion-tensor MRI. J Magn Reson B, 111(3):209-19.

Bounova, G., de Weck, O.L. (2012). Overview of metrics and their correlation patterns for multiple-metric topology analysis on heterogeneous graph ensembles. Phys. Rev. E 85, 016117.

Bullmore E, Sporns O. (2009). Complex brain networks: graph theoretical analysis of structural and functional systems. Nature;10:186-198.

Chung, F.R.K., Faber, V., Manteuffel, T. A. (1994). SIAM J. Discrete Math. 7(3):443-457.

Euler, L. (1741). Solutio Problemat is ad Geometriam Situs Pertinentis, Commentarii Academiae Scientiarum Imperialis Petropolitanae 8, 128-140 = Opera Omnia (1);7:1-10.

Fiedler, M. (1973). Algebraic connectivity of graphs, Czechoslovak Math. J. 23:298-305.

Hammond, D.K., Scherrer, B, Warfield, S.K. (2013). Cortical graph smoothing: a novel method for exploiting DWI derived anatomical brain connectivity to improve EEG source estimation. IEEE Trans Med Imaging. 32(10):1952–1963.

Jahanshad, N., Rajagopalan, P., Hua, X., Hibar, D.P. et al. (2013). Genome-wide scan of healthy human connectome discovers SPON1 gene variant influencing dementia severity. PNAS 2013; 110(2): 4768–4773.

Lee, H., Kang, H., Chung, M.K., Kim, B.N., Lee, D.S. (2012). Persistent Brain Network Homology from the Perspective of Dendrogram. IEEE Trans Med Imaging;31(12):2267-77.

Mohar, B. (1991). The Laplacian spectrum of graphs. Graph Theory, Combinatorics, and Applications, vol. 2, pp. 1-28.

Norman, B. (1993). Algebraic Graph Theory (2nd ed.), Cambridge: Cambridge University Press. pp. 7-52.

Petrella, J.R. (2011). Use of graph Theory to Evaluate Brain Networks: A clinical Tool for a Small World? Radiology; 259(2):317-320.

Rubinov, M. and Sporns, O. (2010). Complex network measures of brain connectivity: uses and interpretations. Neuroimage;52(3):1059-69.

Seeley, W.W. (2010) Anterior insula degeneration in frontotemporal dementia. Brain Struct Funct.;214(5-6):465-75.

Sporns O. (2011). Networks of the Brain. Cambridge, MA: MIT Press, pp. 5–31.

Thompson, P.M., Hayashi, K.M., de Zubicaray, G., Janke, A.L., Rose, S.E., Semple, J., Herman, D., Hong, M.S., Dittmer, S.S., Doddrell, D.M., Toga, A.W. (2003). Dynamics of Gray Matter Loss in Alzheimer's Disease, J Neuroscience 23(3):994-1005.

Toga, A.W., Thompson, P.M. (2003) Mapping Brain Asymmetry. Nature Reviews Neurosci;4(1):37-48.

Tuch, D.S., Reese, T.G., Wiegell, M.R., Makris, N., Belliveau, J.W., & Wedeen, V.J. (2002). High angular resolution diffusion imaging reveals intravoxel white matter fiber heterogeneity. Magn Reson Med, 48(4), 577-82.

van den Heuvel, M.P. and Sporns O. (2011). Rich-club organization of the human connectome. J Neurosci, 2011;31(44):15775-15786.

van den Heuvel, M.P., Kahn, R.S., Goñi, J., Sporns, O. (2012). High-cost, high-capacity backbone for global brain communication. Proc. Natl. Acad. Sci.; 109(28):11372-11377.

Wedeen, V.J., Rosene, D.L., Wang, R., Dai, G., Mortazavi, F., Hagmann, P., Kaas, J.H., & Tseng, W.Y. (2012). The geometric structure of the brain fiber pathways. Science, 335(6076), 1628-34.